EFFECTS OF MICROSTRUCTURE ON THE SPALL BEHAVIOR OF ALUMINUM-MAGNESIUM ALLOYS
BY RICKY L. WHELCHEL

A Thesis
Presented to
The Academic Faculty

by

Ricky L. Whelchel

In Partial Fulfillment
of the Requirements for the Degree
Doctor of Philosophy in the
School of Materials Science and Engineering

Georgia Institute of Technology
March 2014

Copyright © 2014 by Ricky L. Whelchel

EFFECTS OF MICROSTRUCTURE ON THE SPALL BEHAVIOR OF ALUMINUM-MAGNESIUM ALLOYS
BY RICKY L. WHELCHEL

Approved by:

Dr. Naresh Thadhani, Advisor
School of Materials Science and Engineering
Georgia Institute of Technology

Dr. Thomas Sanders Jr., Co-Advisor
School of Materials Science and Engineering
Georgia Institute of Technology

Dr. Arun M. Gokhale
School of Materials Science and Engineering
Georgia Institute of Technology

Dr. Sunil Dwivedi
School of Materials Science and Engineering
Georgia Institute of Technology

Dr. Suveen Mathaudhu
Synthesis and Processing
Army Research Office

Victor Dangerfield
Research and Development
Universal Alloys Corporation

Date Approved: 24 February 2014

ACKNOWLEDGEMENTS

I would like to gratefully acknowledge the funding provided for this research provided by the United States Army Research Office under grant number W911NF-09-1-0403.

I wish to express my gratitude to my two thesis advisors, Dr. Naresh Thadhani and Dr. Thomas Sanders, for providing me with a project for my PhD thesis and for their advice and assistance throughout my time in the School of Materials Science and Engineering at the Georgia Institute of Technology. Their guidance throughout the years has been critical in my success as a graduate student.

I also wish to thank my committee members Dr. Arun Gokhale, Dr. Sunil Dwivedi, Dr. Suveen Mathaudhu, and Victor Dangerfield for agreeing to serve on my committee and providing helpful advice towards the completion of my thesis.

Dr. Gregory Kennedy deserves special thanks for his constant help, support, and experimental expertise. His contributions towards my individual learning of high strain-rate and plate impact testing were invaluable to me as a researcher.

Finally, I wish to thank both of my research groups under Dr. Thadhani and Dr. Sanders for providing guidance and teamwork during my graduate studies.

TABLE OF CONTENTS

LIST OF TABLES

LIST OF FIGURES

SUMMARY

This research focuses on the dynamic tensile (spall) properties of aluminum-magnesium (Al-Mg) alloys. Aluminum alloy 5083 (Al 5083) was used as a model alloy for the work performed in this study. Al-Mg alloys represent a light-weight and corrosion resistant alloy system often used in armor plating. It is desirable to process armor plate material to yield a microstructure that provides maximum resistance to spall failure due to blast and projectile impacts. The blast and impact resistance has often been quantified based on the measurement of the spall strength and the Hugoniot elastic limit (HEL).

The spall properties of Al-Mg alloys were measured for four different microstructural states resultant from varying processing conditions. The four microstructures include: (a) textured grain structure from a rolled Al 5083-H116 plate, (b) sub-micron grain structure produced using equi-channel angular pressing (ECAP), (c) equiaxed grain structure produced by annealing, and (d) precipitation hardened microstucture from an Al-9wt.% Mg alloy. Symmetric plate-on-plate impact experiments were performed using an 80 mm diameter single-stage light-gas gun. Rear free surface velocity profiles were measured during impact testing using the VISAR interferometry system, from which the spall strength and HEL were determined. Plate impact experiments were performed through the plate thickness and along all three principal axes of plate specimens. Soft recovery of the specimens allowed the post-mortem microstucture to be characterized, to identify the spall damage.

The highly textured grain structure of the rolled Al 5083-H116 plate resulted in orientation dependence for both the HEL and spall strength. The spall strength was measurably higher along the longitudinal direction, due to spall damage occurring both along grain boundaries and in the direction of impact. The fracture surface for impact in the short transverse direction showed a mixed mode of ductile and brittle failure, which was not present in either of the other two impact directions.

Equi-channel angular pressing (ECAP) produced plates showing a higher HEL and spall strength as compared to the rolled plates. Subsequent warm and cold rolling after ECAP further increased the HEL, but at the expense of the spall strength. The specimens rolled after ECAP also showed spall strength values dependent on orientation, with the through-thickness direction having the lowest value in both cases. The alignment and cracking of large inclusions appears to be the dominant cause for the decrease in spall strength through the thickness of both ECAP and rolled plates

The rolled Al 5083-H116 plate stock was pre-strained and annealed to produce an equiaxed grain structure. The HEL showed an upper and a lower limit, which can be attributed to its lower dislocation density. The lower limit of the HEL is below that of the Al 5083-H116 plate, while the upper limit increases with peak stress and exceeds the HEL of the original cold rolled plate. The spall strength of the annealed material is higher than that for Al 5083-H116 rolled plate.

An Al-9wt.% Mg alloy was precipitation hardened using a two-step solution treatment, to produce the least amount of solute segregation prior to aging, followed by aging at 150°C. The HEL for this precipitation hardened alloy increased dramatically; however the spall strength remained unaffected.

The overall results show that grain size is not the most dominant microstructural feature affecting spall strength in aluminum alloys, when the impact conditions are the same. Texture, especially if brittle inclusions align along the grains, appears to have the most dominant effect resulting in decreased spall strength. Furthermore, one-dimensional modeling shows that the inclusion size and distribution is the controlling factor for void formation during spalling. Grain size does affect the decompression rate dependence of each microstructure, whereby smaller grain sizes result in a larger power law exponent for fits of spall strength versus decompression rate. Unlike the spall strength, the HEL shows an increasing trend with decreased grain size, as would be expected from a Hall-Petch type effect, indicating that a smaller grain size is best for penetration resistance. Samples processed using ECAP alone provide the best combination of spall strength and HEL and therefore the most promise for improved blast and penetration resistance of aluminum-magnesium alloy armor plates.

CHAPTER 1

INTRODUCTION

Aluminum-magnesium (5XXX series) alloys are a class of light-weight and corrosion resistant alloys that can be significantly strain hardened via cold working. Al 5083, a common 5XXX series alloy with principal alloying elements of magnesium (5 wt.%) and manganese (1 wt.%), is commonly used for marine applications such as in drilling rigs as well as armor plating for military transport vehicles.

A useful armor plate material system for transport vehicles should have a high resistance to dynamic tensile failure, known as spalling, as spall damage is often induced during blast from embedded explosives or projectile impact. The use of a strain hardenable aluminum alloy (such as Al 5083), as opposed to precipitation hardened aluminum alloys typically used in static load-bearing applications, is desirable since precipitation hardened alloys are prone to damage nucleation near precipitates during spalling.

The spall strength of a crystalline metal is often found to be a function of the combined effects of grain structure, amount and type of secondary phases, and degree of hardening, in addition to the experimental impact conditions including stress magnitude, stress pulse duration, and decompression rate. For metals, spalling often occurs by ductile nucleation, growth, and coalescence of voids; although, the cracking of brittle inclusions in ductile materials is a known contributor to the nucleation of voids during spalling. However, the role of specific microstructural contributors that control spallation in polycrystalline metals is not fully understood. Past research on the effects of grain size and grain orientation on spall properties in metals has shown contradictory behaviors, yielding no clear results on how various microstructural features of different alloys relate to their corresponding spall strength. In addition, the effects of brittle inclusions and their presence along the grain boundaries is interconnected with the effects of the grain structure and orientation. The microstructure of a rolled armor plate is highly textured with the grains lengthening along

the rolling direction and inclusions aligning along the grain boundaries. This can result in varying spall properties depending on the impact direction with respect to the plate rolling direction.

During impact of a plate on a thicker target plate, a state of tension is induced in the target, which can result in spall failure if the magnitude of the tension generated exceeds the tensile strength of the material. The interaction of the shock waves within the target material can be monitored by measuring the back free surface velocity versus time profiles with a Velocity Interferometer System for Any Reflector (VISAR). The dynamic tensile (spall) strength and the Hugoniot Elastic Limit (HEL) are respectively determined from the pullback signal and the elastic-plastic discontinuity. The dynamic tensile strength and compressive strength (obtained from the HEL) are the two important mechanical properties associated with blast and projectile impact resistance. Similar to static mechanical properties, these dynamic properties are also influenced by various microstructural features generated during processing.

For this project, the spall properties of Al-Mg alloys, with Al 5083 representing the model system, were investigated for a variety of processing conditions, microstructural states, and magnesium contents. The overall objective of this research was to determine the influence of the alloy microstucture on spall resistance. Plate impact experiments are a common high strain-rate testing method that involve the application of planar shock waves and a state of uniaxial strain within an impacted target. In the present work, plate impact experiments were performed to understand the effects of blast and impact damage on Al-Mg alloys with varying microstructures in a reproducible manner. The experiments were performed with the impact direction through the alloy plate thickness and along each orientation of the sample plates to measure the orientation dependent spall behavior. Microstructural features investigated include: the grain structure and orientation, inclusion and dispersoid phases, and precipitate phases. Experiments were complemented with one-dimensional numerical simulations to identify the effects of microstructure on void size prior to complete spall failure.

Four key microstructures were investigated in this project. The first microstructure was that of a rolled Al 5083-H116 plate. This microstructure represents the baseline for armor plating that is already in service for military transport vehicles. Since the plate was rolled, the grain structure was highly textured with grains lengthening along the rolling direction and inclusions and dispersoid phases aligning in this same direction along grain boundaries. The second microstructure had a highly refined grain structure produced via equi-channel angular pressing (ECAP), wherein the workpiece is subjected to large shear strains while maintaining the same cross-sectional area. The spall behavior of large Al 5083 plate specimens having a sub-micron grain structure were tested for samples processed using both ECAP and rolling. The third microstructure was an equiaxed grain structure obtained by first straining and then annealing the rolled Al 5083-H116 plate. This removed the highly textured grain structure of the initial plate to yield a more uniform and equiaxed grain structure. Finally, the effects of precipitation hardening on the spall properties of Al-9wt.% Mg alloy were studied to see how precipitate phases effect the dynamic tensile (spall) and compressive strength properties.

In this thesis, Chapter 2 provides the background information on Al-Mg alloys, dynamic tensile (spall) failure, and the effects of microstructure on spall properties. The experimental procedure is described in Chapter 3, followed by the results of the effects of plate thickness on spall strength and HEL in Chapter 4. The spall behavior of rolled Al 5083-H116 plate, Al 5083 processed using ECAP, Al 5083 with equiaxed grains, and precipitation hardened Al-9wt.% Mg are presented in Chapters 5–8. One-dimensional numerical simulations of the spall behavior of Al-5083 are presented in Chapter 9, followed by a discussion of the spall behavior of all the microstructures studied in Chapter 10. The conclusions and suggestions for future work are given in Chapter 11.

CHAPTER 2

BACKGROUND

This research focuses on the effects of microstructure on the spall response of polycrystalline Al-Mg alloys. This chapter discusses the key microstructural features affecting the spall response in Al-Mg alloys—namely the grain structure, inclusions, and precipitate phases. Two novel processing techniques for Al-Mg alloys are discussed—one where the microstructure can be highly refined through equi-channel angular pressing (ECAP) and one where Al-Mg alloys can be precipitation hardened. The effects of the key microstructural features on the dynamic mechanical response are measured experimentally using plate impact testing. Background on the material response to shock compression during such plate impact testing and the propagation of shock waves (which can ultimately lead to spalling) are also discussed. Previous research on the effects of microstructure on the spall behavior of polycrystalline metals and Al-Mg alloys is discussed with particular emphasis on grain structure and secondary phases. Computer simulations are used to complement the experimental plate impact data; therefore, the background also provides analytical models for spall damage in ductile materials. Finally, the effects of experimental impact conditions such as peak stress, pulse duration, and strain rate on the spall response of ductile materials is provided.

2.1 Al-Mg Alloy Microstructure

Al-Mg (5XXX) alloys are a class of light-weight, high strength, and corrosion resistant alloys used in cryogenics, marine applications, missile components, and armor plate. The mechanical properties of Al-Mg alloys are imparted by alloying with magnesium and manganese and by strain hardening. The Al-Mg phase diagram is shown in Figure 1. Alloying with magnesium results in solid solution strengthening, while manganese additions refine the grain structure through the formation of grain-pinning dispersoid particles [1]. As shown in Figure 1, the precipitate phase, β, is stable under ambient conditions for a wide range of

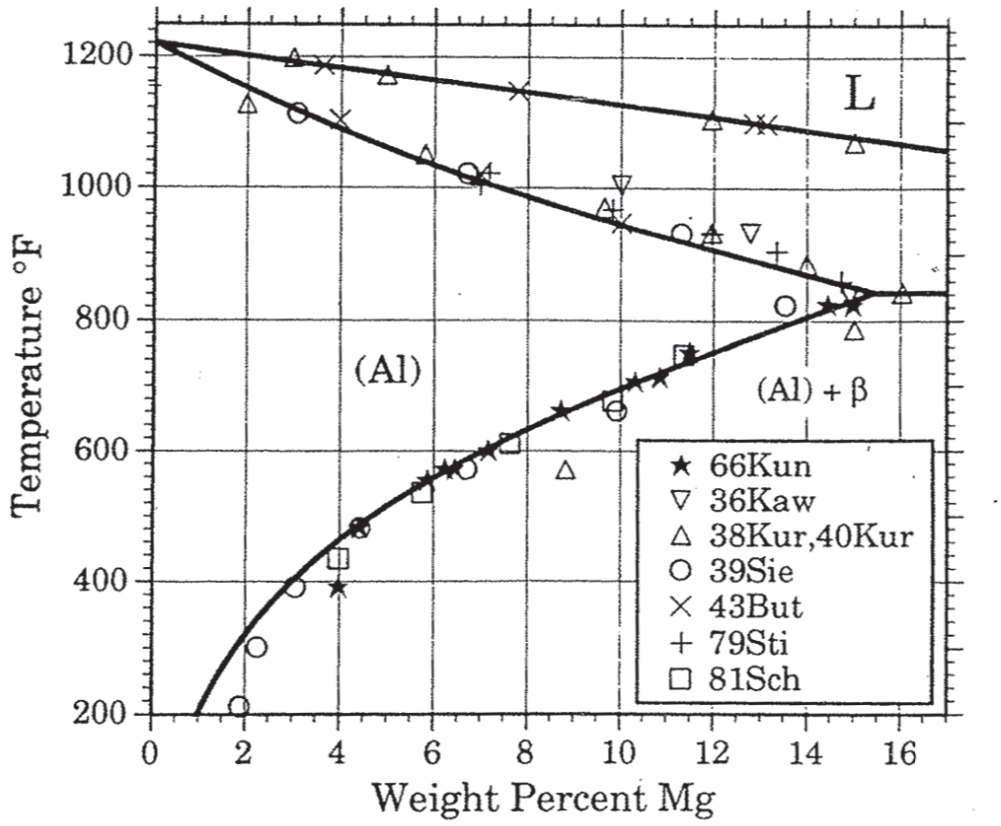

Figure 1: Al-Mg phase diagram as reported by Mondolfo [3]

magnesium compositions; however, significant precipitation hardening cannot be achieved for Al-Mg unless the composition is above 10 wt.% [2].

The use of Al-Mg alloys for armor plate, especially for military vehicles, necessitates research in optimizing this material's microstructure to achieve maximum resistance to dynamic failure caused from blast and projectile impacts. Since such armor is typically manufactured as a rolled plate, the grain structure and the mechanical properties can vary significantly with orientation in the plate. In addition, secondary phases such as inclusions and precipitates can be detrimental to the dynamic strength of ductile materials and can also align along the rolling direction for an armor plate. Therefore, the role of alloy processing on each of these microstructural features and their effects on the dynamic mechanical properties for Al-Mg is examined.

2.1.1 Grain Structure and Recrystallization

Armor plate manufactured from Al-Mg alloys is processed via hot and cold working to yield the desired shape and degree of strain hardening. During such processing, both recovery and recrystallization of the initial grain structure can occur. Recovery is the process where dislocations rearrange to either annihilate or form subgrains. During recrystallization, new strain-free high angle grain boundaries are formed within the microstructure [4]. For both processes, the stored strain energy from cold working is the driving force to return to an as-annealed state.

For aluminum alloys, static recrystallization (SRX) is the normal process by which strain-free grains are formed [5]. The term "static" denotes that recrystallization occurs after the hot working process. Dynamic recrystallization (DRX) denotes recrystallization during the hot working process and is more common for low stacking fault energy metals [6]. The high stacking fault energy in aluminum results in a corresponding decrease in the stacking fault width and increased dislocation mobility when compared to low stacking fault energy metals [7]. The high mobility of the dislocations can result in fast recovery. Dynamic recovery (DRV) then removes a significant portion of the strain energy imparted during processing of aluminum alloys, making DRX unlikely. Consequently, most aluminum alloys can undergo DRV, but not DRX [8]. Some instances of DRX have been reported for pure aluminum ($>$ 99.99 wt.%) [9–11]; however, this is a result of the highly mobile grain boundaries in the pure metal as opposed to the less mobile grain boundaries in the alloy forms [8].

Al-Mg alloys are an exception from this expected recrystallization behavior, in that they have been shown to undergo DRX [12–15]. The addition of small amounts of magnesium (near 1 wt.%) can reduce the stacking fault energy in aluminum by a factor of four [16, 17]. This in turn reduces the dislocation mobility, resulting in a larger available dislocation density during hot working. The dislocations can form tangles that evolve into new high angle grain boundaries via DRX. Aluminum alloys with high magnesium content ($>$ 5 wt.%) are especially likely to undergo both dynamic and static recrystallization due to a large driving force from strain hardening [12–15].

Dynamic recrystallization can proceed by two main methods. The classical method is known as discontinuous dynamic recrystallization (DDRX), whereby recrystallization occurs by a nucleation and growth process from induced strains [18]. Existing grain boundaries then sweep the microstructure to remove dislocations and lower their density. The second method is continuous dynamic recrystallization (CDRX), which involves the transformation of sub-grains into new high angle grain boundaries through the continuous accumulation of dislocations at sub-grain boundaries [6]. The dominant recrystallization process (DDRX or CDRX) is determined by the competition between grain boundary mobility and sub-grain formation. For high purity aluminum, the mobile grain boundaries sweep the microstructure before sub-grains can evolve into high angle grain boundaries, causing DDRX to be the dominant recrystallization mechanism [8]. In Al-Mg alloys, such as Al 5083, the grain boundaries are less mobile and recrystallization can occur via CDRX.

Two sub-types of DRX are geometric dynamic recrystallization (GDRX) and particle stimulated dynamic recrystallization—both of which are possible in Al 5083 [18]. GDRX is the process where grain boundaries become serrated during hot working, due to the accumulation of sub-grains at the high angle boundary. If the grain size reduces to less than three subgrains, the serrations can pinch off from the main grain boundary, resulting in a new high angle grain [19–25]. Particle stimulated DRX is a form of DDRX, whereby large particles and inclusions act as the strain nucleation sites for recrystallized grains. Inclusions must have sizes above 0.5 μm in order to nucleate grains in this way [26–31].

The grain size and orientation have both been shown to affect the spall properties of polycrystalline alloys [32–40]. As shown in Figure 2, intergranular fracture becomes more likely with decreasing grain size for spalling of Al-3wt.% Mg. Alloys with higher magnesium content, which can result in better strain hardening characteristics but also a higher driving force for recrystallization are investigated in the present work. Therefore, great care must be taken during hot and cold working of these alloys to yield the proper degree of strain hardening without resulting in an inhomogeneous grain structure caused by DRX. These alloys also contain manganese to form grain-pinning dispersoids. The size and distribution of these phases will also determine whether recrystallization is impeded or stimulated.

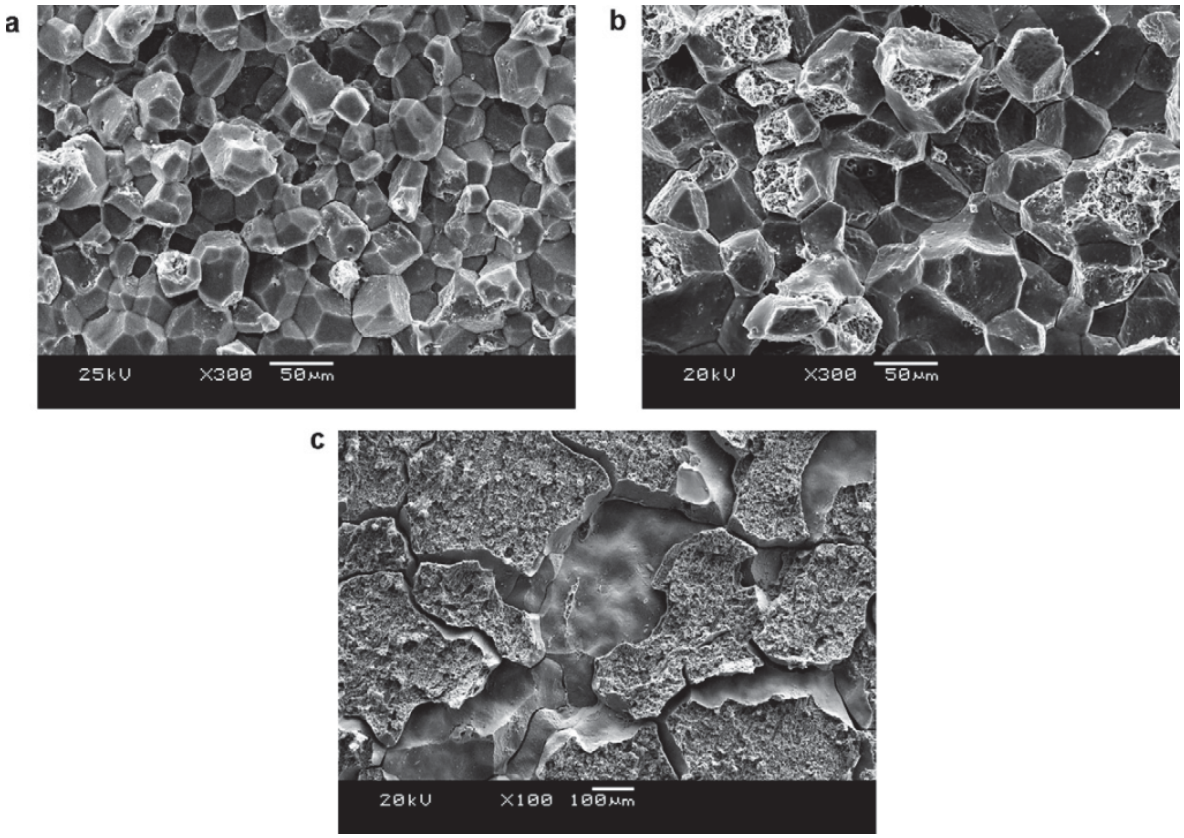

Figure 2: Fracture surfaces due to spalling for an Al-3wt.% Mg alloy with grain sizes of (a) 29 μm, (b) 44 μm, and (c) 295 μm as reported by Pedrazas et al. [39]. The fracture type transitions from intergranular to transgranular as the grain size increases.

2.1.2 Secondary Phases

Al-Mg alloys have an equilibrium precipitate phase, β, that is stable under ambient conditions (see Figure 1); however, this phase does not contribute to strengthening of the material. Section 2.2.2 will discuss how the β phase can be transformed to a strengthening phase by changing the magnesium composition. In addition to precipitate phases, brittle inclusions and dispersoid phases are often present in the Al-Mg microstructure. The larger inclusions form from trace amounts of iron and silicon present in the melt during casting, while dispersoids are intentionally formed through alloying with manganese and by solid state precipitation to control the extent of recrystallization during hot working [1]. For Al 5083, manganese additions of up to 1 wt.% are used to form dispersoids, although scandium and zirconium have also been used for this purpose in other Al-Mg alloys [41]. The dispersoids impart recrystallization resistance by preventing sub-grain boundary motion through a process known as Zener drag [42], whereby the large interfacial energy from the particles exerts a pinning force on the boundary. 5XXX series aluminum, such as Al 5083, are strengthened via cold working and need recrystallization resistance to maintain a high enough dislocation density to achieve sufficient strain hardening.

The manganese dispersoids are formed during preheating prior to the hot working process by solid state precipitation. The nucleation sites of the dispersoids are controlled by the solute segregation and diffusion during casting and preheating respectively. In Al-Mg alloys, manganese dispersoids have been shown to nucleate just inside the dendrite arm boundaries, due to a favorable composition of both manganese and magnesium in these areas [43]. The size and spacing of these dispersoids can be controlled by the preheat treatment chosen, whereby a uniformly dispersed phase is desirable for good recrystallization resistance. This recrystallization resistance can be reversed if the dispersoids become too large (> 0.5 μm), as the dispersoids can then become nucleation sites for recrystallized grains due to the strain field near the interface [26–31]. Therefore, when hot working Al 5083 and similar Al-Mg alloys, the pre-heat treatment should be chosen such that a significant number density of dispersoids is formed to yield recrystallization resistance, but these dispersoids should not be allowed to coarsen such that particle stimulated recrystallization can occur.

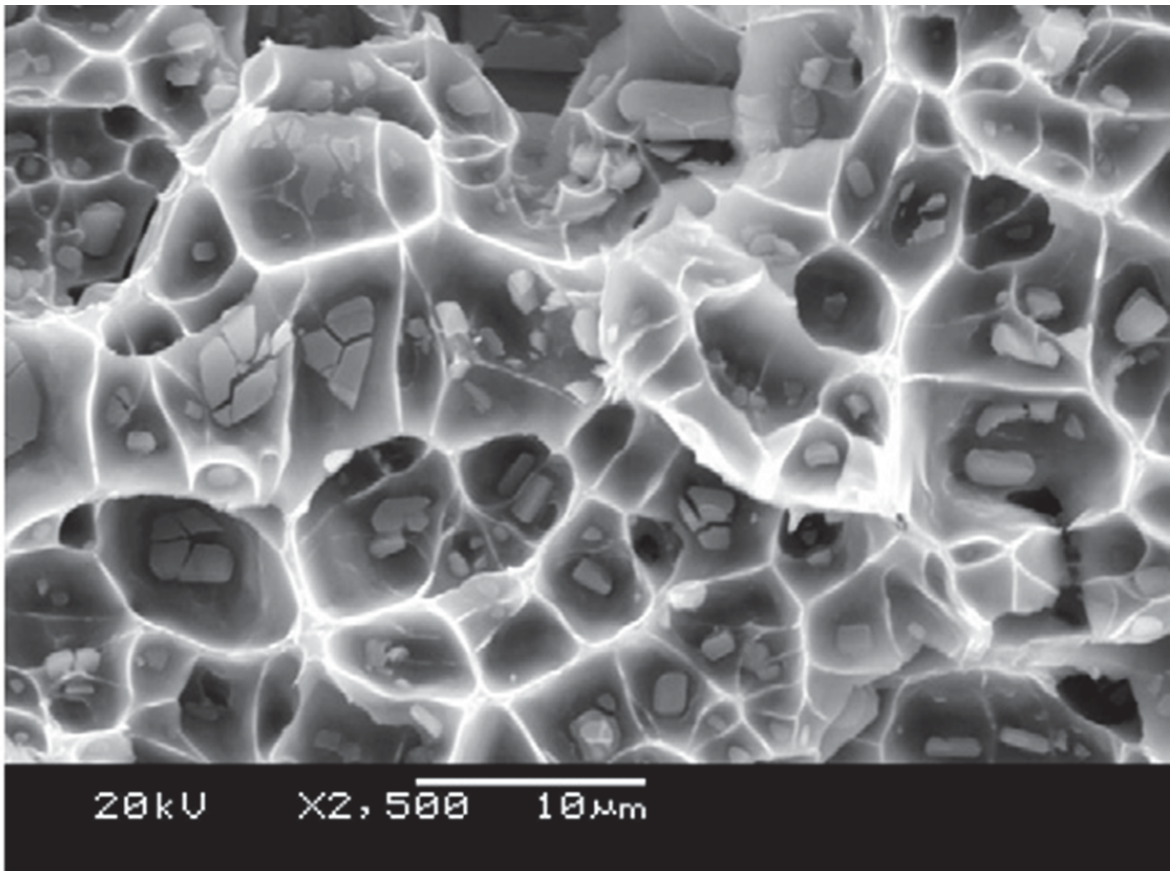

Figure 3: SEM image showing cracked inclusions within the fracture surface of an Al 1100 sample following dynamic spall testing performed by Pedrazas et al. [39]

While dispersoids are useful for refining the grain structure in Al-Mg alloys, they are also brittle nucleation sites for spall damage [44]. Figure 3 shows an SEM image of the spall fracture surface in an Al 1100 sample. Damage was found to nucleate preferentially at cracked inclusions, making them detrimental to the dynamic strength of the alloy. The extent of inclusions and dispersoids formed in Al-Mg alloys for armor should thus be a trade-off between grain refinement and spall strength.

2.2 Novel Processing Techniques for Al-Mg Alloys

The two processing techniques discussed in this section, equi-channel angular pressing (ECAP) and precipitation hardening, were both performed on Al-Mg alloys for this research. The processing approach and the resulting unique microstructures produced are described next.

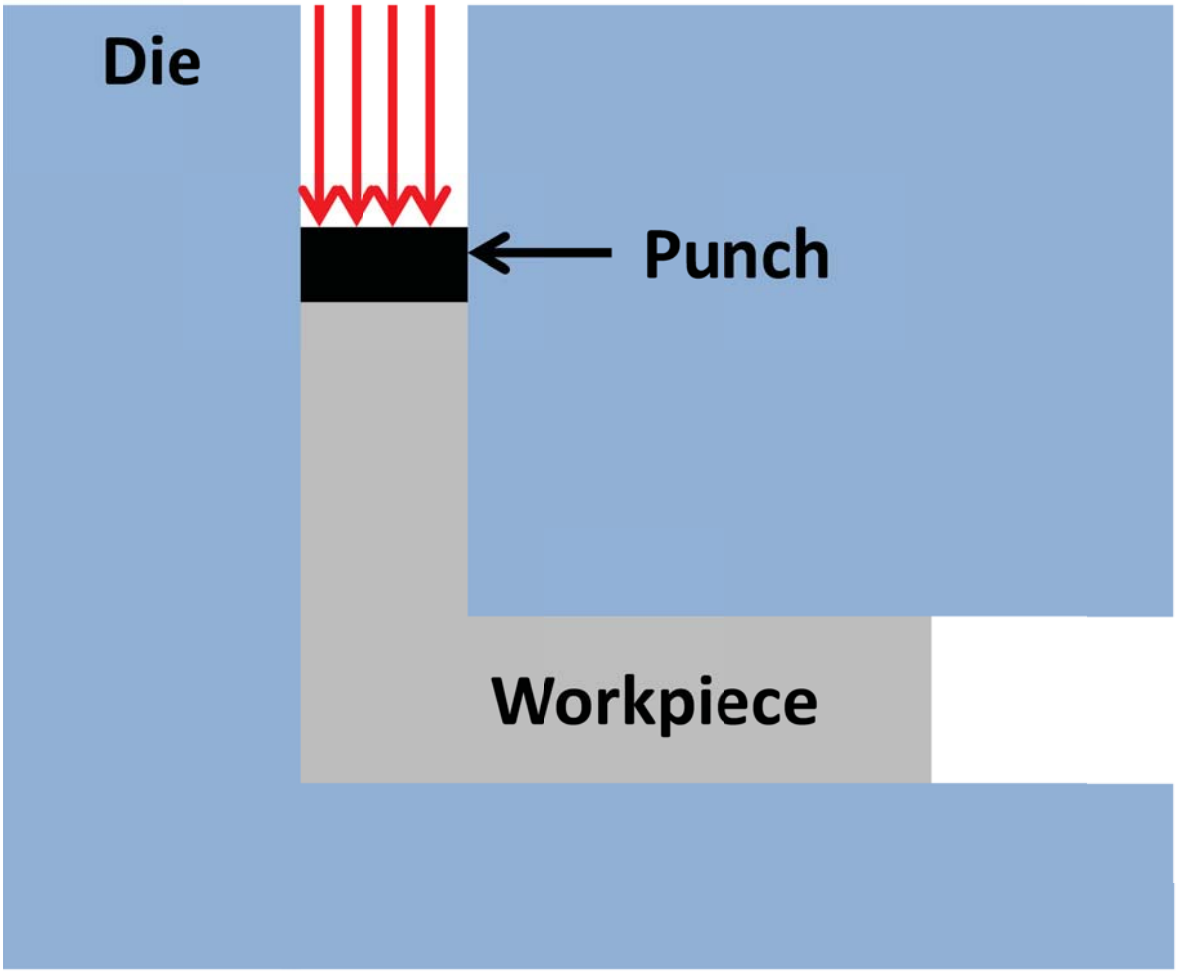

Figure 4: Schematic of an equi-channel angular pressing (ECAP) setup. The workpiece is pressed through an angular die with no change in cross-sectional area upon exiting the press such that it undergoes large shear strain.

2.2.1 Equi-Channel Angular Pressing (ECAP)

Equi-channel angular pressing (ECAP), also known as equi-channel angular extrusion (ECAE), is a processing technique whereby a billet is pressed through an angled die, to obtain large shear strains with no change in cross-sectional area. A schematic of an ECAP press is shown in Figure 4.

Processing of metal alloys using ECAP results in severe plastic deformation in the billet that can refine the grains to sub-micron sizes. The microstructure produced using ECAP can increase both the alloy strength and ductility through the Hall-Petch effect and activation of low temperature grain boundary sliding as a deformation mechanism [45].

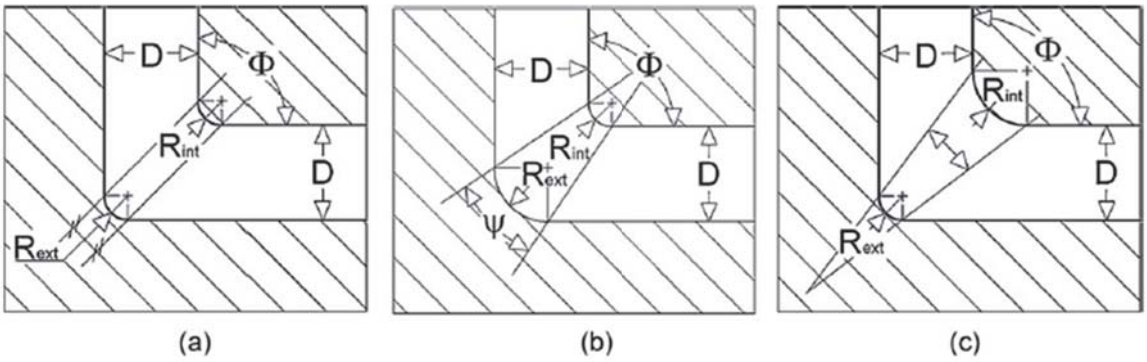

Figure 5: Schematic showing three ECAP die geometries for extrusion about a 90° angle. The three die shapes have (a) equal internal and external radius of curvature, (b) a larger external radius of curvature, and (c) a larger internal radius of curvature. [46]

The properties and microstructure produced in the extruded metal sample depend on the pressing parameters such as ram speed, die geometry, and temperature. The angle of the die is often chosen to be 90° or 120°, with the 90° geometry resulting in greater deformation [45]. In addition to the angle of the die, the internal and external radius of curvature (R_{int} and R_{ext}) also affect the properties of the extruded material. A schematic showing three different die geometries for extrusion about a 90° angle is shown in Figure 5.

Figures 5(a)–(c) show the die geometries for the case of $R_{int} = R_{ext}$, $R_{int} < R_{ext}$, and $R_{int} > R_{ext}$ respectively, while keeping the internal angle (Φ) and die diameter (D) constant. Luri et al. [46] processed Al 5083 via ECAP using the three die geometries shown in Figure 5. Their results showed that the amount of strain imparted to the workpiece increased with increasing R_{int} or decreasing R_{ext} or Φ. The amount of damaged regions (areas with cracks or voids) in the Al 5083 workpiece increased with decreasing R_{int} or increasing R_{ext} or Φ. The minimum amount of damage was observed for Al 5083 pressed using equal internal and external radii, as shown in Figure 5(a). The maximum amount of damage was observed for Al 5083 pressed using a larger external radius, as shown in Figure 5(b). Thus the geometry shown in Figure 5(a) represents the optimum die geometry, as it results in the best combination of strain hardening with the least amount of damage for Al 5083 processed using ECAP.

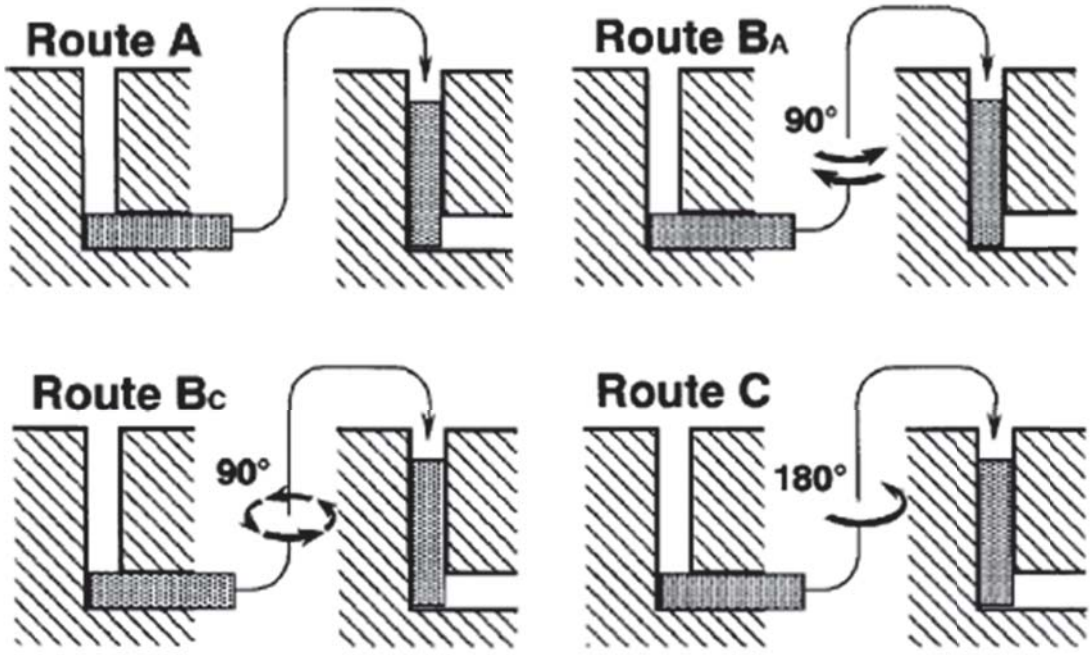

Figure 6: Schematic showing the different ECAP processing routes, whereby the workpiece is rotated about the extrusion direction between each pass. Route A involves no rotation. Route B_A involves anti-continuous rotation by 90°, and route B_C involves continuous rotation by 90°. Route C involves rotation by 180° between passes. The schematic was first published by Nakashima et al. [47].

Materials processed with ECAP are often subjected to multiple passes through the die to yield an increasingly refined grain size and to ensure microstructural uniformity [45]. Each ECAP pass is often followed by rotation about the extrusion direction so that yielding occurs along planes with different orientations with respect to the workpiece for consecutive passes. The different procedures for rotating the billet between each pass are referred to as ECAP routes and are shown schematically in Figure 6.

Route A involves no rotation between each pass, which has been shown to result in a less uniform microstructure and worse mechanical properties when compared to the other processing routes [48–50]. Both routes B_A and B_C use 90° rotation between passes; route B_A uses anti-continuous rotation by ±90°, whereas route B_C uses continuous rotation in the same direction. Route C uses rotation by 180° between each ECAP pass. The ECAP

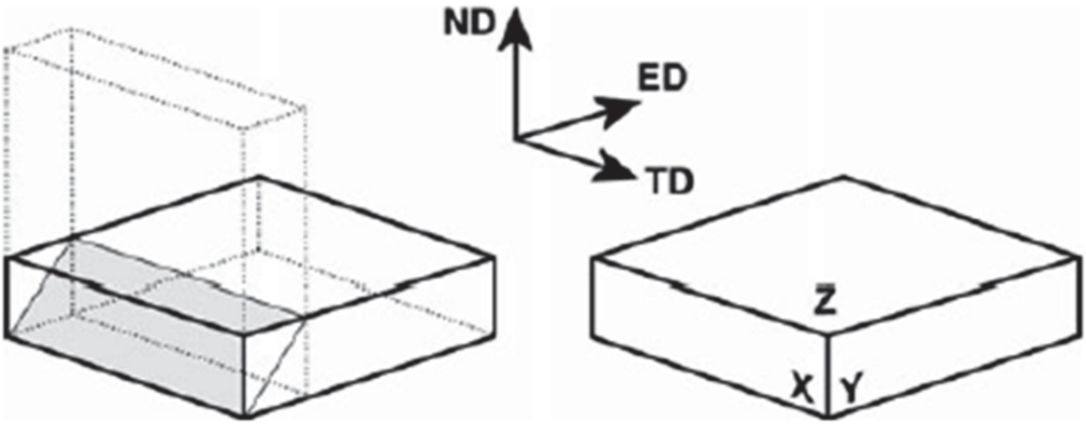

Figure 7: Schematic of the equi-channel angular pressing (ECAP) process for a plate geometry. The various planes in the plate are defined by the plate normal direction (ND) or through-thickness direction, the transverse direction (TD), and the extrusion direction (ED). Plate processing routes consist of rotation about the normal direction between each pass. The schematic was first published by Mishin et al. [52].

processing routes can have a great influence over the grain structure produced in the workpiece. Most experimental results have shown that route B_C results in the most highly refined and uniform grain structure after pressing. Soliman et al. [48] observed that route B_C resulted in more instances of high angle grain boundaries and a smaller grain size when compared to route A for Al 1050; however, the tensile and compressive strengths were both higher for the aluminum processed using route A. Rebhi et al. [51] observed that aluminum processed using route B_C displayed a higher dislocation density than aluminum processed similarly using route C, due to increased recovery during processing with route C. In addition, Al 5083 processed using route B_C resulted in the best improvement to the mechanical properties, with route A resulting in significant particle cracking during pressing [50].

ECAP is often performed on rods or bars, which is how the presses are depicted in Figures 4–6; however, ECAP has also been performed on large plates [52, 53]. Figure 7 depicts how the ECAP die shown in Figure 4 can be modified to perform ECAP on plate specimens.

The processing route for ECAP on plates is different from that shown in Figure 6. Instead of rotation about the extrusion direction (ED), plates processed using ECAP are

rotated about the through-thickness or normal direction (ND). Mishin et al. [52] used ECAP to process large Al 1050 plates using both no rotation and consecutive 90° rotation about the normal direction between passes. The microstructures produced by Mishin et al. [52] both with and without rotation are shown in Figures 8 and 9, respectively, in the form of EBSD images in each of the three planes shown in Figure 7.

Figures 8 and 9 show that ECAP can produce highly refined grain structures in large plates similarly to those produced in rods. The average grain size is less than one micrometer for either case. Rotating the plate by 90° between each pass (as shown in Figure 8) results in a more uniform grain structure throughout the plate. The plate processed without rotation, shown in Figure 9, has a number of coarse grains with significant sub-grain structure in each plane of the plate. The plane normal to the through-thickness direction, shown in Figure 9(c), displays a large number of these coarse grains and is the most anisotropic of the three plate directions. The plate processed using rotation between pressing shows some coarse grains visible in Figure 8(c), but they are much smaller than the coarse grains visible in Figure 9(c). Jin et al. [53] used ECAP to process large Al 5083 plates, similarly to Mishin et al. [52]. Using the route with 90° rotation between each pass, they were able to produce a uniform grain structure with a grain size near 0.4 μm.

ECAP has already been used on aluminum [48, 49, 51, 52, 54–58] and Al-Mg alloys [46, 50, 53, 59–69] specifically, to yield highly refined grain structures within the material. Processing using ECAP has resulted in increases to both the strength and ductility simultaneously in several cases [50, 55, 69]. Al 5083 processed with ECAP has also displayed superplastic behavior [60, 61], reaching an elongation near 350% in one test case [61]. Al 5083 also displays strain-rate dependent properties when processed using ECAP [66, 67]. High strain rate mechanical testing using a split-Hopkinson bar versus quasi-static tensile testing has shown that Al 5083 processed with ECAP becomes more ductile with increasing strain rates (up to a value of $1.6\text{x}10^3$ s^{-1}) [66].

The microstructure of aluminum processed using ECAP is also dependent on the number and size of brittle particles such as inclusions and dispersoids. Similar to traditional rolling and extrusion, dispersoid particles help to pin gain boundaries during ECAP and result in a

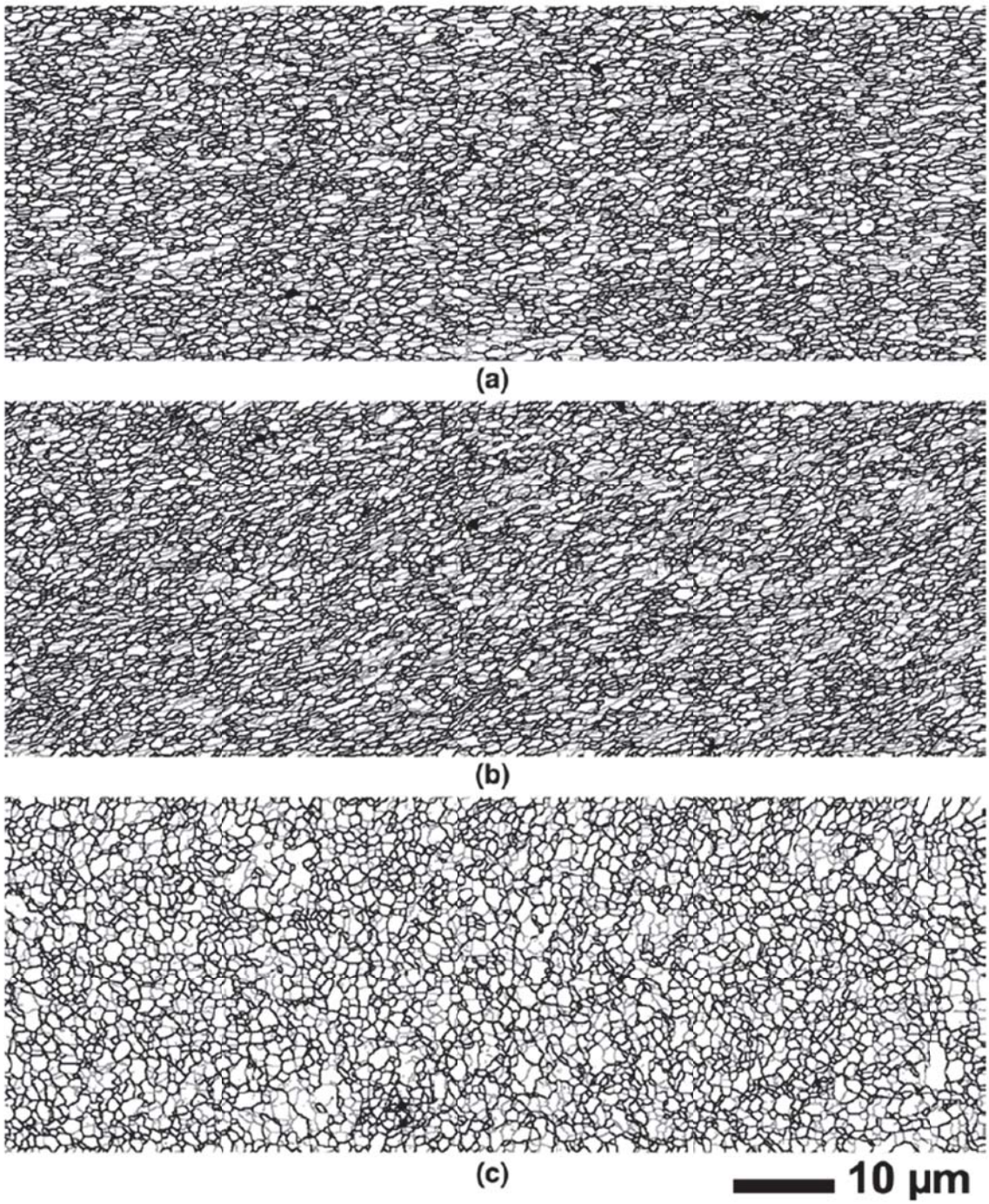

Figure 8: EBSD misorientation maps showing the grain structure in each plane of an Al 1050 plate processed using ECAP with 90° rotation between passes. The images show (a) plane X, (b) plane Y, and (c) plane Z depicted in Figure 7. Dark lines represent high angle grain boundaries, whereas light lines represent sub-grain boundaries. ECAP using rotation results in a more uniform grain structure than without rotation. [52]

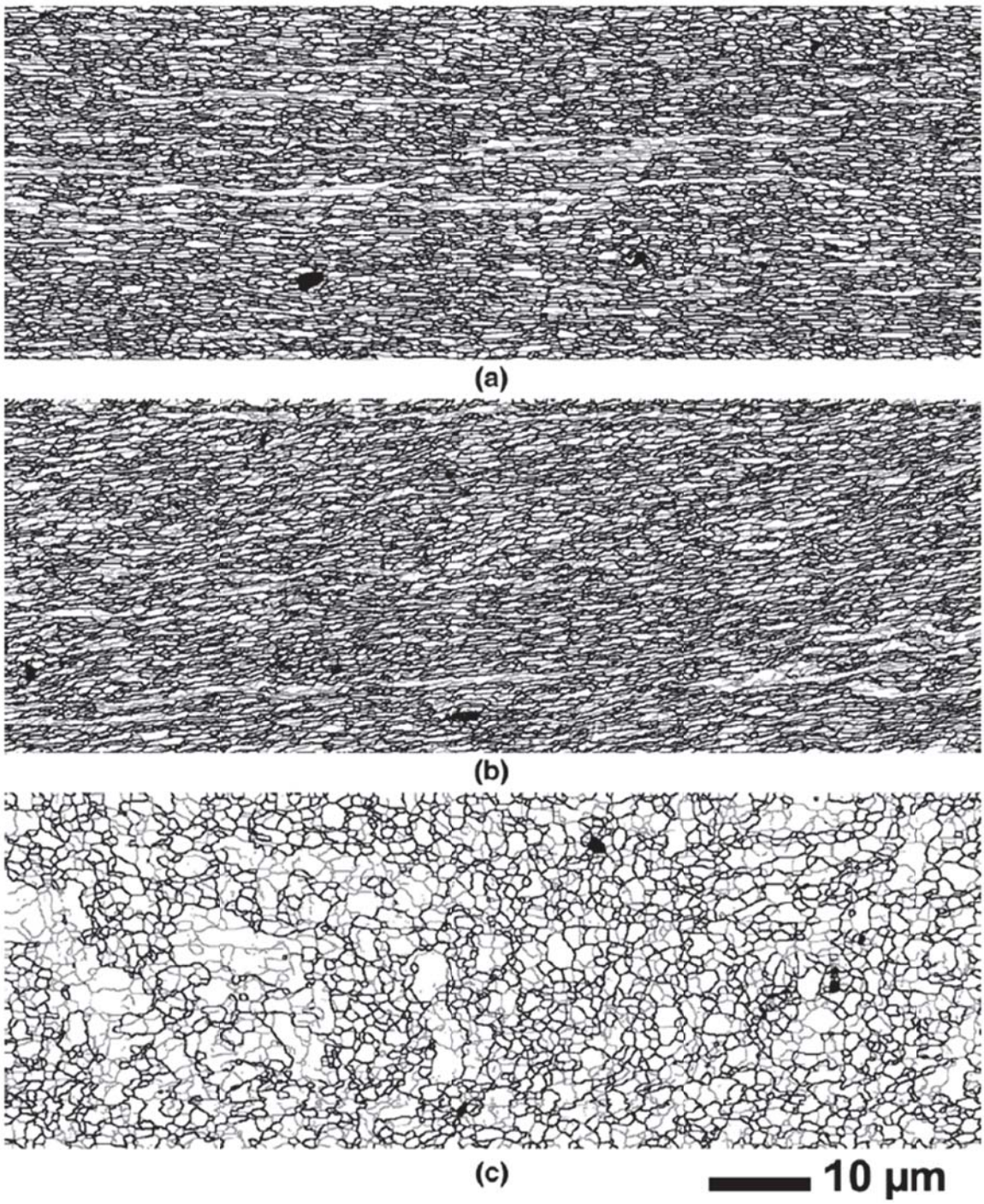

Figure 9: EBSD misorientation maps showing the grain structure in each plane of an Al 1050 plate processed using ECAP with no rotation between passes. The images show (a) plane X, (b) plane Y, and (c) plane Z depicted in Figure 7. Dark lines represent high angle grain boundaries, whereas light lines represent sub-grain boundaries. ECAP using rotation results in a more uniform grain structure than without rotation. [52]

more stable grain structure by slowing the rate of recovery and recrystallization [54, 67, 70]. Since Al-Mg alloys are prone to dynamic recrystallization, dispersoids can be beneficial in small amounts. Large brittle particles can be detrimental to the mechanical properties of aluminum processed using ECAP as they can be cracked, creating stress localization sites [59, 68]. Nikulin et al. [59] observed that the fracture behavior of an Al-6wt.% Mg alloy processed with ECAP was dominated by such cracked inclusions during tensile testing, with large voids growing preferentially from the damaged particles.

2.2.2 Precipitation Hardening

Al-Mg alloys are strain hardenable and thus not considered heat treatable; however, it has been reported that increasing the magnesium content or adding trace additions of silver can result in a precipitation hardenable system [2, 71–77]. As shown in Figure 1, the precipitate phase that is stable under ambient conditions for Al-Mg alloys is known as the β phase and has the chemical formula Al_3Mg_2 or Al_8Mg_5 [3]. This phase is not usually considered to be a strengthening precipitate phase, but for an Al-10wt.% Mg alloy moderate precipitation hardening was achieved [2]. Adding trace amounts of silver resulted in increased strengthening above that of the original Al-10wt.% Mg alloy. Furthermore, cold work in addition to precipitation hardening has been found to result in additional strengthening [2]. Age hardening has also been achieved in alloys with lower magnesium content. Specifically, an Al-5wt.% Mg alloy with silver additions has also shown evidence of precipitation hardening [75]; therefore, age hardening can be achieved with magnesium compositions similar to that used in Al 5083.

For Al-Mg alloys with silver additions, the hardness maximum has been observed to be due to a larger volume fraction of a metastable rod-like phase, instead of the expected β phase. This metastable, T, phase has the chemical formula $Mg_{32}(Al, Ag)_{49}$ [72]. Age hardening of Al-Mg alloys with no silver additions has not resulted in the formation of T phase, and the maximum in hardness is associated with a metastable β' precipitate phase, having a hexagonal crystal structure [74]. Cousland and Tate [77] showed that Al-Mg-Ag alloys should be considered as a ternary system even with only trace amounts of silver. The

silver additions result in a progression from metastable T' phases with a quasicrystalline structure, to the strengthening T phase with a body centered cubic (BCC) crystal structure [76–78]. The equilibrium β phase has a face centered cubic (FCC) crystal structure. The additional strengthening in Al-Mg alloys with silver is therefore due to changes in both the type and volume fraction of the strengthening precipitates.

Precipitates and other secondary phases are usually considered nucleation sites for damage during dynamic loading [44, 79]; however, precipitation hardening has resulted in increased spall resistance in some cases [80]. Previous work has shown that the interaction between precipitates and brittle inclusions was the key factor in determining damage nucleation during spalling. Figure 10 shows images of spall damage in precipitation hardened aluminum as a function of aging time. In Figure 10(a), the inclusions are closely spaced, and in Figure 10(b) the inclusions are widely spaced. Jones [80] found that the spall strength mirrored the quasi-static hardness trends for the largely spaced inclusions, but spall strength decreased with precipitation for the closely spaced inclusions. When the strain field from the precipitates intersected nearby inclusions, spall fracture became easier [80]. For the case of widely spaced inclusions, the strain field did not intersect the inclusion interface, and the precipitates yielded an increased resistance to spall damage.

2.3 Shock Compression and Dynamic Deformation

The dynamic or shock compression response of materials is an important subject area for investigating blast and other impacts on structural components of vehicles. The plate impact test is a common dynamic testing technique used to induce planar parallel shock waves and generate a state of uniaxial strain within an impacted target [81]. These simplified loading conditions allow for the dynamic mechanical properties to be quantified in a controlled and reproducible manner. Plate impact testing induces high strain rates exceeding 10^4 s^{-1} and large stresses (in the GPa range) within the target which can often result in a material response that is different than during the more common quasi-static testing methods such as hardness or tensile testing [81].

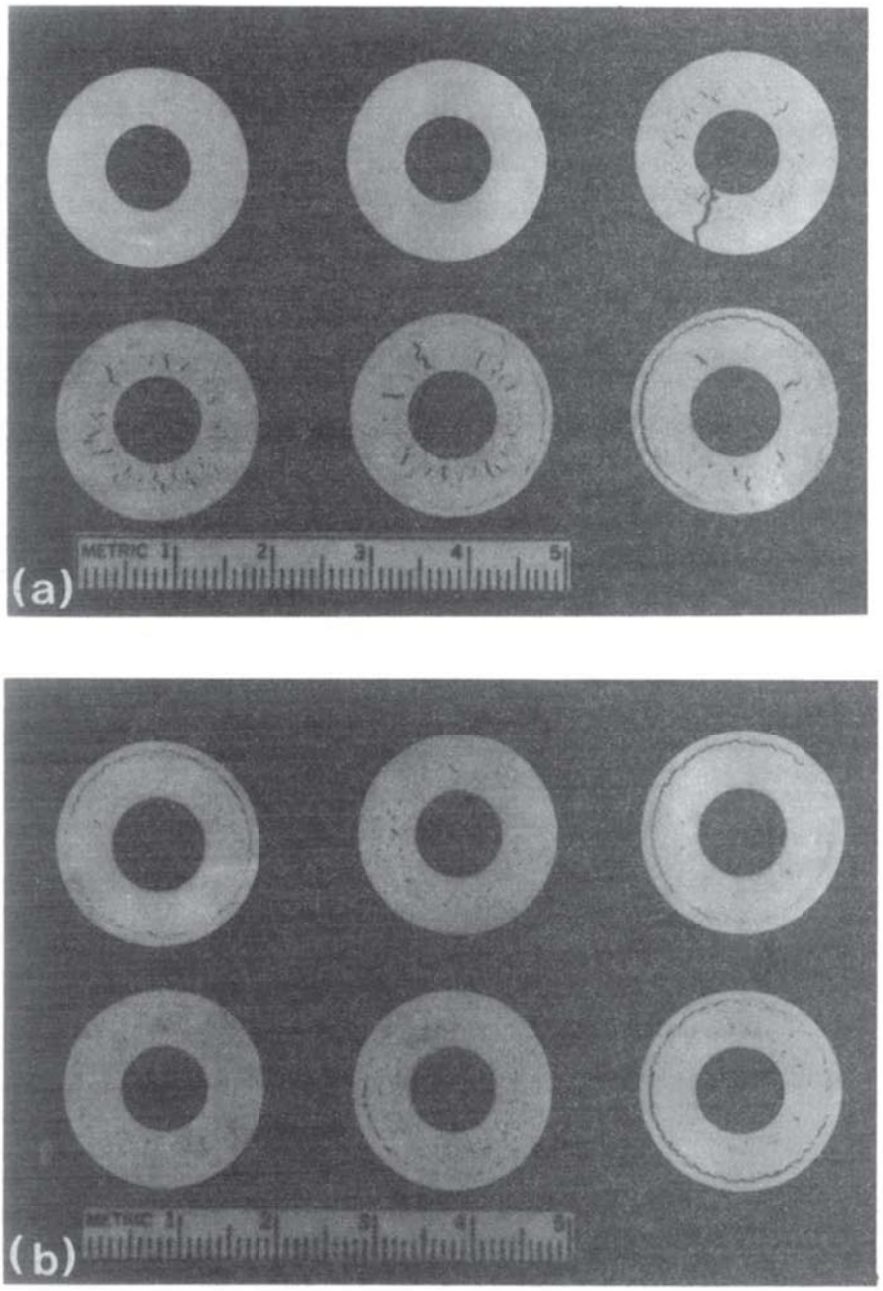

Figure 10: Images of spall damage in explosively detonated hollow cylinders machined from precipitation hardened aluminum. The aluminum alloys shown have (a) small inclusion spacing and (b) large inclusion spacing. The aluminum alloy with large inclusion spacing was found to have increased spall strength due to precipitation hardening [80].

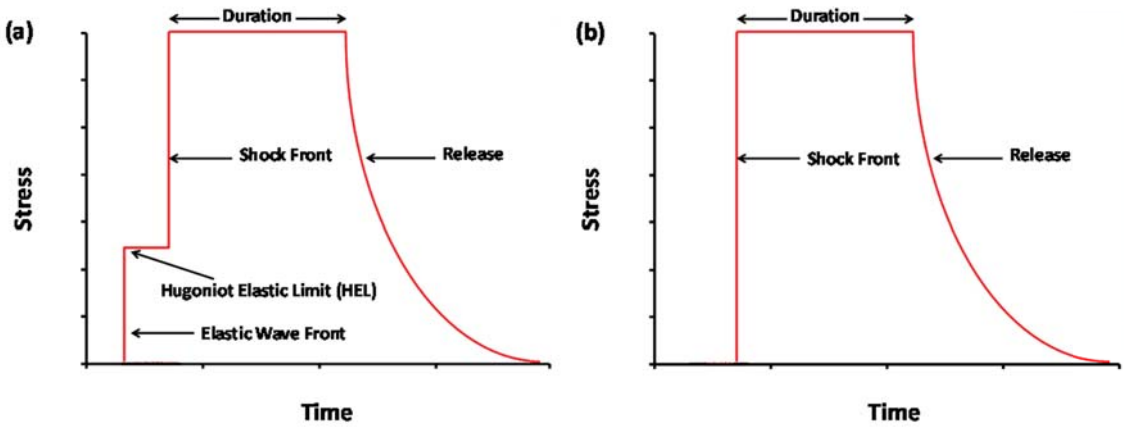

Figure 11: Idealized shock wave profile showing the rise to peak stress, duration, and release back to zero stress for the (a) weak shock case and (b) the strong shock case. For a weak shock, the shock wave is preceded by an elastic precursor, whereby the stress rises up to the Hugoniot elastic limit (HEL) prior to plastic behavior.

Blast or plate impact loading of materials generates shock waves which significantly alter the state of materials during their propagation. A shock wave can be defined as a discontinuity in pressure, density, and temperature (internal energy) [81]. An idealized schematic of a shock wave profile is given in Figure 11 for the case of a weak shock and a strong shock. The weak shock case shown in Figure 11(a) is for low peak shock stresses, whereby an elastic wave precedes the shock wave in the material. For this case, the stress rises up to the Hugoniot elastic limit (HEL), which is the limiting value of the elastic stress and is the transition point from elastic to plastic behavior. The shock wave, which causes plastic deformation, lags behind the elastic wave for this case. After the shock arrives, there is a rapid increase to the peak stress or pressure. This high stress state is maintained for a certain duration until it releases back down to a zero stress state. The strong shock case, shown in Figure 11(b), is for large peak stresses, whereby the shock wave overtakes the elastic wave with no transition from elastic to plastic behavior.

Across the shock wave front, mass, momentum, and energy must all be conserved. These conditions lead to the Rankine-Hugoniot [82, 83] equations for conservation of mass, momentum, and energy, given by Equations 1-3 respectively, for a one-dimensional case of shock propagation.

$$\rho_0 U_S = \rho \left(U_S - u_p \right) \tag{1}$$

$$P - P_0 = \rho_0 U_S u_p \tag{2}$$

$$E - E_0 = \frac{1}{2} \left(P + P_0 \right) \left(V_0 - V \right) \tag{3}$$

The material density (ρ) and the corresponding specific volume (V) are known quantities, while the shock velocity, particle velocity (atomic displacement velocity), pressure, and internal energy (U_S, u_p, P, and E respectively) are unknown quantities. Since there are three independent equations and four unknown variables, another equation is necessary to relate the properties in front of (subscript 0) and behind the shock front. The fourth equation is known as the equation of state (EOS) and often takes the form given in Equation 4. This type of EOS is a linear empirical relationship between the shock wave velocity and particle velocity, having intercept C_0 and slope S as constants. The EOS constants are often tabulated for common materials or can be experimentally measured during plate impact experiments. The EOS for Al 5083-H116 measured from free surface velocity data during plate impact experiments is given in Appendix A.

$$U_S = C_0 + S u_p \tag{4}$$

Using Equations 1–4, any two of the shock wave parameters can be related with no unknown variables. One such relationship is the induced shock pressure, P, versus the particle velocity behind the shock front, u_P, which is used to generate the P-u_P plot often known as a shock Hugoniot. The Hugoniot is a locus of all possible shock states [81] and is shown in Figure 12. The line connecting the shock's end states on the Hugoniot is known as the Rayleigh line. From Equation 2, the slope of this line is equal to $\rho_0 U_S$ which is known as the material's shock impedance. Figure 12 displays schematic Hugoniot curves for the case of symmetric impact (where the impactor and target are the same), and asymmetric impact (where the materials are different).

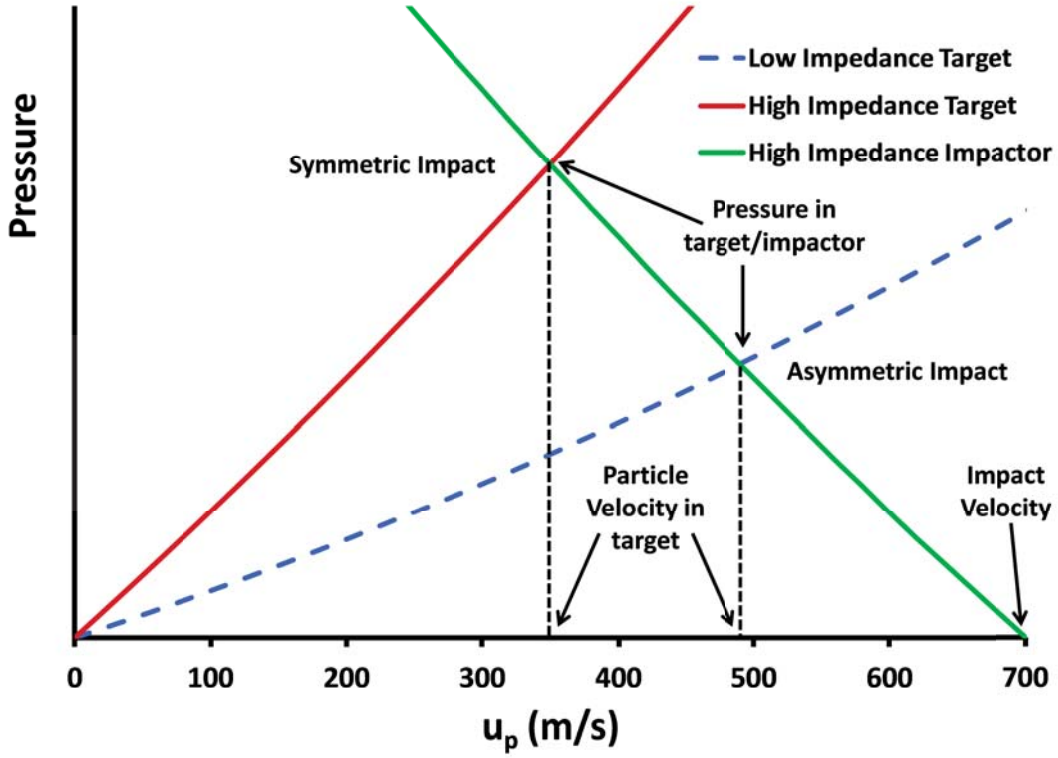

Figure 12: Schematic Hugoniot curve for both symmetric and asymmetric impact at 700 m/s. The particle velocity in the target is half the impact velocity for the symmetric case, while the particle velocity is faster in the lower impedance target material.

Upon impact, the pressure in the target and impactor must be equal. The shock parameters in both the target and impactor can both be obtained by using the impedance matching technique. This technique can be represented graphically by reflecting the Hugoniot of the impactor about the pressure axis, followed by shifting the origin in pressure to the impact velocity, as shown in Figure 12. The intersection of the Hugoniot curves for the target and impactor gives both the Hugoniot pressure and particle velocity in the target material. The particle velocity in the impactor is then the difference between this particle velocity and the impact velocity. As seen in Figure 12, the particle velocity is half the impact velocity for the case of symmetric impact. For the case of a high impedance impactor and a lower impedance target, the particle velocity in the target is faster than that of the impactor. Symmetric impact tests are often performed, such that the particle velocity can be obtained directly as one-half of the measured impact velocity, while asymmetric plate impact experiments require independent measurement of the particle velocity.

2.4 Spalling

During blast or plate impact experiments a state of dynamic tension may be formed within the impacted material. Failure due to these tensile stresses is known as "spallation" or "spalling" and is the primary failure mode for vehicle components subjected to blast waves or impact loading. Specifically, spalling is a dynamic tensile failure mode that occurs within the interior of a material due to the interaction of two release—or rarefaction—waves [81]. The material resistance to spalling can be quantified by measuring the degree of damage to post-impact specimens or by measuring the tensile stress required to initiate spall damage. This tensile stress is known as the spall strength of the material, which can be measured from the free surface velocity of the sample along with appropriate approximations [44, 84].

2.4.1 Shock Wave Propagation

In typical plate impact experiments, a flyer plate is impacted against a target plate of twice the thickness. Elastic and plastic compression waves produced in both the flyer and target materials propagate and reflect from respective free surfaces. Intersection of the reflected waves are what control the dynamic mechanical response and eventually spalling

of the material. The in-situ response of a material to shock waves is not directly measured. Instead, the diagnostics focus on a particular surface of the material, such as the rear free surface of the sample. Therefore, any wave produced in the sample will not be detected until it has traveled through the sample to this surface. For this reason, the interferometry or stress measurement methods are often used to monitor the velocity (or stress) state at the sample rear free surface or at the interface between the sample rear surface and a backer material. The velocity interferometer system for any reflector (VISAR) measures velocity by taking advantage of the Doppler shift of light that is out of phase; it references reflected light from a surface to light through a known time lag [85]. Accurate velocity measurements with nanosecond time resolution can be obtained in this manner. Under uniaxial strain and constant stress, measurements can be performed using piezoresistive (such as manganin) or piezoelectric (such as PVDF) stress gauges [86–91].

The wave dynamics during plate impact can be summarized with the Lagrangian distance versus time (or x-t) diagram shown in Figure 13(a). An example of the resulting sample rear free surface velocity that is recorded by the VISAR diagnostic system is given in Figure 13(b). The data presented in Figure 13 was for an Al 5083-H116 sample impacted near 350 m/s and is representative of the data obtained for other spall experiments on Al-Mg alloys.

As shown in Figure 13(a), the sample is first impacted at the origin in time. This induces an elastic precursor and a shock wave in both the sample and flyer plate. For the case of weak shock (shown in Figure 11(a)), the elastic precursor has a faster velocity (traveling with velocity C_L) than the shock wave (traveling with velocity U_S) and arrives at the sample rear surface at time t_1. As shown by Equation 4, the shock velocity is dependent on the induced particle velocity and will increase with increasing impact velocity. After the arrival of the elastic precursor, the free surface velocity measured from the VISAR system then shows a rise up to the Hugoniot elastic limit (HEL). The HEL is related to the dynamic yield strength of the material and is calculated from the free surface velocity at the HEL, u_{HEL} [81]. The HEL is followed by elastic-plastic yielding, indicated by the gradual rise in free surface velocity. This is followed by a "bump" in the free surface velocity data due

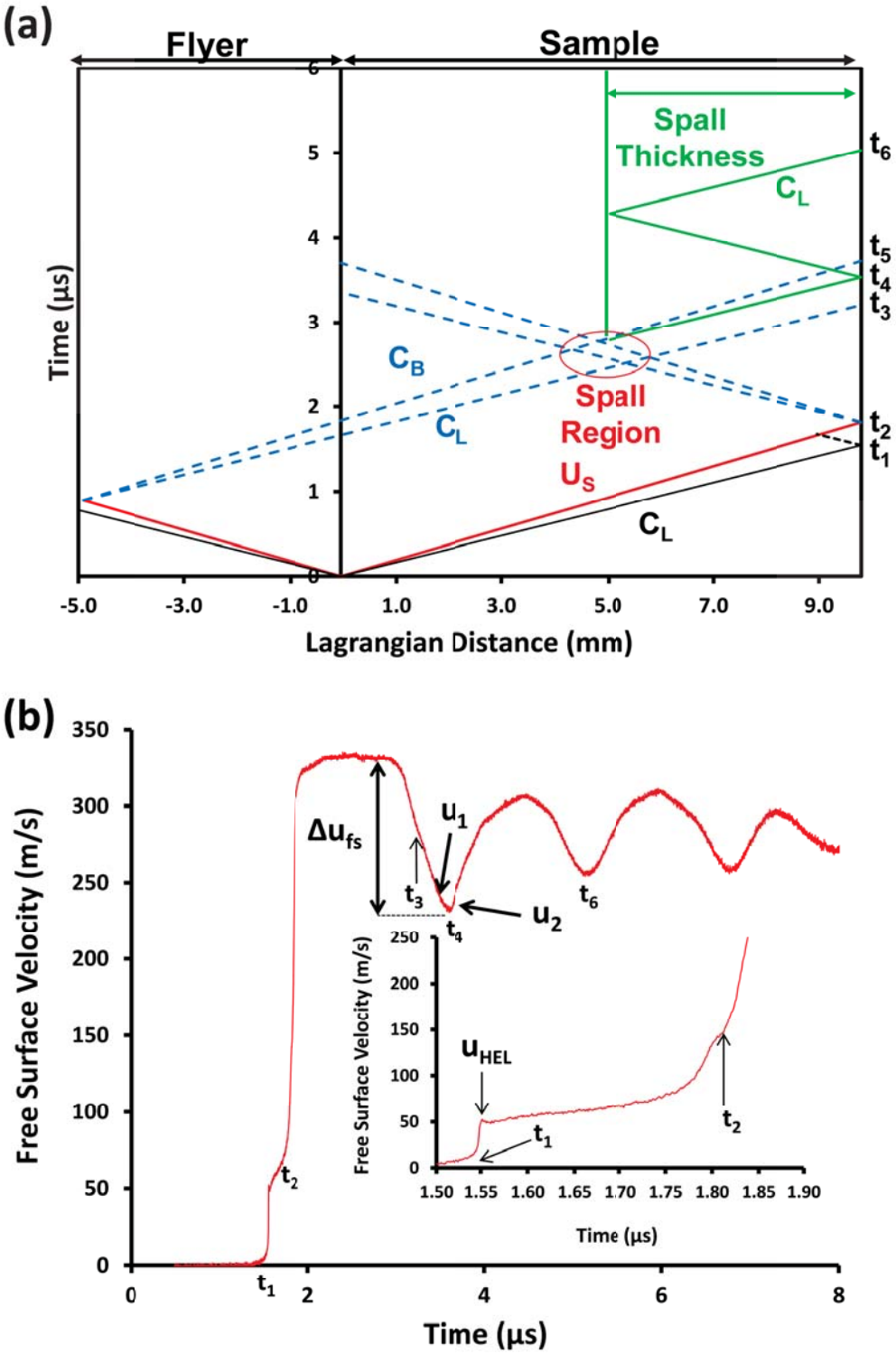

Figure 13: Representative example (a) x-t diagram and (b) free surface velocity data for an Al 5083-H116 sample impacted through the thickness of a rolled plate near 350 m/s

to a region in time where the elastic precursor has reflected back into the oncoming shock wave [92]. Just after this region, the shock wave, traveling with velocity U_S, reaches the sample rear free surface at time t_2. The shock wave arrival results in a rapid increase in free surface velocity up to the peak velocity.

As the shock waves reach the flyer plate and sample free surfaces, they are reflected backwards as rarefaction waves—also known as release waves. As shown schematically in Figure 11, the release wave reduces the material back to zero stress. The arrival of the plastic release wave occurs at time t_3, which is preceded by an elastic release wave. A slight inflection in the free surface velocity data during the release from the peak velocity corresponds to the transition from an elastic to plastic release. Aluminum often displays quasi-elasticity during release, whereby the transition from elastic to plastic behavior is not abrupt and displays an average release slope over the expected elastic and plastic regions [93].

It can be assumed that the head of the release wave travels with the material's longitudinal sound speed, C_L, whereas the tail of the release wave travels with the bulk sound speed, C_B. These are measured material properties that can be obtained with standard ultrasonic testing methods. The intersection of these two release waves creates an area of tension over a region as indicated by the x-t diagram. If the tensile stress is large enough, the material will fail and spalling will occur. This will result in formation of a new free surface at the spall plane and generation of a recompressive spall pulse. The spall pulse arrives at the sample rear free surface at time t_4, followed by a characteristic "pullback" in velocity that is indicative of spalling. The change in free surface velocity from the peak to the first minimum (Δu_{fs}) is known as the pullback velocity and is a measure of the spall strength of the material. It can be assumed that this spall pulse travels with the longitudinal sound speed within the spalled layer. The smaller peaks seen after the free surface velocity maximum are known as ringing and are due to the spall pulse reverberating within this layer after failure has occurred.

2.4.2 Calculation of HEL and Spall Strength

Both the Hugoniot elastic limit (σ_{HEL} or HEL) and spall strength (σ_{spall}) can be calculated from the measured sample rear free surface velocity (u) profile like that shown in Figure 13(b) using Equations 5 and 6 respectively.

$$\sigma_{HEL} = \frac{1}{2}\rho_0 C_L u_{HEL} \tag{5}$$

$$\sigma_{spall} = \frac{1}{2}\rho_0 C_B \left(\Delta u_{fs} + \delta\right) \tag{6}$$

The density (ρ_0) and sound speeds (C) are measurable material properties. The free surface velocity at the HEL, u_{HEL}, and the change in velocity from the peak to the pullback minimum, Δu_{fs}, can be obtained from the free surface velocity data as shown schematically in Figure 13(b). Attenuation of the wave from the spall plane to the rear surface (a distance of x_{spall}) is accounted for by a correction factor (δ) given by Equation 7 [84].

$$\delta = x_{spall}\left(\frac{1}{C_B} - \frac{1}{C_L}\right)\left(\frac{|\dot{u_1}\dot{u_2}|}{|\dot{u_1}| + \dot{u_2}}\right) \tag{7}$$

Equation 7 depends on the rate of change of the free surface velocity before and after the velocity pullback due to spall (denoted with subscripts 1 and 2 respectively). These two slopes account for elastic-plastic effects from the plastic release wave (with velocity u_1) before the pullback and the elastic recompression wave (with velocity u_2) after the pullback.

The spall strength is often plotted as a function of the peak stress (σ_{peak}). For symmetric plate impact experiments the particle velocity is half of the measured free surface velocity. For such an impact scenario, σ_{peak} becomes a summation of the stresses from the elastic and plastic loading regimes and is given by Equation 8.

$$\sigma_{peak} = \sigma_{HEL} + \sigma_{plastic} = \rho_0 C_L u_e + \frac{\rho_0 \left(U_S - u_e\right)\left(u_p - u_e\right)}{1 - \frac{u_e}{C_L}} \tag{8}$$

Equation 8 is the same as that used by Boteler and Dandekar [92, 94] for plate impact of Al 5083. The elastic and plastic stresses are calculated from the particle velocities at the HEL and peak velocity respectively (u_e and u_p). The shock wave speed (U_S) can be

calculated using the known sample thickness, elastic wave speed (C_L), and the arrival times t_1 and t_2, as shown schematically in Figure 13.

2.5 Spalling of Polycrystalline Metals

The spall strength of a polycrystalline metal is a function of the grain structure, amount and type of secondary phases, and degree of hardening, in addition to the experimental impact conditions such as stress magnitude and pulse duration [44, 79]. Previous work on other metal alloys has shown that precipitates can be nucleation sites for spall [79]; however, as shown in Figure 10, precipitation hardening has increased spall resistance in other aluminum alloys with large inclusion spacing. Microstructural examination of post-impact Al 5083 samples has revealed that spalling often initiates at brittle inclusions [35]. The effects of the grain size on the spall strength of polycrystalline metals are often complex. In some cases, the spall strength has obeyed a Hall-Petch type relationship, with smaller grains resulting in higher spall strength [36]. In other cases, the spall strength increased with increasing grain size [37, 38]. In one case, Al-3wt.% Mg samples with varying grain sizes showed no dependence of spall strength on grain size; however, the propensity for transgranular fracture increased with increasing grain size [39, 40].

Metal plates formed through rolling have a resultant grain structure that aligns along the rolling direction, yielding "pancake" shaped grains. For textured grain structures such as these, the spall strength has been shown to vary depending on the plate orientation with respect to impact [32–34]. In some cases impact along the longitudinal direction resulted in a higher spall strength as compared to impact through the thickness of the plate [32, 33], while in other cases the reverse was observed [34]. In one case the spall strength increased with impact stress for impact in the longitudinal direction, while it decreased with impact stress for impact through the thickness [34]. A study on Al 5083-H32 has shown no spall strength difference based on impact orientation with the rolled plate [35]. It is possible that the effects of inclusions, grain size, and grain orientation all contribute to the spall strength in an interconnected fashion, resulting in the somewhat confusing results described above. For instance, in the case of eutectoid steel, it was shown that brittle particles align along the

rolling direction similarly to the grains. These brittle particles, not the grains themselves, control the spall strength's orientation dependence for this material [32, 33].

Few spall tests have been performed on Al-Mg alloys specifically. As opposed to plate impact testing, several past experiments have focused on penetration resistance of Al 5083 [95–98]. Recently the spall strength and Hugoniot elastic limit (HEL) of Al 5083 were reported for the armor grade tempers H131 and H32 [35, 92, 94]. The spall strength data for Al 5083-H131 is presented in Figure 14 as a function of peak stress. It can be seen that the spall strength of Al 5083-H131 displays little peak stress dependence. The average spall strength and HEL were reported as 0.936 GPa and 0.573 GPa respectively for peak stresses between 1.5 and 8.0 GPa. For Al 5083-H32, the spall strength and HEL have been reported as 1.23 GPa and 0.60 GPa over a similar stress range [35]; however, the HEL was reported as 0.40 GPa in a different study [94]. The H131 and H32 tempers are both similarly strain hardened, but the H32 temper is given an annealing treatment after cold work. The spall strength for the O temper of Al 5083 is also presented in Figure 14 and has a value of 1.6 GPa, which is significantly higher than either armor grade system [99]; however, the spall strength of ductile materials greatly depends on the experimental impact conditions, making it difficult to compare spall strength values reported by different research groups.

For the spall experiments performed on Al 5083 to date, most samples have been oriented such that impact is through the thickness of a rolled plate. The microstructure (which will affect the spall properties) is orientation dependent for rolled plates, which necessitates impact along multiple orientations to gain a full understanding of the spall response. In one case, plate impact with Al 5083-H32 samples was performed such that impact was through the thickness and along the longitudinal (rolling) direction of a plate. Micrographs of the post-impact spall damage for impact along the through-thickness and longitudinal directions are presented in Figures 15 and 16 respectively. For those experiments, the spall strength had no apparent dependence on orientation with respect to impact [35]. Impact along the longitudinal direction (Figure 16) resulted in more instances of transgranular fracture, as opposed to the intergranular fracture observed when impacted through the thickness (Figure 15); however, the spall strengths were within the measured error for both orientations. The

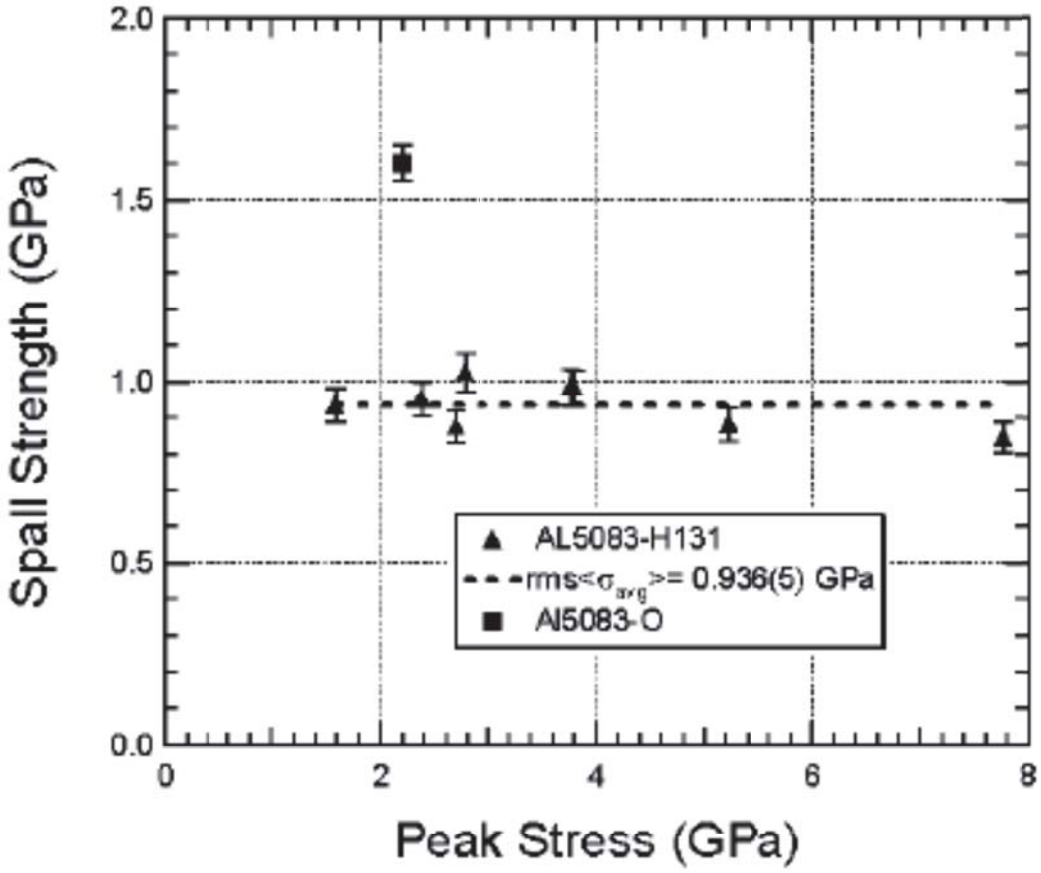

Figure 14: Spall strength of Al 5083-H131 reported by Boteler and Dandekar [92] with the spall strength of Al 5083-O included [99]

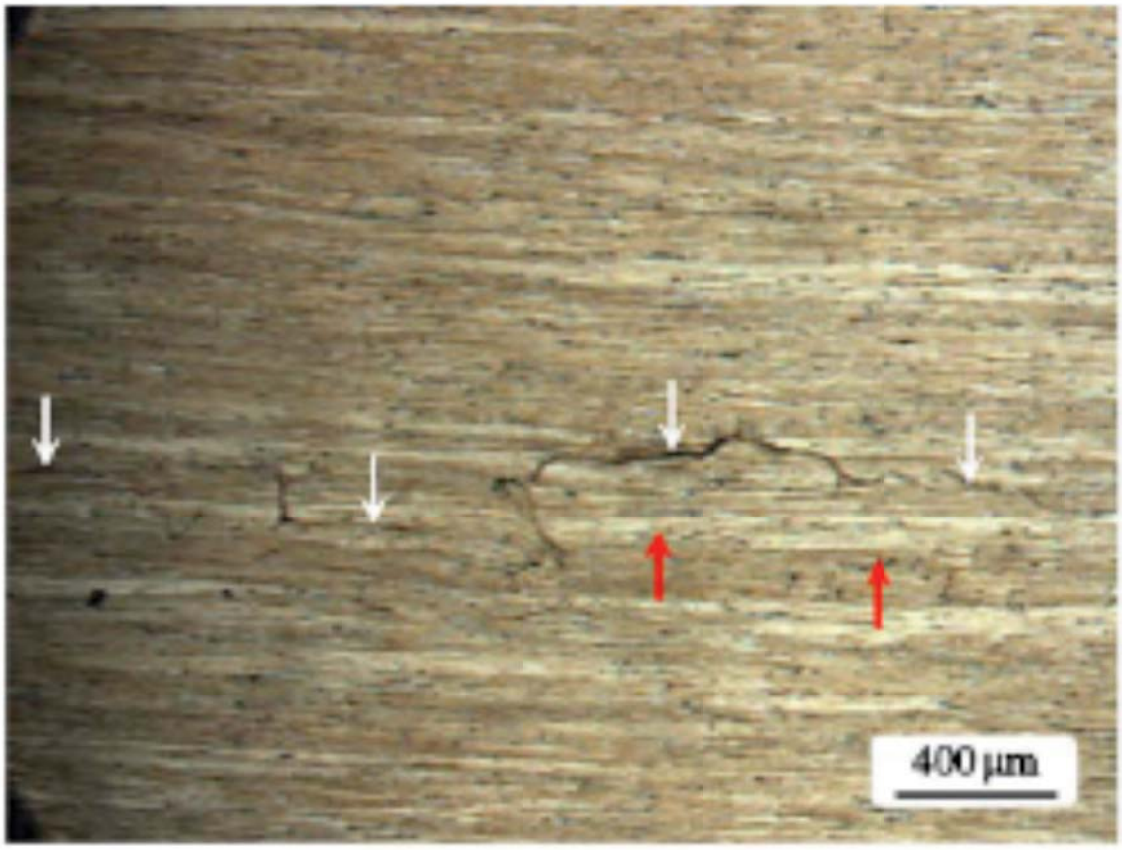

Figure 15: Optical microscope images taken by Appleby-Thomas and Hazell [35] of spall damage in post-impact Al 5083 samples. The impact direction is up the screen, and was performed through the thickness of a rolled plate. The white and red arrows correspond to primary and secondary spall planes respectively.

authors speculated that the spall strength was significantly higher than the transgranular fracture strength, making fracture type an insignificant factor for the spall strength of Al 5083-H32 [35].

2.6 Spall Damage Models

Numerous quantitative models accounting for the extent of damage produced during spalling have been developed. Failure due to ductile and brittle modes caused by spalling are shown in Figure 17. For metals, spalling often occurs by ductile nucleation, growth, and coalescence of voids as seen in Figure 17(b) as opposed to microcracking shown in Figure 17(a) , which is considered a brittle fracture mechanism [100]; however, the cracking of brittle inclusions within ductile materials is a known contributor to the nucleation of voids during spalling

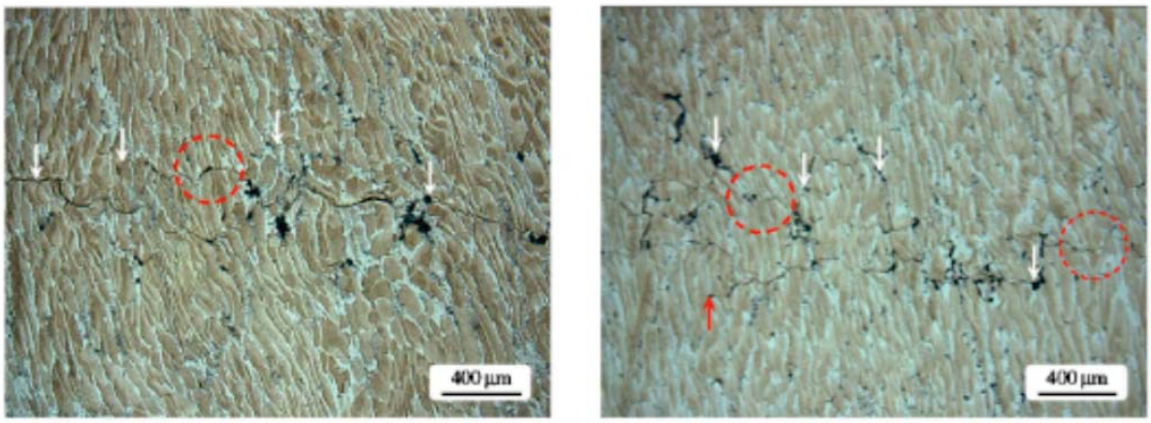

Figure 16: Optical microscope images taken by Appleby-Thomas and Hazell [35] of spall damage in post-impact Al 5083 samples. The impact direction is up the screen, and was performed along the rolling direction of a rolled plate. The white and red arrows correspond to primary and secondary spall planes respectively, and dashed circles correspond to regions exhibiting transgranular fracture.

[32, 33, 35, 37, 39, 40, 44, 79, 101]. Spall damage models thus quantify the nucleation and growth rates of damage (either voids or microcracks) during spalling as a function of the stress state.

2.6.1 Davison and Stevens Models

Davison and Stevens [102] developed a continuum spall damage model that accounts for continuous measures of damage throughout the spalling process. For continuous damage accumulation, spalling depends on the history of the continuum field variables, whereas, instantaneous spall damage only depends on current values of the continuum field variables. Davison and Stevens [102] further categorized continuous damage accumulation into simple and compound damage accumulation. For simple damage accumulation further damage formation is independent of damage history, while for compound damage accumulation, further damage formation is dependent on the damage history.

The simple damage accumulation model may be explained using Equations 9 and 10. In Equation 9, the time to produce a specific level of damage, D_0, is $\hat{\tau}$. This time decreases with increasing tensile stress, σ. The simple damage model states that any increment of damage, ΔD_i, will require a time, Δt_i, that is independent of any previous level of damage.

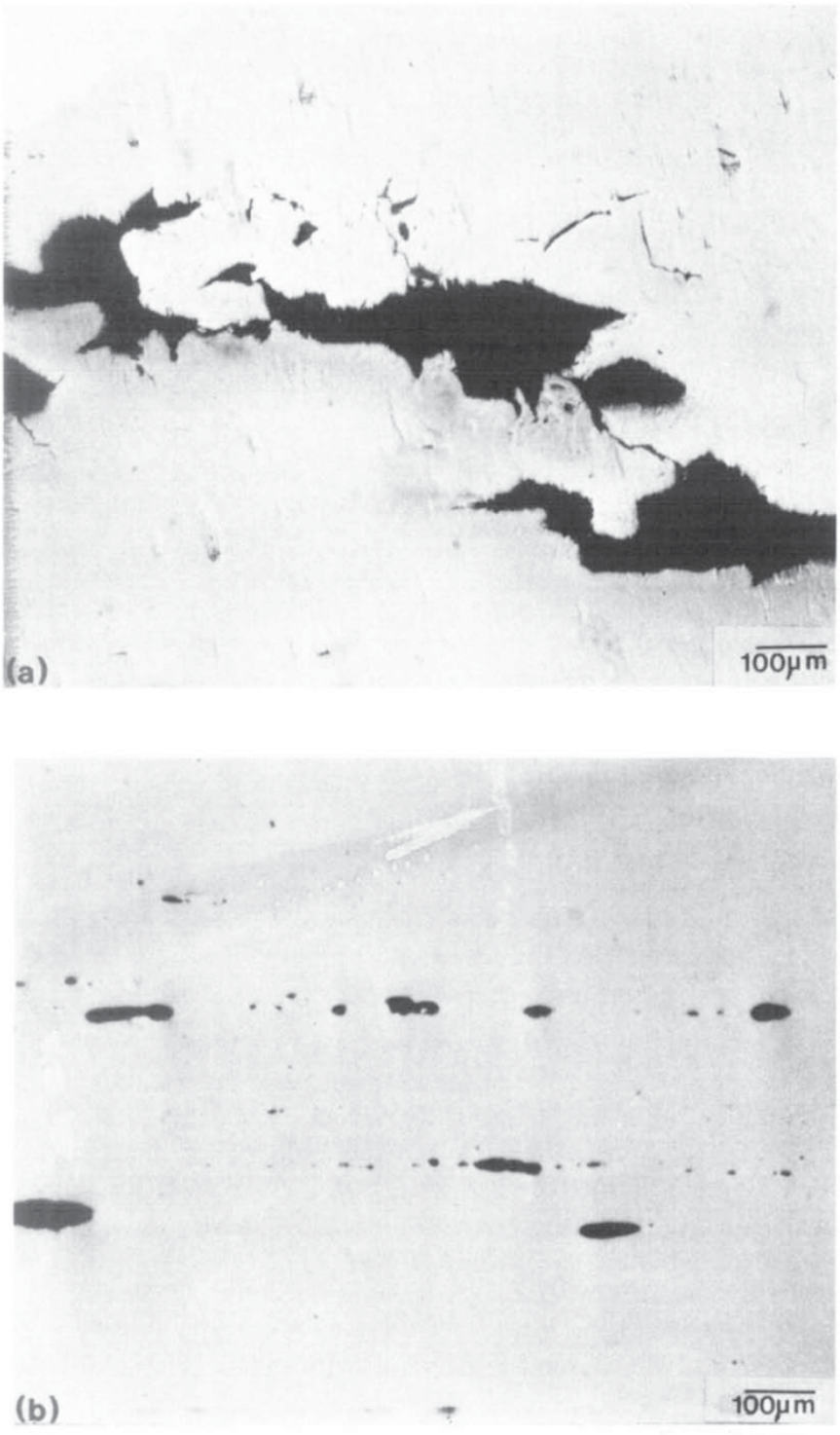

Figure 17: Optical microscope images of (a) brittle spall damage in a low carbon steel compared to (b) ductile spall damage in a nickel alloy [79]

$$\Delta D_i = \Delta t_i \frac{D_0}{\hat{\tau}} \tag{9}$$

The total level of damage as a function of location (x) and time (t) may be obtained by integrating Equation 9 over the total time period of damage accumulation to yield Equation 10.

$$D\left(x,t\right) = D_0 \int \frac{dt}{\hat{\tau}\left[\sigma\left(x,t\right)\right]} \tag{10}$$

Davison and Stevens [102] used an inverse power law function to describe the time dependence of spalling. This equation was initially presented by Tuler and Butcher [103] and is shown in Equation 11; it uses a critical tensile stress (σ_0) below which no damage will be produced. The variable, λ, is a material dependent parameter that describes the degree to which spalling is time dependent.

$$\hat{\tau} = \tau \left[\frac{\left(\sigma - \sigma_0\right) + \left|\sigma - \sigma_0\right|}{2\sigma_0}\right]^{-\lambda} \tag{11}$$

Equations 10 and 11 give a simple estimate of the time, stress, and location dependence of spall damage, whereby previous damage does not affect the current values. A more realistic model would result in faster damage accumulation once existing damage has been formed. The compound damage model of Davison and Stevens [102] uses a damage rate function, $\dot{D}$, that is a function of the stress and the current level of damage, D. This damage rate function is for low amounts of spall damage (incipient spall), such that $\dot{D}$ can be approximated by a first order power expansion from the non-spalled state. The completely spalled state is given by D^* in Equation 12.

$$\dot{D} = \frac{D^*}{\tau_0}\left[\phi_0 + \phi_1 \frac{D}{D^*}\right] \tag{12}$$

For a constant stress level, Davison and Stevens [102] attributed the following values to the functions ϕ_0 and ϕ_1.

$$\phi_0 = \frac{1}{2}\tau V_N B \sigma_G \left(\Sigma - \Sigma_N + \left|\Sigma - \Sigma_N\right|\right) \tag{13}$$

$$\phi_1 = 3\tau C \sigma_G \Sigma \tag{14}$$

$$\Sigma = \frac{1}{2}\left(\sigma - \sigma_G + |\sigma - \sigma_G|\right) \tag{15}$$

$$\Sigma_N = \frac{1}{2}\left(\sigma_N - \sigma_G + |\sigma_N - \sigma_G|\right) \tag{16}$$

In Equations 13-16, $\tau, V_N, B, C, \sigma_G$, and σ_N are all material constants, with σ_G and σ_N as the threshold stresses required for damage growth and nucleation respectively. By inserting Equations 13-16 into Equation 12 and solving for D, Davison and Stevens [102] derived Equation 17 as the model for compound damage accumulation during spalling.

$$D = \frac{BV_N\left(\Sigma - \Sigma_N + |\Sigma - \Sigma_N|\right)}{6C\Sigma}\left[exp\left(3C\sigma_G\Sigma t\right) - 1\right] \tag{17}$$

Equation 17 describes a generic model for damage accumulation due to nucleation and growth of any quantified damage parameter. It was not calculated based on microscopic observations of damage in spalled samples. A more experimentally rigorous spall damage equation was derived by Barbee et al. [104] as a part of the Stanford Research Institute (SRI) spall damage model. The SRI model presented in the next section reaches the same equation for damage accumulation shown in Equation 17 from experimental quantification of damage size distributions in spalled samples.

2.6.2 Stanford Research Institute Model

The Stanford Research Institute (SRI) spall model was developed by Barbee, Seaman, Crewdson, Curran, Shockey, and co-workers [44, 100, 104–106]. The model is based on calculating nucleation and growth rate functions for voids or microcracks based on statistical counting of flaws in impacted specimens. The methodology used to derive the SRI model is summarized by Barbee et al. [104] in a number of steps and is shown below.

1. Perform plate impact testing to produce spalling in target specimens.

2. Section and polish the post-impact specimens to view spall damage.

3. Count the position, size, and orientation of each flaw (either voids or microcracks) and group the data into appropriate areal size distribution bins.

4. Transform the areal distributions of spall damage into volume distributions.

5. Calculate the nucleation rate ($\dot{N}$) and growth rate ($\dot{R}$) of the damage for each impact velocity (or impact stress) from the volume distributions.

An example of the volume distributions calculated from a plate impact test on Al 1145 is shown in Figure 18. For a single plate impact test such as that shown in Figure 18, a family of void size distributions can be generated based on their location within the sample. The nucleation rates ($\dot{N}$) and growth rates ($\dot{R}$) can be obtained from data similar to that shown in Figure 18 by finding the intersections of the data with lines of constant size and constant volume distribution respectively. For each location within the sample (represented by a single distribution curve in Figure 18), the pulse duration will be different, which will yield the time (t) dependence of the spall process. If multiple plate impact tests are performed using a variety of impact velocities, then the stress (σ) dependence of damage accumulation can also be found in this way.

The equations describing the extent of damage and the nucleation and growth rates of damage during ductile spalling are listed below in Equations 18-22. These equations describe the nucleation and growth of spherical voids due to yielding of a ductile matrix. The growth of microcracks in brittle materials is dominated by the fracture toughness of the material, whereby the cracks must reach a critical size before rapid growth can take place [104].

$$f_V = \frac{8\pi \dot{N} R_0^3}{3A} \left[exp\left(3At\right) - 1 \right] \tag{18}$$

$$A = \frac{\sigma - \sigma_{g0}}{4\eta} \tag{19}$$

$$\dot{N} = \dot{N}_0 exp\left(\frac{\sigma - \sigma_{n0}}{\sigma_1} \right) \tag{20}$$

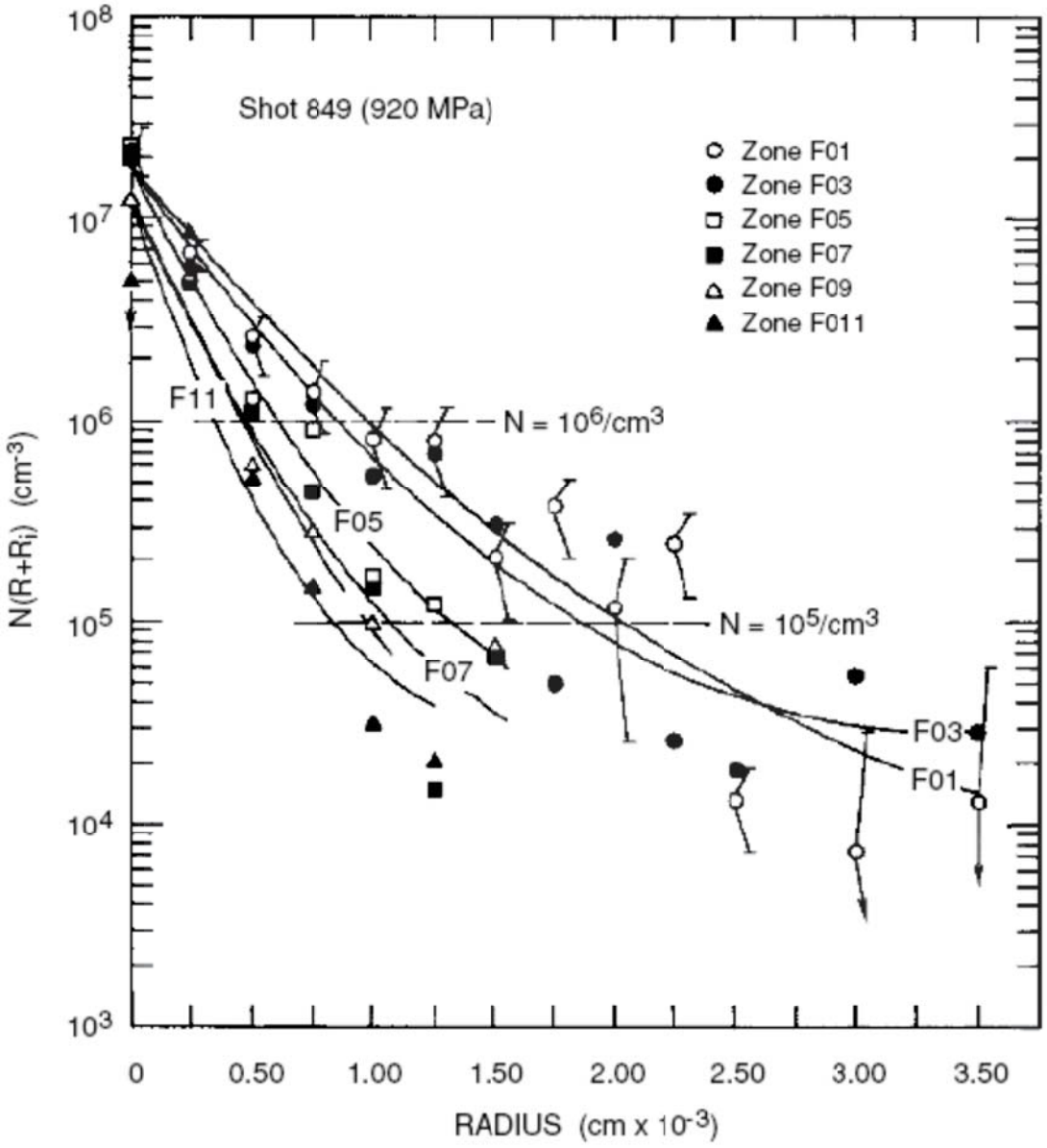

Figure 18: Void volume distribution data from post-impact Al 1145 samples. The data was originally published by Antoun et al. [44] and is presented as the volume density of voids greater than a given void radius (R).

$$\dot{R} = AR \tag{21}$$

$$R = R_0 exp\,(At) \tag{22}$$

The void volume fraction (f_V), shown in Equation 18, is a measure of the total extent of damage. This equation derived by the SRI research group [44, 100, 104–106] using the void counting techniques described above is similar to the generic damage parameter derived by Davison and Stevens [102] shown in Equation 17. Similar to the Davison and Stevens model, the SRI model uses threshold stresses for nucleation and growth of voids (σ_{n0} and σ_{g0} respectively). The variables σ_1 and $\dot{N}_0$ are material fitting parameters, whereas η and R_0 are the material viscosity and smallest visible void size respectively. Barbee et al. [104] used a value of 1 μm for R_0 for plate impact testing of Al 1145.

2.6.3 Cochran and Banner Model

Cochran and Banner [107] developed a one-dimensional computational spall model that was compared to experimental data from plate impact tests on uranium. This Lagrangian, finite difference code employed both a Gruneisen equation of state and an elastic-plastic yielding model. The model also accounts for the transition from the initial compression state to the tensile state through an additional model for the Bauschinger effect [107]. The spall damage model is simple—having only two parameters—the spall strength (Σ) and a critical damage parameter (D_0) that is related to a strength function (F). The strength function reduces the strength (σ) of the material as the extent of damage (D) increases, similarly to the compound damage accumulation model described by Davison and Stevens [102]. The variables σ and F are given by Equations 23 and 24 respectively.

$$\sigma = F\Sigma \tag{23}$$

$$F = 1 - \left(\frac{D}{D_0}\right)^{\frac{2}{3}} \tag{24}$$

Similar to the SRI model, Cochran and Banner [107] used a statistical representation of damage to yield the continuum material response to spalling. For the SRI model, the volume fraction of voids or cracks was used as the damage parameter. For the case of one-dimensional simulations, the damage is reduced to the volume per unit area (A) normal to the strain. Once the damage reaches the critical value (D_0), given by Equation 25, both F and σ go to zero. This is meant to model the fast fracture of ductile materials following void coalescence. For failure of ductile materials, r_2 is the characteristic void size before coalescence will occur, and N_0 is the total number of flaws. The exponent in Equation 24 is for ductile spalling only; however, the expression can be modified to account for spalling in brittle materials [108].

$$D_0 = 8\pi r_2^3 \frac{N_0}{A} \tag{25}$$

The Cochran and Banner [107] model has shown good agreement with the measured free surface velocity during plate impact experiments on uranium. The simulated and experimental data are both shown in Figure 19. The good agreement between the model and the measured results implies that this model is useful for one-dimensional simulations of spalling in ductile materials.

2.7 Effects of Peak Stress, Strain Rate, and Duration on the Spall Strength and Hugoniot Elastic Limit of Ductile Materials

Spall strength values for a given material are often presented as a function of the peak stress in the literature. The peak stress induced within an impacted specimen will depend both on the impactor material and the impact velocity as shown in the schematic Hugoniot curve in Figure 12. However, the decompression strain rate during spalling is another parameter that has been shown to affect the spall strength of a material [44]. The decompression rate will change with impactor type and impact velocity, similarly to the peak stress, and will also change with target sample thickness. Spall strength has also varied with changes to the peak stress duration [109], which can be changed by varying the flyer plate thickness in

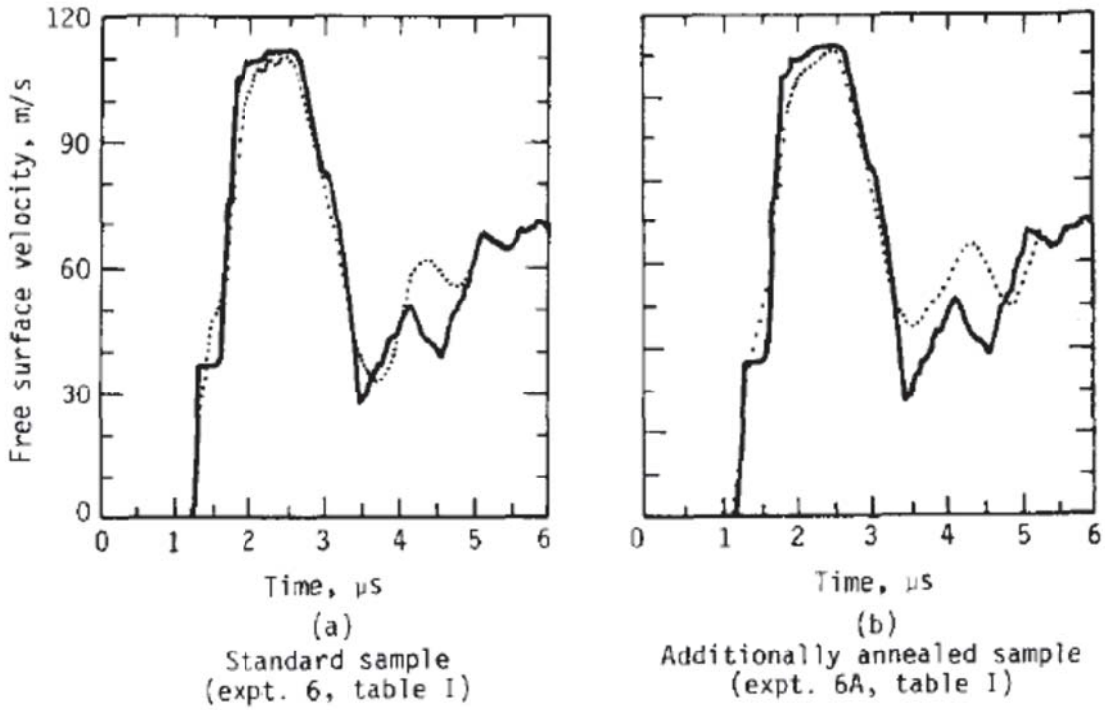

Figure 19: Simulated (solid line) vs. experimental (dotted line) free surface velocity data for spalled uranium samples as reported by Cochran and Banner [107]

a plate impact experiment. The HEL has also shown strain rate dependence, whereby the elastic precursor decays with increasing sample thickness.

The dependence of the spall strength and HEL on the impact experimental setup suggests that these values should not be considered to be material properties. Instead, comparisons between the HEL and spall strength for different materials should only be used when the impact setup is similar.

2.7.1 Effects of Peak Stress on Spall Strength

The spall strength is often presented as a function of the peak stress; however, the spall strength of ductile materials does not often change due to the peak stress alone. For brittle materials, where sudden catastrophic failure often occurs, the spall strength is often peak stress dependent [44, 110]. The spall strength of ductile materials may be peak stress dependent if the material undergoes a high pressure phase change, whereby the spall strength will display a sudden change at the phase transition pressure [44]. Aluminum does not undergo a high pressure phase change; however, all ductile materials display peak stress dependent spall strength at shock pressures large enough to induce melting (which is itself a phase change). Figure 20 displays the spall strength of tin as a function of the peak stress for peak stresses large enough to induce melting. For peak stresses less than 10 GPa, tin displays little peak stress dependence, but for peak stresses above 10 GPa melting occurs and the spall strength falls to zero. The peak stress required to melt aluminum is beyond the capability of the facilities used for this research, so there should be little peak stress dependence for the measured spall strength values.

2.7.2 Effects of Decompression Strain Rate on Spall Strength

The spall strength often shows strain rate dependence for ductile materials [44]. The strain rate of interest is not the incident compressive strain rate as the material rises to the peak stress, but instead it is the decompressive strain rate as the material falls from the peak compressive state into the tensile state that causes spallation. This strain rate ($\dot{\epsilon}$) is given by Equation 26 and can be directly measured using the time gradient of the release in the free surface velocity data (u_1 in Figure 13). The strain rate in Equation 26 is actually the

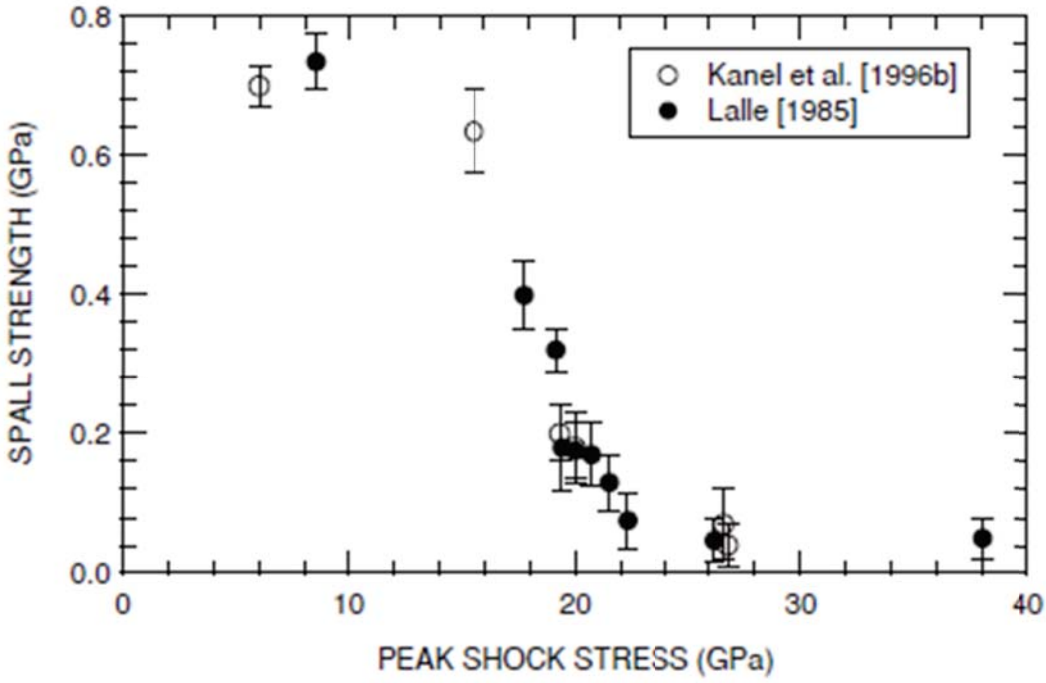

Figure 20: Spall strength of tin as a function of the peak stress for stresses large enough to induce melting. As melting occurs, the spall strength falls to zero. [44]

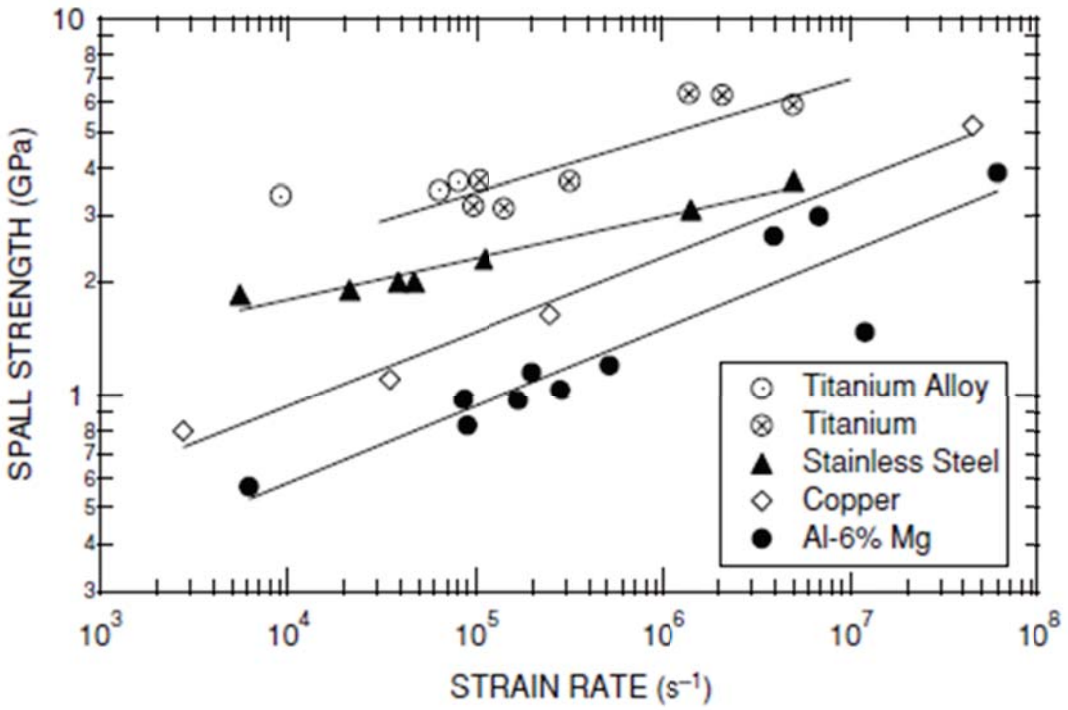

Figure 21: Spall strength as a function of decompressive strain rate for several ductile materials. The spall strength displays a power law strain rate dependence for each ductile material. The power law function is fit to the data for each material and appears as a straight line for the log-log axes used. [44]

rate of change of the volume (V) normalized by the initial volume, which yields the rate of decompression from the peak state.

$$\dot{\epsilon} = \frac{\dot{V}}{V_0} = \frac{-\nabla_t u_1}{2C_B} \tag{26}$$

The spall strength of several ductile materials as a function of the strain rate given in Equation 26 is shown in Figure 21. Each ductile material type shows an increasing spall strength with decompressive strain rates spanning several orders of magnitude. For such a wide range of strain rates, it has been shown that spall strength of ductile materials displays a power law dependence [44]. These power law fits are included in Figure 21 and display a good fit to the measured spall strength trends over such a large strain rate range.

The decompressive strain rate in an impacted target will change with changes to the impactor material, impact velocity, or target thickness; however, the impactor material and

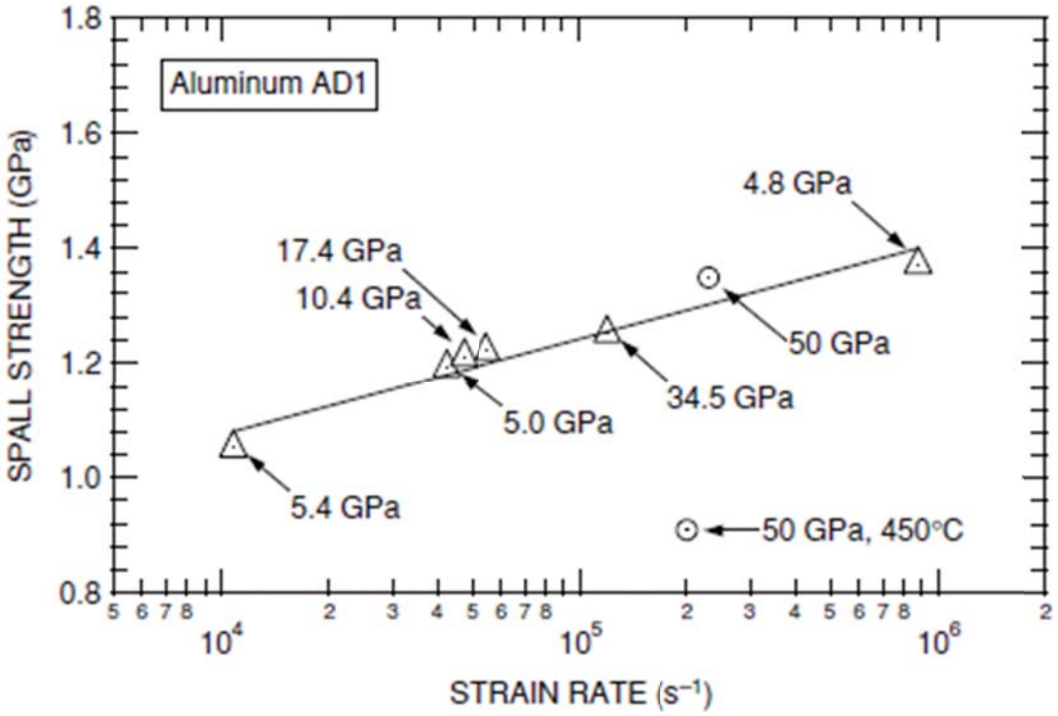

Figure 22: Spall strength as a function of decompressive strain rate for aluminum AD1 samples impacted using a wide range of strain rates and peak stresses. The peak stress is listed next to each datapoint. Two experiments were performed at a peak stress of 50 GPa, with one of the experiments performed at high temperature (450°C) to induce melting. The results show that aluminum is highly dependent on the strain rate but not on the peak stress unless melting has occurred. [44]

velocity will also determine the peak stress value, which can lead to uncertainty as to which parameter (strain rate or peak stress) results in changes to the spall strength. Kanel et al. [44] performed a series of experiments on an Al-Mg alloy (aluminum AD1) using a variety of both peak stress and decompressive strain rates. The results are plotted in Figure 22.

Kanel et al. [44] impacted the aluminum samples using a gas gun and using explosively driven flyer plates to give a wide range of both peak stresses and strain rates. Figure 22 clearly shows that the spall strength of aluminum displays a strong dependence on the decompressive strain rate for any peak stress value. The peak stress does not appear to play a role in the spall strength values presented in Figure 22. This is evidenced by the fact that similar peak stress values of 5.4 GPa and 4.8 GPa resulted in widely different spall strength values of approximately 1.0 GPa and 1.4 GPa respectively, due to large differences

in the strain rate. Furthermore, similar spall strength values near 1.2 GPa were measured for widely different peak stress values of 5.0, 10.4, and 17.4 GPa at a similar strain rate.

Two experiments were performed near 50 GPa, whereby one of the specimens was heated to 450°C prior to impact. The heated specimen displayed a large decrease in the spall strength compared to the room temperature specimen at a similar strain rate value. The decreased spall strength was due to melting induced by the combination of pre-heating and impacting with a large peak stress, similarly to the spall strength of tin shown in Figure 20. Therefore, the spall strength of aluminum displays no strong dependence on the peak stress accept for the case where the peak stress is large enough to induce melting.

2.7.3 Effects of Shock Duration on Spall Strength

The peak stress duration has also been shown to affect the spall strength of ductile materials. Since spalling of ductile materials requires the time-dependent processes of nucleation and growth of voids [44], it is to be expected that the time at the peak stress would play some role in the failure process. Gray et al. [109] used both triangular stress pulses (Taylor waves), where the material immediately releases from the peak stress, and square-topped waves (like those shown in Figure 11) with a duration near 0.9 μs to measure the spall properties of a ductile 316L stainless steel. The longitudinal stress traces recorded by manganin stress gauges located at the interface between the stainless steel rear surface and a PMMA backer are shown in Figure 23.

Gray et al. [109] impacted the stainless steel specimens at peak stresses of 6.6 GPa, 10.2 GPa, and 14.5 GPa using both square-topped waves and Taylor waves at each peak stress value. As Figure 23 shows, spalling occurred for each of the three peak stress values using square-topped waves, as evidenced by the pullback in the longitudinal stress traces. However, the material did not spall until the maximum peak stress value measured (14.5 GPa) when using Taylor waves. The data shows that decreasing the stress duration causes the spall strength to increase. In fact, a similar level of damage was measured for impact using the square-topped wave at 6.6 GPa as was measured for impact with the Taylor wave at 14.5 GPa—more than double the peak stress value [109].

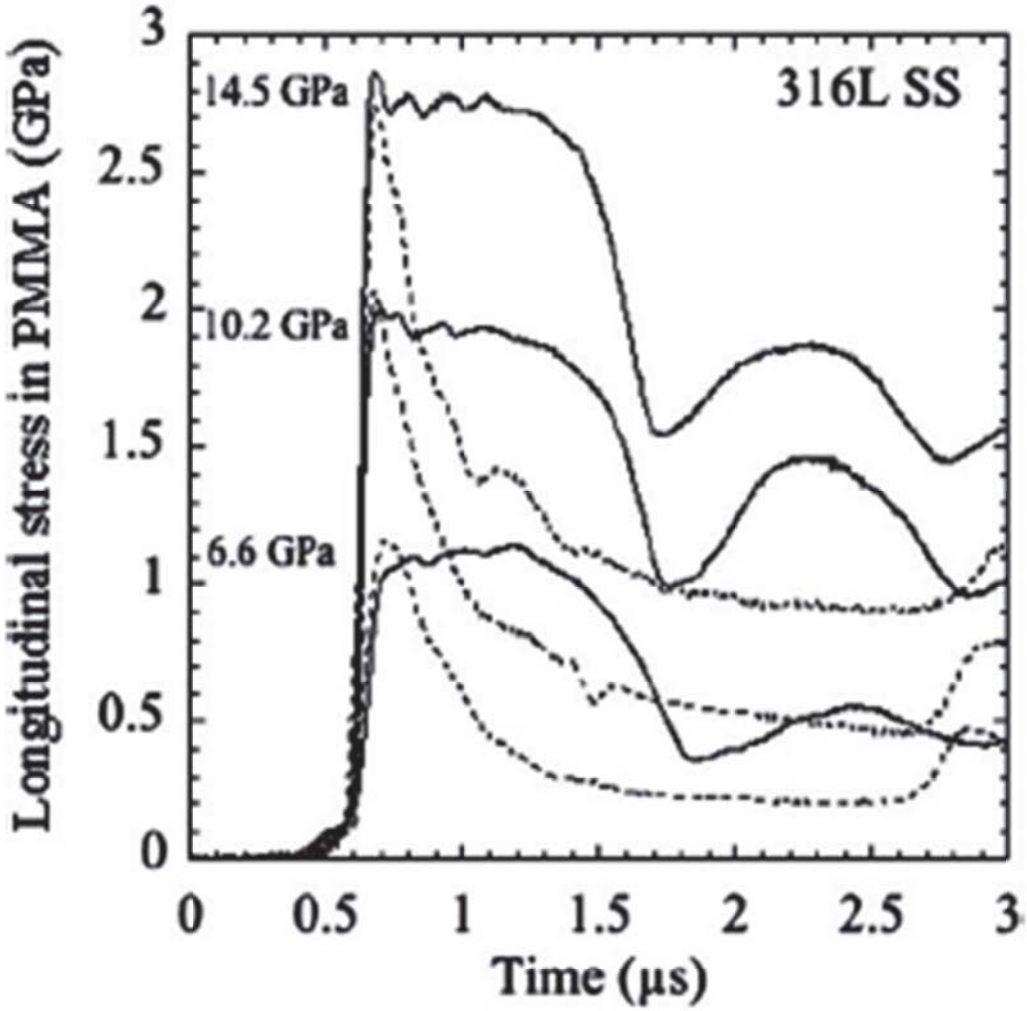

Figure 23: Longitudinal stress gauge traces for stainless steel impacted using Taylor waves and square-topped waves of the same peak stress. For a given impact stress, the spall damage was higher for impact using square-topped waves, indicating that decreased stress duration results in higher spall strength. [109]

Gray et al. [109] observed similar levels of damage (indicating similar spall strength values) for similar stress impulses measured using the area under the stress time curve up to the pullback signal. The area under the stress curves for the sample impacted using a square-topped wave at 6.6 GPa and the sample impacted using a Taylor wave at 14.5 GPa are shown in Figure 24. Since both the stress impulses and spall damage levels were similar for the two experimental gauge traces shown in Figure 24, the results indicate that the stress impulse is indicative of the measured spall strength value when both peak stress and duration are varied for ductile materials.

For the spall damage studies performed by Gray et al. [32], the duration was varied by several orders of magnitude. Chen et al. [38], performed several plate impact experiments on aluminum whereby the duration was changed but kept on the order of one microsecond. For those experiments, the spall strength did not depend on the duration, but instead varied with the decompression rate which changed with sample thickness. It is possible that the spall strength of ductile materials only depends on the duration when the duration is very short. Once the material has enough time to nucleate and grow voids, the duration should no longer affect the spall strength. This would account for the differences in the data presented by Gray [32] that used short durations and observed duration dependent spall strength versus that presented by Chen et al. [38] that used long durations and observed duration independent spall strength.

For the case of brittle materials, Escobedo et al. [110] have shown that the spall strength and damage level of brittle tungsten heavy alloy samples did not depend on shock duration. Instead, the spall behavior was heavily dependent on the peak stress level. Since brittle fracture is often characterized by abrupt catastrophic failure due to cracking, rather than the time-dependent process of nucleation and growth of voids, the trends in the spall strength for brittle versus ductile materials match well with their underlying failure mechanisms.

2.7.4 Elastic Precursor Decay and Strain Rate Dependence of the Hugoniot Elastic Limit

The Hugoniot elastic limit (HEL) of aluminum has also shown dependence on the target thickness [111–113]. This phenomenon is referred to as “precursor decay” in the literature,

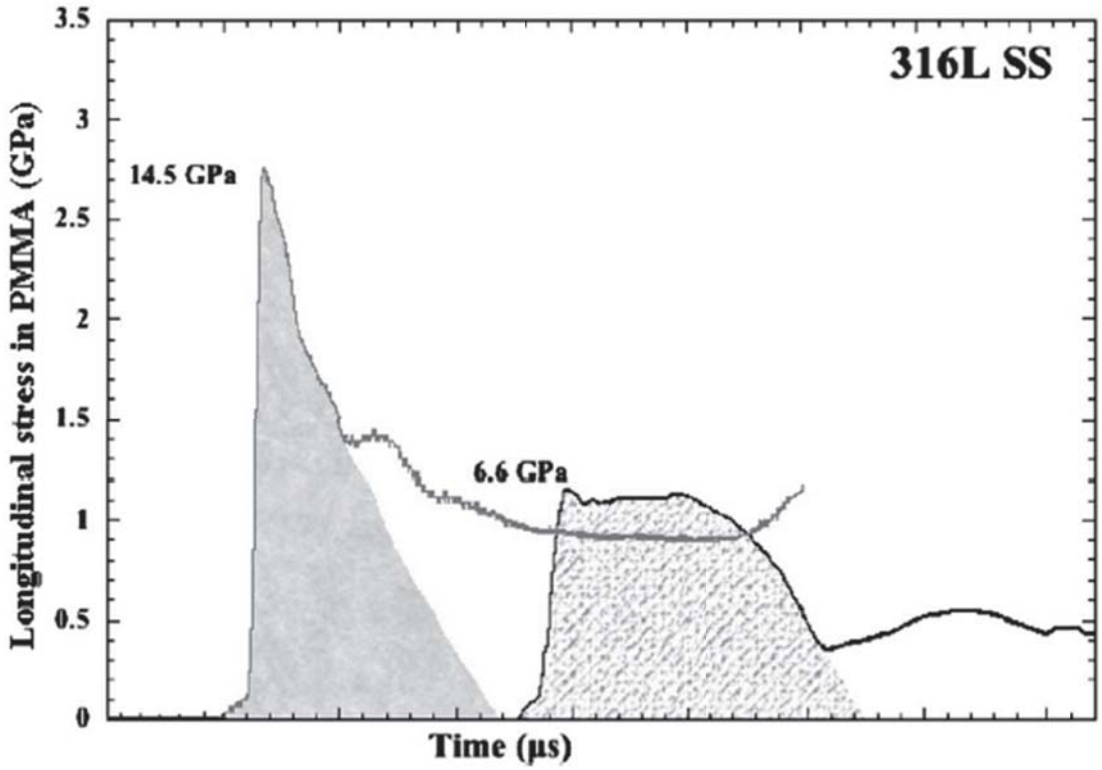

Figure 24: Longitudinal stress gauge traces for stainless steel impacted using a similar stress impulse. The impulse was calculated using the area under the stress time curve up to the pullback signal. For the two traces shown, both the stress impulse and level of spall damage were similar, indicating that similar stress impulses will result in similar measured spall strength values. [109]

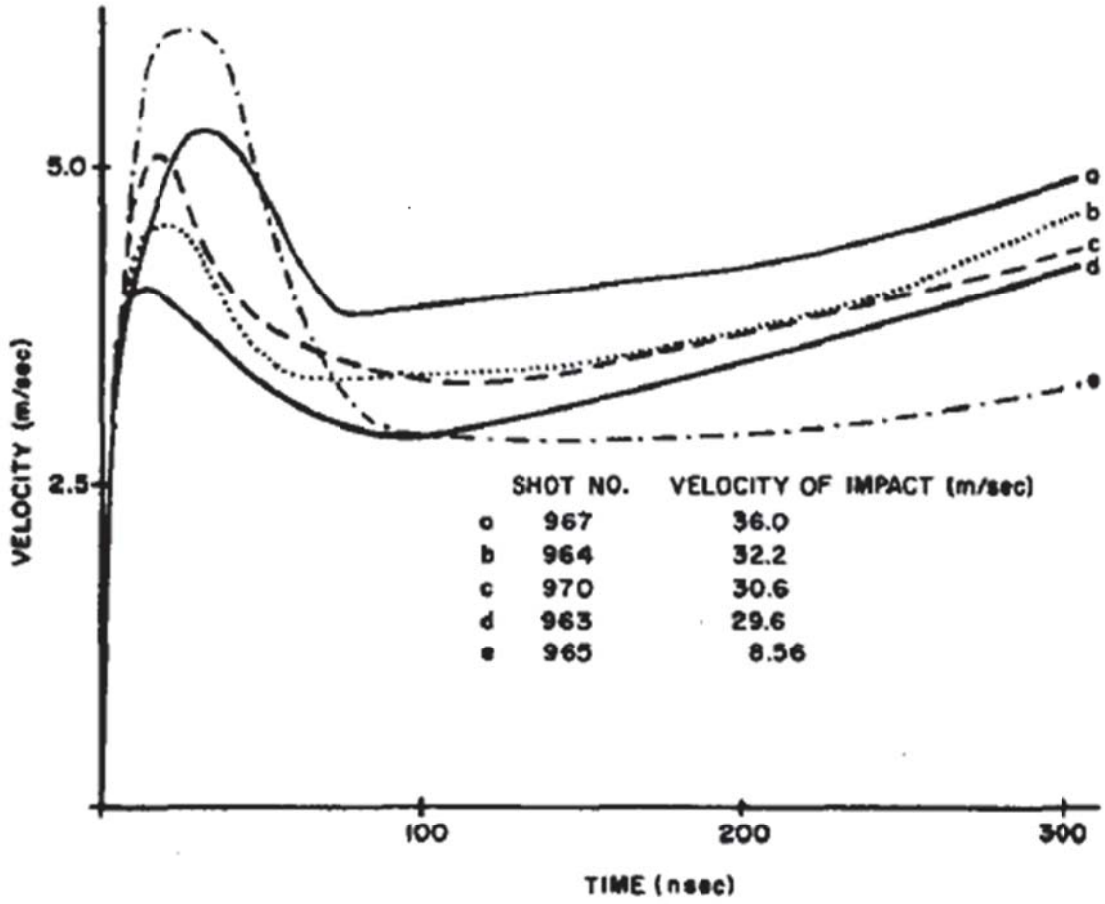

Figure 25: Free surface velocity vs. time for Al 1060 samples displaying upper and lower yielding. The upper yield point increases with increasing impact velocity. [113]

and is characterized by a steep drop in the HEL as target thickness increases along with upper and lower yielding at the HEL. The phenomenon was initially reported by Barker et al. [85] for experiments on annealed Al 1060 samples. The free surface velocity near the HEL that was reported by Barker et al. [85] is shown in Figure 25.

Each velocity trace in Figure 25 displays both an upper and lower yield point near the HEL. The upper yield point increases with increasing impact velocity, indicating that the phenomenon is rate dependent. Nicholas et al. [114] were able to use computer simulations to prove that the precursor decay phenomenon is not possible without using a strain-rate dependent mechanical model, which fits well with the upper yield point's rate dependence.

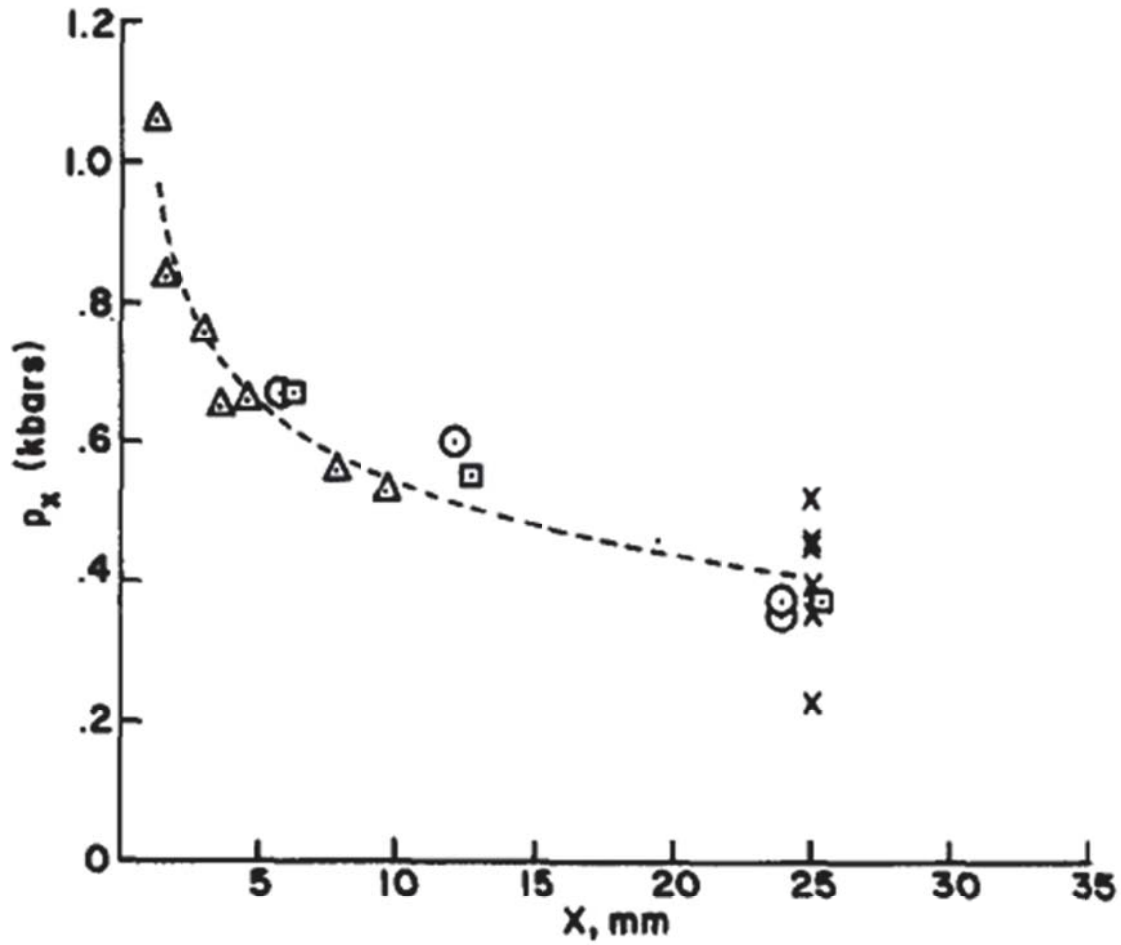

Figure 26: HEL data as a function of sample thickness for Al 1060 samples. The HEL quickly decays with increasing sample thickness to a near constant value. [112]

Arvidsson et al. [112] impacted Al 1060 samples as a function of the target thickness. The HEL value fell from 1.06 kbar for a 1.38 mm thickness to a value of 0.53 kbar for a 9.68 mm thickness. The HEL data measured by Arvidsson et al. [112] along with similar data on Al 1060 is presented in Figure 26.

Figure 26 shows that the HEL rapidly decreases to a near constant value as thickness increases. Billingsley [111] calculated that the decay limit of the HEL, where the HEL reaches a constant value at large thicknesses, is limited by the DeBroglie wave velocity (V_1) given by Equation 27.

$$V_1 = \frac{h}{2md_1} \tag{27}$$

In Equation 27, h is Planck's constant, and m and d are the mass of one atom in the unit cell and the closest atomic distance respectively. The DeBroglie velocity limiting HEL (P_{V_1}) is then given by Equation 28.

$$P_{V_1} = \rho_0 C_L V_1 \tag{28}$$

Billingsley [111] reported that this limiting HEL value matched the experimental HEL values measured for iron, Al 6061-T6, PMMA, a nickel alloy (MAR-M200), and lithium fluoride.

While the physical cause of elastic precursor decay has not yet been ascertained, it is often attributed to the initial high stress required to nucleate dislocations near the impact surface followed by ease of yielding after dislocations have already been nucleated [112]. This explanation accounts for the rapid decrease in HEL as the wave moves away from the impact face as well as the upper and lower yielding phenomenon.

CHAPTER 3

EXPERIMENTAL PROCEDURE

The overall goal of this research is to investigate the effects of the microstructure of Al-Mg alloys for enhanced spall resistance. To achieve this goal, a variety of microstructures were produced using several different processing techniques and characterized both before and after dynamic impact loading. The dynamic mechanical properties of the Al-Mg alloys were measured using plate impact experiments and one-dimensional computer simulations using proper spall damage models. Following plate impact, the post-mortem microstructure was characterized to observe the damage pathways taken during dynamic failure as well as to identify the microstructural features that nucleate spall damage. Size distributions of damage were also used to compare the observed post-mortem damage to that predicted during spall simulations.

3.1 Materials

Several Al 5083 plates were tested in different tempers, signifying different conditions of processing. The principal alloying elements in Al 5083 are Mg and Mn, having compositions of 4.0-4.9 wt.% and 0.4-1.0 wt.%, respectively. The Mg content results in strain hardenability for the alloy, while Mn additions form dispersoid phases that refine the grain structure. An Al 5083-H116 rolled plate was acquired from McMaster-Carr as a 0.75″ (approximately 19 mm) thick plate. The H116 temper designation denotes that the material was strain hardened. The spall properties of the H116 plate will be presented in Chapter 5. Materials processed via equi-channel angular pressing (ECAP) used Al 5083-H321 as the initial billet. The H321 temper denotes that the material was strain hardened followed by a partial annealing treatment yielding identical mechanical properties as the H116 temper of Al 5083 [115]. The spall behavior of Al 5083 processed using ECAP is presented in Chapter 6. The Al 5083-H116 plate was also used as the starting material for another set of specimens processed to yield equiaxed grains. The spall properties for this equiaxed

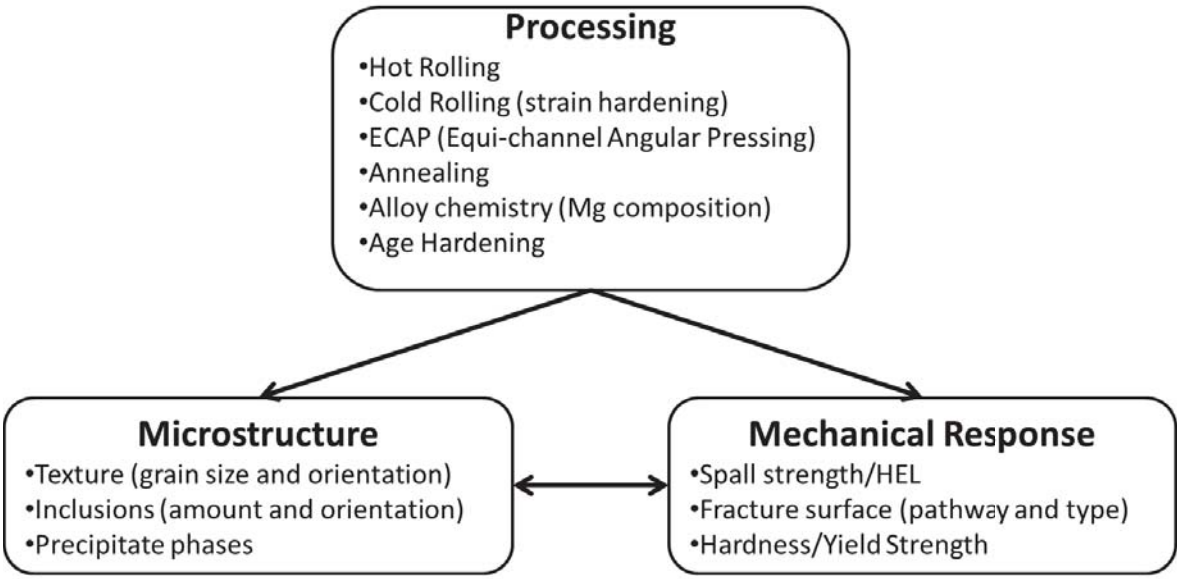

Figure 27: Flowchart showing the connection between processing, microstructure, and spall response for Al-Mg alloys

grain structure are presented in Chapter 7. One set of experiments used an Al-9wt.% Mg alloy with trace additions of Ag. The as-received plate was indirectly extruded by Universal Alloys, Inc., while some specimens were later precipitation hardened. The precipitation hardening behavior and the spall behavior of this alloy are presented in Chapter 8.

This research focuses on the interplay between processing, resulting microstructure, and spall response of Al-Mg alloys (such as Al 5083) with varying Mg content, as illustrated in Figure 27. The processing parameters shown in Figure 27 each result in microstructural changes that can either increase or decrease the spall strength. Therefore, the key microstructural features that affect the spall strength were characterized via optical and scanning electron microscopy after each stage of processing and related to the spall response of the material measured by plate impact experiments.

The effects of each processing step on the microstructure of Al-Mg alloys is as follows. The extent of hot and cold working will determine the final grain structure as well as the strength of the finished product. Al-Mg alloys for armor are often produced in plate form, which will yield a textured grain structure with varying mechanical properties based on impact direction with the rolled plate. The three principal directions of a rolled plate

(longitudinal, short transverse, and long transverse) are shown schematically in Figure 28 along with the grain shape produced in each plane of the plate. Furthermore, brittle particles such as inclusions formed during casting or dispersoids formed during the pre-heat treatment align along grain boundaries in the rolling direction of rolled plates. In this project, one of the tested materials was a rolled Al 5083-H116 plate having a textured microstructure. A more uniform and sub-micron grain structure was produced via equi-channel angular pressing (ECAP) of an Al 5083-H321 plate. In addition, a uniform grain structure with moderately-sized (34 μm) grains was formed by stretching and annealing the rolled Al 5083-H116 plate. The effects of grain and inclusion size and orientation were all of interest for these three sample types.

An Al-9wt.% Mg alloy with trace amounts of silver was precipitation hardened in order to measure the effects of precipitate phases on the spall properties of Al-Mg alloys. Increasing the magnesium composition can result in a precipitation hardenable system for Al-Mg alloys, but this can also lead to dynamic recrystallization of the material during hot working. Therefore, the extent of precipitation hardening was of interest, in addition to any changes to the grain structure due to recrystallization. Age hardening can result in increased alloy strength when measured quasi-statically; however, precipitate phases may also decrease the spall strength—especially if these are located near the brittle particles. The microstructure of the precipitates and grain structure and their effects on spall properties were thus characterized for this stage.

3.2 Microstructure Characterization

Samples for optical microscopy were polished using a series of 400, 600, 800, and 1200 US grit grinding papers followed by fine polishing with 1 μm alumina and 0.05 μm colloidal silica polishing suspensions. The Barker's anodizing procedure was used to view the sample grain structure, whereby an oxide film is deposited on the aluminum grains. The oxide film maintains the orientation of the underlying grain, causing adjacent grains (with large enough misorientation angle) to appear differently colored when viewed under polarized light. Anodization consisted of immersing the samples for approximately 30 s in a solution

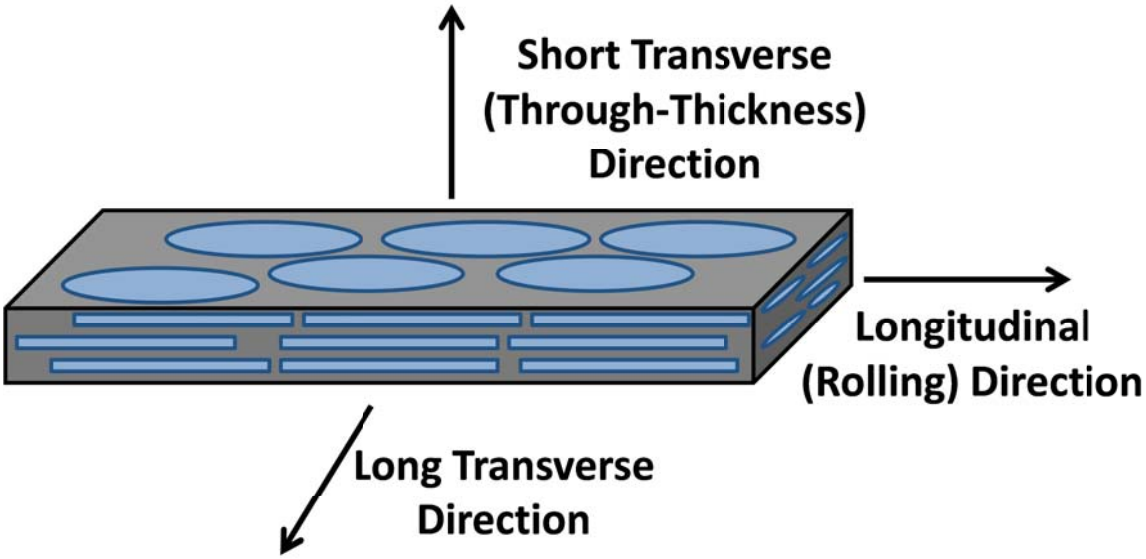

Figure 28: Schematic showing the three principal orthogonal directions in a rolled plate along with the microstructure produced in each plane of the plate.

of 1.8% fluoboric acid in water. A voltage of 30V DC with a current of approximately 1 A/in^2 was applied using a stainless steel electrode attached to a Goldstar GP-4303D DC power supply. Keller's reagent was used to preferentially etch the precipitate phases. The Keller's reagent consists of 0.5 mL hydrofluoric acid, 1 mL nitric acid, and 3 mL hydrochloric acid, in 95 mL of water. Samples were immersed for approximately 30 s, followed by rinsing in warm water.

Optical microscope images were obtained using either a Leica DM IRM reverse stage microscope or a Leica DM6000 M microscope. Images were taken under both bright field and polarized light. Recovered specimens for scanning electron microscopy (SEM) were kept unpolished so that imaging could be performed within the preserved spall plane. Examination of these fracture surfaces after spall testing was performed using an Amray 1810 SEM.

3.3 Ultrasonic Testing

The density (ρ_0) and sound speeds (C) of the tested materials were needed to calculate the HEL and spall strength, as shown in Equations 5 and 6 respectively. The density was measured using a standard Archimedes measurement. Sound speed measurements were

made using an Olympus 5072PR pulser/receiver in the pulse echo configuration attached to both Ultran VSP-200 and SRD50-5 ultrasonic probes for longitudinal and shear wave velocity measurements, respectively. The data were recorded using a Tektronix DPO 5104 1 GHz oscilloscope.

The longitudinal and shear wave velocities (C_L and C_S) were measured directly using the known sample thicknesses and the transit time of the respective transmitted waves. The bulk sound speed (C_B) and the elastic constants shear modulus (G), bulk modulus (B), elastic modulus (E), and Poisson's ratio (ν) were calculated using Equations 29-33 and the known values of C_L, C_S, and ρ_0.

$$C_L = \sqrt{\frac{B + 4G/3}{\rho_0}} \tag{29}$$

$$C_S = \sqrt{\frac{G}{\rho_0}} \tag{30}$$

$$C_B = \sqrt{\frac{B}{\rho_0}} \tag{31}$$

$$E = \frac{9BG}{3B + G} \tag{32}$$

$$\nu = \frac{3B - 2G}{2\,(3B + G)} \tag{33}$$

3.4 Plate Impact Gas Gun Experiments

Plate impact experiments were performed using the 80 mm diameter (7.6 m length) light-gas gun located at the Georgia Institute of Technology. A schematic of the plate impact experimental setup is given in Figure 29. The projectiles consisted of 80 mm diameter aluminum sabots with 70 mm diameter Al 5083 flyer plates mounted at the head. The flyer plates had an air gap backer to cause release waves from the flyer plate rear surface to reflect back into the sample during testing. The intersection between this release wave and another from the sample rear surface produces the tension necessary for spallation.

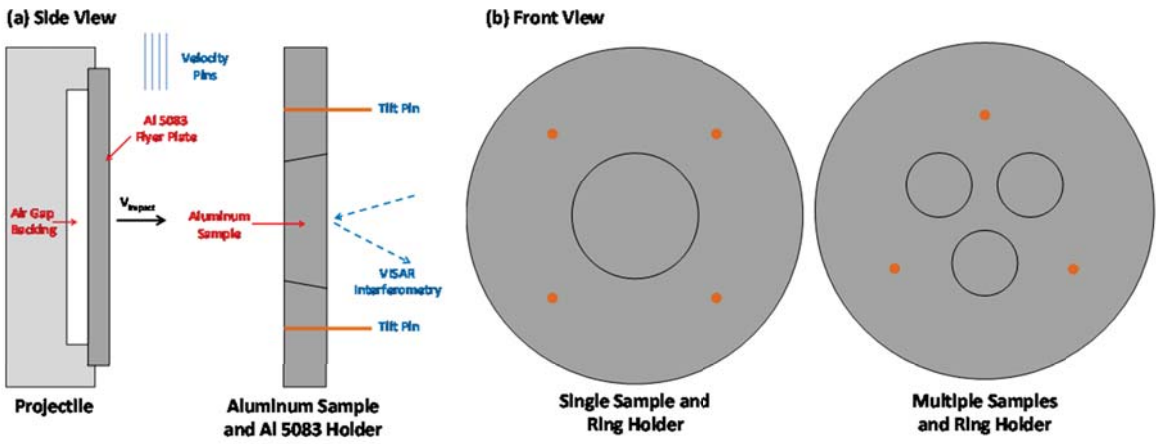

Figure 29: Schematic setup for plate impact experiments performed on Al 5083 as viewed from the (a) side and (b) front. Two different sample and holder geometries were used corresponding to single and multiple sample orientations with respect to the impact direction.

The disc-shaped samples rested within a surrounding ring holder, with a 10° taper designed such that it can break free from the holder during impact. The sample surround rings were 80 mm in diameter. This design prevented release waves from the outer edges reaching the sample center during the time of the experiment (thus ensuring a 1-D state of strain). The projectile and sample holder were slowed down by a polycarbonate plate with an opening large enough to allow the sample to pass through for subsequent soft-recovery. Projectile velocity measurements and triggering of the VISAR recording oscilloscope were achieved with a series of electrically charged metal pins of known spacing. Rear free surface velocity measurements were acquired during the plate impact experiment via a VISAR probe located approximately 30 mm behind the sample. The VALYN VISAR interferometry system uses a 532 nm wavelength laser, and has nanosecond time resolution. The rear free surface velocity was used to calculate the HEL and spall strength as shown in Equations 5 and 6.

As shown in Figure 29(b), experiments with two types of target sample geometries were performed. In one case, a single sample oriented with the impact direction through the thickness of the plate was used, and in the other case, three samples (corresponding to all three orthogonal plate directions) were impacted simultaneously. For experiments with the single through the thickness sample, the diameters were 30 mm at the impact face.

In the case of testing with the three samples having different principal directions, smaller 15.5 mm diameter tapered samples were used. The diameter of these smaller specimens was constrained by the thickness of the plate specimens. The thicknesses of the flyer plate and sample were 5 mm and 10 mm respectively for the single sample experiments. For the multiple sample case, the flyer and target thicknesses were 3 mm and 6 mm respectively. The choice of thicknesses and symmetric impact (same material) for the flyer plate and sample ensures that the spall plane occurs near the mid-plane of the sample for each experiment. Since the flyer plate and sample thicknesses were changed for certain experimental setups, comparisons between the spall properties of different materials will only be made when the thickness values and peak stress values are similar. One set of experiments, presented in Chapter 4, was performed using the same flyer plate thickness (3 mm), but different sample thicknesses (6 mm, 8 mm, and 10 mm) to measure the effects of sample thickness on the spall strength. For this set of experiments, the spall plane was approximately 3 mm from the rear free surface for each sample thickness.

3.5 Post-Impact Recovery

Following plate impact, the samples were soft recovered for microscopic examination. The location of the spall damage, whether intergranular or transgranular may control the spall behavior of the sample. The fracture surfaces were imaged using scanning electron microscopy (SEM) to yield further evidence of the type of fracture during spall testing. The extent of void damage was quantified in some cases, as this is another indicator of the resistance of the material to spall damage. Specifically the size and location of the voids in the target sample were quantified to yield volume distributions of damage as a function of distance from the rear free surface. The size distributions are presented in Appendix B, and are compared to the spall behavior from computational modeling presented in Chapter 9.

3.6 Numerical Modeling

One-dimensional numerical modeling of plate impact experiments was performed using the Shock-1D [116] program to further assess the spall response of Al-Mg alloys. Shock-1D is a

Lagrangian finite element program that uses the Cochran and Banner [107] spall model to simulate failure due to dynamic tensile stress. Modeling was first performed to match the peak state of the experimental impact data, over a wide range of peak stresses, such that a valid equation of state for Al 5083 was obtained. After a good fit to the peak state was achieved, further modeling was performed to assess the spall response of Al-Mg alloys using the Cochran and Banner [107] spall model.

The measured flyer plate and sample thickness and impact velocity were used for simulations of each plate impact experiment. The Shock-1D program also uses several material parameters to simulate the shock response during impact. The density, shear modulus, and bulk modulus were experimentally obtained as described in Section 3.3. The Gruneisen parameter (γ) is related to the change in pressure (P) with energy (E) at constant volume (V) and is given by Equation 34. The Gruneisen parameter has a value of 1.98 for Al 5083.

$$\gamma = V \left(\frac{dP}{dE} \right)_V \tag{34}$$

The viscoplastic response of the material was modeled as linear elastic followed by linear strain hardening behavior in the plastic strain (ϵ_p) regime using the average tangent modulus of the flow stress (H'). The yield function (σ_y) is then given by Equation 35.

$$\sigma_y = \sigma_{y0} + H' \bar{\epsilon}_p \tag{35}$$

The yield strength (σ_{y0}) and strain hardening parameter (H') were first estimated using tabulated quasi-static tensile test data available in the literature [117]. The values were then adjusted to match the yielding behavior from the experimental free surface velocity traces.

The equation of state (EOS) used by the Shock-1D program is a fourth order polynomial given by Equation 36 describing the pressure (P) as a function of the compression (μ) given by Equation 37. Equation 36 is described in greater detail by Dwivedi et al. [93].

$$P = \left(K_1 \mu + K_2 \mu^2 + K_3 \mu^3 + K_4 \mu^4 \right) \left(1 - \frac{\gamma \mu}{2} \right) + \frac{\gamma E}{V} \tag{36}$$

$$\mu = \frac{\rho}{\rho_0} - 1 \tag{37}$$

The variable K_1 is the bulk modulus, and the remaining variables K_2, K_3, and K_4 are fitting parameters describing the pressure over a range of compressions. The EOS was determined by fitting these three variables to give a best match of the simulated data to the peak state in the experimentally measured free surface velocity data over a large range of peak stresses (1.5 GPa to 6.2 GPa).

The remaining parameters needed to model the spall response are the variables from the Cochran and Banner [107] spall model described in Section 2.6.3. These parameters are the spall strength (σ_{spall}), the damage parameter (D_0), and damage exponent (m). The spall strength was first estimated as that measured from the free surface velocity data. The damage parameter (a measure of the void volume) was estimated from the void size distributions obtained from post-impact microscopy. The values of σ_{spall} and D_0 were then adjusted to yield a best fit to the experimental results. The damage exponent should have a value of 2/3 for ductile materials and a value of 2 for brittle materials [107, 108]. The exponent was thus kept at 2/3 to simulate the expected ductile response of aluminum.

Numerical modeling in Shock-1D was performed for all of the microstructural states produced for Al 5083 using various processing methods. The void size parameter from the best fit to the experimental data was then used to compare the spall response as a function of microstructural state.

3.7 Presentation of the Results

The following chapters will discuss the spall behavior of several different microstructural states in Al-Mg alloys. The presentation of this information is organized as follows:

- **Chapter 4:** The effects of shock duration and strain rate on the spall strength and Hugoniot elastic limit (HEL) will be discussed. The results of this chapter will determine under which conditions the spall strength and HEL can be compared between different experiments for the chapters to follow.

- **Chapter 5:** The spall response of a rolled Al 5083-H116 plate will be discussed. This microstructure will serve as the baseline to which the other Al-Mg alloy microstructures will be compared. The effects of the grain texture on the dynamic mechanical properties will be the main topic of this chapter.

- **Chapter 6:** The effects of a sub-micron grain structure produced using equi-channel angular pressing (ECAP) will be discussed. The effects of the refined grain structure and the aligning and cracking of brittle particles on the spall behavior will be the main topics of this chapter.

- **Chapter 7:** The effects of an equiaxed grain structure produced through annealing will be discussed. The effects of both the size and uniformity of the grain structure and the decreased dislocation density in the fully annealed state on the dynamic mechanical behavior will be the focus of this chapter.

- **Chapter 8:** The ability to precipitation harden an Al-9wt.% Mg alloy along with the subsequent spall response of precipitation hardened Al-Mg alloys will be the focus of this chapter. Changes to the grain structure produced during heat treatment and the effects on the dynamic response will also be presented.

- **Chapter 9:** Results of one-dimensional numerical simulations of all Al 5083 microstructures studied will be presented in this chapter. The void size from simulations will be compared to voids measured from post-impact microscopy.

- **Chapter 10:** Comparisons between all of the investigated microstructures will be presented. This chapter is meant as a discussion of the effects of microstructure on spall behavior of Al-Mg alloys and the broader impact of the overall research.

- **Chapter 11:** A summary of results on the effects of microstructure and concluding remarks on the spall behavior of Al-Mg alloys will be presented.

CHAPTER 4

EFFECT OF PULSE DURATION AND DECOMPRESSION RATE ON THE SPALL STRENGTH OF AL 5083-H116

This chapter focuses on the changes to the spall strength of Al 5083-H116 brought about by changing the pulse duration and the decompression rate through variations in the flyer plate and target sample thicknesses, respectively. In addition to the spall strength, the HEL of aluminum alloys has also shown thickness dependence [111–113]; hence, the effects of plate thickness on the HEL will also be investigated. Throughout this research, two different impact configurations were used where individual samples were impacted with the shock direction through the thickness or where three samples (of different orientation) were impacted simultaneously (see Figure 29). These two impact configurations used 5 mm thick flyer plates and 10 mm thick samples, and 3 mm thick flyer plates and 6 mm thick samples, respectively. Such changes in the thickness can result in changes to the spall strength or HEL, that are not necessarily a consequence of the microstructural state, but of the loading conditions. This chapter will quantify the effects, if any, on the spall strength and HEL, as the flyer and sample thicknesses are changed.

Previous research has shown spall strength increasing with decreasing shock pulse duration in ductile materials due to the time necessary to nucleate and grow voids during spalling [109]. Other research has shown that the decompression rate from the peak stress has a more pronounced effect on the spall strength of aluminum than does changing the duration [38]. Gray et al. [109] compared short durations produced by explosive loading to long durations produced by plate impact testing. Chen et al. [38] compared durations produced using plate impact testing alone such that all durations were relatively long (on the order of 1 μs). Since plate impact testing is the only experimental technique that was used to produce spalling in the present research, effects of longer durations will be compared similarly to Chen et al. [38].

4.1 Experimental Procedure

4.1.1 Materials

The material studied was Al-5083-H116, a strain-hardened rolled plate. This rolled plate will serve as the baseline material to which all other microstructures are compared for this research, which is why this material was chosen for experiments to investigate the effects of pulse duration and decompression rate. The spall behavior and microstructure of Al 5083-H116 will be quantified and discussed in greater detail in Chapter 5. For this chapter, the effects of flyer and sample plate thickness on the dynamic mechanical properties are the greatest concern—rather than the effects of the microstructural state. A more detailed description of the microstructure of Al 5083-H116 both before and after plate impact testing is provided in Chapter 5. Briefly, the Al 5083 material is alloyed with magnesium and manganese having compositions of 4.0–4.9 wt% and 0.4–1.0 wt% respectively. The material density (ρ_0) is 2.666 ± 0.001 g/cm^3. The sound speeds (C) in the through-thickness direction were measured for calculation of the spall strength, HEL, and elastic constants. Table 1 lists the longitudinal wave speed (C_L), shear wave speed (C_S), bulk wave speed (C_B), shear modulus (G), bulk modulus (B), elastic modulus (E), and Poisson's ratio (ν) for the Al 5083-H116 samples.

4.1.2 Plate Impact Gas Gun Experiments

Plate impact gas gun experiments were performed through the plate thickness for an impact velocity near 300 m/s, which corresponds to a peak stress of approximately 2.2 GPa. Three experiments were performed using 3 mm thick flyer plates, with sample thicknesses of 6 mm, 8 mm, and 10 mm to assess the effects of target sample thickness on the HEL and spall strength. One experiment was performed using a 5 mm thick flyer plate and a 10 mm thick sample to assess the effects of flyer plate thickness and pulse duration on the spall strength and HEL.

Table 1: Measured sound speed and elastic constants for Al 5083-H116 samples measured through the plate thickness. The data represents a 95% confidence interval in all cases.

C_L [mm/μs]	C_S [mm/μs]	C_B [mm/μs]	G [GPa]	B [GPa]	E [GPa]	ν
6.364 ± 0.007	3.180 ± 0.004	5.197 ± 0.014	27.0 ± 0.1	72.0 ± 0.4	71.9 ± 0.4	0.334 ± 0.004

4.2 Results

Table 2 lists the various measured experimental conditions for the experiments performed to investigate the effects of pulse duration and decompression rate. The impact velocity (V_{impact}) was measured using velocity pins, as shown in Figure 29. The free surface velocities at the peak state (u_{peak}) and the HEL (u_{HEL}) along with the pullback velocity (Δu_{fs}) were measured from the free surface velocity profiles, as shown in Figure 13. The shock wave velocity (U_S) was measured using the impact timing and shock wave arrival time visible in the free surface velocity profiles. The HEL stress (σ_{HEL}), spall strength (σ_{spall}), and peak stress (σ_{peak}) were calculated using Equations 5–8, with the spall strength correction factor (δ) calculated using Equation 7.

4.2.1 Free Surface Velocity

The Al 5083-H116 samples were impacted near 300 m/s in every case using a variety of flyer plate and sample thicknesses. The free surface velocity measured at the sample rear free surface for each experiment is shown in Figure 30. Each data trace in Figure 30 was shifted in time to match the elastic wave arrival time for the experiment using a 5 mm thick flyer plate and a 10 mm thick sample.

The HEL for each experiment is shown in the inset of Figure 30 and remains constant regardless of changes to either the flyer plate thickness or sample thickness. When keeping the flyer plate thickness constant (at 3 mm), it is seen that the pullback velocity, which is indicative of the spall strength, decreases as the sample thickness increases. When the sample (target) thickness is kept constant (at 10 mm), increasing the flyer plate thickness from 3 mm to 5 mm has no effect on the pullback velocity. Thus for these impact conditions, the spall strength is observed to be dependent on the sample thickness, but not on the flyer plate thickness.

4.2.2 Spall Strength and HEL

The spall strength (σ_{spall}) and HEL (σ_{HEL}) values were calculated using the free surface velocity data shown in Figure 30 along with Equations 5–7. The free surface velocity data

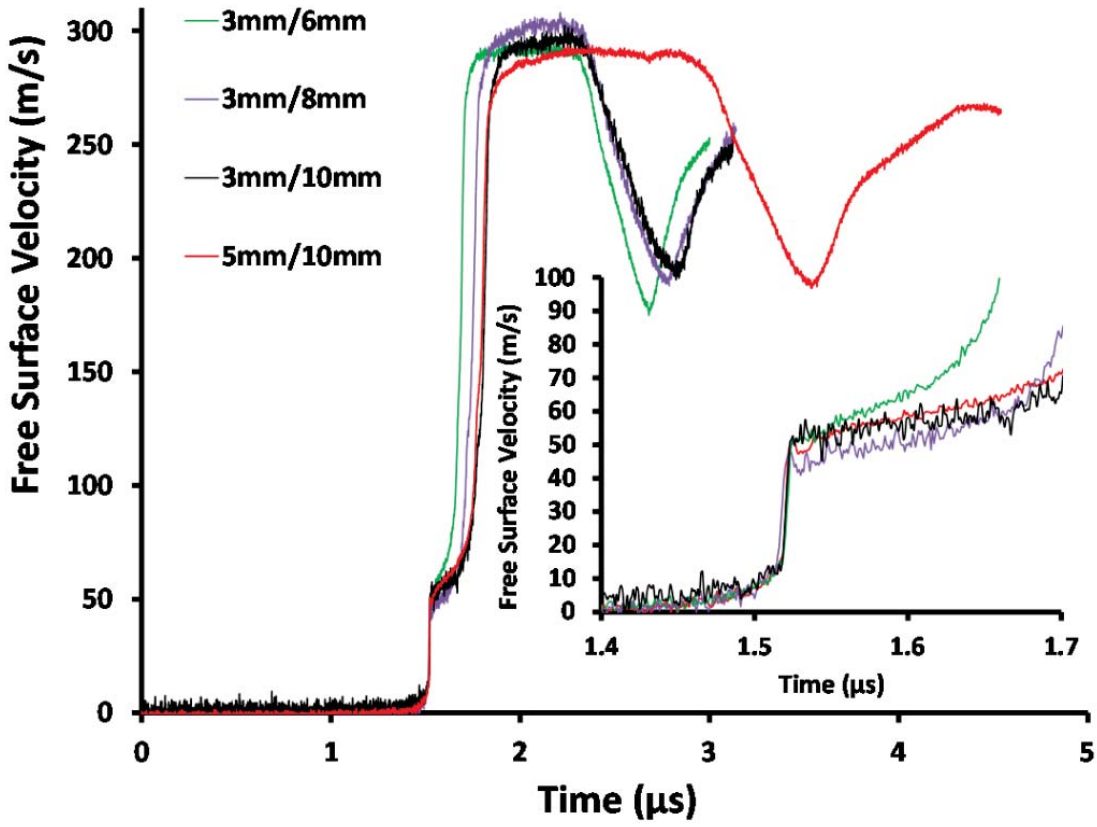

Figure 30: VISAR free surface velocity data for Al 5083-H116 samples with different flyer plate and sample thicknesses. The inset better displays the HEL for each experiment. The HEL remains constant with changes to flyer plate or sample thickness, while the pullback velocity decreases with increasing sample thickness regardless of flyer plate thickness. The data traces were shifted in time to match the elastic wave arrival time of the sample impacted using a 5 mm thick flyer plate and a 10 mm thick sample.

Table 2: Calculated and measured free surface velocity data for Al 5083-H116 samples with different flyer plate and sample thicknesses

Shot Number	V_{impact} [m/s]	u_{peak} [m/s]	U_S [km/s]	σ_{Peak} [GPa]	u_{HEL} [m/s]	σ_{HEL} [GPa]	Δu_{fs} [m/s]	δ [m/s]	σ_{Spall} [GPa]
1209 (3mm/6mm)	305	295	5.31	2.16	51.4	0.44	120.3	17.1	0.95
1339 (3mm/8mm)	306	295	5.36	2.17	47.8	0.41	120.2	12.0	0.92
1340 (3mm/10mm)	306	302	5.41	2.24	50.8	0.43	111.9	7.6	0.83
1224 (5mm/10mm)	295	294	5.37	2.17	50.8	0.43	106.8	15.8	0.85

used in Equations 5–7 is listed in Table 2. The calculated values of HEL and spall strength are shown respectively as a function of the target sample thickness in Figures 31 and 32.

The HEL shows no dependence on either flyer or sample thickness, with all data points lying within the range of the error bars. The average value of the HEL is 0.43 ± 0.03 GPa. The HEL of ductile materials is known to rapidly decay to a constant value as sample thickness increases [111–113], so it is likely that the thinnest sample measured (near 6 mm) was already thick enough to have reached this constant value for Al 5083-H116.

The spall strength shows a smooth and continuous decrease as sample thickness increases. For impact using 3 mm thick flyer plates, the spall strength decreases from a value of 0.95 GPa for a 6 mm thick sample, to a value of 0.83 GPa for a 10 mm thick sample. For the two 10 mm thick samples, the spall strength is essentially identical when impacted with a 3 mm thick flyer plate versus a 5 mm thick flyer plate (0.83 GPa and 0.85 GPa respectively). The spall strength of Al 5083 does not depend on the shock duration for the flyer plate thicknesses used in this research. Since the spall strength is highly dependent on the sample thickness, it is expected that the decompression strain rate is affecting the measured spall strength values similarly to previous work on ductile materials [44].

The strain rate dependence of the spall strength of Al 5083-H116 is plotted in Figure 33 as a log-log plot with the decompression strain rate, defined in Equation 26. The spall strength shows a clear increasing trend with increasing decompression strain rate, which is

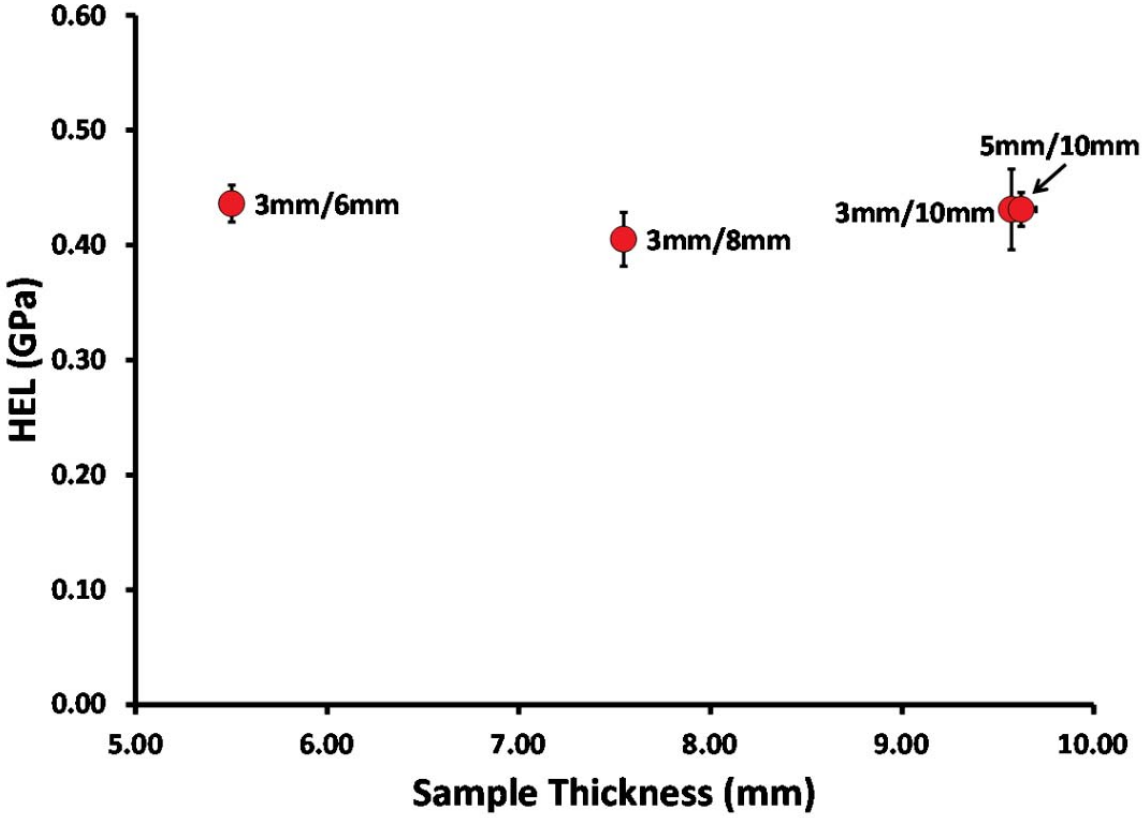

Figure 31: Calculated HEL values as a function of target sample thickness for Al 5083-H116 samples. The flyer plate and sample thicknesses are listed next to each data point. The HEL shows no dependence on flyer or sample thickness.

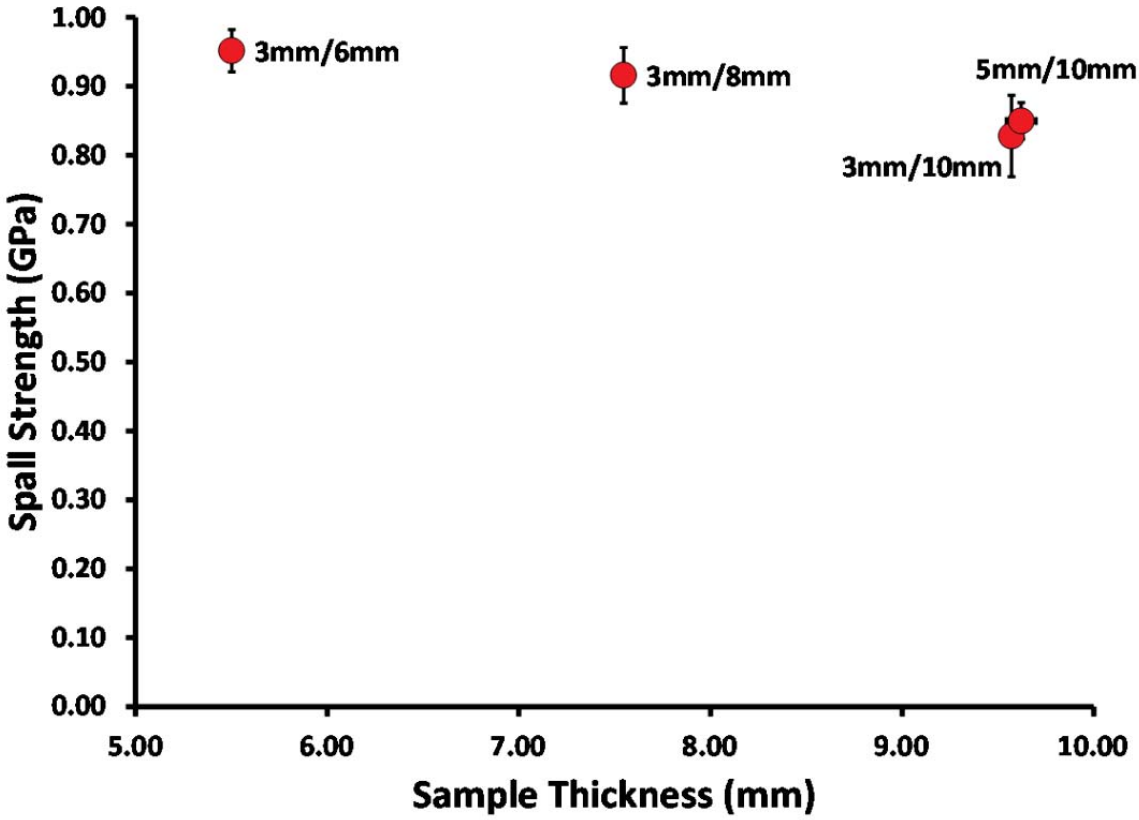

Figure 32: Calculated spall strength values as a function of target sample thickness for Al 5083-H116 samples. The flyer plate and sample thicknesses are listed next to each datapoint. The spall strength decreases with sample thickness but is not dependent on the flyer plate thickness.

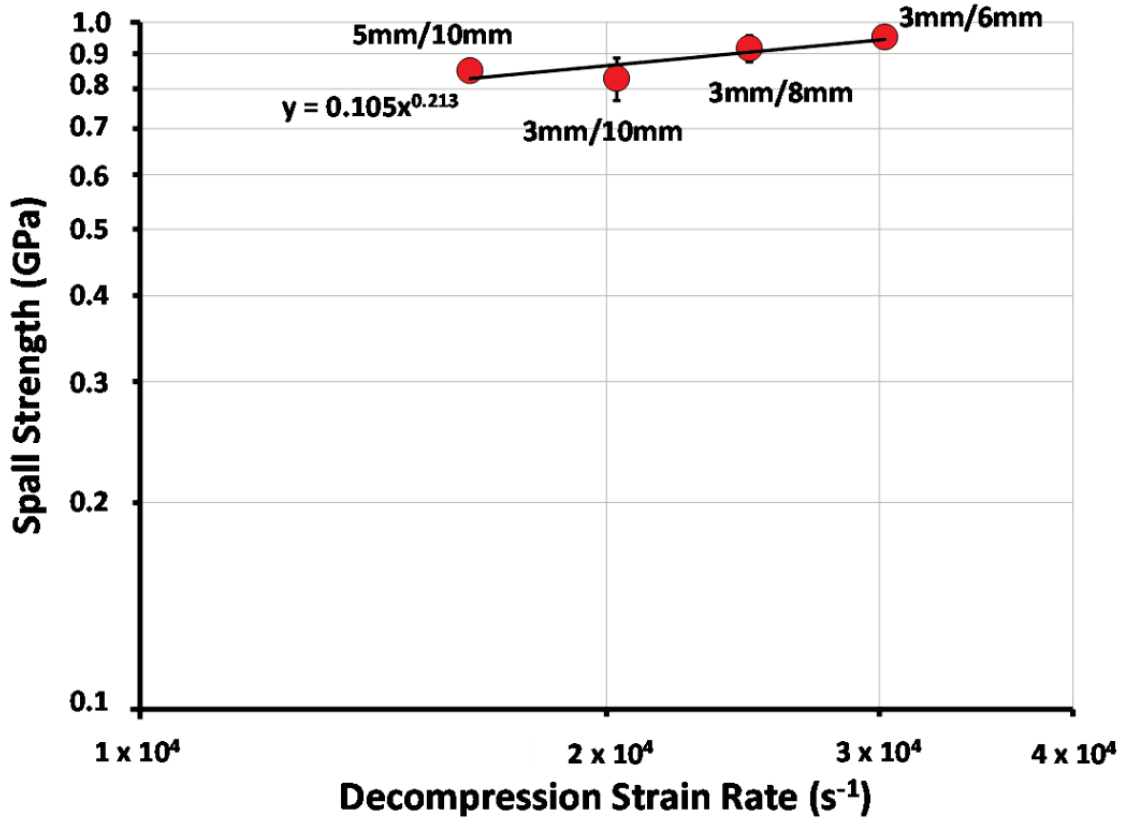

Figure 33: Calculated spall strength values as a function of decompression strain rate for Al 5083-H116 samples. The spall strength increases with strain rate and obeys the power law function fit to the data. The flyer plate and sample thicknesses are listed next to each datapoint.

a result of the decreasing sample thickness. Similarly to previous researchers [44], the data are fit with a power law function given by Equation 38.

$$\sigma_{spall} = A\dot{\epsilon}^m = 0.105\left(\dot{\epsilon}\left[s^{-1}\right]\right)^{0.213}[GPa] \tag{38}$$

The power law fit constants from Equation 38 (A and m) for Al 5083 (an Al-5wt.% Mg alloy) are found to be very similar to those for an Al-6wt.% Mg alloy plotted in Figure 21. For the case of Al-6wt.% Mg, A and m were reported as 0.088 and 0.210 respectively [44] as compared to 0.l05 and 0.213 for the data reported here.

4.3 Conclusions

Al 5083-H116 samples were impacted using 3 mm versus 5 mm thick flyer plates and for sample thicknesses ranging from 6 mm to 10 mm. These values represent the thickness limits for all experiments reported in this thesis. The results show that the HEL is independent of both the flyer plate and sample target thickness. The spall strength is not dependent on the flyer plate thickness, and is therefore not dependent on changes in the shock duration for the experimental setup used in this research. The spall strength is found to be dependent on the sample thickness, with the values of the spall strength decreasing from 0.95 GPa for the 6 mm thick sample to 0.83 GPa for the 10 mm thick sample. Increasing the sample thickness decreases the decompression strain rate, which is known to affect the spall strength of ductile materials. The spall strength of Al 5083 shows a good fit to a power law function with decompression strain rate, and the fitted power law function is similar to that of Al-6Mg, which is similar in composition to the Al 5083 alloy.

The results of this chapter will allow for meaningful conclusions to be drawn on the effects of microstructure on the spall strength and HEL of Al-Mg alloys. Based on the data reported in this chapter, comparisons may be drawn between HEL values for any flyer plate or sample thickness, but comparisons of spall strength values can only be made for similar target sample thicknesses (regardless of the flyer plate thickness). The following chapters will discuss the spall properties of Al-Mg alloys displaying a variety of microstructures. Plate impact experiments correspond to those performed using either 3 mm and 6 mm thick flyer plates and target samples or 5 mm and 10 mm thick flyer plates and target samples. Comparisons of the spall strength will only be made when the same sample thickness is used.

CHAPTER 5

SPALL BEHAVIOR OF ROLLED AL 5083-H116 PLATE

This chapter focuses on the spall behavior of a rolled Al 5083 plate. Specifically, the effects of grain structure—both size and orientation—on the spall strength and HEL are of interest, as rolling produces a highly textured microstructure with grains and inclusions aligning along the rolling direction (see Figure 28).

Previous research on rolled alloy plates has shown varying spall properties based on the impact orientation relative to the rolling direction; however, the results are not consistent between each set of experiments and material types [32–35]. In the case of a eutectoid steel, the spall strength is higher for impact in the rolling direction versus the through-thickness direction [32, 33], but for Al 7010 an opposite trend is observed [34]. For the case of Al 5083-H32, the spall strength is similar for either direction, but impact in the longitudinal direction results in more instances of transgranular fracture than for impact through the plate thickness [35].

Recently the spall strength and HEL of rolled Al 5083-H131 and Al 5083-H32 plates have been reported. For the H131 alloy, the average spall strength and HEL were reported as 0.936 GPa and 0.573 GPa, respectively, for peak pressures between 1.5 and 8.0 GPa [92, 94]. For Al 5083-H32, the spall strength and HEL have been reported as 1.23 GPa and 0.60 GPa over a similar stress range [35]; however, the HEL was reported as 0.40 GPa in a different study [94].

In this chapter, the spall behavior of a rolled Al 5083-H116 plate is investigated using symmetric plate impact experiments at peak stresses ranging between 1.5 to 6.2 GPa. The experiments were performed with impact through the plate thickness and along all three orthogonal plate orientations. Since rolled plates are already used for armor plating, this microstructure will serve as the baseline for spall testing performed on other microstructures

to be discussed in the following chapters. Improvements to the spall properties presented in this chapter would thus represent a better armor plate microstructure than those in service.

5.1 Experimental Procedure

5.1.1 Materials

The tested samples were machined from a 0.75″ (approximately 19 mm) thick rolled Al 5083 plate in the H116 temper commercially acquired from McMaster Carr. The H116 temper indicates strain hardening only, and has the same mechanical properties as the H32 temper commonly used for armor plates [115]. The principal alloying elements in the Al 5083 plate are 4.0–4.9 wt.% magnesium and 0.4–1.0 wt.% manganese. The density of the material was measured as 2.666 $\pm$ 0.001 g/cm^3 using the standard Archimedes measurement method. Since the Al 5083 was obtained in rolled plate form, the grain structure is similar to that shown schematically in Figure 28 with the grains elongating along the rolling direction and thinning through the thickness of the plate. The microstructure of the as-received Al 5083-H116 plate is shown in Figure 34. Micrographs in Figure 34(a) through 34(c) show the grain structure along the different directions in the rolled plate as outlined in Figure 28.

The grain structure of the as-received material shown in Figure 34 is highly textured, as would be expected for a rolled plate. The mean intercept grain size ($< G >$) measured for each orientation is given in Table 3. It can be seen that $< G >$ varies from 9 μm through the thickness of the sample (along the short transverse direction) to 66 μm along the rolling (longitudinal) direction. Spall experiments were performed for single specimens through the thickness and along all three plate orientations simultaneously to measure the effects of this grain texture on spall properties, using the setup shown in Figure 29.

Figure 34(d) displays a number of brittle inclusions and manganese dispersoids present in the rolled plate. The inclusions are often larger than the dispersoids and are removed from the surface during polishing. They appear as dark areas in the micrograph. The dispersoid particles are light brown and form at the grain boundaries, which acts to prevent recrystallization during processing. Brittle particles such as these are nucleation sites for spall damage and can be detrimental to the dynamic mechanical properties of Al 5083 alloy

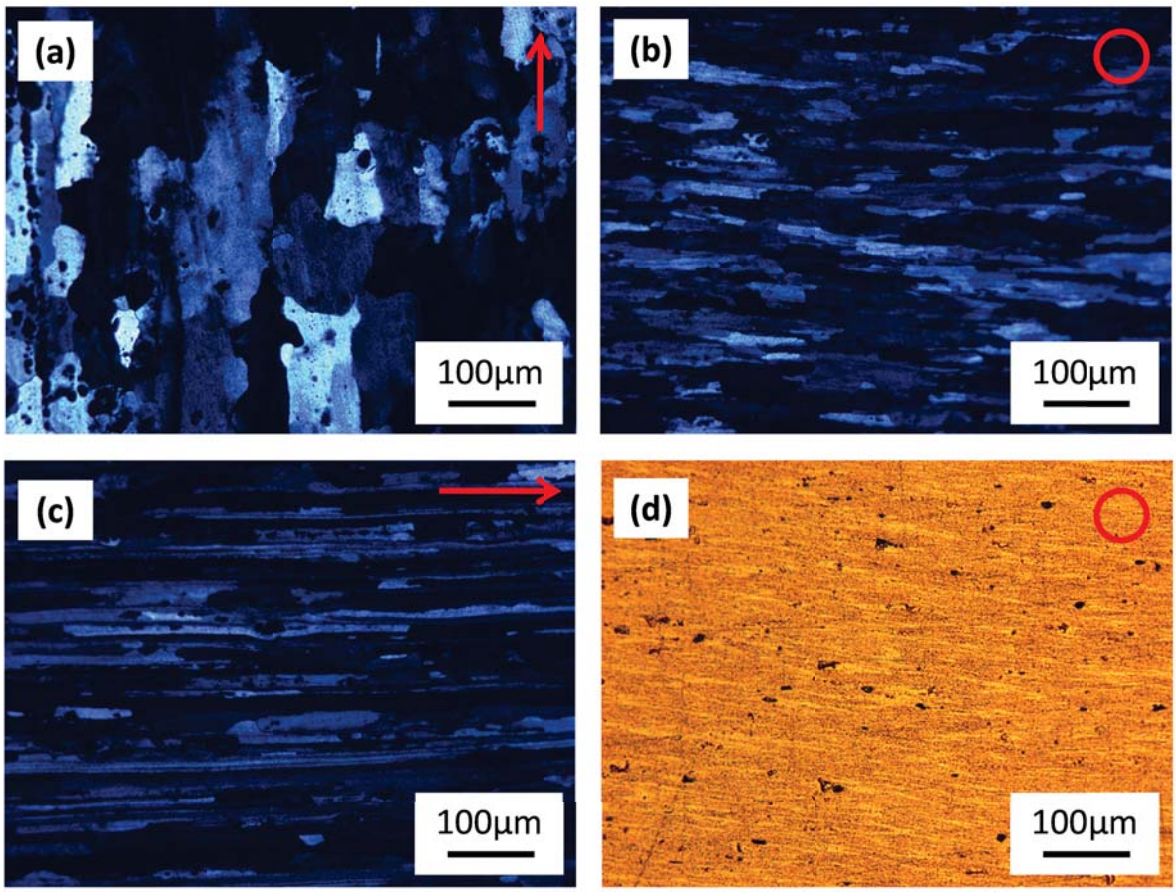

Figure 34: Optical microscope images of the as-received Al 5083-H116 material. The rolling direction is indicated by red markers in each image. The grain structure is visible under polarized light for planes normal to the (a) short transverse, (b) longitudinal, and (c) long transverse directions. Under bright field, (d), inclusions and Mn dispersoids are visible as black and light brown particles and are indicated with broken and solid blue circles respectively.

[32, 33, 35, 37, 39, 40, 44, 79, 101]. One of the goals of this research is to ascertain the effects of these brittle particles on the spall properties of Al-Mg alloys in addition to the effects of the grain structure.

Table 3: Material properties of Al 5083-H116 along the three principal directions of a rolled plate. The error represents a 95% confidence interval in all cases.

	Short Transverse	**Longitudinal**	**Long Transverse**
C_L [mm/μs]	6.364 ± 0.007	6.452 ± 0.075	6.430 ± 0.004
C_S [mm/μs]	3.180 ± 0.004	3.154 ± 0.033	3.149 ± 0.004
C_B [mm/μs]	5.197 ± 0.014	5.325 ± 0.118	5.303 ± 0.009
G [GPa]	27.0 ± 0.1	26.5 ± 0.6	26.4 ± 0.1
B [GPa]	72.0 ± 0.4	75.6 ± 3.3	75.0 ± 0.2
E [GPa]	71.9 ± 0.4	71.2 ± 3.4	71.0 ± 0.3
ν	0.334 ± 0.004	0.343 ± 0.036	0.342 ± 0.003
$< G >$ [μm]	9 ± 1	66 ± 20	39 ± 7

The longitudinal, shear, and bulk sound speeds (C_L, C_S, and C_B respectively) were measured using ultrasonic testing, and the corresponding elastic constants G (shear modulus), B (bulk modulus), E (elastic modulus), and ν (Poisson's ratio) are also included in Table 3. The equations for the sound speeds and elastic constants listed in Table 3 are given by Equations 29–33. The sound speed values were used to calculate the spall strength and Hugoniot Elastic Limit (HEL) of the Al 5083-H116 material along each of the plate directions from the free surface velocity traces measured during plate impact testing.

5.1.2 Plate Impact Experiments

Plate impact experiments were performed for impact velocities ranging from approximately 200 m/s to 800 m/s, with a corresponding peak stress range of 1.5 GPa to 6.2 GPa. One set of experiments was performed through the plate thickness, while varying the impact velocity, to measure the effects of peak stress on the spall strength and HEL. Another set of experiments was performed where all three plate orientations were impacted simultaneously in order to measure the effects of the textured microstructure on spall properties. This set of experiments was performed at approximate impact velocities of 200 m/s, 300 m/s, and 400 m/s. Samples were recovered following impact, and the post-mortem sample

cross-sections and fracture surfaces were characterized using optical microscopy and SEM respectively.

5.2 Results

Table 4 lists the measured parameters for each experiment. The impact velocity (V_{impact}) was measured using velocity pins, as shown in Figure 29. The free surface velocities at the peak state (u_{peak}) and the HEL (u_{HEL}) along with the pullback velocity (Δu_{fs}) were measured from the free surface velocity profiles, as shown in Figure 13. The shock wave velocity (U_S) was measured using the impact timing and shock wave arrival time visible in the free surface velocity profiles. The HEL stress (σ_{HEL}), spall strength (σ_{spall}), and peak stress (σ_{peak}) were calculated using Equations 5–8, with the spall strength correction factor (δ) calculated using Equation 7.

5.2.1 Free Surface Velocity

The rear free surface velocity data for all measured Al 5083-H116 samples are given in Figures 35 and 36. For the data shown in Figure 36 for impact along all three directions simultaneously, the free surface velocity data along the long transverse direction failed to record for impact near 430 m/s. Likewise, for the slowest impact velocity shown in Figure 36, near 200 m/s, the signal is too noisy approximately 3 μs after impact for the long transverse and longitudinal directions; therefore, the data for these traces is not presented for later times.

The insets of Figures 35 and 36 both show a distinct HEL for every impact experiment, indicating the transition from elastic to plastic behavior during testing. The free surface velocities at the HEL range from approximately 45 m/s to 55 m/s for all experiments with very little change occurring with impact velocity; however, slight changes are observable along the different plate orientations for experiments at a given velocity. Specifically, the long transverse direction displays the highest HEL values, and the longitudinal direction displays the lowest values.

The other characteristic regions expected from spall experiments such as the shock wave arrival, velocity pullback, and ringing are also present in every data set displayed in Figures

35 and 36. Similar to the HEL, the pullback velocity, a measure of the spall strength, varies little with the impact velocity for similar specimens; however, the velocity pullback does depend on grain orientation and sample plate dimensions for samples impacted at similar velocities. The pullback velocity in the longitudinal direction displays a noticeable increase for all three experiments shown in Figure 36. The pullback velocity for impact in the short transverse direction is also larger for 6 mm thick specimens impacted with 3 mm thick flyer plates (shown in Figure 36) versus the single sample experiments for 10 mm thick samples (shown in Figure 35) for similar velocities. As discussed in Chapter 4, the spall strength of Al 5083 increases with increasing decompression rate resultant from decreasing the sample thickness. Therefore, the spall strength measured using the multiple sample configuration (with thinner samples) will be higher than that measured for the single sample configuration (with thicker samples). The exact values of the HEL and spall strength will be quantified and discussed in the next section.

An interesting feature from the free surface velocity data is an apparent change in slope observed after the velocity pullback. This feature has been described as a "shoulder" for spall experiments on 1060, 6061, and ultra-pure aluminum, whereby the slope change was said to be indicative of a change from brittle to a more ductile failure [38]. The authors observed that increasing the loading rate or the grain size made this transition more prominent. As shown in Figure 36, the change in slope is most apparent when impacted along the short transverse direction (through the thickness)—the direction with the smallest grain size along the impact direction but the largest grain area in the plane of impact. Conversely, the longitudinal direction, having the largest grain size along the impact direction and the smallest grain area in the plane of impact, has no such noticeable "shoulder" feature in this region.

While the cause of this shoulder has not yet been determined, Chen et al. [38] speculated that it may be due to a quasi-elastic response. Quasi-elasticity has been observed for both reloading [93, 118] and unloading [93] of aluminum subjected to plate impact experiments and has been attributed to a mesoscale phenomenon due to a local heterogeneous response from inclusions and grain boundaries [93]. Since impact through the thickness of the plate

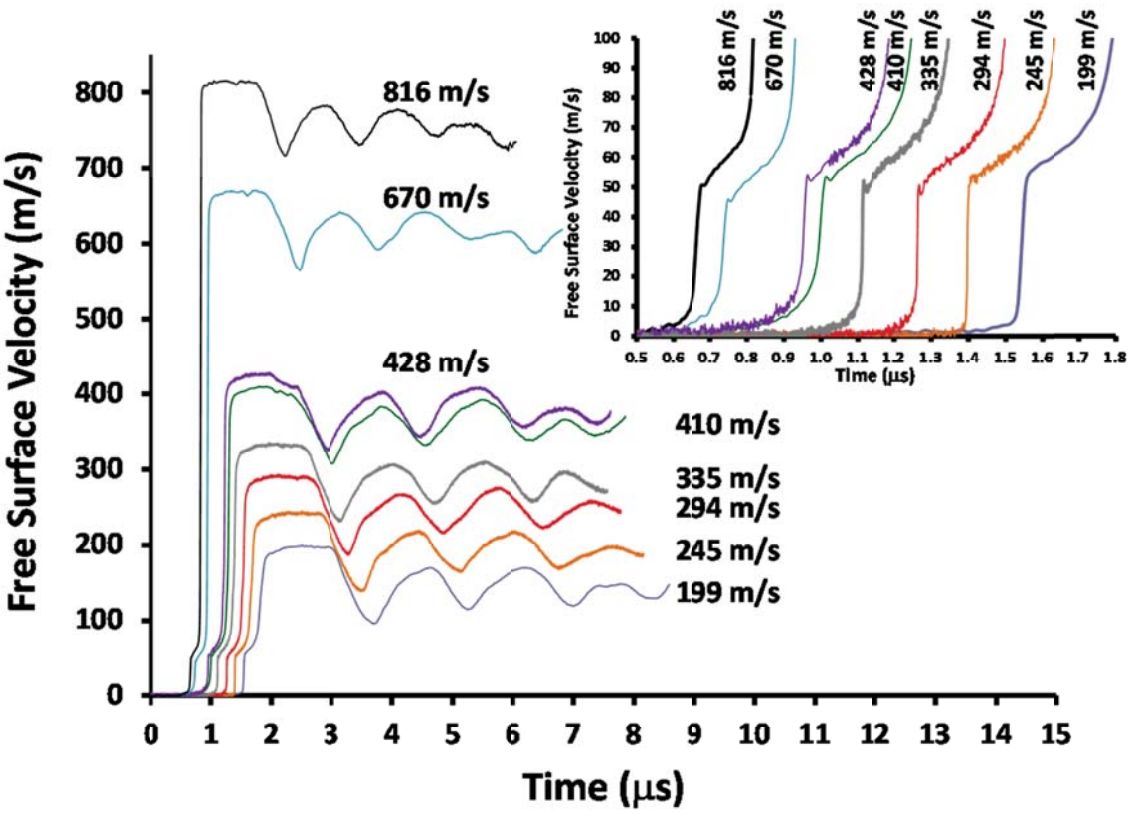

Figure 35: Al 5083-H116 sample rear free surface velocity vs. time for samples impacted through the thickness of the plate. The inset better displays the HEL for each data set.

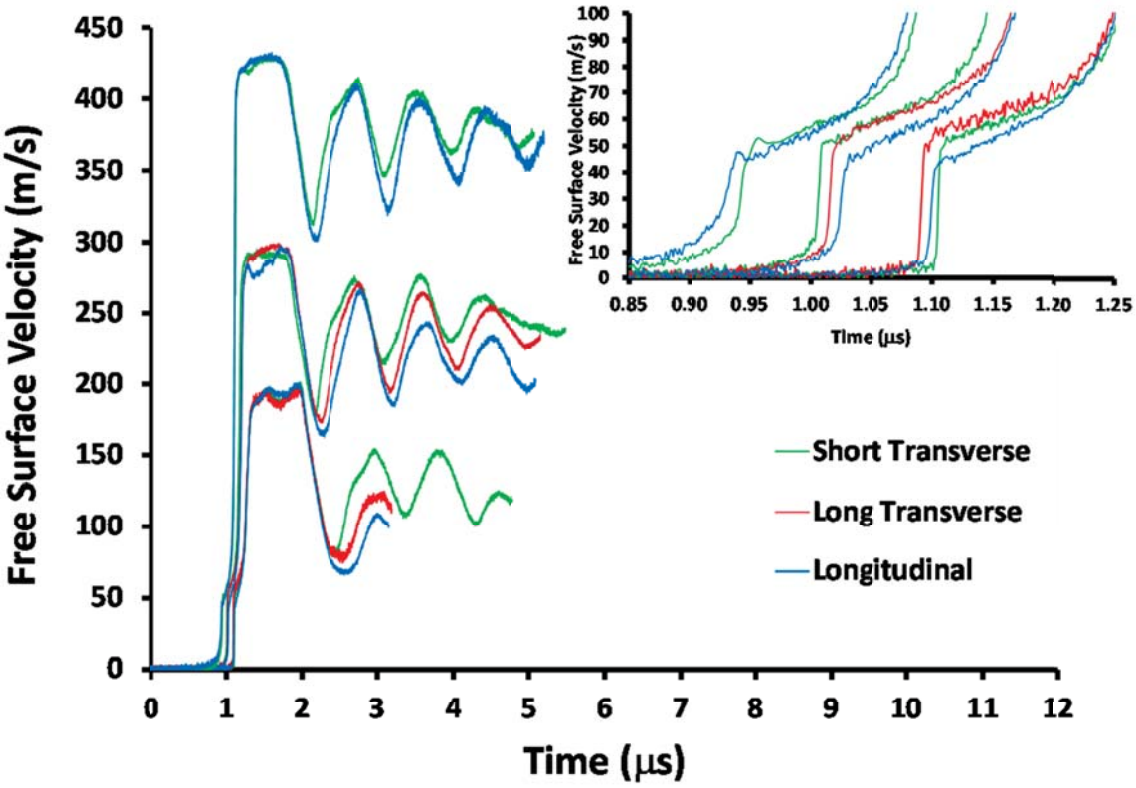

Figure 36: Al 5083-H116 sample rear free surface velocity vs. time for impact along the three principal directions of a rolled plate. The inset better displays the HEL for each data set.

maximizes the amount of inclusions and grain boundary area within the plane of the spall pulse, this would seem to be a reasonable microstructural explanation for the shoulder phenomenon observed in the free surface velocity data. A further explanation for the shoulder is secondary spalling away from the primary spall plane. Johnson et al. [119] measured a similar feature in spall studies on tantalum. They were able to reproduce this feature using simulations by adding an additional secondary spall resistance function to their existing spall model.

5.2.2 Spall Strength and HEL

The free surface velocity data shown in Figures 35 and 36, along with Equations 5–7, were used to calculate the HEL and spall strength for the Al 5083-H116 samples. All free surface velocity data used to calculate the HEL and spall strength are given in Table 4. The data is plotted in Figures 37 and 38 for the single orientation and multiple orientation experiments respectively. The data in Figures 37 and 38 is presented as a function of the peak stress (σ_{peak}) given by Equation 8.

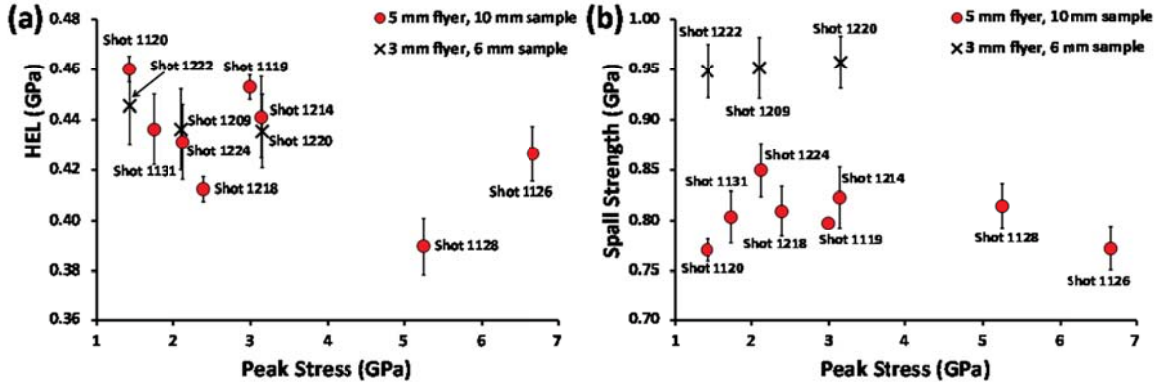

Figure 37: Calculated (a) spall strength and (b) HEL values for impact through the thickness of a rolled Al 5083-H116 plate. The data are presented for impact with thick (5 mm) and thin (3 mm) flyer plates.

The root mean square best fit of the U_S versus u_p data given in Table 4 is given by Equation 39. The equation of state (EOS) given by Equation 39 is very similar to the EOS measured by Boteler and Dandekar [94] for the H32 temper, which had C_0 and S values of 5.14 and 1.27 respectively. The H32 and H116 tempers have very similar specifications

Table 4: Calculated and measured free surface velocity data for Al 5083-H116. Multiple sample experiments are designated with ST (short transverse), LT (long transverse), or L (longitudinal) to denote the impact direction with respect to the orientation of the rolled plate.

Shot Number	V_{impact} [m/s]	u_{peak} [m/s]	U_S [km/s]	σ_{Peak} [GPa]	u_{HEL} [m/s]	σ_{HEL} [GPa]	Δu_{fs} [m/s]	δ [m/s]	σ_{Spall} [GPa]
1120	208	199	5.27	1.48	54.2	0.46	103.0	8.2	0.77
1131	249	245	5.42	1.84	51.4	0.44	106.4	9.5	0.80
1224	295	294	5.37	2.17	50.8	0.43	106.8	15.8	0.85
1218	344	335	5.43	2.49	48.6	0.41	104.6	12.2	0.81
1119	421	410	5.27	2.96	53.4	0.45	101.7	13.4	0.80
1214	426	428	5.37	3.13	52.0	0.44	103.9	14.8	0.82
1128	687	670	5.53	4.99	45.9	0.39	105.6	11.9	0.81
1126	830	816	5.68	6.22	50.3	0.43	99.7	11.8	0.77
1222 ST	204	201	5.34	1.51	52.5	0.45	122.8	14.1	0.95
1222 LT	204	198	5.28	1.48	54.5	0.47	123.5	12.3	0.96
1222 L	204	201	5.36	1.50	44.2	0.38	134.4	11.4	1.03
1209 ST	305	295	5.31	2.16	51.4	0.44	120.3	17.1	0.95
1209 LT	305	299	5.29	2.19	54.3	0.47	126.2	8.3	0.95
1209 L	305	298	5.34	2.19	45.5	0.39	135.3	15.6	1.07
1220 ST	408	431	5.27	3.10	51.3	0.44	118.8	19.4	0.96
1220 LT	408	-	-	-	-	-	-	-	-
1220 L	408	433	5.36	3.16	46.9	0.40	132.4	16.1	1.05

for mechanical response [115], which explains the good fit of the measured data for H116 to that previously reported for H32. The EOS of Al 5083-H116 is compared to the armor grade tempers H32 and H131 in more detail in Appendix A.

$$U_S = C_0 + Su_p = (5.2 \pm 0.1) + (1.0 \pm 0.5)\, u_p\, [mm/\mu s] \tag{39}$$

The average HEL and spall strength are 0.43 ± 0.04 GPa and 0.81 ± 0.05 GPa for impact through the thickness for 10 mm sample target thicknesses. For impact with the thinner 6 mm sample targets (tested using the multiple sample configuration shown in Figure 29), the HEL remains the same at 0.44 ± 0.01 GPa, but the spall strength increases to 0.95 ± 0.01 GPa, which is consistent with the data presented in Chapter 4. For impact using thinner samples, the decompression rate increases resulting in higher spall strength. As

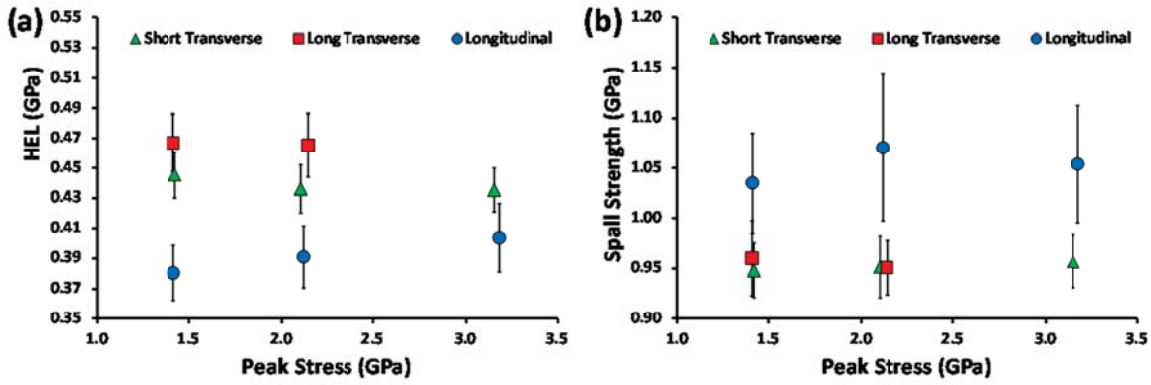

Figure 38: Calculated (a) spall strength and (b) HEL values for impact along the three principal directions of a rolled Al 5083-H116 plate

shown in Figure 31, the HEL is not thickness dependent for the thicknesses used in this research.

While the HEL displays no dependence on flyer or sample thickness, it does display orientation dependence. The long transverse direction has the largest and most consistent average value at 0.465 ± 0.002 GPa. The short transverse and longitudinal directions have progressively lower values of 0.44 ± 0.01 GPa and 0.40 ± 0.02 GPa respectively. This is consistent with quasi-static mechanical data for rolled Al 5086, whereby the compressive yield strength is higher along the long transverse direction [117].

For the multiple sample impact configuration, the spall strength is noticeably higher for impact along the longitudinal direction. The average value is 1.06 ± 0.03 GPa as compared to 0.95 ± 0.01 GPa for both the short transverse and long transverse directions. Therefore, the grain orientation plays some role in influencing the spall strength of a material. However, the strength is not purely a function of the grain size, since the short and long transverse directions have grain sizes of 9 μm and 39 μm respectively yet identical values for spall strength. It is believed that the spall strength trends with orientation can be explained in terms of how the damage propagates through the microstructure, and this will be discussed in detail in the next section based on the results of microstructure characterization of the recovered samples.

The average values reported here (for 5 mm thick flyer plates and 10 mm thick target samples) for HEL and spall strength are both lower than for the H131 temper measured by Boteler and Dandekar [92, 94]. For the H131 samples, the HEL and spall strength were reported as 0.573 GPa and 0.936 GPa. Spall testing of the Al 5083-H32 temper has also yielded higher values than those reported here. The HEL and spall strength are 0.60 GPa and 1.23 GPa respectively for those experiments [35]. The increased HEL can be attributed to the greater degree of work hardening for the armor grade tempers as compared to the H116 temper, whereby the extra hardening results in increased resistance to plastic deformation. As described in Chapter 4, the spall strength is dependent on the decompression rate, which will change with sample thickness and impactor material. Boteler and Dandekar [92, 94] used asymmetric impact (different flyer plate material) and varied the sample thickness from 6 mm to 8 mm, so the average values of spall strength cannot be directly compared for the different Al 5083 tempers. Impact using the 6 mm thick specimens is closest to the experimental setup used by Boteler and Dandekar [92, 94]. For the case of 6 mm thick specimens, the spall strength was 0.95 GPa, which is similar to the value of 0.936 GPa reported by Boteler and Dandekar [92, 94] for Al 5083-H131.

5.3 Post-Impact Recovered Microstructure Characterization

All samples were soft recovered following plate impact testing for microstructural examination. Complete spallation occurred in all cases except for impact at approximately 200 m/s. For the sample impacted at 200 m/s, post impact void counting was performed to quantify the void size distributions after spalling. This data is presented in Appendix B.

Figures 39 and 40 display some representative optical microscope and SEM images respectively for impact along all three plate orientations. In Figure 39, the images were taken perpendicular to the spall plane, and in Figure 40 the images were taken within the spall fracture surface. In Figure 39(a), for impact through the thickness of the plate, the spall damage is large compared to the grain size, making it difficult to ascertain whether the damage is propagating along the boundaries or within them; however, the fracture surface shown in Figure 40(a) displays a large degree of intergranular fracture for this same

impact direction. For impact along the long transverse and longitudinal directions, the damage is seen to propagate by transgranular fracture as evidenced by Figures 39(b) and 39(c). The dimpled fracture surfaces seen in Figures 40(b) and 40(c) are further evidence for transgranular fracture for impact in these directions. The type of fracture does not appear to affect the spall strength, as the short transverse and long transverse directions display essentially the same spall strength; however, the difference in fracture type could be a microstructural explanation for the shoulder observed in the free surface velocity data for impact in the short transverse direction that was not evidenced in the other two directions. The shoulder phenomenon was previously attributed to a shift from an initial brittle fracture mechanism to a more ductile fracture mechanism by Chen et al. [38] for spall experiments on aluminum alloys. The mixed mode of intergranular fracture and dimple fracture visible in Figure 40(a), but not Figures 40(b) and 40(c) is consistent with that explanation.

As seen in Figure 39(c), the spall damage takes a more tortuous path through the microstructure for impact along the longitudinal direction than for the other two directions. The spall damage travels laterally across the grains via transgranular fracture; however, the damage often travels away from the spall plane along the impact direction via intergranular fracture. The grain boundaries are the path of least resistance for the growth of voids during spall failure, but the large grain size along the longitudinal direction prevents the spall damage from coalescing to form a continuous damage plane. As seen in Figure 39(c), the damage propagates along the grain boundaries for a finite distance and then halts. It is believed that this more tortuous damage path is the microstructural basis for the higher spall strength for impact along this direction.

Brittle inclusions are often considered to be nucleation sites for spall damage [32, 33, 35, 37, 39, 40, 44, 79, 101]. As Figures 41 and 42 show, these inclusions are often located near large voids in the recovered plate following impact. Within the fracture surfaces, cracked inclusions were often located near the bottom of the largest dimples. Cracked inclusions were also visible near large voids when imaged perpendicular to the spall plane as shown in Figure 42(a). In some cases damage occurred next to uncracked particles such as the

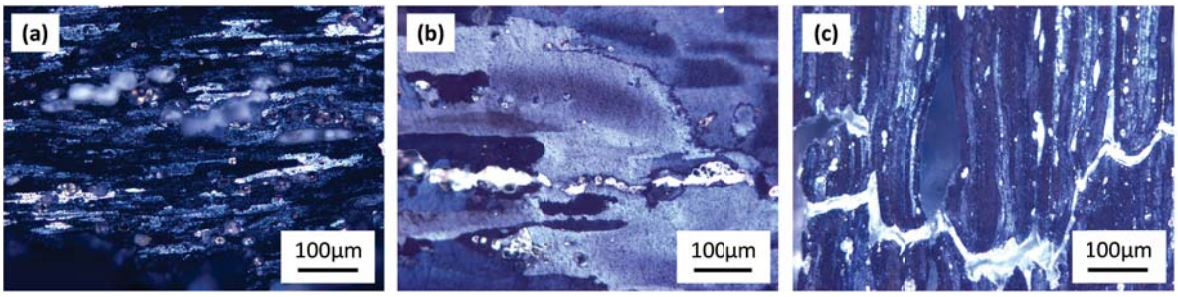

Figure 39: Optical microscope images of damage in Al 5083-H116 samples following plate impact in the (a) short transverse (b) long transverse and (c) longitudinal directions.

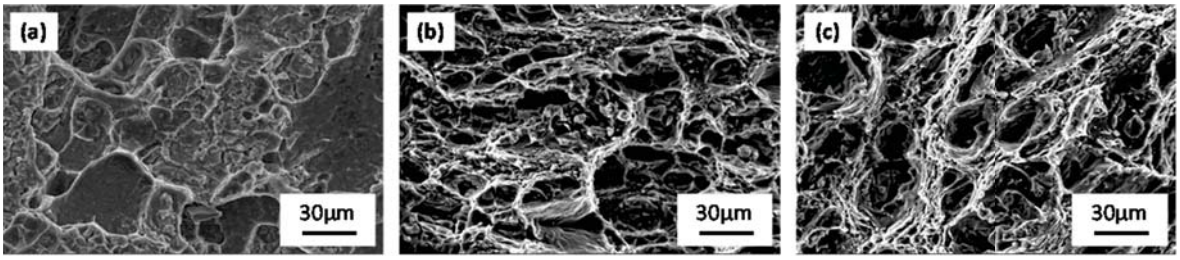

Figure 40: SEM images of the fracture surfaces in Al 5083-H116 samples following plate impact in the (a) short transverse (b) long transverse and (c) longitudinal directions.

one shown in Figure 42(b), which indicates that matrix-particle debonding is either a void nucleation or growth mechanism.

5.4 Conclusions

The spall behavior of rolled Al 5083-H116 plate was investigated using plate impact experiments at peak stresses ranging from 1.5 GPa to 6.2 GPa and for varying impact orientations with respect to the rolling direction. The average HEL and spall strength for the H116 samples, with values of 0.43 GPa and 0.81 GPa, respectively, are lower than previous reports

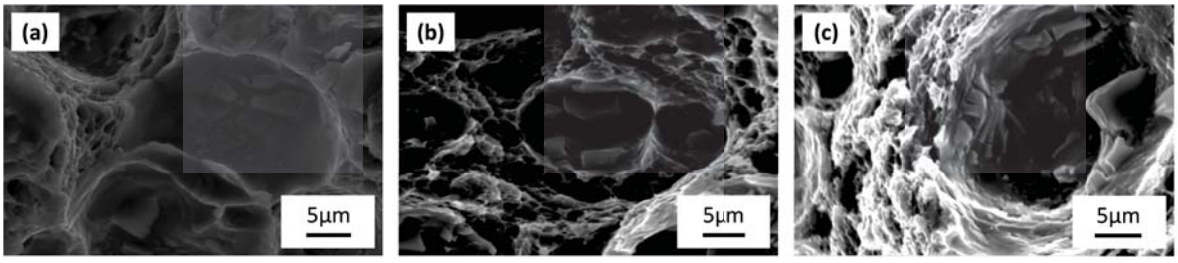

Figure 41: SEM images of inclusions within the fracture surfaces of Al 5083-H116 samples following plate impact in the (a) short transverse (b) long transverse and (c) longitudinal directions.

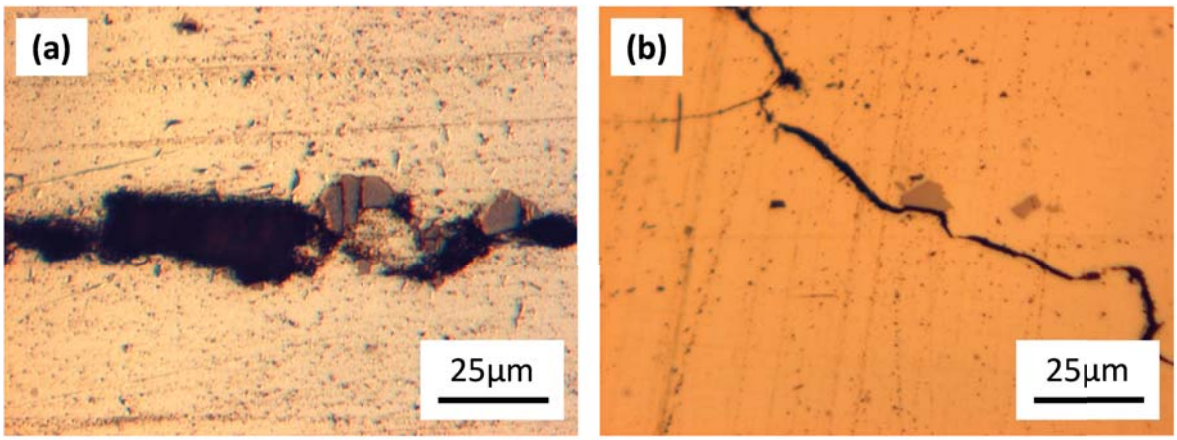

Figure 42: Optical microscope images of inclusions located near spall damage in Al 5083-H116 samples. Damage was observed near (a) cracked inclusions and (b) along the interface with inclusions.

for the H131 temper. The lower HEL value can be attributed to the lesser degree of work hardening achieved with the H116 temper, but the difference in spall strength can be attributed to the difference in the target sample thickness. Use of flyer and sample target plates of same ratio but different thickness resulted in different values of spall strength, but the HEL remained the same. For impact along multiple plate directions, the long transverse direction displayed the largest HEL at 0.465 GPa, followed by the short transverse direction and longitudinal direction at 0.44 GPa and 0.40 GPa, respectively. The longitudinal direction displayed the highest spall strength of 1.06 GPa as compared to 0.95 GPa along either transverse direction—despite a large difference in grain size for these two transverse orientations. The spall strength therefore appears to depend more on the orientation of the grains, and is not necessarily a direct function of the grain size for these experiments.

Post impact microscopy of recovered samples revealed that the damage for impact along the longitudinal direction took a more tortuous path through the microstructure than for the two transverse directions. Spall damage often propagated along the grain boundaries in the direction of impact rather than growing laterally across the sample. The large grain size in this direction prevented this type of spall damage from coalescing, which could account for the higher values of spall strength observed along the longitudinal direction. SEM images of the fracture surfaces revealed a ductile dimpled fracture surface for both the longitudinal

and long transverse directions, but a mixed mode of intergranular and dimple fracture for impact through the thickness of the plate. This mixed fracture mode seems to correspond to a shoulder in the free surface velocity data observed just after the velocity pullback for impact in this direction. The effects of brittle inclusions as spall nucleation sites were seen in all recovered samples, with cracked and de-bonded inclusions occurring near large voids in all cases. The cracked inclusions were primarily observed at the bottom of the largest dimples for each fracture surface.

CHAPTER 6

SPALL BEHAVIOR OF AL 5083 PLATE FABRICATED USING EQUI-CHANNEL ANGULAR PRESSING (ECAP) AND ROLLING

This chapter focuses on the spall behavior of a highly refined grain structure produced via equi-channel angular pressing. Equi-channel angular pressing (ECAP), also known as equi-channel angular extrusion (ECAE), is a processing method that can produce a highly refined, sub-micron, grain structure in metals and alloys [45]. ECAP involves pressing a billet through an angular die, with no change in cross-sectional area after pressing through the die. Processing using ECAP yields a unique and highly refined microstructure. The small grain sizes produced from ECAP strengthens the material through the Hall-Petch effect, while also maintaining low temperature ductility, due to the ease of grain boundary sliding [45].

ECAP has been used to produce highly refined grain structures in large aluminum plates and in Al 5083 in particular [52, 53]. In this chapter, symmetric plate impact experiments were performed on large Al 5083 plates that were processed using both ECAP and post-ECAP rolling. Impact experiments were performed both through the thickness and along all plate orientations to compare the relatively uniform microstructure produced by ECAP to the textured microstructure produced by rolling. The effects of the unique microstructure produced by ECAP on the spall strength and HEL are examined and compared with that for a standard rolled Al 5083 plate.

6.1 Experimental Procedure

6.1.1 Materials

The as-received Al 5083 was obtained as a rolled plate in the H321 temper, indicating strain hardening and a partial annealing treatment. The composition of the alloy is 4.0-4.9 wt.% Mg and 0.4-1.0 wt.% Mn, in addition to trace elements. Magnesium gives the alloy its strain hardening capability, while manganese forms dispersoid phases that refine the grain

structure. Four different Al 5083 plates were tested corresponding to different degrees of processing via rolling and ECAP as listed below:

1. As-received Al 5083-H321
2. ECAP four passes at 250°C
3. ECAP four passes followed by rolling at 150°C (55% reduction) and cold rolling (20% reduction)
4. ECAP four passes followed by cold rolling (30% reduction)

In addition to the as-received plate, three other sample types were tested corresponding to different degrees of processing with ECAP and rolling. The first of these samples was only processed using ECAP, with no subsequent rolling. An image of an extruded ECAP billet is shown in Figure 43(a) along with a schematic illustrating the extrusion and rolling directions during processing in Figure 43(b). The billets were pressed about a 90° angle using a die geometry similar to Figure 5(a). As Figure 43 shows, the ECAP billets were large plates (15.2″ x 15.0″ x 3.2″) that were given four passes through the die at 250°C with subsequent turning by 90° about the through-thickness normal between each pass. This processing technique has been shown to yield a uniform grain structure throughout the large Al 5083 plate with a grain size of 400 nm [53]. Two other sample types were processed similarly using ECAP followed by varying degrees of rolling. One sample was first warm rolled at 150°C to 55% thickness reduction followed by cold rolling at room temperature to give a further 20% reduction. The final sample type was processed with ECAP followed by cold rolling at room temperature to 30% thickness reduction.

Values of the density (ρ) and sound speed (C) of each sample type were measured for calculation of the spall strength, HEL, and elastic constants. Table 5 lists the longitudinal wave speed, shear wave speed, bulk wave speed, shear modulus, bulk modulus, elastic modulus, and Poisson's ratio (C_L, C_S, C_B, G, B, E, and ν respectively) along each direction of the four sample plates.

Table 5: Measured sound speed, density, and elastic constants for Al 5083 samples processed using ECAP and post-ECAP rolling. The samples were tested along the short transverse (ST), long transverse (LT), and longitudinal (L) directions for rolled specimens. The samples processed using ECAP only were tested along the two ECAP directions and through the plate thickness. The data represents a 95% confidence interval in all cases.

	C_L [mm/μs]	C_S [mm/μs]	C_B [mm/μs]	G [GPa]	B [GPa]	E [GPa]	ν
As-Received Al 5083-H321: $\rho = 2.665 \pm 0.001$ [g/cm^3]							
ST	6.36 ± 0.03	3.20 ± 0.02	5.17 ± 0.05	27.4 ± 0.3	71 ± 1	73 ± 2	0.33 ± 0.02
LT	6.45 ± 0.02	3.16 ± 0.01	5.32 ± 0.04	26.7 ± 0.2	75 ± 1	72 ± 2	0.34 ± 0.01
L	6.45 ± 0.02	3.17 ± 0.01	5.31 ± 0.04	26.8 ± 0.1	75 ± 1	72 ± 2	0.34 ± 0.01
ECAP 4 Passes: $\rho = 2.664 \pm 0.001$ [g/cm^3]							
ECAP 1	6.39 ± 0.01	3.17 ± 0.01	5.24 ± 0.03	26.7 ± 0.2	73 ± 1	71 ± 1	0.33 ± 0.01
ECAP 2	6.43 ± 0.02	3.18 ± 0.05	5.27 ± 0.07	27.0 ± 0.9	74 ± 2	72 ± 3	0.34 ± 0.02
Thickness	6.41 ± 0.02	3.18 ± 0.03	5.26 ± 0.05	26.9 ± 0.5	74 ± 1	72 ± 3	0.34 ± 0.02
ECAP + Warm and Cold Rolling: $\rho = 2.663 \pm 0.001$ [g/cm^3]							
ST	6.36 ± 0.02	3.22 ± 0.02	5.16 ± 0.05	27.6 ± 0.4	71 ± 1	73 ± 2	0.33 ± 0.02
LT	6.44 ± 0.04	3.15 ± 0.05	5.31 ± 0.10	26.5 ± 0.9	75 ± 3	71 ± 4	0.34 ± 0.03
L	6.41 ± 0.02	3.17 ± 0.05	5.27 ± 0.07	26.7 ± 0.9	74 ± 2	71 ± 3	0.34 ± 0.02
ECAP + Cold Rolling: $\rho = 2.665 \pm 0.001$ [g/cm^3]							
ST	6.40 ± 0.03	3.20 ± 0.01	5.23 ± 0.04	27.4 ± 0.2	73 ± 1	73 ± 1	0.33 ± 0.01
LT	6.42 ± 0.08	3.17 ± 0.04	5.27 ± 0.13	26.8 ± 0.6	74 ± 4	72 ± 4	0.34 ± 0.04
L	6.47 ± 0.02	3.17 ± 0.02	5.34 ± 0.05	26.8 ± 0.4	76 ± 1	72 ± 3	0.34 ± 0.02

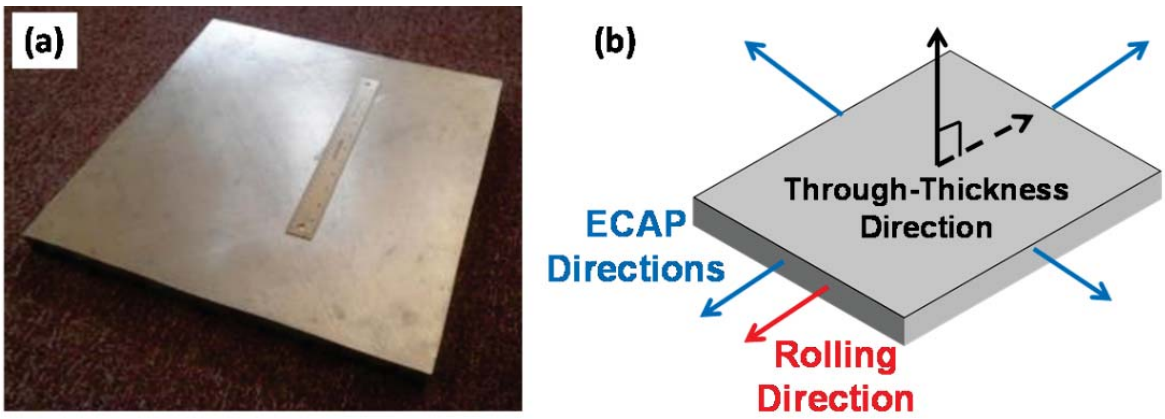

Figure 43: Images showing (a) an extruded ECAP billet and (b) a schematic of the extrusion and rolling directions. ECAP samples were extruded four times, turning 90° about the through-thickness normal each time. Some samples were rolled in a single direction following ECAP. The image of the extruded billet was obtained from an SBIR contract report to the Army Research Laboratory [120]

6.1.2 Plate Impact Experiments

Symmetric Al 5083 on Al 5083 plate impact experiments were performed on the four differently processed plates at impact velocities near 430 m/s, corresponding to a peak stress near 3 GPa. The peak stress value is near the middle of the range used for testing of Al 5083-H116 presented in the previous chapter. All four plate materials were tested using two different impact configurations: one where impact was performed through the plate thickness only (using 5 mm thick flyer plates and 10 mm thick samples), and one where impact was performed along all three plate directions simultaneously (using 3 mm thick flyer plates and 6 mm thick samples). Specimens were soft recovered for post-impact microscopy in all cases.

6.2 Results

Table 6 lists the calculated and measured parameters for each experiment. The impact velocity (V_{impact}) was measured using velocity pins, as shown in Figure 29. The free surface velocities at the peak state (u_{peak}) and the HEL (u_{HEL}) along with the pullback velocity (Δu_{fs}) were measured from the free surface velocity profiles, as shown in Figure 13. The shock wave velocity (U_S) was measured using the impact timing and shock wave arrival

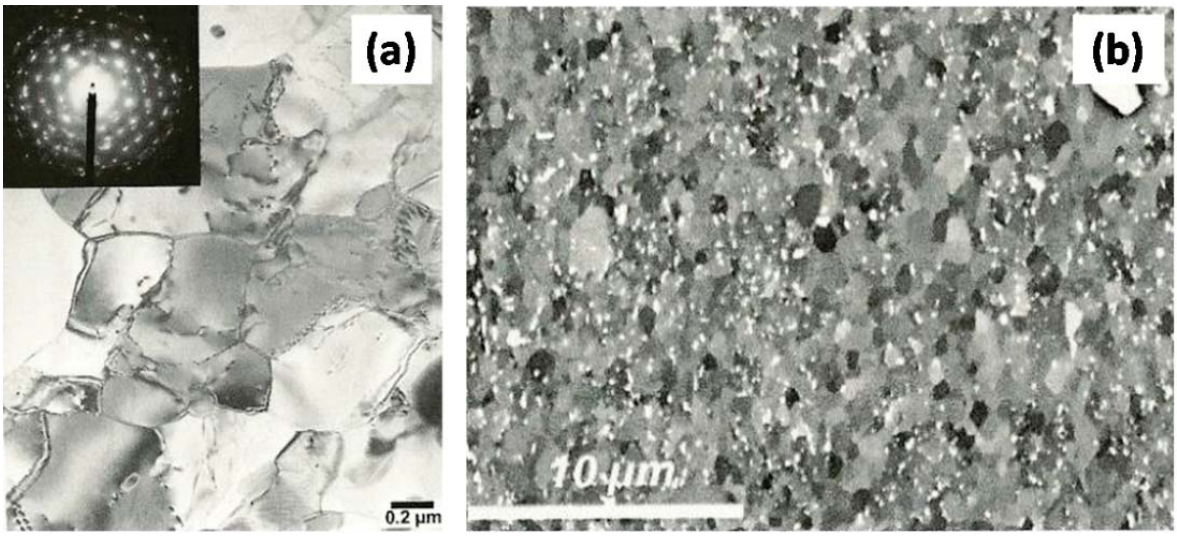

Figure 44: Microstructural images obtained by (a) TEM (along with selected area diffraction pattern) and (b) EBSD for the plate extruded four times using ECAP. The grain size was approximately 400 nm for this plate, with low misorientation angle between the grains. Images were taken by Jin et al. [53].

time visible in the free surface velocity profiles. The HEL stress (σ_{HEL}), spall strength (σ_{spall}), and peak stress (σ_{peak}) were calculated using Equations 5–8, with the spall strength correction factor (δ) calculated using Equation 7.

6.2.1 Microstructure

As reported previously, the sample processed using ECAP only has a highly refined grain structure with approximately 400 nm grain sizes [53]. TEM and EBSD images of the grain structure after processing with ECAP are shown in Figures 44(a) and 44(b) respectively. As Figure 44(a) shows, the grain structure is a mixture of grains and sub-grains, whereby dislocations are present at both the grain boundaries and sub-grain boundaries but with little dislocation density within the bulk of the grains. Figure 44(b) shows the highly refined grain structure, whereby both the grain size and misorientation angle are both small for processing using ECAP.

Optical microscope images along all three plate orientations of each sample type are given in Figures 45–48. Due to the low grain misorientation angle and small grain size for samples processed using ECAP (see Figure 44), the grain structure is not visible in the optical microscope for those samples. The grain boundary visibility increases when ECAP

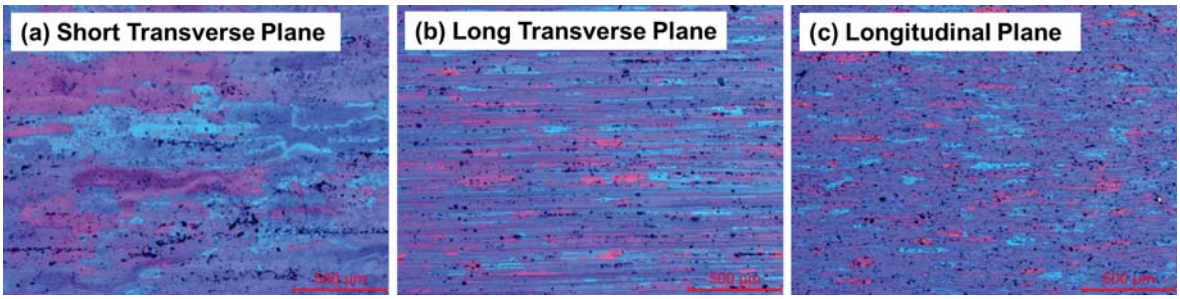

Figure 45: Optical micrographs showing planes normal to the (a) short transverse, (b) long transverse, and (c) longitudinal directions for the as-received Al 5083-H321 plate. The grain structure is highly textured with grains elongating along the rolling (longitudinal) direction and thinning through the plate thickness (along the short transverse direction). Inclusions are visible as black areas on the micrographs and align in the rolling direction along grain boundaries.

is followed by rolling and when viewed in the long transverse plane. This plane contains the short transverse direction, along which the grain boundary misorientation is maximized. For the as-received Al 5083-H321 (shown in Figure 45), the grain structure is typical of a rolled plate, with grain boundaries aligning and lengthening along the rolling direction. This textured microstructure is similar to that produced in the Al 5083-H116 plate shown in Figure 34 and presented in the previous chapter.

Secondary phases such as iron and silicon rich inclusions and manganese dispersoids appear as black areas in the micrographs shown in Figures 45–48. For the as-received plate, shown in Figure 45, the particles align in the rolling (longitudinal) direction along the grain boundaries. Figure 46 shows the microstructure after four ECAP passes. The particles grow in size from that of the as-received plate after processing with ECAP; however, they are uniformly dispersed, with no apparent preferred orientation as seen in the rolled plate. Post-ECAP rolling (as shown in Figures 47 and 48) results in increasing inclusion size from that of the sample processed using ECAP alone. As Figures 47(a) and 48(a) show, these particles are often damaged. In addition, the particles are aligned in the rolling direction at grain boundaries similar to the as-received rolled plate (see Figures 47(b) and 48(b)). Brittle particles such as these are known nucleation sites for spall damage and are expected to be detrimental to the spall strength [32, 33, 35, 37, 39, 40, 44, 79, 101].

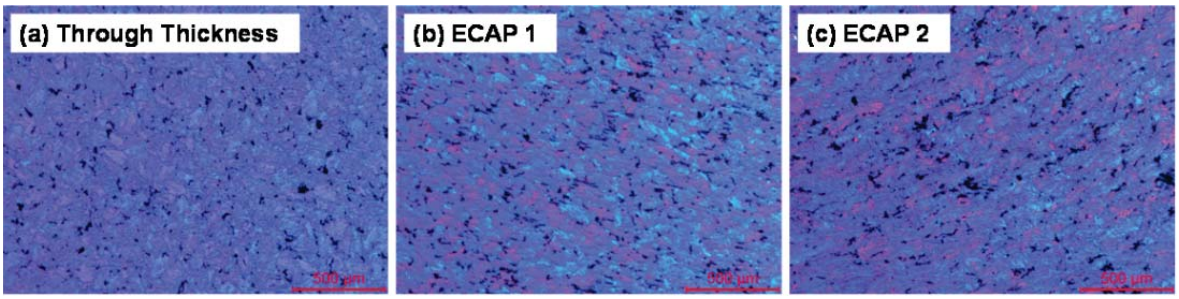

Figure 46: Optical micrographs showing planes normal to the (a) through-thickness direction, (b) one of the ECAP directions, and (c) another orthogonal ECAP direction. Due to the low misorientation between grains and small grain size, the grain structure is not visible. Inclusions are visible as black areas on the micrographs and are larger than observed for the as-received Al 5083-H321. No preferred orientation is observed for the inclusions for this sample type.

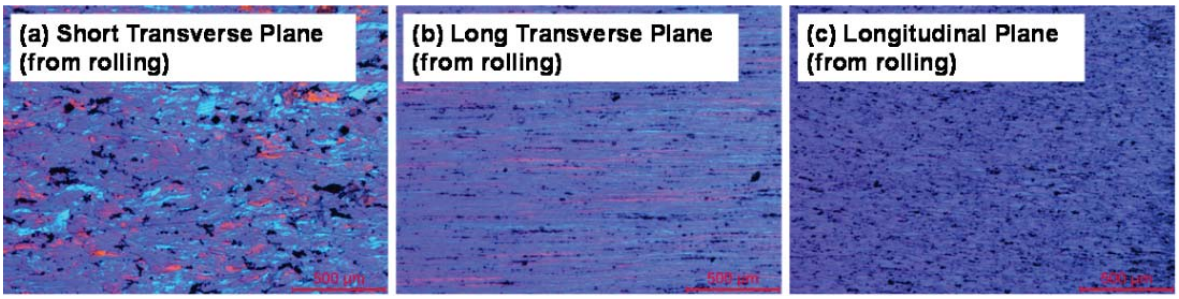

Figure 47: Optical micrographs showing planes normal to the (a) short transverse, (b) long transverse, and (c) longitudinal directions for the plate processed using ECAP followed by warm and cold rolling. Due to the low misorientation between grains and small grain size, the grain structure is not visible except for the long transverse plane where the grain misorientation angle is highest. Inclusions are visible as black areas on the micrographs and align in the rolling direction along grain boundaries. Large cracked inclusions are visible in the short transverse plane.

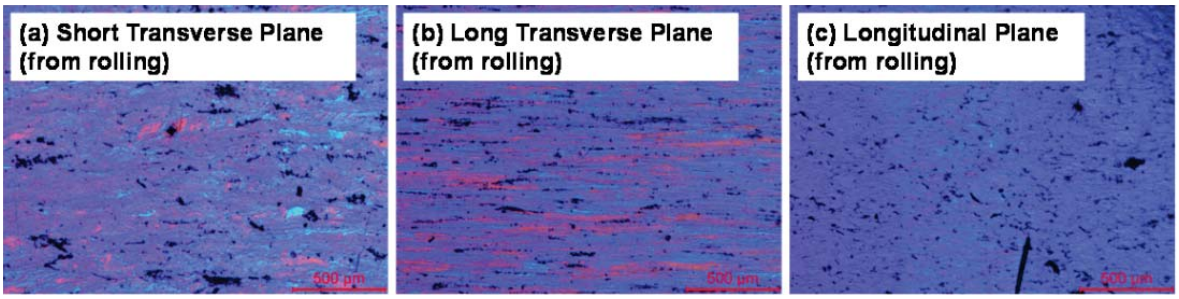

Figure 48: Optical micrographs showing planes normal to the (a) short transverse, (b) long transverse, and (c) longitudinal directions for the plate processed using ECAP followed by cold rolling. Due to the low misorientation between grains and small grain size, the grain structure is not visible except for the long transverse plane where the grain misorientation angle is highest. Inclusions are visible as black areas on the micrographs and align in the rolling direction along grain boundaries. Large cracked inclusions are visible in the short transverse plane.

6.2.2 Plate Impact Experiment Results

6.2.2.1 VISAR Free Surface Velocity

The VISAR free surface velocity profiles for impact through the plate thickness and along all three plate orientations are given in Figures 49 and 50 respectively. The inset of each figure better displays the trends in the HEL with processing and plate orientation.

Figure 49 clearly shows that processing with ECAP increases the HEL from that of the as-received rolled plate. Subsequent rolling of the plates processed with ECAP results in even larger gains to the HEL—especially for the plate processed using both warm and cold rolling; however, the pullback velocity, a measure of the material's spall strength, shows a different trend with processing. ECAP alone results in an increased pullback velocity relative to the as-received plate, but rolling in addition to ECAP results in decreased pullback velocity for both rolled specimens measured through the plate thickness.

Figure 50 displays the orientation dependence of both the HEL and spall properties for each specimen. The as-received plate shows the largest difference in the HEL as a function of orientation, with the long transverse direction showing the largest HEL value. This is similar to the HEL trends for Al 5083-H116 discussed in the previous chapter. The plate processed using ECAP has a lower HEL value through the thickness than either of the two ECAP directions, both of which had similar HEL values. Subsequent rolling of the plate

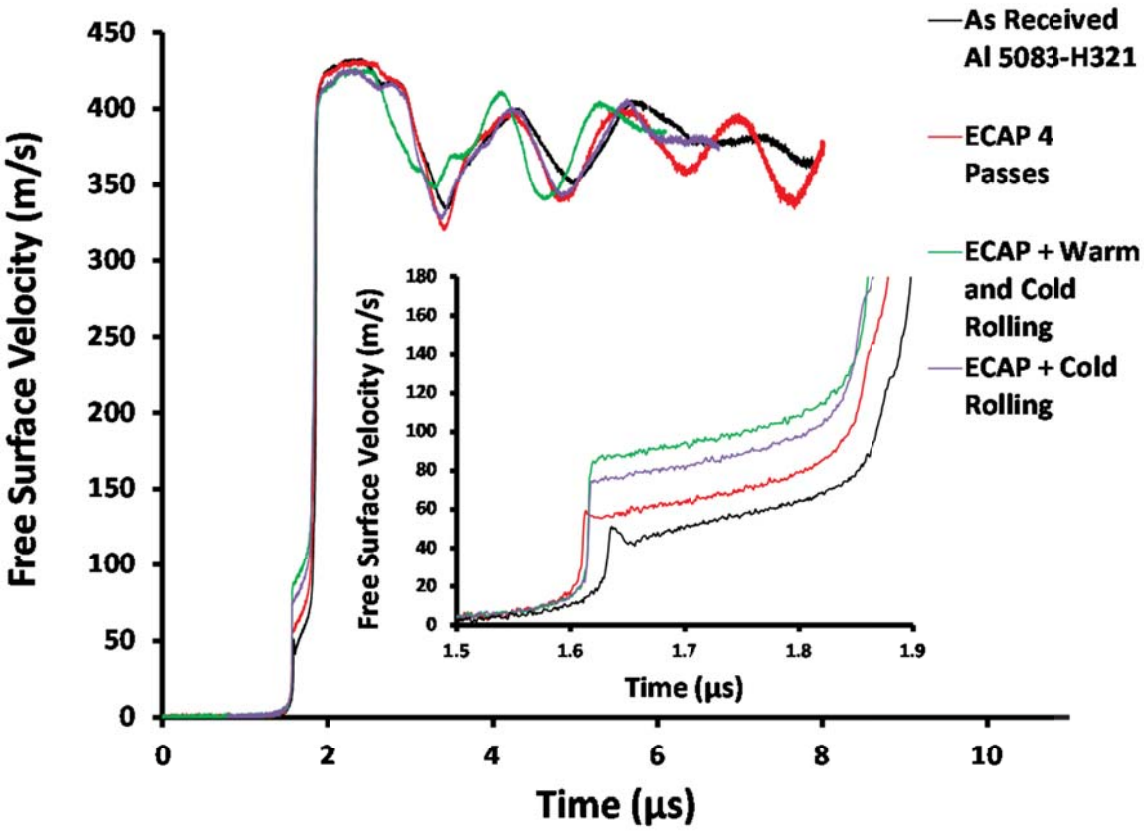

Figure 49: Rear free surface velocity vs. time for impact through the plate thickness of Al 5083 samples processed via ECAP and rolling. The inset better displays the HEL for each data set.

results in similar HEL values for each of the three impact directions. The as-received and ECAP specimens show slight decreases in the pullback velocity when measured through the plate thickness, as shown in Figures 50(a) and 50(b); however, there is a much larger decrease in the pullback velocity through the thickness for the samples processed using both rolling and ECAP, as shown in Figures 50(c) and 50(d).

6.2.2.2 Spall Strength and Hugoniot Elastic Limit

The spall strength (σ_{spall}) and HEL (σ_{HEL}) values were calculated using the free surface velocity data shown in Figures 49 and 50 along with Equations 5–7. The free surface velocity data used in Equations 5–7 is listed in Table 6. The calculated values of spall strength and HEL are shown for impact through the plate thickness and along all three plate orientations in Figures 51 and 52 respectively.

Figures 51 and 52 quantify the trends mentioned in Section 6.2.2.1. For impact through the plate thickness, the highest spall strength value is 0.90 GPa for the specimen processed using ECAP only. For comparison, the as-received Al 5083-H321 plate has a spall strength value of 0.77 GPa, which is similar to the value of 0.81 $\pm$ 0.05 GPa corresponding to the Al 5083-H116 plate discussed in the previous chapter. Post-ECAP rolling results in decreased spall strength for both specimens processed using either warm and cold rolling or cold rolling alone, despite the large gains to the HEL value for both of these specimen types. The sample processed using both warm and cold rolling shows the lowest spall strength value of 0.60 GPa, followed by the next lowest value of 0.74 GPa for the sample processed using ECAP and cold rolling.

Unlike the spall strength, both ECAP and post-ECAP rolling increase the HEL value. The as-received plate has an HEL value of 0.40 GPa, which is again similar to the value of 0.43 $\pm$ 0.04 GPa corresponding to Al 5083-H116. ECAP alone increases the HEL from the rolled plate value to a value of 0.48 GPa. Post-ECAP rolling then results in tremendous increases to the HEL. The largest HEL value is 0.72 GPa for the specimen processed using ECAP followed by both warm and cold rolling. Processing using ECAP and cold rolling

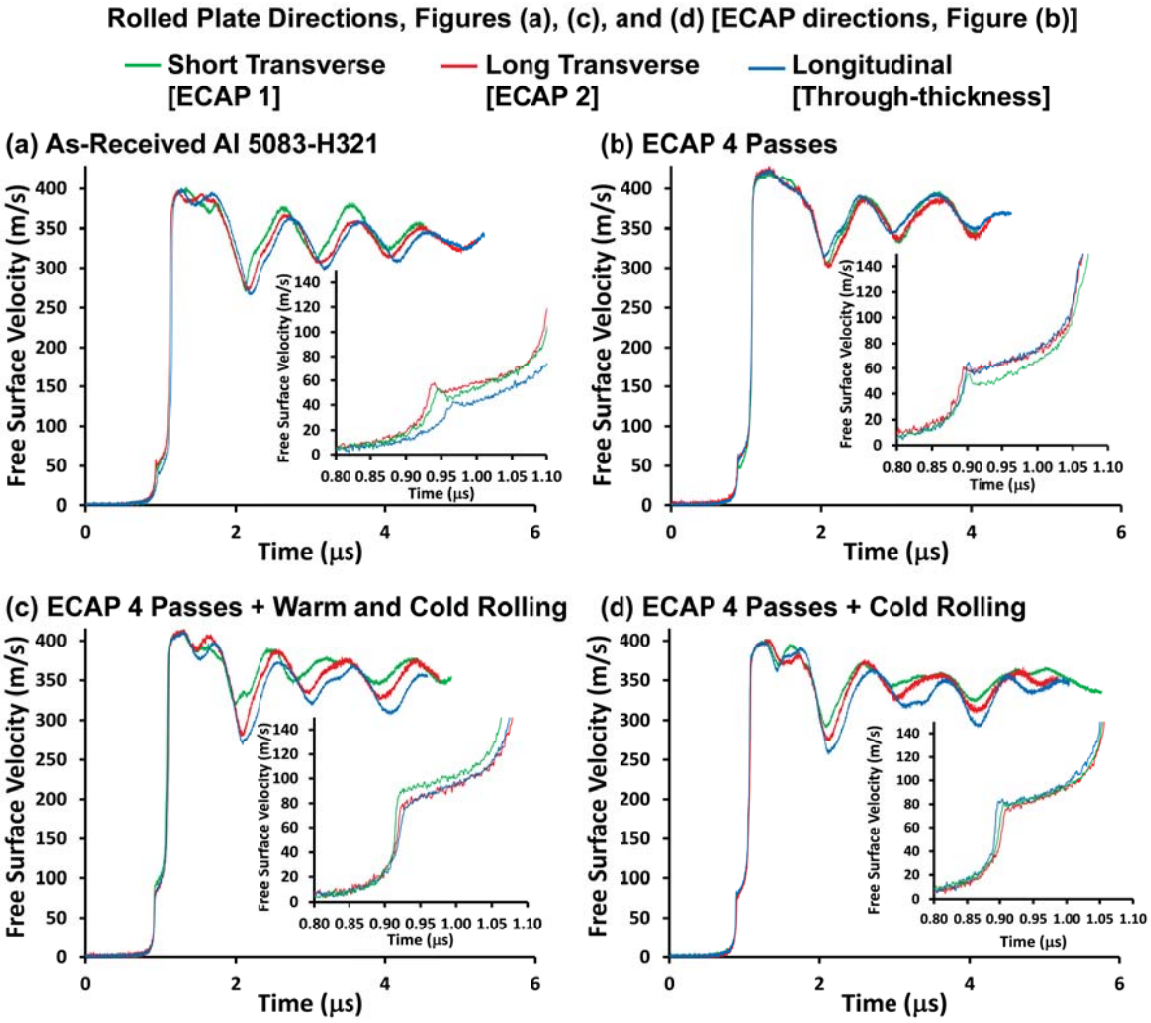

Figure 50: Rear free surface velocity vs. time for impact along all plate directions of Al 5083 samples processed via ECAP and rolling. The different sample types are (a) as-received rolled Al 5083-H321, (b) ECAP four passes, (c) ECAP followed by warm and cold rolling, and (d) ECAP followed by cold rolling. The inset better displays the HEL for each data set.

Table 6: Calculated and measured free surface velocity data for Al 5083 samples processed using ECAP and rolling. Multiple sample experiments for rolled specimens are designated with ST (short transverse), LT (long transverse), or L (longitudinal) to denote the impact direction with respect to the orientation of the rolled plate. The multiple sample experiment for the plate processed using ECAP alone is designated withe the through thickness direction and the two independent ECAP directions measured. The data represents a 95% confidence interval in all cases.

Shot Number	V_{impact} [m/s]	u_{peak} [m/s]	U_S [km/s]	σ_{Peak} [GPa]	u_{HEL} [m/s]	σ_{HEL} [GPa]	Δu_{fs} [m/s]	δ [m/s]	σ_{Spall} [GPa]
As-Received Al 5083-H321									
1306	440	433	5.37	3.16	46.6	0.40	99.3	12.9	0.77
1313 ST	418	401	5.16	2.85	53.4	0.45	131.4	24.1	1.07
1313 LT	418	398	5.19	2.85	58.0	0.50	126.4	15.5	1.01
1313 L	418	401	5.07	2.78	42.8	0.37	134.7	15.2	1.06
ECAP 4 Passes									
1226	438	432	5.34	3.15	56.7	0.48	112.2	16.6	0.90
1321	438	425	5.20	3.05	65.0	0.56	111.8	8.4	0.84
Thickness									
1321	438	421	5.20	3.00	55.4	0.47	115.9	15.4	0.92
ECAP 1									
1321	438	429	5.18	3.06	61.2	0.52	129.0	14.0	1.00
ECAP 2									
ECAP + Warm and Cold Rolling									
1301	441	427	5.36	3.16	85.3	0.72	79.9	6.8	0.60
1322 ST	437	414	5.37	3.07	89.6	0.76	94.4	10.6	0.72
1322 LT	437	415	5.28	3.04	79.6	0.68	134.9	19.2	1.09
1322 L	437	412	5.30	3.02	77.1	0.66	143.2	10.1	1.08
ECAP + Cold Rolling									
1303	440	426	5.45	3.18	74.0	0.63	98.8	7.6	0.74
1312 ST	426	402	5.29	2.95	81.6	0.70	111.3	8.9	0.84
1312 LT	426	402	5.24	2.92	75.5	0.65	128.5	14.8	1.01
1312 L	426	400	5.28	2.94	82.6	0.71	142.9	10.1	1.09

alone results in an HEL value of 0.63 GPa, which is still much larger than that of either the rolled plate or the plate processed using ECAP alone.

Figure 52 shows the values of spall strength and HEL as a function of orientation for each plate specimen. The as-received and ECAP samples show little variation in spall strength with all values within the error bars for each orientation; however, the HEL shows some orientation dependence. For the as-received specimens, the HEL ranges between 0.37 GPa to 0.50 GPa, and for the ECAP samples, the HEL ranges between 0.47 GPa to 0.56 GPa. ECAP followed by rolling results in a larger and consistent HEL of approximately 0.7 GPa for any plate orientation; however, the spall strength is drastically reduced for the through-thickness orientation. The spall strength for the samples processed using ECAP followed by warm and cold rolling drops from a maximum value of 1.09 GPa to 0.72 GPa, and the spall strength for the samples processed using ECAP followed by cold rolling drops from 1.09 GPa to 0.84 GPa.

As shown in Figures 45–48, brittle particles, such as Mn dispersoids and Fe and Si rich inclusions, grow and align along the grain boundaries after processing with ECAP and rolling. Therefore, void nucleation sites are preferentially located along planes perpendicular to the impact direction for impact through the plate thickness and are likely responsible for the reduced spall strength for impact in this direction. As shown in Figure 46, the specimen processed by ECAP alone does not have a preferential alignment of inclusions, and consequently, shows higher spall strength than the rolled specimens and little orientation dependence. Figure 53 is a post-mortem optical micrograph of the sample processed using ECAP followed by warm and cold rolling. It clearly shows that spall damage grows from similar large and cracked particles visible in Figure 47(a) for the samples prior to plate impact. It is therefore likely that these brittle particles are controlling the spall response for the samples given post-ECAP rolling.

6.3 Conclusions

The spall properties of large Al 5083 plates processed using equi-channel angular pressing (ECAP) and post-ECAP rolling were investigated using plate impact testing at peak stresses

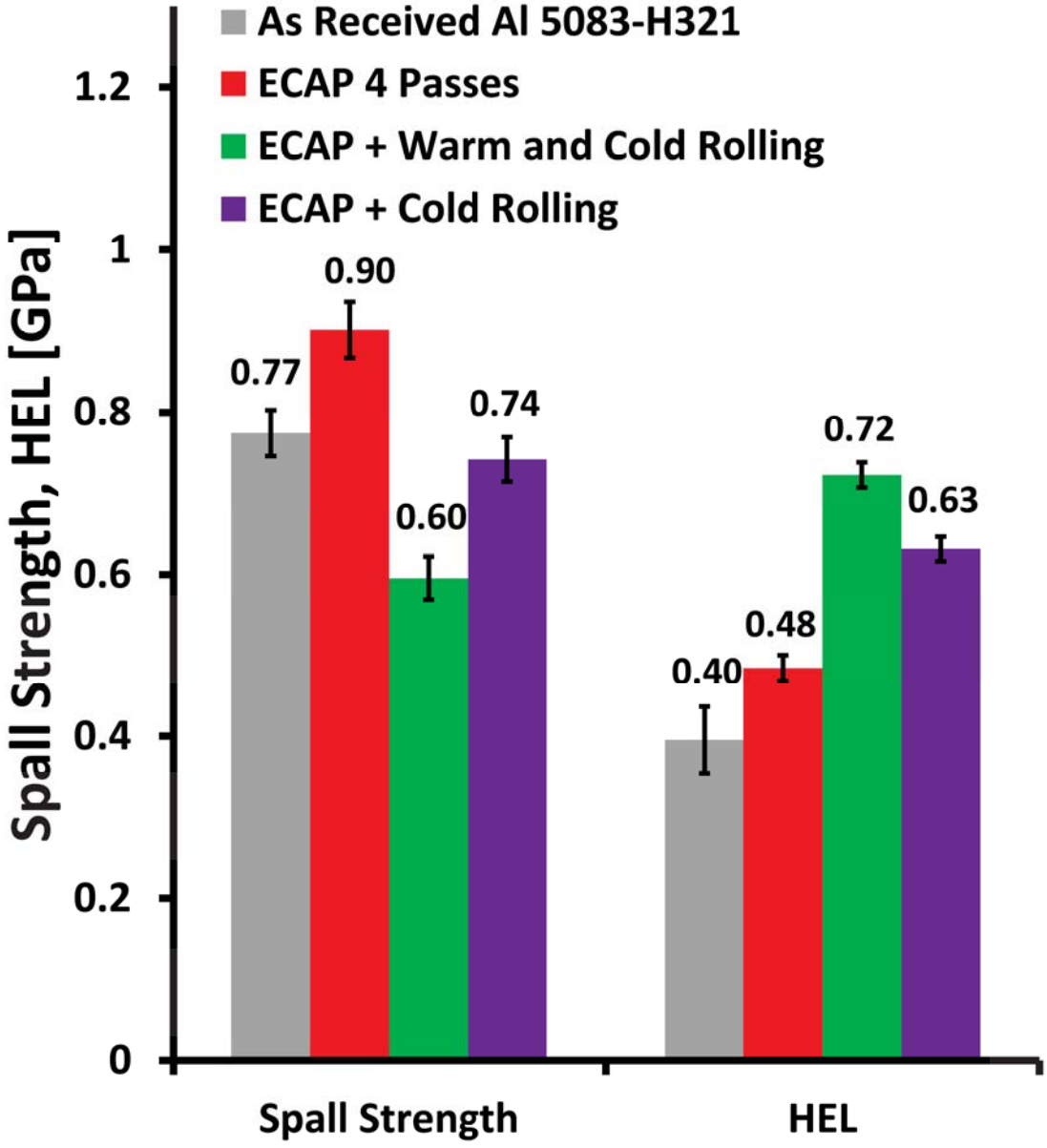

Figure 51: Calculated spall strength and HEL values for impact through the plate thickness of Al 5083 samples processed via ECAP and rolling

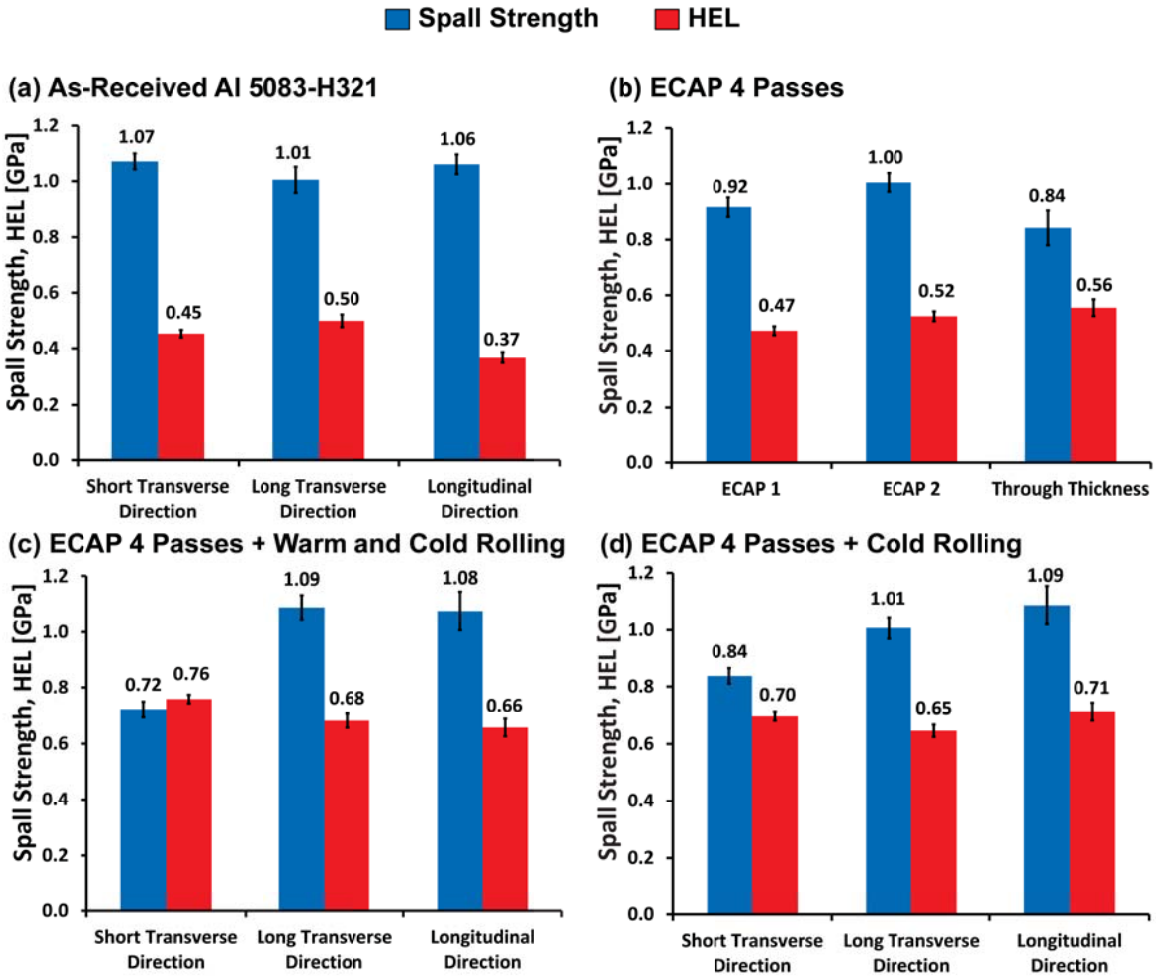

Figure 52: Calculated spall strength and HEL values for impact along all plate directions of Al 5083 samples processed via ECAP and rolling. The different sample types are (a) as-received rolled Al 5083-H321, (b) ECAP four passes, (c) ECAP followed by warm and cold rolling, and (d) ECAP followed by cold rolling.

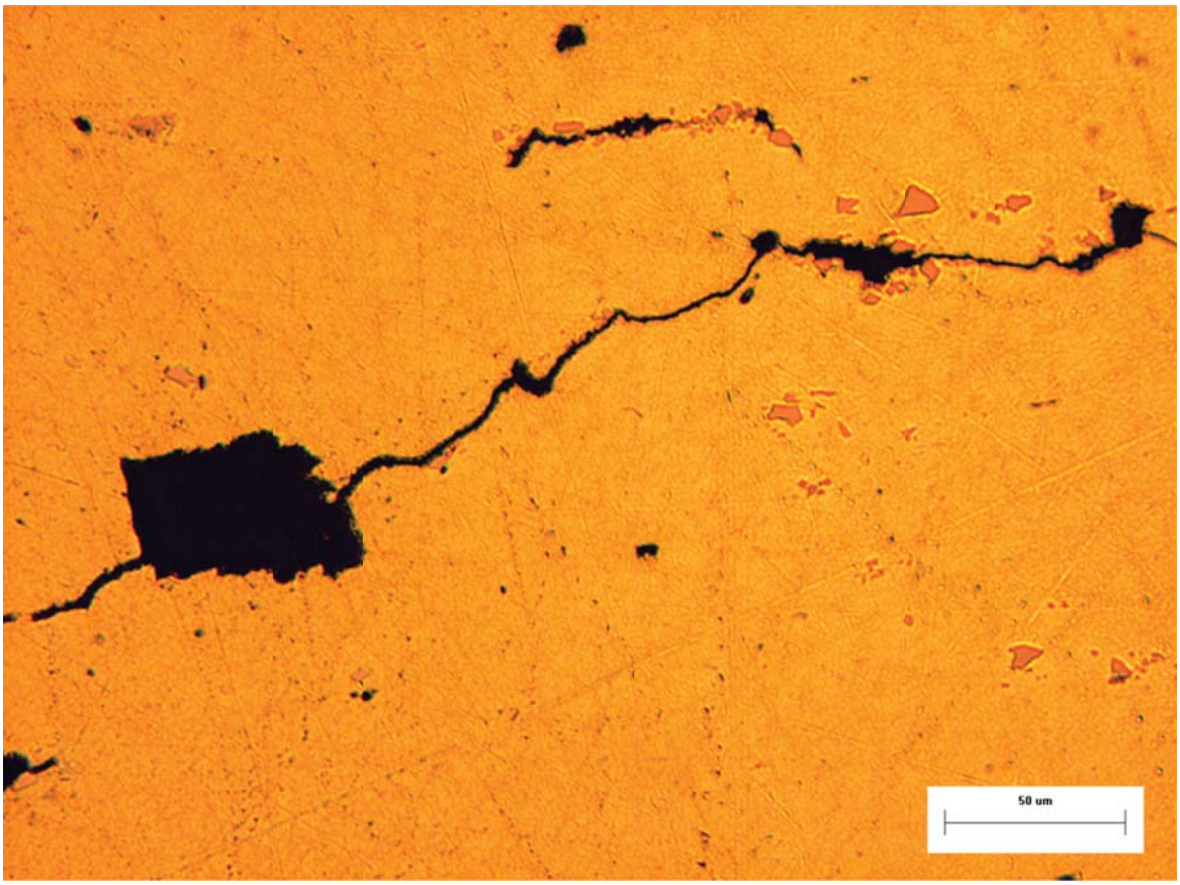

Figure 53: Optical micrograph showing spall damage growing near large and damaged inclusions for the sample processed using ECAP followed by warm and cold rolling

near 3 GPa. Processing using ECAP resulted in a uniform sub-micron grain structure with approximately 400 nm grain size and low misorientation angle between the grains. Large inclusions and dispersoid particles were present in the microstructure after ECAP, but the particles were uniformly dispersed. Post-ECAP rolling resulted in cracking and alignment of the particles along the rolling direction.

The spall strength of Al 5083 processed using both ECAP and post-ECAP rolling is largely controlled by the alignment and cracking of the brittle particles evolved during processing. Processing via ECAP alone results in no alignment of particles, causing increased spall strength and HEL when compared to a standard rolled plate. The spall strength and HEL have values of 0.90 GPa and 0.48 GPa respectively for impact through the plate thickness. In addition, the plates processed using ECAP show little orientation dependence for either property.

Subsequent rolling of the ECAP plates results in significant increases to the HEL, but at the expense of the spall strength. The HEL values were 0.72 GPa and 0.63 GPa for plates processed using warm followed by cold rolling and cold rolling alone respectively. The spall strength decreases dramatically through the plate thickness for both samples rolled after ECAP. The through-thickness spall strength was 0.60 GPa for the sample processed using warm and cold rolling, and 0.74 GPa for the sample processed using cold rolling. Post-ECAP rolling also results in orientation dependent spall properties. For experiments performed along all three plate orientations, the spall strength fell to 0.72 GPa through the thickness for the sample processed using warm and cold rolling and 0.84 GPa for the sample processed using cold rolling from a maximum value of 1.09 GPa in both cases. The orientation dependent spall properties and decreased spall strength through the thickness are due to the preferential alignment and cracking of inclusions during the rolling process. Spall damage was observed to grow from large and damaged inclusions for these sample types. Since rolling aligns brittle particles along planes perpendicular to the through thickness direction, the number of spall nucleation sites is maximized for impact in this direction.

Processing via ECAP alone shows promise for increasing the impact resistance of aluminum alloy plates, as this resulted in the best combination of both HEL and spall strength.

Post-ECAP rolling results in an enhanced HEL, which is expected to yield better ballistic properties; however, the decreased spall strength can result in decreased blast resistance. Since ECAP increases both the HEL and spall strength, this processing technique is expected to yield better penetration resistance and blast resistance for Al 5083 armor plates.

CHAPTER 7

SPALL BEHAVIOR OF AL 5083 WITH AN EQUIAXED GRAIN STRUCTURE

This chapter focuses on the spall behavior of Al 5083 with an equiaxed grain structure. Similar to the previous chapter, the grain structure discussed here is uniform with plate direction; however, the grain size is much larger (approximately 34 μm) than the sub-micron grain structure produced by ECAP. This uniform microstructure removes the effects of grain texture on the spall properties that were observed for a rolled plate. The uniform grain structure can then be compared to the smaller uniform grain structure produced via ECAP, allowing for the effects of grain size on spall strength to be determined. Symmetric plate impact testing was performed over a similar stress range as that for the Al 5083-H116 material studied in Chapter 5. Experiments were performed through the plate thickness in all cases.

7.1 Experimental Procedure

7.1.1 Materials

An equiaxed grain structure was produced using the Al 5083-H116 plate described in Chapter 5 as the starting material. An approximately 12″ x 1.5″ x 0.5″ (approximately 305 mm x 38 mm x 13 mm) rectangular rod was cut from the original rolled plate with the long axis of the rod along the original rolling direction. The rod was first annealed at 415°C for 10 min to soften the strain hardened plate, and then stretched to approximately 3% strain under a strain rate of approximately 1x10^{-5} s^{-1} using a 10-ton screw driven Instron tensile testing machine. This allowed for a uniform state of strain to be achieved in the center of the rod to act as the driving force for grain growth. The ends of the rod were removed after stretching as they were deformed from the clamping mechanism attached to the tensile tester. The center of the rod was annealed again at 415°C for 24 h to allow significant grain

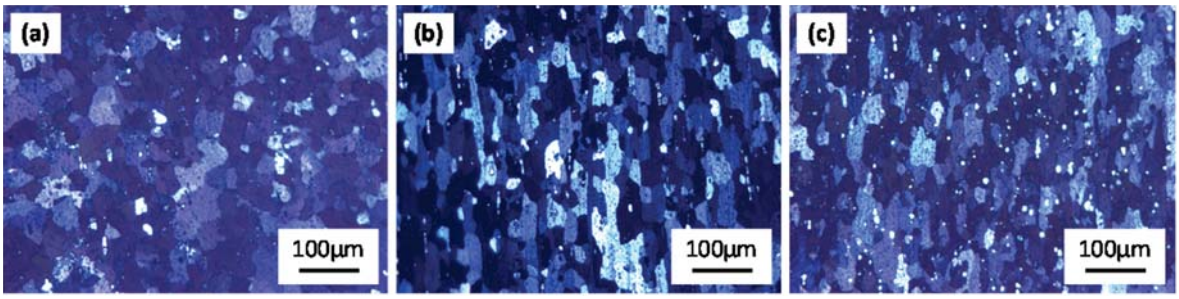

Figure 54: Optical microscope images showing the equiaxed grain structure produced after stretching and annealing an Al 5083-H116 plate. The images show the former (a) short transverse, (b) long transverse, and (c) longitudinal planes respectively. The original rolled Al 5083 plate was stretched to a 3% strain followed by annealing at 415°C for 24 h to produce this microstructure.

growth to occur. Figure 54 displays the microstructure along each of the three orthogonal plate directions after the final 24 h annealing treatment.

Figure 54 shows that the stretching and annealing treatments result in a uniform equiaxed grain structure with orientation. The mean intercept grain size ($< G >$) was measured as 34 ± 11 μm along any of the three orthogonal plate directions. This can be compared to the large difference in $< G >$ for the original Al 5083-H116 plate shown in Table 3, whereby the values range from 66 ± 20 along the rolling direction to 9 ± 1 through the plate thickness. This microstructure should thus remove the effects of grain texture on the spall properties that were observed for plate impact testing of the original rolled plate.

7.1.2 Plate Impact Experiments

Three target samples were machined from the stretched and annealed bar for plate impact testing over the stress range between 1.4 and 5.5 GPa. Impact experiments were performed in the through-thickness direction of the original rolled plate. The density (ρ) of the Al 5083 samples was measured as 2.664 ± 0.007 g/cm^3, which is similar to the value for the rolled Al 5083-H116 plate. The sound speeds (C) for the equiaxed samples were measured for calculation of the spall strength, HEL, and elastic constants. Table 7 lists the longitudinal wave speed, shear wave speed, bulk wave speed, shear modulus, bulk modulus, elastic modulus, and Poisson's ratio (C_L, C_S, C_B, G, B, E, and ν respectively) for the equiaxed samples.

Table 7: Measured sound speed and elastic constants for Al 5083 samples with an equiaxed grain structure. The data represents a 95% confidence interval in all cases.

C_L [mm/μs]	C_S [mm/μs]	C_B [mm/μs]	G [GPa]	B [GPa]	E [GPa]	ν
6.367 ± 0.003	3.193 ± 0.004	5.191 ± 0.028	27.2 ± 0.1	71.8 ± 0.6	72.4 ± 0.7	0.332 ± 0.007

7.2 Results

Three Al 5083 samples with an equiaxed grain structure were impacted at 194 m/s, 430 m/s, and 744 m/s for a stress range between 1.4 and 5.5 GPa. Table 8 lists the measured parameters for each experiment. The impact velocity (V_{impact}) was measured using velocity pins, as shown in Figure 29. The free surface velocities at the peak state (u_{peak}) and the HEL (u_{HEL}) along with the pullback velocity (Δu_{fs}) were measured from the free surface velocity profiles, as shown in Figure 13. The shock wave velocity (U_S) was measured using the impact timing and shock wave arrival time visible in the free surface velocity profiles. The HEL stress (σ_{HEL}), spall strength (σ_{spall}), and peak stress (σ_{peak}) were calculated using Equations 5–8, with the spall strength correction factor (δ) calculated using Equation 7.

7.2.1 Free Surface Velocity

The VISAR rear free surface velocity data for the impacted Al 5083 samples is shown in Figure 55. Two unique features are observed in the velocity profiles. The first feature is that of upper and lower yielding at the HEL visible in the inset of Figure 55. This phenomenon is known as precursor decay and has been observed previously for annealed aluminum samples [113]. Precursor decay is often attributed to an initially high stress required to nucleate dislocations followed by a steep drop-off in stress after dislocations have been nucleated [112]. Since this material was annealed, the initial dislocation density should be negligible, requiring the nucleation of dislocations for dynamic yielding to occur; therefore, the upper and lower yielding is consistent with the microstructural state of the material. The lower yield point in Figure 55 remains relatively constant with impact velocity (or peak stress); however, the upper yield point is stress dependent and increases with increasing impact velocity.

The second unique feature in the data is a "dip" in the release from the peak velocity, which becomes more prominent as the impact velocity increases. For impact at 744 m/s the initial dip is followed by a smaller "pullback" and then the expected release. While the cause of this phenomenon is not yet known, it is possible that the upper and lower yielding and this second feature are both related to changes in dislocation density.

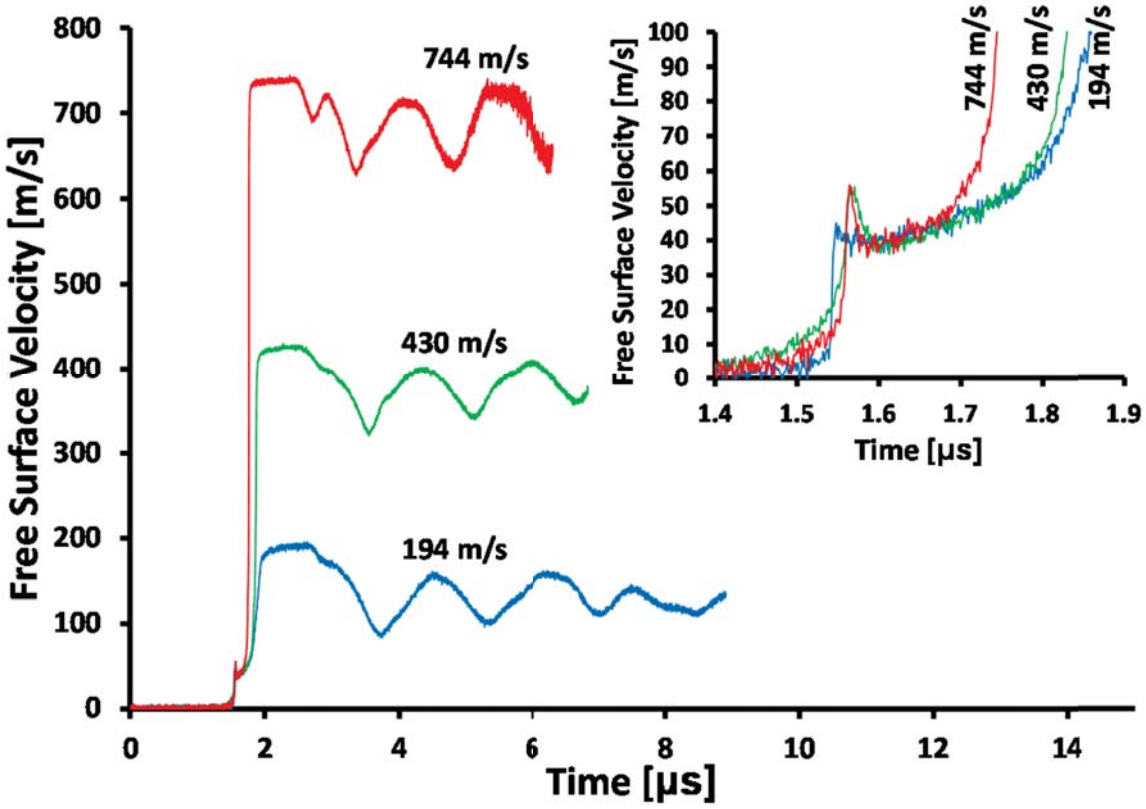

Figure 55: Rear free surface velocity data for Al 5083 samples with an equiaxed grain structure. The inset better displays the HEL for each data set.

The pullback velocity increases with increasing impact velocity, indicating that the spall strength is impact stress dependent for the case of the equiaxed grain structure. This is in contrast to the rolled Al 5083-H116 plate that showed a relatively constant spall strength with impact stress. The HEL and spall strength values will be quantified and discussed in the next section.

7.2.2 Spall Strength and HEL

The spall strength (σ_{spall}) and HEL (σ_{HEL}) values were calculated using the free surface velocity data shown in Figure 55 along with Equations 5–7. The free surface velocity data used in Equations 5–7 is listed in Table 8. The calculated values of spall strength and HEL are shown for impact through the plate thickness in Figure 56.

Table 8: Calculated and measured free surface velocity data for Al 5083 samples with an equiaxed grain structure

Shot Number	V_{impact} [m/s]	u_{peak} [m/s]	U_S [km/s]	σ_{Peak} [GPa]	u_{HEL} [m/s]	σ_{HEL} [GPa]	Δu_{fs} [m/s]	δ [m/s]	σ_{Spall} [GPa]
1318	196	194	5.26	1.43	39.5	0.34	112.0	10.0	0.84
1323	433	430	5.20	3.04	37.9	0.32	109.3	15.6	0.86
1317	743	744	5.54	5.53	38.1	0.32	116.7	16.7	0.92

The HEL and spall strength values are shown in Figure 56 as a function of the peak stress. Both the upper and lower HEL values are given in Figure 56(a). The lower HEL value remains relatively constant with peak stress and has an average value of 0.33 ± 0.02 GPa. This is lower than the HEL value of 0.43 GPa measured for the Al 5083-H116 plate. Since this plate was in the fully annealed condition compared to the heavily strain hardened rolled plate, it is to be expected that yielding would occur at a lower stress. The upper HEL, on the other hand, displays stress dependent behavior and increases from a value of 0.38 GPa at a peak stress of 1.4 GPa to a value of 0.48 GPa at a peak stress of 5.5 GPa. Therefore, the upper HEL value for the equiaxed microstructure increases to a value above that of the original rolled plate as peak stress increases.

It has been shown that the HEL of materials displaying precursor decay should be limited by a stress value corresponding to a particle velocity equal to the DeBroglie wave velocity [111]. This DeBroglie limiting HEL value is given by Equations 27 and 28, and corresponds to a value of 0.24 GPa for the equiaxed Al 5083 microstructure. The value corresponds well to the value of 0.33 GPa for the lower yield point at the HEL.

The spall strength values, shown in Figure 56(b), may also reflect peak stress dependence; however, the values are all within the error bars, making this difficult to ascertain. The spall strength ranges from 0.84 GPa at a peak stress of 1.4 GPa to 0.92 GPa at 5.5 GPa peak stress. The average spall strength value is 0.87 ± 0.08 GPa, which is within the error bars of the spall strength for the rolled plate (0.81 GPa); however, for individual impact velocities, the spall strength is higher and outside the error bars for the equiaxed microstructure versus the rolled plate microstructure (see Table 8 compared to Table 4).

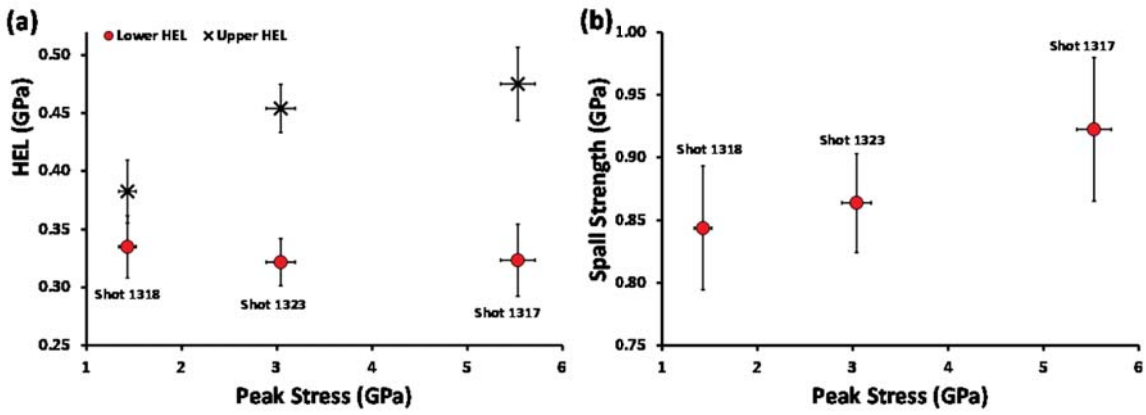

Figure 56: Calculated (a) HEL and (b) spall strength data as a function of the peak stress for Al 5083 samples with an equiaxed grain structure

7.3 Conclusions

Stretching and annealing a rolled Al 5083-H116 plate results in an equiaxed grain structure with a 34 μm grain size. Plate impact testing of this material reveals an upper and lower yielding behavior at the HEL. The lower HEL value remained relatively constant at 0.33 GPa, but the upper HEL value increased from 0.38 GPa to 0.48 GPa over the stress range of 1.4 GPa to 5.5 GPa. It is likely that the upper and lower yielding are related to the lower dislocation density after annealing, whereby an initially high stress is required to nucleate dislocations at the wave front. The lower yield point corresponds well to the DeBroglie limiting HEL value of 0.24 GPa for this alloy. The spall strength of the equiaxed grain structure is 0.87 GPa, which is higher than that of the rolled Al 5083 plate, but there were large error bars in the spall strength values.

The microstructure produced by ECAP in Chapter 6 (with a 0.4 μm grain size) and the equiaxed grain structure presented here (with a 34 μm grain size), result in higher spall strength values than that of the rolled Al 5083 plate. Therefore, spall strength does not appear to be a direct function of grain size for Al 5083 samples. Instead, the uniformity of the microstructure appears to result in the increasing spall strength.

CHAPTER 8

SPALL BEHAVIOR OF PRECIPITATION HARDENED ALUMINUM-9WT.% MAGNESIUM

This chapter focuses on the spall behavior of an extruded Al-9wt.% Mg plate as a function of various heat treatments. The plate was provided by Universal Alloys, Inc., and had trace silver additions. Al-Mg alloys with high magnesium content, especially along with silver additions, are known to result in a precipitation hardenable system [2, 71–77]. Al-Mg (5XXX) alloys, such as Al 5083, used for armor plating traditionally rely on strain hardening as the primary strengthening mechanism since secondary phases, such as precipitates, can preferentially nucleate spall damage during blast or impact loading [79]. However, contrary to previous studies, precipitation hardened Al 6061 has shown increased resistance to spalling with aging [80]. The Al-9wt.% Mg alloy was therefore investigated to further explore the effects of precipitation on the spall behavior.

Symmetric plate impact experiments were performed on the Al-9wt.% Mg alloy, named U506, which was processed using a variety of solution and aging heat treatments to ascertain the best processing method to precipitation harden the material. Plate impact experiments were performed on the highest strength precipitation hardened sample, a solution treated sample, and the as-received extruded plate. Experiments were performed through the thickness at a peak stress near 3 GPa, which is near the middle of the range tested for the rolled Al 5083-H116 plate presented in Chapter 5. The purpose of these experiments was to determine the effects of precipitate phases on the spall strength of Al-Mg alloys.

8.1 Experimental Procedure

8.1.1 Materials

As previously mentioned, increasing the magnesium content in Al-Mg alloys, especially along with the addition of trace amounts of silver, can result in an age-hardenable system. An Al-9wt.% Mg alloy (U506) with silver additions was provided by Universal Alloys, Inc.

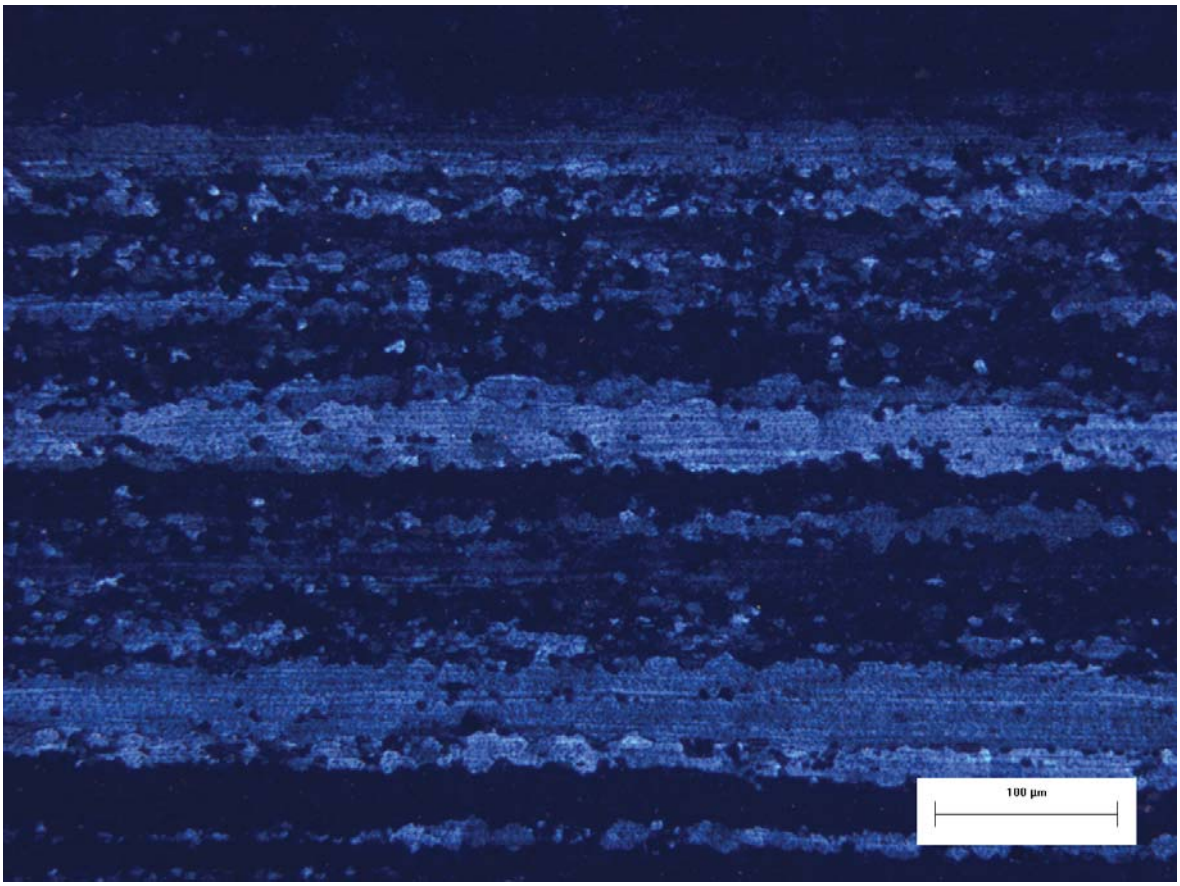

Figure 57: Optical micrograph showing the grain structure of an Al-9wt.% Mg alloy after extrusion. The image displays some partial recrystallization likely due to dynamic recrystallization during extrusion.

for selected heat treatments. The grain structure of the as-extruded material is shown in Figure 57. Some recrystallization is visible as seen in the micrograph, but there are large regions that are devoid of recrystallization. Since Al-Mg alloys with high magnesium content are known to dynamically recrystallize, it is likely that recrystallization occurred during extrusion.

8.1.2 Heat Treatments

The Al-Mg phase diagram is shown in Figure 1. In order to adequately solution heat treat the U506 material, the solution treatment temperature should be well within the single phase field at 9 wt.% Mg; however, care must be taken to avoid non-equilibrium melting during the solution treatment caused by solutionizing at a temperature too close to the

solidus line. With these requirements in mind, solution heat treatment was performed at 800°F (approximately 430°C) for times up to 24 h.

Previous work by Kubota and co-workers [2, 71–74] for a similar high magnesium content alloy used a much higher temperature (500°C) for solution treatment. This temperature was judged to be too close to the solidus line shown in Figure 1 to yield an effective microstructure. Instead, a dual solution heat treatment was also used with an initial heat treatment at the lower (430°C) temperature for four hours followed by a slow 50°F/h (approximately 25°C/h) ramp up to a higher temperature of 900°F (approximately 480°C) for 1 h. This dual solution heat treatment was designed to adequately solutionize the large degree of solute within the alloy without resulting in detrimental melting during heat treatment.

After solution treatment, precipitation hardening was performed at temperatures of 150°C, 200°C, and 250°C for times up to 200 h. Optical microscopy and Vickers microhardness measurements were performed on the solution treated and age hardened specimens in order to characterize the microstructure resultant from heat treatments and to quantify the strengthening behavior of the precipitate phases generated. The location of the precipitate phases, whether at the grain boundaries or within the bulk interior of the grains, was of particular interest, as this will determine the effectiveness of strengthening the U506 alloy via these heat treatment procedures.

8.1.3 Plate Impact Experiments

Plate impact experiments were performed on the U506 specimens using Al 5083-H116 flyer plates. This material is the same as that described in Chapter 5. The sound speeds and elastic constants were similar enough that spalling would occur near the mid-plane of the sample (as in symmetric plate impact experiments) using the setup shown in Figure 29. The experiments were performed at an impact velocity near 430 m/s (approximately 3 GPa) for three specimens corresponding to different degrees of heat treatment. The three specimens include:

1. As-received extruded Al-9wt.% Mg (U506)

2. Solution treated U506 (heat treatment at 430°C for 4 h followed by 480°C for 1 h)

3. Precipitation hardened U506 (solution treated followed by age hardening at 150°C for 200 h)

The reason for the particular heat treatment schedules chosen for the plate impact specimens will be reported and discussed in the following section. The results of the plate impact tests will show the spall properties for a microstructure devoid of precipitates and a microstructure at the peak aged condition compared to the standard extruded plate.

The density (ρ) of U506 was measured as 2.616 ± 0.003 g/cm^3 regardless of heat treatment condition. The sound speeds (C) of each sample type were measured for calculation of the spall strength, HEL, and elastic constants. Table 9 lists the longitudinal wave speed, shear wave speed, bulk wave speed, shear modulus, bulk modulus, elastic modulus, and Poisson's ratio (C_L, C_S, C_B, G, B, E, and ν respectively) for each of the three impacted samples.

Table 9: Material properties of an Al-9wt.% Mg alloy (U506) as a function of heat treatment condition. Solution treatment consisted of a dual solution heat treatment at 430°C for 4 h followed by 480°C for 1 h. Age hardening was performed at 150°C for 200 h. The error represents a 95% confidence interval in all cases.

	As-Received	**Solution Treated**	**Precipitation Hardened**
$\boldsymbol{C_L}$ **[mm/**$\boldsymbol{\mu}$**s]**	6.31 ± 0.02	6.32 ± 0.02	6.27 ± 0.01
$\boldsymbol{C_S}$ **[mm/**$\boldsymbol{\mu}$**s]**	3.18 ± 0.01	3.26 ± 0.01	3.08 ± 0.01
$\boldsymbol{C_B}$ **[mm/**$\boldsymbol{\mu}$**s]**	5.13 ± 0.04	5.08 ± 0.04	5.16 ± 0.03
$\boldsymbol{G}$ **[GPa]**	26.5 ± 0.3	27.9 ± 0.3	24.8 ± 0.2
$\boldsymbol{B}$ **[GPa]**	69 ± 1	67 ± 1	70 ± 1
$\boldsymbol{E}$ **[GPa]**	70 ± 1	73 ± 9	66 ± 9
$\boldsymbol{\nu}$	0.33 ± 0.01	0.32 ± 0.01	0.34 ± 0.01

8.2 Results

8.2.1 Solution Treatment

The Al-9wt.% Mg samples were first solution treated for up to 24 h at 430°C, which is well within the single phase field for this composition (see Figure 1). The progression in the aluminum microstructure with time at the solution treatment temperature can be

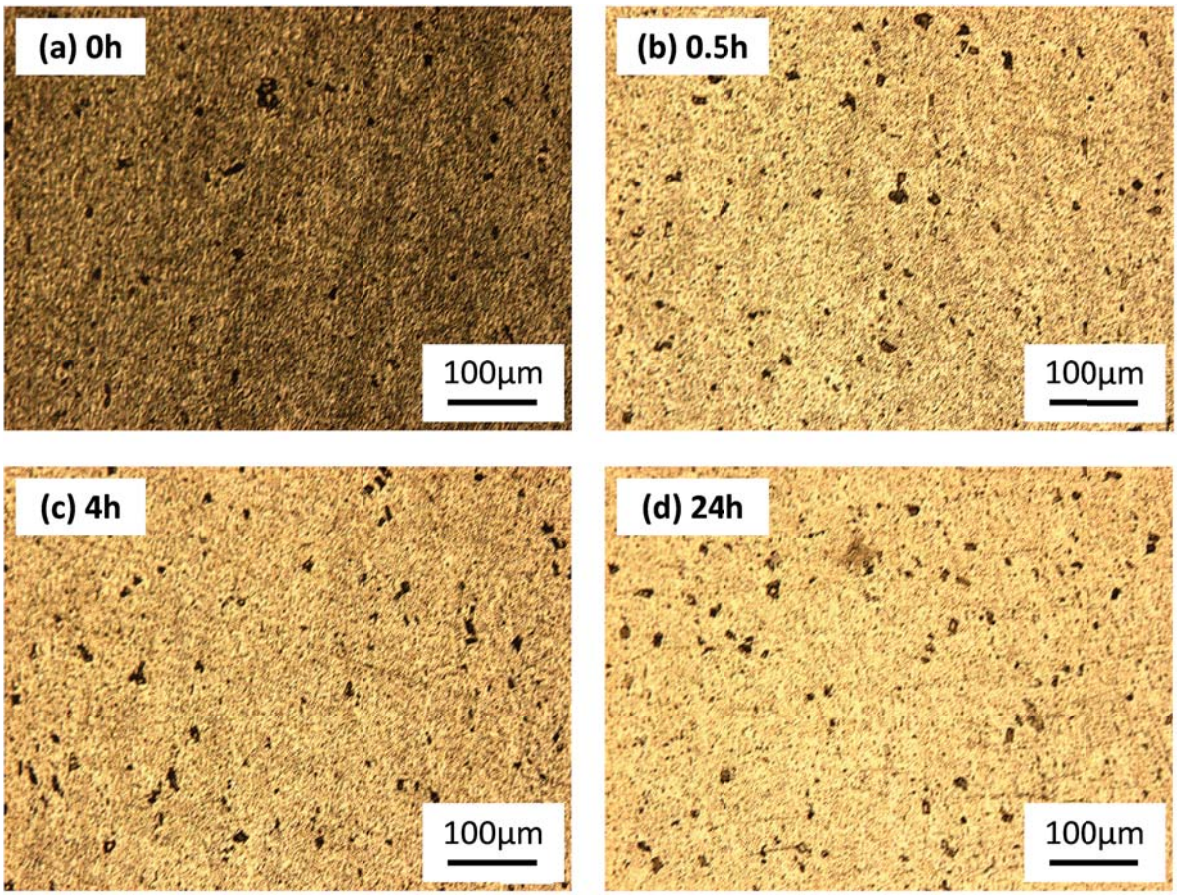

Figure 58: Optical micrographs of an Al-9wt.% Mg alloy during solution heat treatment at 430°C for (a)0 h, (b) 0.5 h, (c) 4 h, and (d)24 h. The samples were etched with Keller's reagent to reveal secondary phases.

seen in Figure 58. The samples were etched with Keller's reagent to selectively remove secondary phases within the material. As Figure 58(a) shows, the initial microstructure appears dark due to the large degree of β phase precipitates removed during etching. As solution treatment progresses, the micrographs lighten dramatically as the precipitates go back into solution in the matrix phase. After solution treatment for 24 h, additional heat treatment results in little change to the microstructure. There are still precipitates visible in the microstructure even after 24 h of heat treatment. Therefore, the single solution treatment does not yield a clean microstructure suitable for age hardening.

A dual solution heat treatment was also performed at 430°C for 4 h followed by 480°C for 1 h. The microstructure after the first stage of heat treatment is shown in Figure 59(a), and the microstructure after the second stage of heat treatment is shown in Figure 59(b). The

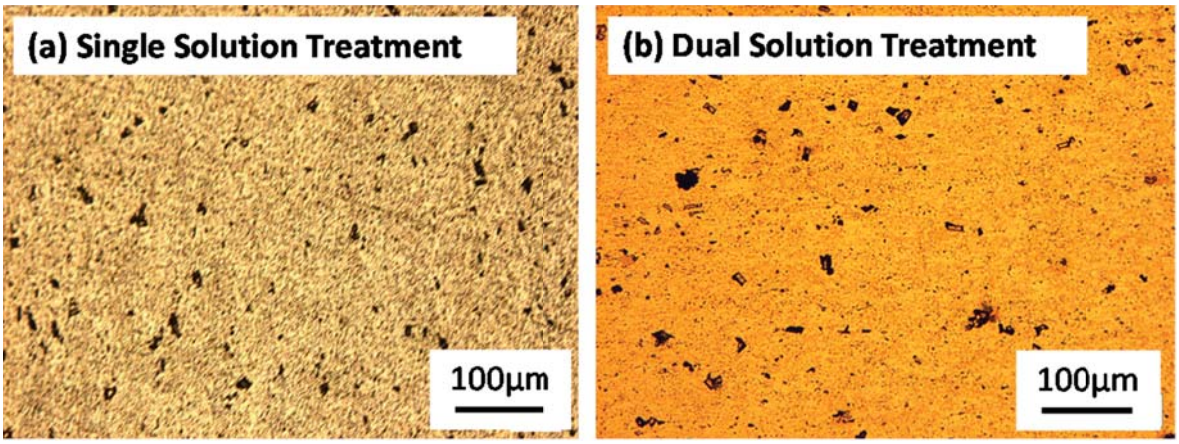

Figure 59: Optical micrographs comparing the extent of secondary phases remaining in an Al-9wt.% Mg alloy after (a) a single solution heat treatment at 430°C for 24 h and (b) a dual solution heat treatment at 430°C for 4 h followed by 480°C for 1 h. The samples were etched with Keller's reagent to reveal secondary phases.

dual solution treatment results in a cleaner microstructure than a single solution treatment at lower temperature. The microstructure of the sample from this two-stage treatment, shown in Figure 59(b), is cleaner than the 24 h single solution treatment, shown in Figure 58(d). Therefore, a dual heat treatment is more effective at solutionizing the precipitates in the microstructure of U506.

The grain structure after the dual solution heat treatment is shown in Figure 60. When compared to the as-received material shown in Figure 57, there is a larger degree of recrystallized grains with few of the original high angle grain boundaries visible in the micrograph. Therefore, the dual solution treatment necessary to remove the precipitate phase, also affects the initial grain structure.

8.2.2 Age Hardening

The microstructure shown in Figure 58(d) for single solution treatment for 24 h and the microstructure shown in Figure 59(b) for dual solution treatment were used as the starting microstructures for age hardening. After solution treatment, the Al-9wt.% Mg alloy was age hardened at 150, 200, and 250°C for times up to 200 h. The β phase is a stable precipitate phase at these temperatures, as seen in Figure 1. The precipitate microstructure as a function of aging time at each of these temperatures is shown in Figures 61–63 for aging

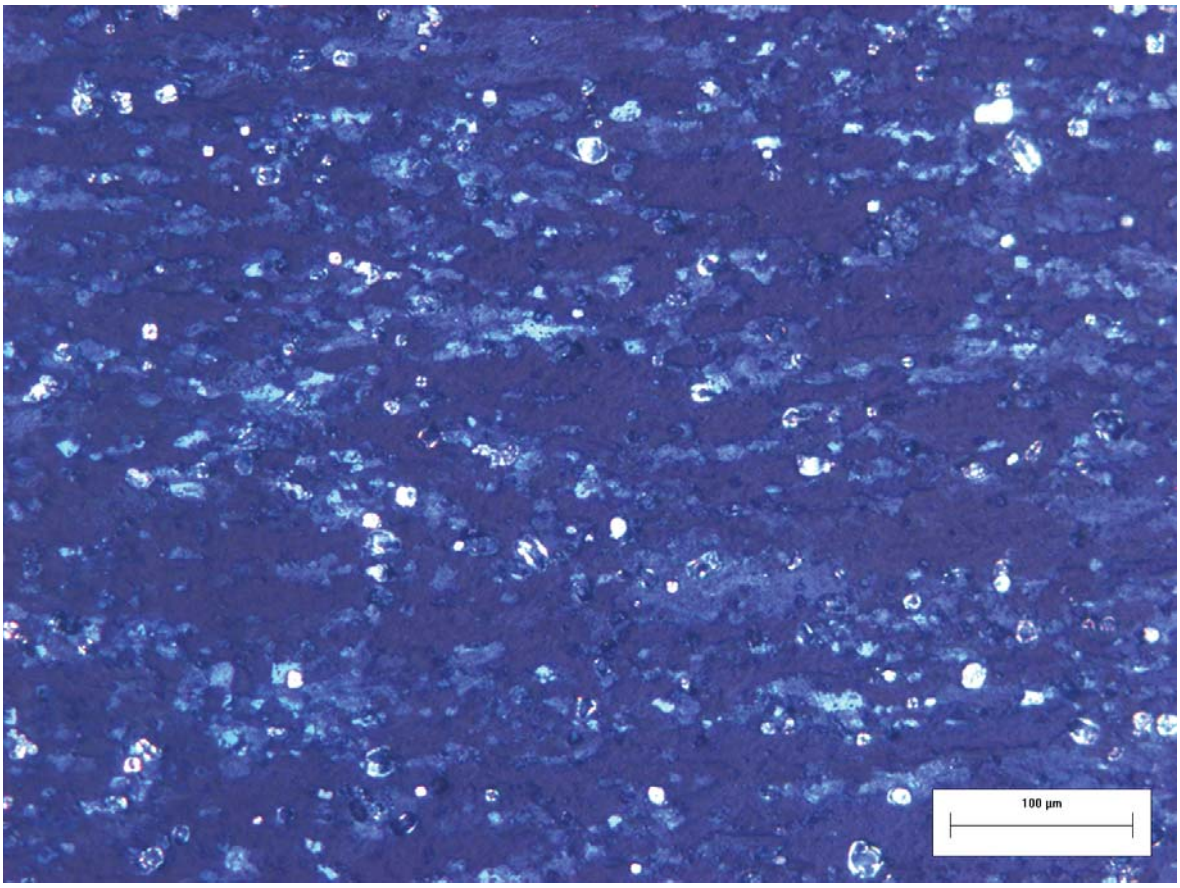

Figure 60: Optical micrographs showing the grain structure of an Al-9wt.% Mg alloy after a dual solution heat treatment at 430°C for 4 h followed by 480°C for 1 h. The samples were anodized using the Barker's etchant to reveal grain structure.

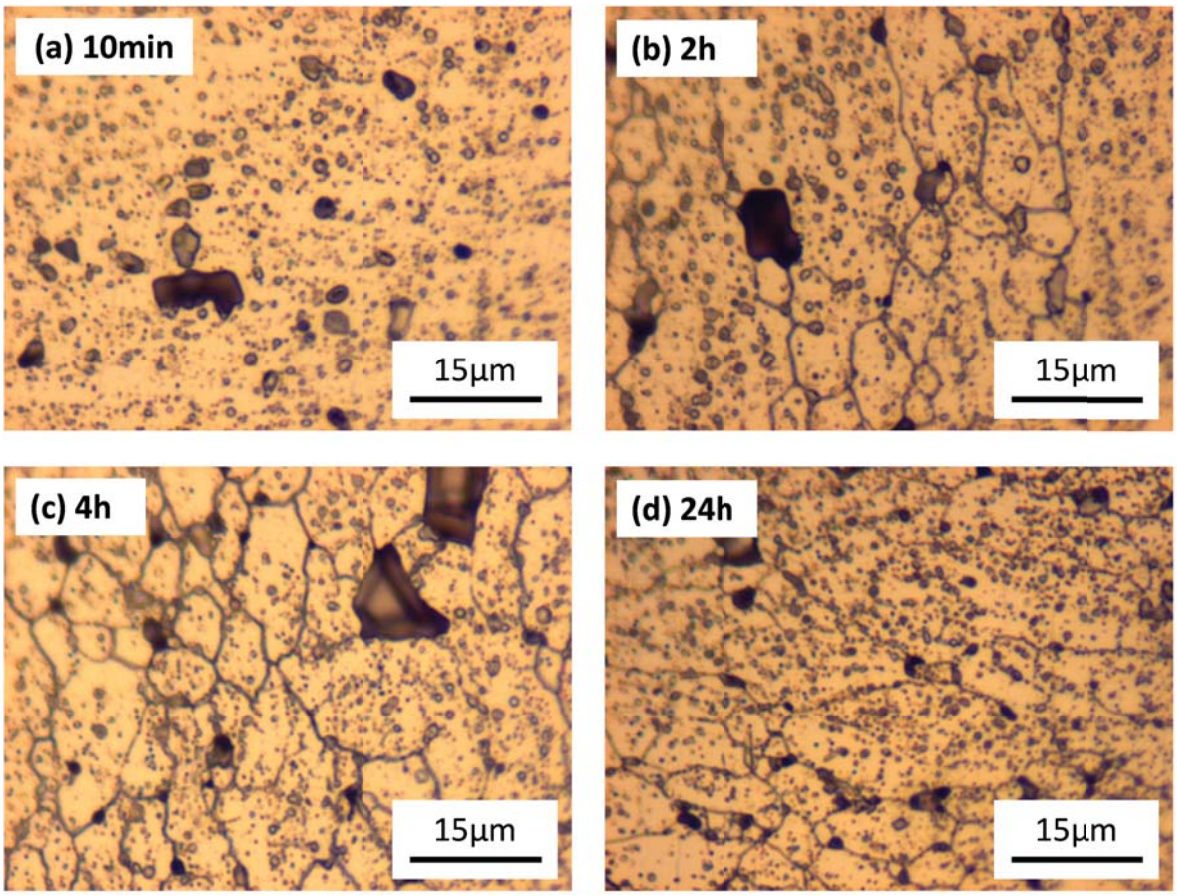

Figure 61: Optical micrographs of an Al-9wt.% Mg alloy during age hardening at 150°C for (a)10 min, (b) 2 h, (c) 4 h, and (d)24 h after a single solution heat treatment at 430°C for 24 h. The samples were etched with Keller's reagent to reveal secondary phases.

after the single solution treatment and Figures 64–66 for aging after the dual solution treatment respectively.

As shown in Figures 61–63, after the single solution heat treatment schedule, the precipitates initially form at the grain boundaries, making the grain structure visible after etching. As the aging time increases, the precipitates begin to form within the grain interiors, yielding a more uniform microstructure. Eventually, the precipitate volume fraction becomes large enough to make the images appear uniformly dark after etching. The progression from precipitation at grain boundaries to the uniform dispersion of precipitates occurs faster with higher temperature with grains disappearing after 24 h, 4 h, and 2 h of aging at 150°C, 200°C, and 250°C respectively.

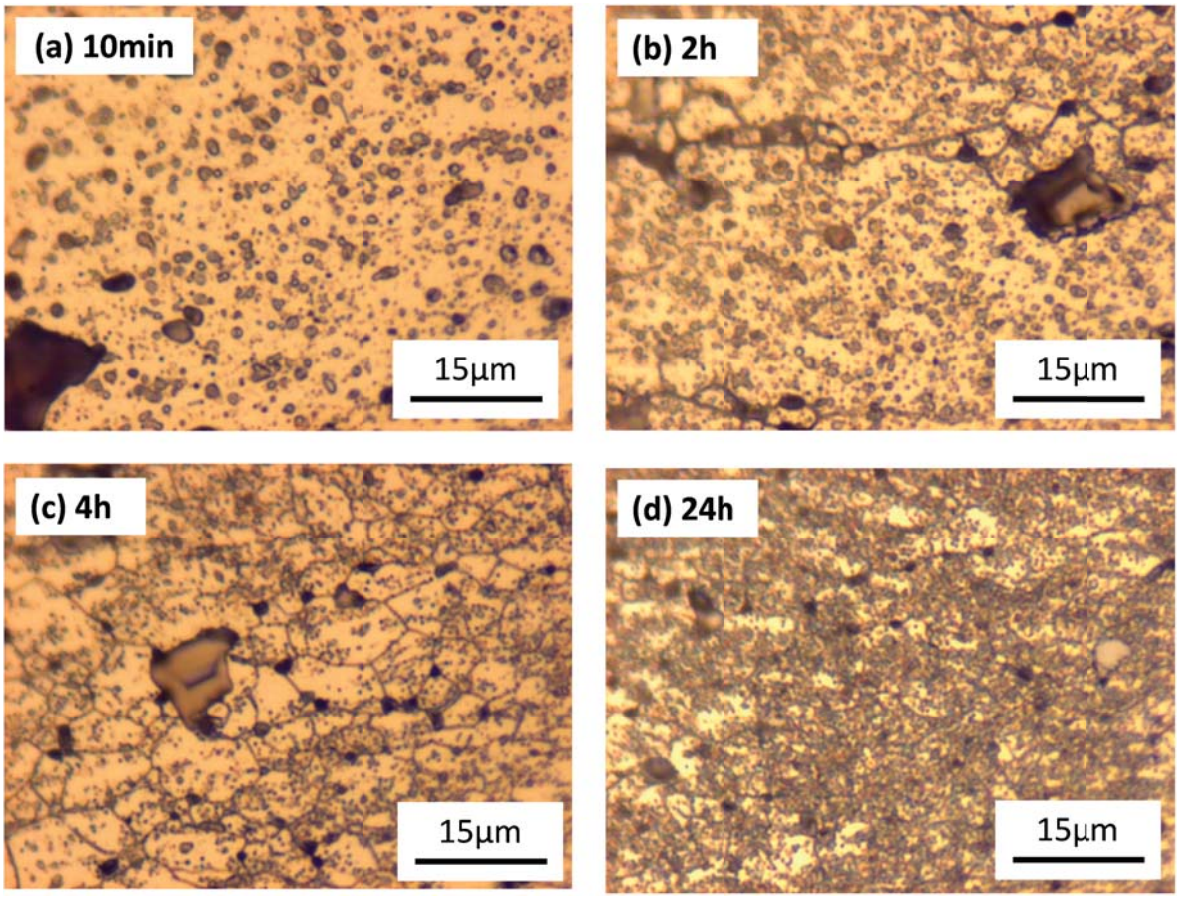

Figure 62: Optical micrographs of an Al-9wt.% Mg alloy during age hardening at 200°C for (a)10 min, (b) 2 h, (c) 4 h, and (d)24 h after a single solution heat treatment at 430°C for 24 h. The samples were etched with Keller's reagent to reveal secondary phases.

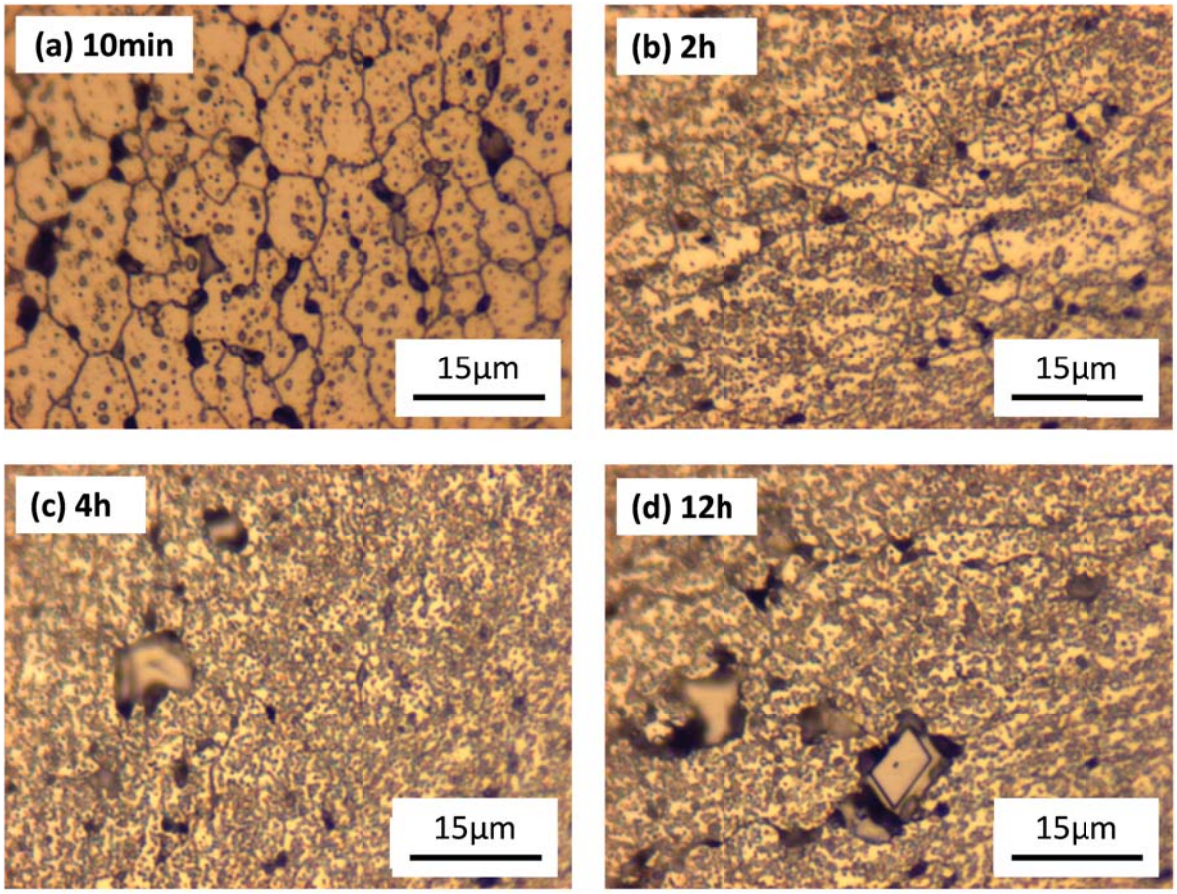

Figure 63: Optical micrographs of an Al-9wt.% Mg alloy during age hardening at 250°C for (a)10 min, (b) 2 h, (c) 4 h, and (d)12 h after a single solution heat treatment at 430°C for 24 h. The samples were etched with Keller's reagent to reveal secondary phases.

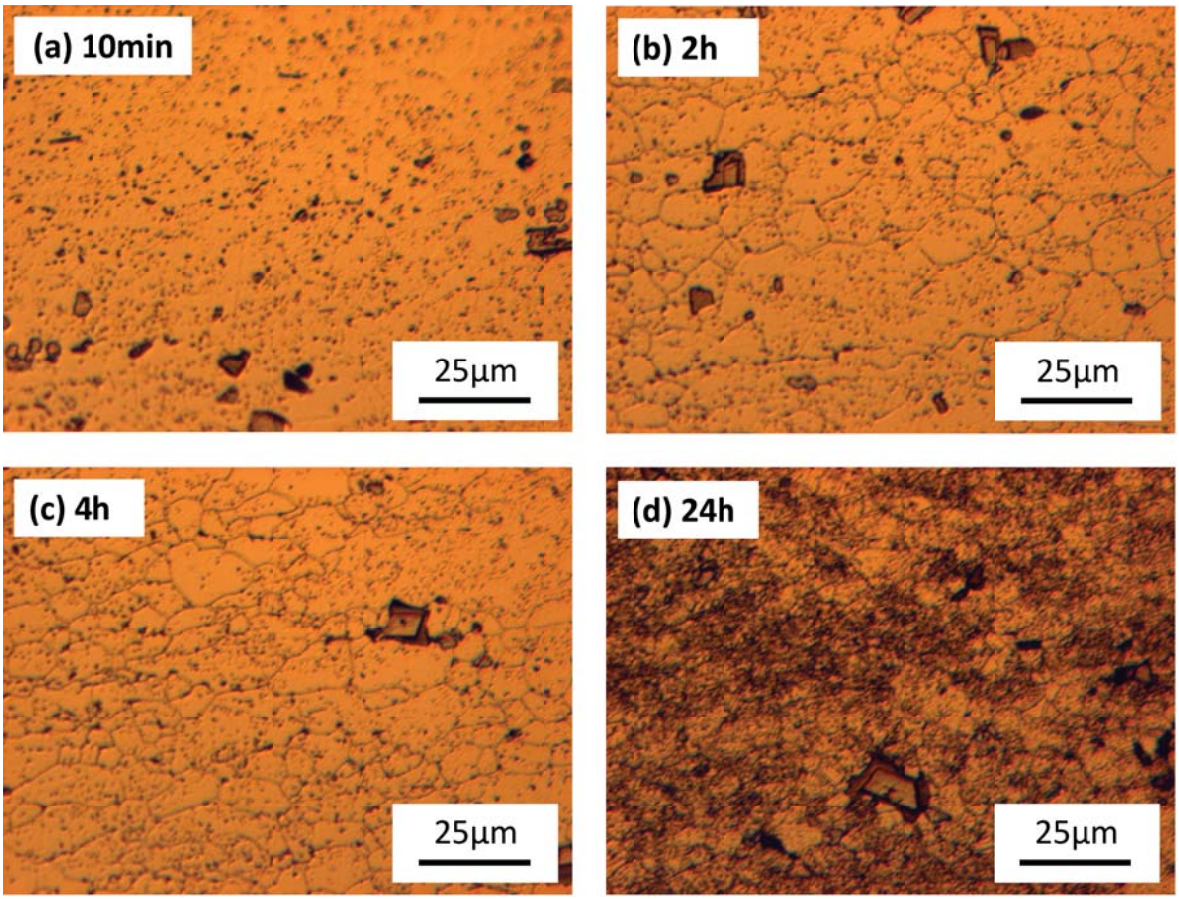

Figure 64: Optical micrographs of an Al-9wt.% Mg alloy during age hardening at 150°C for (a)10 min, (b) 2 h, (c) 4 h, and (d)24 h after a dual solution heat treatment at 430°C for 4 h followed by 480°C for 1 h. The samples were etched with Keller's reagent to reveal secondary phases.

As shown in Figures 64–66, after the dual solution heat treatment schedule, the precipitates also form at the grain boundaries for the earliest aging times; however, the progression from grain boundary precipitation to precipitation within the grain interior occurs more quickly than after the single solution heat treatment. The grain structure is no longer visible after 4 h and 10 min of aging at 150°C and 200°C respectively, and is not visible for any of the aging times sampled for precipitation hardening at 250°C.

The difference in the precipitation behavior for the single solution treatment versus the dual solution treatment is most likely due to a large degree of solute segregation at the grain boundaries in the as-received material. The single solution treatment is not as effective at reducing this solute segregation as the dual solution treatment. This is evidenced by the

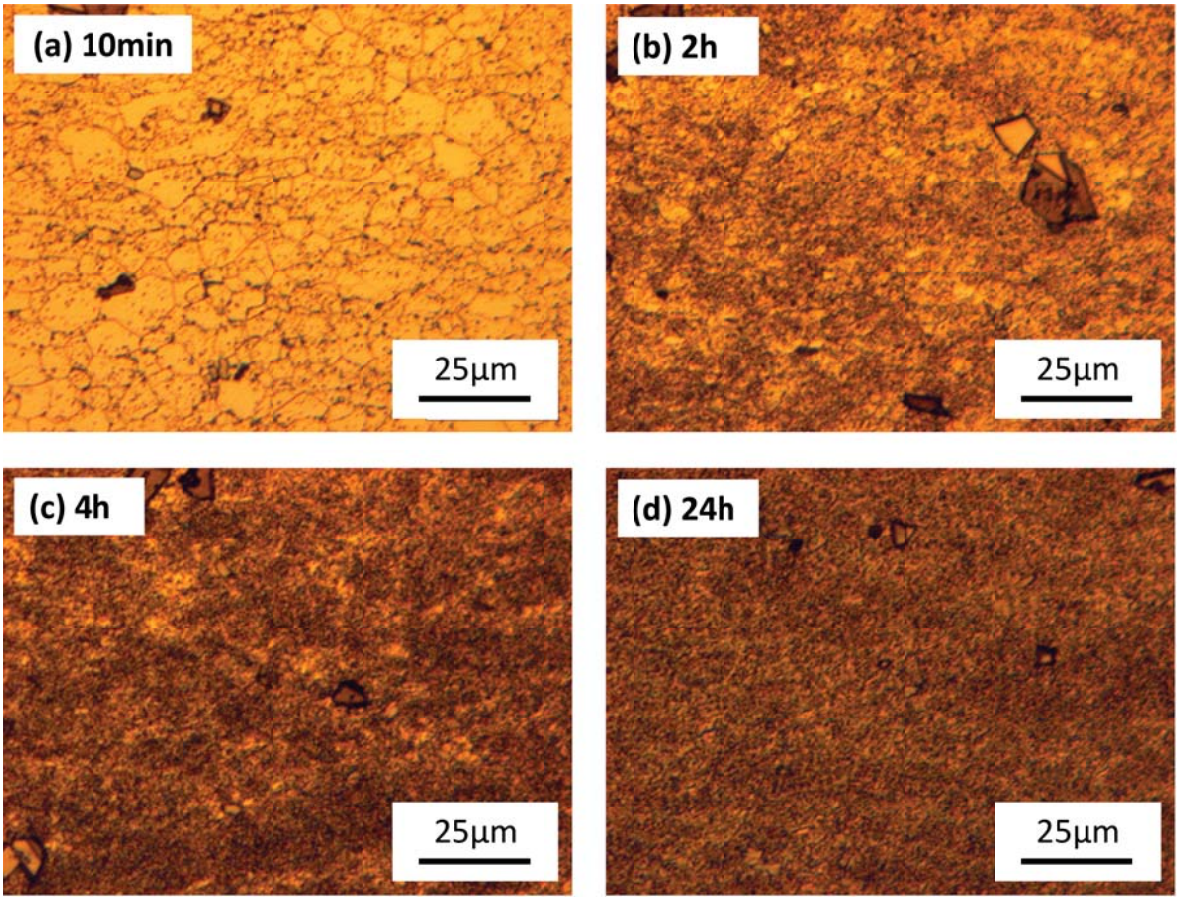

Figure 65: Optical micrographs of an Al-9wt.% Mg alloy during age hardening at 200°C for (a)10 min, (b) 2 h, (c) 4 h, and (d)24 h after a dual solution heat treatment at 430°C for 4 h followed by 480°C for 1 h. The samples were etched with Keller's reagent to reveal secondary phases.

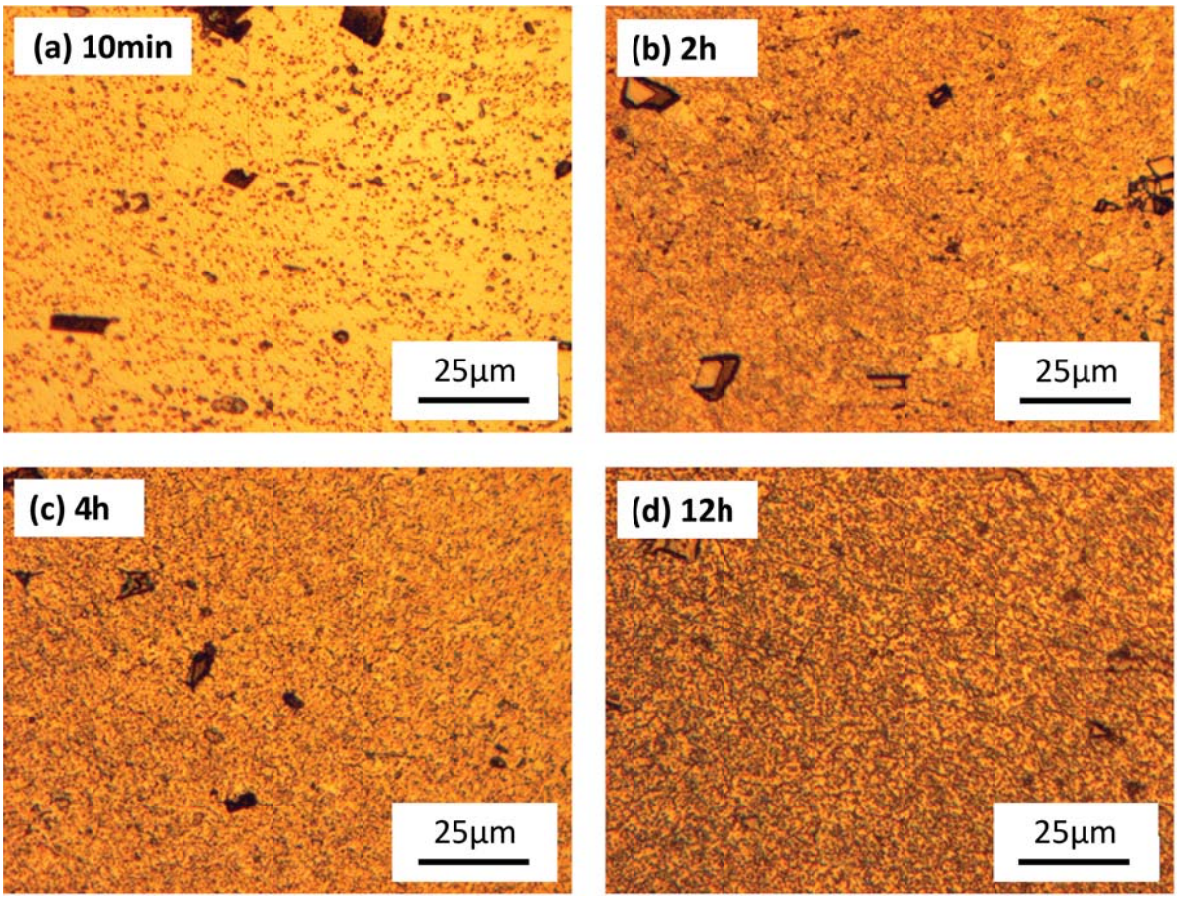

Figure 66: Optical micrographs of an Al-9wt.% Mg alloy during age hardening at 250°C for (a)10 min, (b) 2 h, (c) 4 h, and (d)12 h after a dual solution heat treatment at 430°C for 4 h followed by 480°C for 1 h. The samples were etched with Keller's reagent to reveal secondary phases.

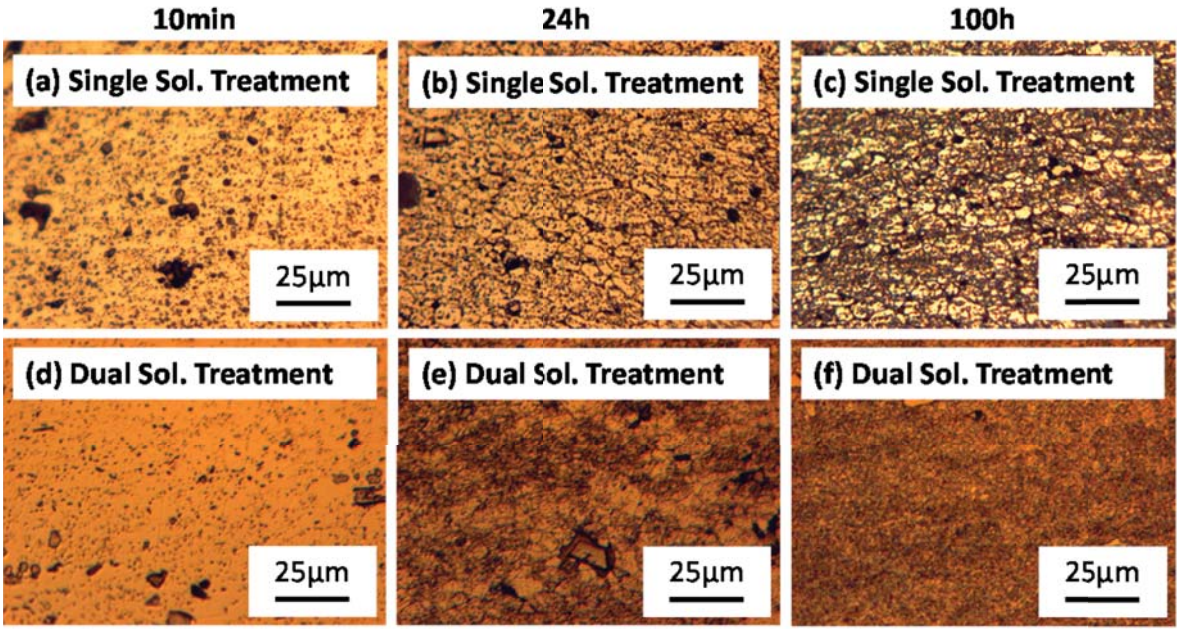

Figure 67: Optical micrographs of an Al-9wt.% Mg alloy during age hardening at 150°C for (a)and (d) 10 min, (b) and (e) 2 h, and (c) and (f) 4 h. Images (a)–(c) show the microstructure for aging after a single solution heat treatment at 430°C for 24 h, and images (d)–(f) show the microstructure for aging after a dual solution heat treatment at 430°C for 4 h followed by 480°C for 1 h. The samples were etched with Keller's reagent to reveal secondary phases.

fact that precipitation occurs preferentially at grain boundaries for longer periods of time for the single heat treatment schedule. Figure 67 shows the precipitation sequence after aging at 150°C for 10 min, 24 h, and 100 h. Figures 67(a)–67(c) show the microstructure after the single solution treatment only, and Figures 67(d)–67(f) show the microstructure after the dual solution treatment. At any given aging time, the dual solution treatment results in a larger degree of bulk precipitation versus grain boundary precipitation than the single solution treatment. Thus, it is expected that age hardening after the dual solution treatment will result in increased strength when compared to aging after a single solution treatment.

The effects of aging treatment on the Vickers microhardness of the Al-9wt.% Mg alloy are shown in Figure 68 and Figure 69 for samples given a single and dual solution heat treatment, respectively. For aging after the single solution treatment, some strengthening is evidenced for each aging temperature with a great deal of scatter in the data with aging

time. The precipitation kinetics are fastest for aging at 250°C as the peak in hardness is reached between 2 to 4 h. Further aging at this temperature results in an overaged system and decreasing hardness with aging time. It is possible the peak hardness has just been reached for the longest aging times at 200°C, but the hardness is still increasing for aging at 150°C even after 200 h. The hardness peaks are reached at longer times at the lower temperatures due to slower precipitation kinetics; however, the peak values increase due to an expected higher precipitate volume fraction. The highest measured hardness was 137 HV for aging at 150°C following a single solution heat treatment. This hardness increase can be compared to the solution treated sample's hardness of 117 HV. The hardness never reached the peak value for aging at 150°C, so the material could potentially be strengthened to a higher degree by aging at this temperature for longer times.

In contrast to the data shown in Figure 68, the hardness data shown in Figure 69 for aging after the dual solution heat treatment shows much cleaner trends with time. The hardness reaches a peak value after 2 h for aging at both 250°C and 200°C, which is faster than for the single solution treatment. The peak in hardness may have been reached for age hardening at 150°C after 200 h, as the data has just begun to level off. The maximum hardness values are 150 HV, 135 HV, and 126 HV for age hardening at 150°C, 200°C, and 250°C respectively. The maximum values are similar to those shown in Figure 68 for aging at 200°C and 250°C, but the hardness maximum was not reached even after 200 h at 150°C following a single solution heat treatment. Precipitation hardening after the dual solution heat treatment thus results in a faster rise to the peak in hardness, allowing for strengthening to be imparted to the U506 material after a more practical time frame.

8.2.3 Results of Plate Impact Experiments

Plate impact experiments were performed on the as-received U506 plate, a solution treated sample, and a precipitation hardened sample. The solution treated sample was given a dual solution heat treatment, as this resulted in the least amount of solute segregation and a better microstructure after aging. The precipitation hardened sample was given the dual aging treatment followed by aging at 150°C for 200 h. As shown in Figure 69,

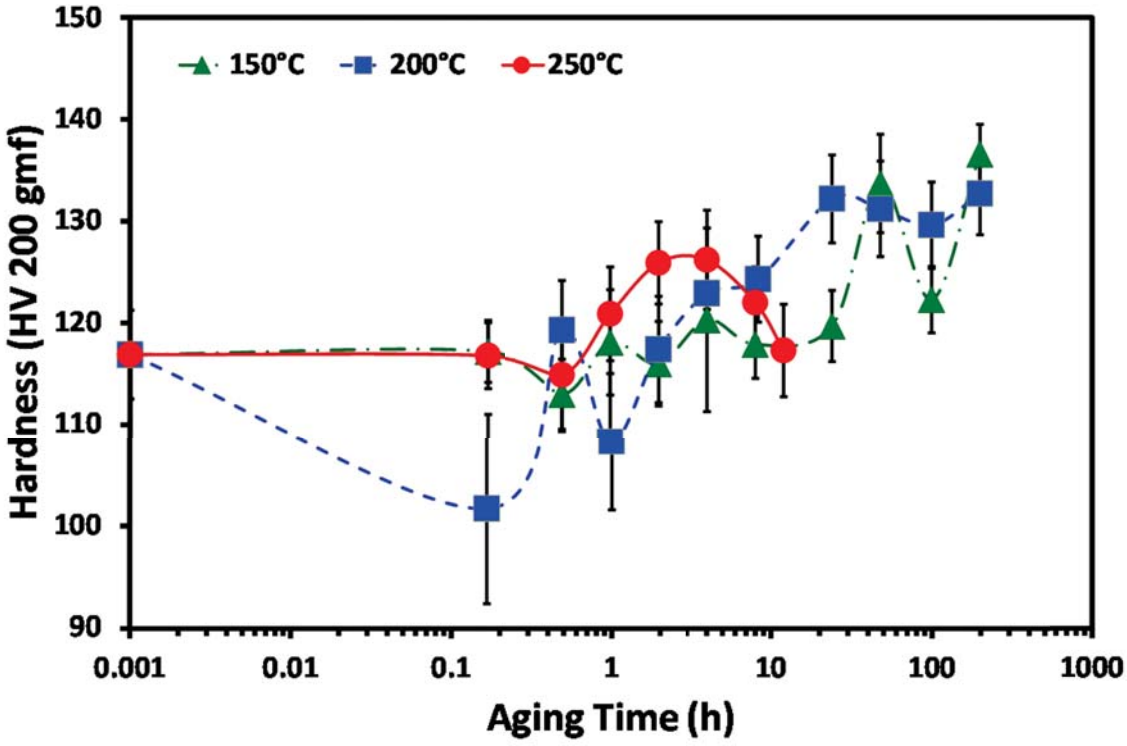

Figure 68: Vickers microhardness data for an age hardened Al-9wt.% Mg alloy after a single solution heat treatment at 430°C for 24 h. Age hardening was performed at 150°C, 200°C, and 250°C. The data points at 0.001 h correspond to the solution treated sample.

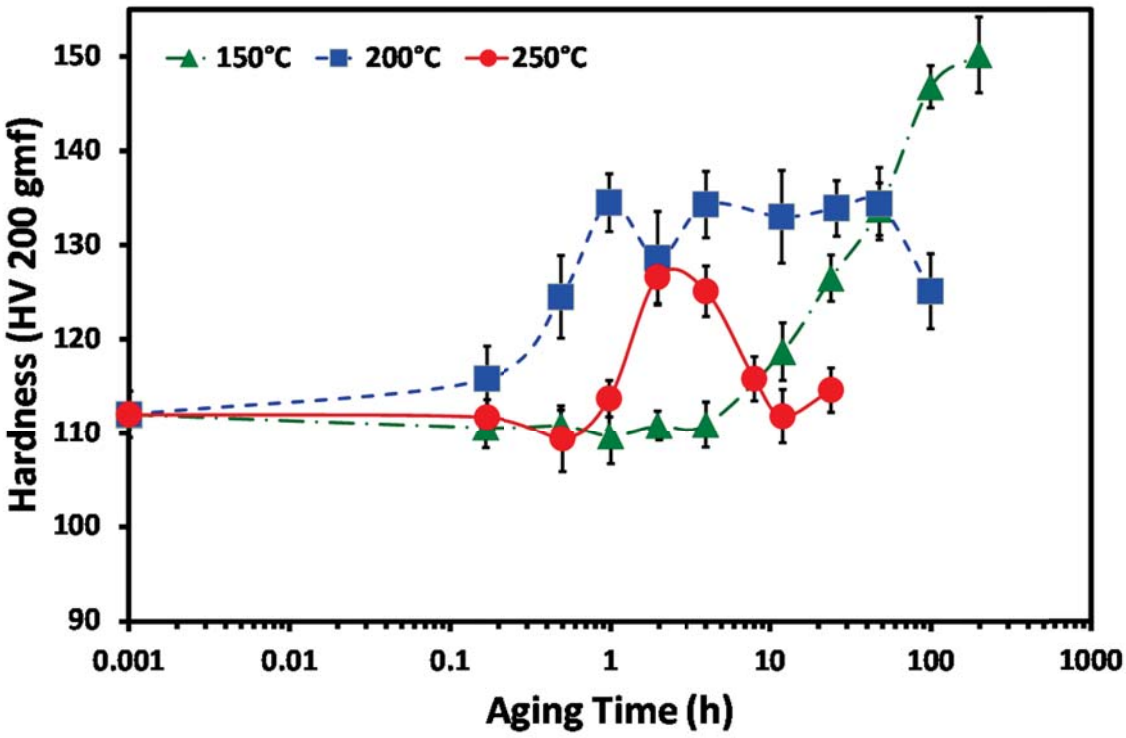

Figure 69: Vickers microhardness data for an age hardened Al-9wt.% Mg alloy after a dual solution heat treatment at 430°C for 4 h followed by 480°C for 1 h. Age hardening was performed at 150°C, 200°C, and 250°C. The data points at 0.001 h correspond to the solution treated sample.

this sample displayed significant strengthening under quasi-static testing conditions. Plate impact testing was then used to determine what effect precipitation hardening has on U506 under dynamic testing conditions.

Table 10 lists the measured parameters for each experiment. The impact velocity (V_{impact}) was measured using velocity pins, as shown in Figure 29. The free surface velocities at the peak state (u_{peak}) and the HEL (u_{HEL}) along with the pullback velocity (Δu_{fs}) were measured from the free surface velocity profiles, as shown in Figure 13. The shock wave velocity (U_S) was measured using the impact timing and shock wave arrival time visible in the free surface velocity profiles. The HEL stress (σ_{HEL}), spall strength (σ_{spall}), and peak stress (σ_{peak}) were calculated using Equations 5–8, with the spall strength correction factor (δ) calculated using Equation 7.

8.2.3.1 Free Surface Velocity

The VISAR free surface velocity traces for the three U506 samples are shown in Figure 70. The inset clearly shows that precipitation hardening dramatically increases the HEL above that of the solution treated sample. The precipitation hardened sample also displays a larger HEL than the as-received plate. The as-received and solution treated specimens display upper and lower yielding, similar to the equiaxed grain structure, discussed in Chapter 7. It is expected that solution treatment would remove significant dislocation density, similar to that in the annealed microstructure presented in Chapter 7, whereby the upper yield point is associated with the stress necessary to nucleate dislocations. As shown in Figure 57, the as-received sample is partially recrystallized. The dislocation density removed during recrystallization can account for the slight upper and lower yielding displayed by the as-received specimen. The upper HEL value for both of these specimens is similar to the HEL of the precipitation hardened specimen. The precipitate microstructure most likely inhibits deformation such that new dislocation nucleation is not sufficient to result in decreasing elastic stress at the HEL.

The data for the U506 specimens is similar to that for the equiaxed specimens in that there are multiple peaks in the data during the release from the peak velocity and during

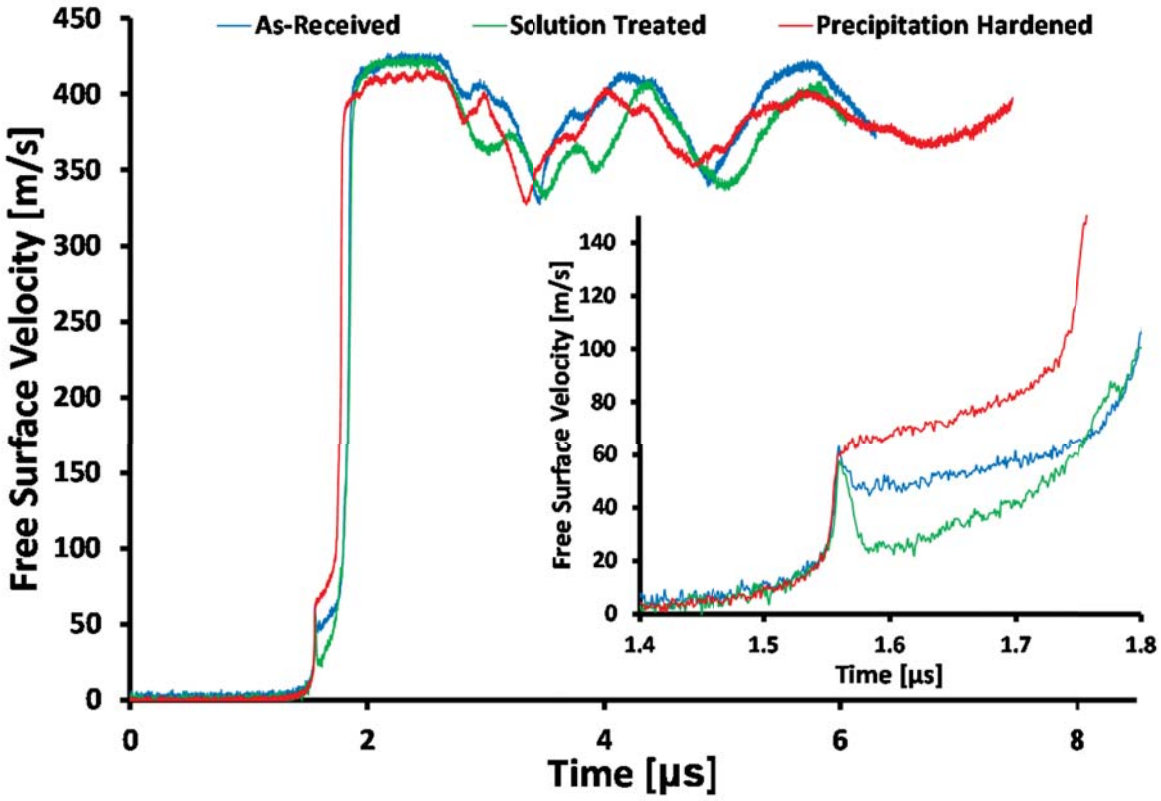

Figure 70: Rear free surface velocity data as a function of heat treatment condition for Al-9wt.% Mg samples impacted near 430 m/s. Solution treatment consisted of a dual solution heat treatment at 430°C for 4 h followed by 480°C for 1 h. Age hardening was performed at 150°C for 200 h. The inset better displays the HEL for each data set.

the recompression after pullback. These features are present for all three samples, indicating that the phenomenon is due to the alloy itself rather than the extent of precipitation hardening resultant from the heat treatments used. This phenomenon is again observed concurrently with precursor decay, which is further evidence that these two features may be correlated.

The pullback velocity is largest for the as-received plate, resulting in the as-received plate having higher spall strength than the solution heat treated and precipitation hardened samples. The spall strength and HEL will be quantified and discussed in the next section.

8.2.3.2 Spall Strength and HEL

The spall strength (σ_{spall}) and HEL (σ_{HEL}) values were calculated using the free surface velocity data shown in Figure 70 along with Equations 5–7. The free surface velocity data

used in Equations 5–7 is listed in Table 10. The calculated values of spall strength and HEL are shown for impact through the plate thickness in Figure 71.

Table 10: Calculated and measured free surface velocity data for an Al-9wt.% Mg alloy (U506) as a function of heat treatment condition. The different sample types are the as-received (AR) extruded plate, the solution treated (ST) sample, and the precipitation hardened (PPT) sample. Solution treatment consisted of a dual solution heat treatment at 430°C for 4 h followed by 480°C for 1 h. Age hardening was performed at 150°C for 200 h.

Shot Number	V_{impact} [m/s]	u_{peak} [m/s]	U_S [km/s]	σ_{Peak} [GPa]	u_{HEL} [m/s]	σ_{HEL} [GPa]	Δu_{fs} [m/s]	δ [m/s]	σ_{Spall} [GPa]
1333 AR	431	428	5.33	3.04	47.7	0.39	100.7	28.2	0.87
1331 ST	426	425	5.31	2.98	25.1	0.21	94.7	15.6	0.73
1324 PPT	422	416	5.46	3.04	63.4	0.52	89.6	17.8	0.72

Figure 71 shows that the precipitation hardened sample displays the highest HEL of 0.52 GPa. This is followed by the as-received sample and the solution treated sample with values of 0.39 GPa and 0.21 GPa respectively. Precipitation hardening is therefore effective at increasing the yield resistance under dynamic loading conditions. Strain hardening via extrusion is also effective at increasing yield resistance, but to a lesser extent than the precipitation hardened sample. The lower HEL value for the solution treated specimen (0.21 GPa) matches well with the DeBroglie limited value of the HEL calculated using Equation 28. This limiting value is 0.18 GPa for this alloy.

The spall strength displays a different trend with processing. The as-received sample displays the highest spall strength at 0.87 GPa, whereas both the solution treated sample and the precipitation hardened sample display essentially identical spall strength values of 0.73 GPa and 0.72 GPa respectively. Hence, precipitation hardening appears to have no effect whatsoever on the spall strength, as the spall strength is the same as the sample completely devoid of precipitates. It is likely that changes to the grain structure during solution treatment decrease the spall strength for both the solution treated and precipitation hardened specimens. As seen in Figures 57 and 60, the grain structure displays significantly more recrystallization after solution treatment. The formation of new high angle grain boundaries could result in additional spall nucleation sites. In addition, the reduction in

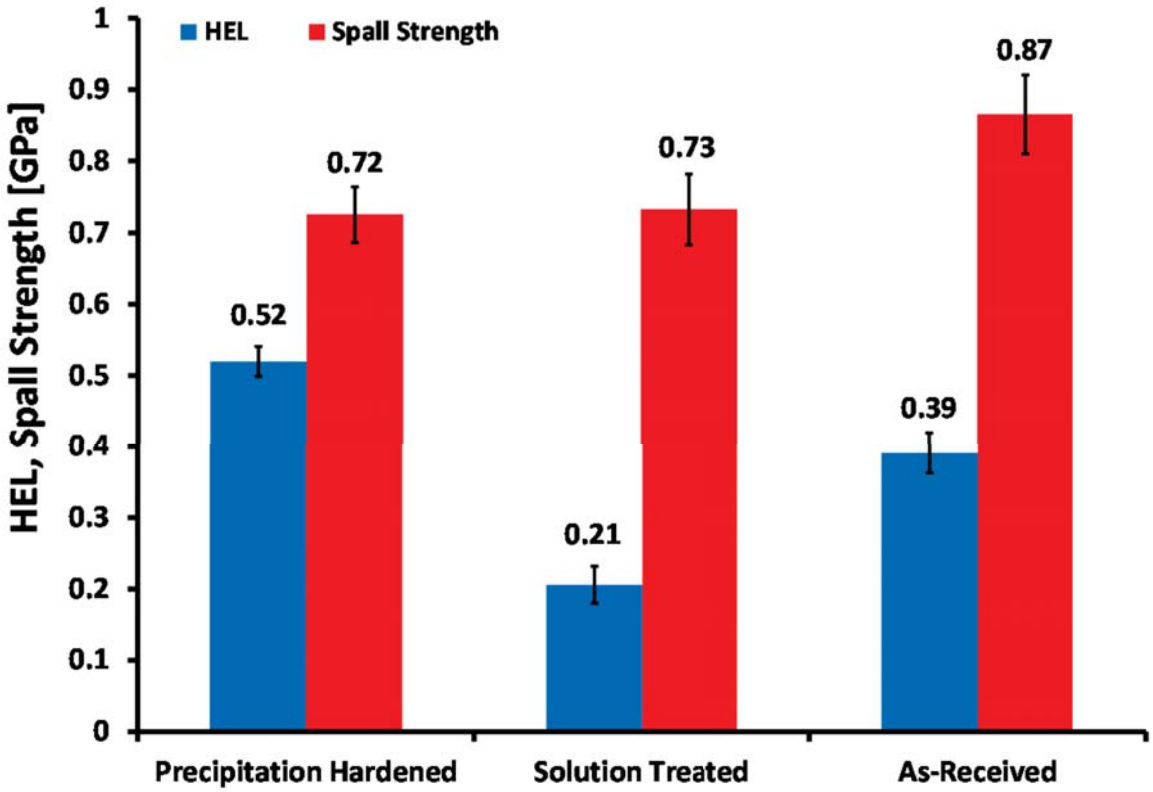

Figure 71: Calculated spall strength and HEL data as a function of heat treatment condition for Al-9wt.% Mg samples impacted near 430 m/s. Solution treatment consisted of a dual solution heat treatment at 430°C for 4 h followed by 480°C for 1 h. Age hardening was performed at 150°C for 200 h.

dislocation density during heat treatment could result in easier void growth during spallation. Strain hardening via extrusion, thus appears to be a better strengthening mechanism than precipitation hardening for U506, as it displays both a moderately high HEL value, without the loss of the spall strength caused by heat treatments.

8.3 Conclusions

An Al-9wt.% Mg alloy with trace additions of silver was found to be precipitation hardenable when heat treated properly. The high magnesium content resulted in a large amount of solute segregated at the grain boundaries in the initial microstructure. In order to properly solutionize the microstructure, a two-step heat treatment method was used with a slow ramp up rate to the second higher temperature. Age hardening at 150°C, 200°C, and 250°C was more effective after the dual solution heat treatment when compared to aging

after a single solution heat treatment at the same temperatures. Aging after the dual solution treatment resulted in precipitation within the bulk interior of grains, rather than at the grain boundaries, over a wider period of time than for the single heat treatment. This in turn resulted in a faster rise to the peak in hardness for samples aged after the dual solution treatment.

Three specimens were tested using plate impact experiments—the as-received plate, a dual solution heat treated sample, and a precipitation hardened sample. Precipitation hardening resulted in the largest value of the HEL at 0.52 GPa, indicating that precipitation hardened Al-Mg alloys would yield better penetration resistant armor plates. However, the as-received plate displayed the largest spall strength value of 0.87 GPa, as compared to identically low values of the spall strength (0.73 GPa and 0.72 GPa) for both the solution treated and precipitation hardened samples. The results indicate that precipitate strengthening has no effect on the spall strength of Al-Mg alloys; however, the spall strength is larger for the strain hardened as-received plate in comparison to heat treated samples. Strain hardening thus appears to be a superior strengthening mechanism for Al-Mg alloys to yield blast resistant armor plates.

CHAPTER 9

ONE-DIMENSIONAL NUMERICAL MODELING OF THE SPALL RESPONSE OF AL 5083

This chapter will discuss the use of one-dimensional (1-D) simulations to model the spall response of Al 5083 as a function of the microstructural state. The simulated data will be compared to experimentally obtained free surface velocity profiles obtained from plate impact experiments presented in the preceding chapters. Dynamic fracture was modeled using the Cochran and Banner [107] spall model, which uses a damage parameter related to the void size distribution prior to coalescence. The damage length scale will be related to the size of the grains and inclusions for each of the differently processed Al 5083 samples (rolled plate, processed with ECAP, and annealed). The results will show which microstructural feature (grains or inclusions) is most responsible for void formation during spalling.

9.1 Procedure

Simulations were performed to fit the experimental free surface velocity data for plate impact using three Al 5083 sample types. The three sample types were a rolled Al 5083-H116 plate, Al 5083 processed using ECAP (without post-ECAP rolling), and Al 5083 with an equiaxed grain structure. Detailed descriptions of these three specimen types along with the results of plate impact experiments are presented in Chapters 5–7.

9.1.1 Plate Impact Experiments

All experimental plate impact results are for impact through the plate thickness using 5 mm thick flyer plates and 10 mm thick target samples. Experimental impact data for Al 5083-H116 was used to fit the equation of state (EOS) over a wide range of impact velocities and their corresponding peak stresses. Impact was performed near 200 m/s, 430 m/s, 670 m/s, and 830 m/s for a peak stress range of 1.5–6.2 GPa. Comparisons of the spall response of each microstructure were made for a similar impact velocity of 430 m/s and a peak stress

near 3 GPa. The plate impact experiment data is mentioned in greater detail in Chapters 5–7 for each individual Al 5083 sample type.

9.1.2 One-Dimensional Simulations

One-dimensional (1-D) simulations of the plate impact tests were performed using the Shock-1D program [116], which is a Lagrangian finite element code. A mesh size of 2 μm was used for each simulation, and the velocity at the sample rear free surface was recorded for every picosecond at the node closest to the rear surface. The simulated rear free surface velocity was fit to the experimental free surface velocity measured by the VISAR system during plate impact experiments.

A set of simulations was first performed to fit the peak state (mean stress value) of the experimental free surface velocity data from Al 5083-H116 plate impact over a wide range of experimental peak stresses. The equation of state (EOS) from this fit was used to simulate the peak states of the other two remaining Al 5083 microstructures for an experimental peak stress near 3 GPa. After a good fit of the peak state was achieved, the spall behavior after the pullback signal was fit for each of the three Al 5083 sample types.

A detailed explanation of the various Shock-1D input parameters is available in Section 3.6. Briefly, the material density (ρ_0), shear modulus (G_0), and bulk modulus (K_0) values obtained from ultrasonic testing, listed in Tables 3, 5, and 7, were used as inputs for each microstructure. The Gruneissen constant for Al 5083 is 1.98 [81]. The remaining polynomial fitting constants (K_2, K_3, and K_4) for the EOS shown in Equation 36 were varied until the simulated peak free surface velocity matched the experimental data over the measured peak stress range. The remaining constants (necessary to calculate the deviatoric stress) are the yield stress (σ_{ys}), hardening constant (H'), and the linear and quadratic artificial viscosity constants. The viscosity constants were kept at the default values of 0.2 and 2 respectively, while the viscoplastic data was estimated using tensile test data available in the literature [120, 121]. The viscoplastic terms were also varied to yield the best fit to the experimental HEL value and shock arrival time observed in the free surface velocity data.

The spall behavior was modeled using the Cochran and Banner [107] spall model, which uses three input parameters—the spall strength, damage parameter, and damage exponent. The damage exponent was kept as 2/3, as this is the expected value for ductile materials [107, 108]. The spall strength was increased from the experimentally measured value so that the simulated free surface velocity could align with the measured free surface velocity after the pullback. The simulated release from the peak velocity from one-dimensional modeling will be steeper than the measured data due to the quasi-elastic release behavior of aluminum. Quasi-elasticitiy is a 2-D effect that cannot be captured using 1-D simulations [93]; therefore, the pullback will occur earlier in time than the measured data for a similar spall strength value using 1-D simulations. Increasing the simulated spall strength results in a larger pullback velocity than the experiment and allows for the re-compression slope after pullback to match the experimental data. The larger simulated spall strength value is not important as the main parameter of interest was the damage size parameter (D_0). D_0 was fit to yield the best match to the experimental data after the pullback signal and was used to make comparisons between the spall response of each microstructure. The grain size and the distribution of brittle phases (inclusions and dispersoids) were quantified and compared to the simulated D_0 value to show which microstructural feature controls the spall behavior of Al 5083.

9.2 Results

Fitting of the experimental Al 5083-H116 plate impact data was performed for impact velocities ranging from 200 m/s to 830 m/s to yield the best fit to the peak state. Fitting of the spall behavior for each Al 5083 microstructure (rolled plate, processed with ECAP, and equiaxed microstructure) was performed for plate impact experiments performed near 430 m/s. The simulated damage parameter value was then compared to the size of the grains and brittle particles present for each microstructure.

9.2.1 Peak Stress and Equation of State

The best fit of the simulated peak free surface velocity to the measured Al 5083-H116 plate impact data using the polynomial Equation of state (EOS) parameters (K_2, K_3, and K_4)

resulted in the values listed in Table 11. As shown in Equation 36, this EOS is a polynomial expansion with the compression (μ), given by Equation 37. For the peak stress range used (up to 6.2 GPa), the data did not depend on K_4. This is because K_4 fits the fourth order dependence of the compression and will thus model the mean stress for very large values of μ. Such large compressions were not experimentally measured for the impact velocities used, so K_4 was unnecessary to describe the change in mean stress with compression for these experiments.

Table 11: Variables for equation of state (EOS) used to calculate mean stress in one-dimensional simulations. The variables are the Gruneissen parameter (γ) and fitting constants (K_2, K_3, and K_4) for the polynomial EOS. The bulk modulus (K_0) from measured ultrasonic data was used for each microstructure.

γ	K_2 [GPa]	K_3 [GPa]	K_4 [GPa]
1.98	8	1300	0

The fits of the simulated free surface velocity data to the peak state of the experimentally obtained profiles for impact at 200, 430, 670, and 830 m/s are shown in Figures 72–75. The simulated data shows a good match to the peak free surface velocity recorded by the VISAR, indicating that the EOS data shown in Table 11 is reasonably accurate.

The experimentally calculated spall strengths (listed in Table 4) were used for the simulated data shown in Figures 72–75. This results in similar values of the pullback velocity in every case; however, the pullback occurs earlier for the simulated results as compared to the experimental results, due to the quasi-elastic release behavior of aluminum, whereby an abrupt transition from elastic to plastic release does not occur. This is at least a two-dimensional behavior [93]; one-dimensional simulations cannot capture the singular slope of the release. Figures 72–75 do show that the spall strength from the Cochran and Banner [107] model results in a good match to the experimental pullback velocity (and the experimental spall strength), hence, Shock-1D can yield accurate spall strength values despite the different release behavior. The simulations discussed in the next section will use higher spall strength values than those experimentally obtained so that the data after the pullback can be fit to yield the damage size parameter for each Al 5083 microstructure.

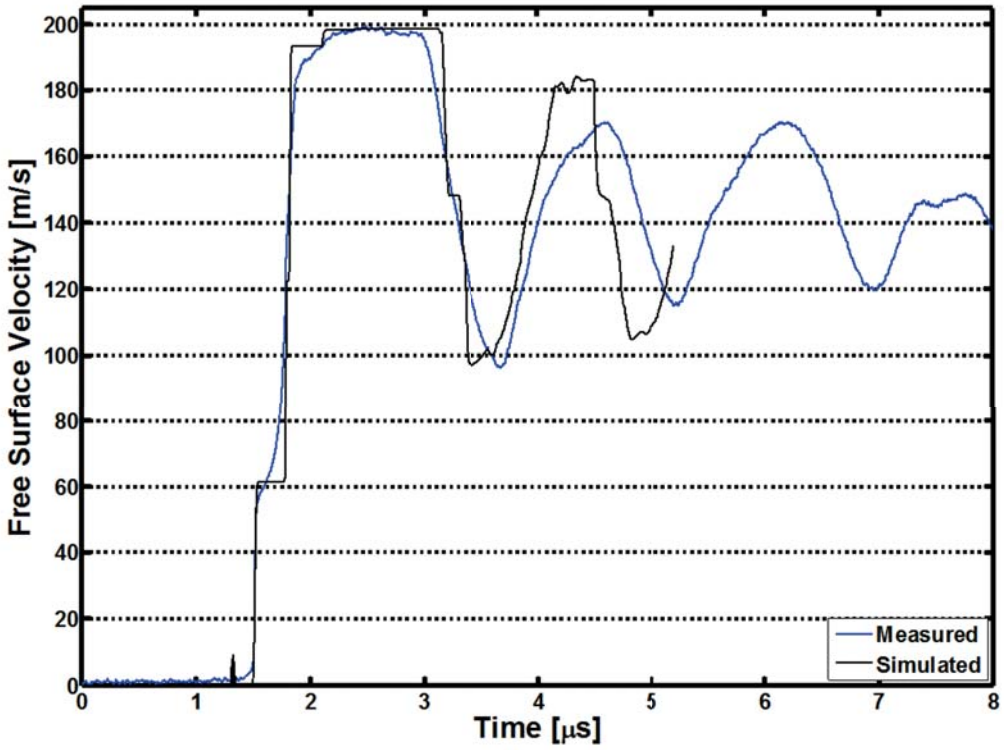

Figure 72: Rear free surface velocity vs. time for both experimental and simulated impact of Al 5083-H116 near 200 m/s. The simulated data was fit to the HEL and peak state for this simulation. The pullback velocity is similar, as the spall strength from experimental measurements was used in the 1-D simulation. The location of the pullback signal is different from experiment due to the quasi-elastic release behavior in the experimental data that cannot be captured using 1-D simulations.

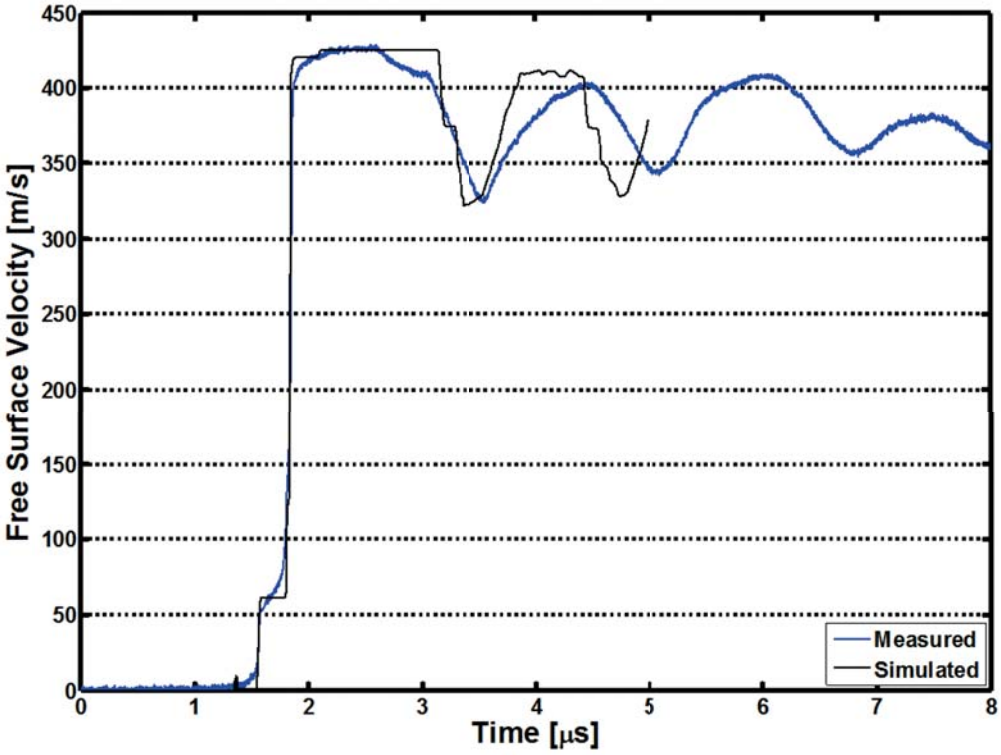

Figure 73: Rear free surface velocity vs. time for both experimental and simulated impact of Al 5083-H116 near 430 m/s. The simulated data was fit to the HEL and peak state for this simulation. The pullback velocity is similar, as the spall strength from experimental measurements was used in the 1-D simulation. The location of the pullback signal is different from experiment due to the quasi-elastic release behavior in the experimental data that cannot be captured using 1-D simulations.

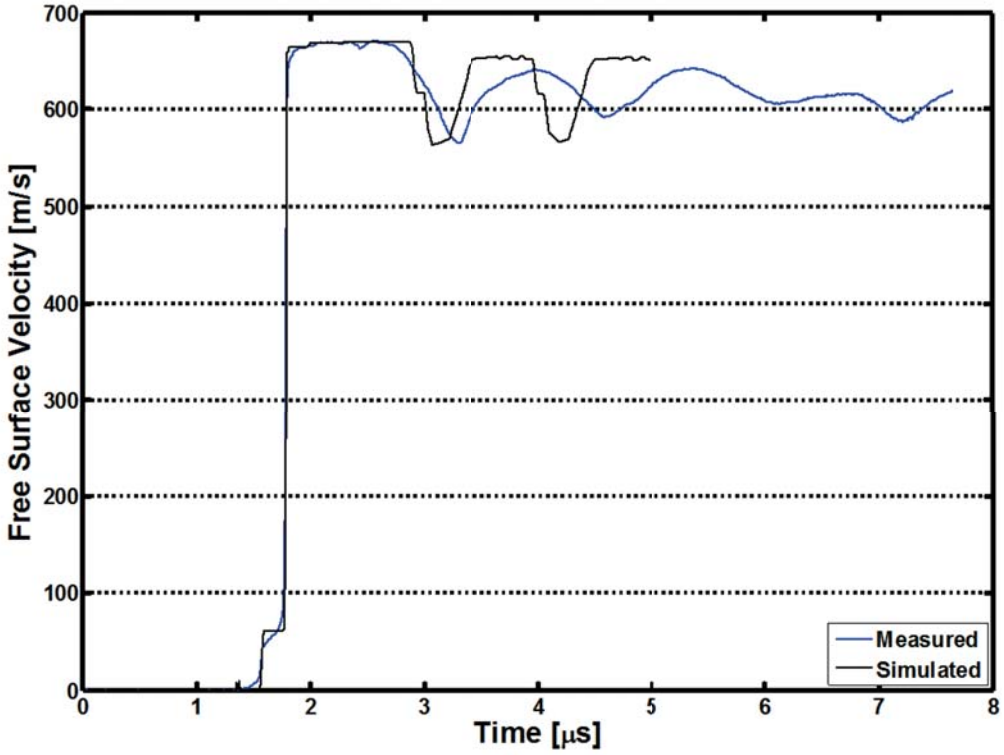

Figure 74: Rear free surface velocity vs. time for both experimental and simulated impact of Al 5083-H116 near 690 m/s. The simulated data was fit to the HEL and peak state for this simulation. The pullback velocity is similar, as the spall strength from experimental measurements was used in the 1-D simulation. The location of the pullback signal is different from experiment due to the quasi-elastic release behavior in the experimental data that cannot be captured using 1-D simulations.

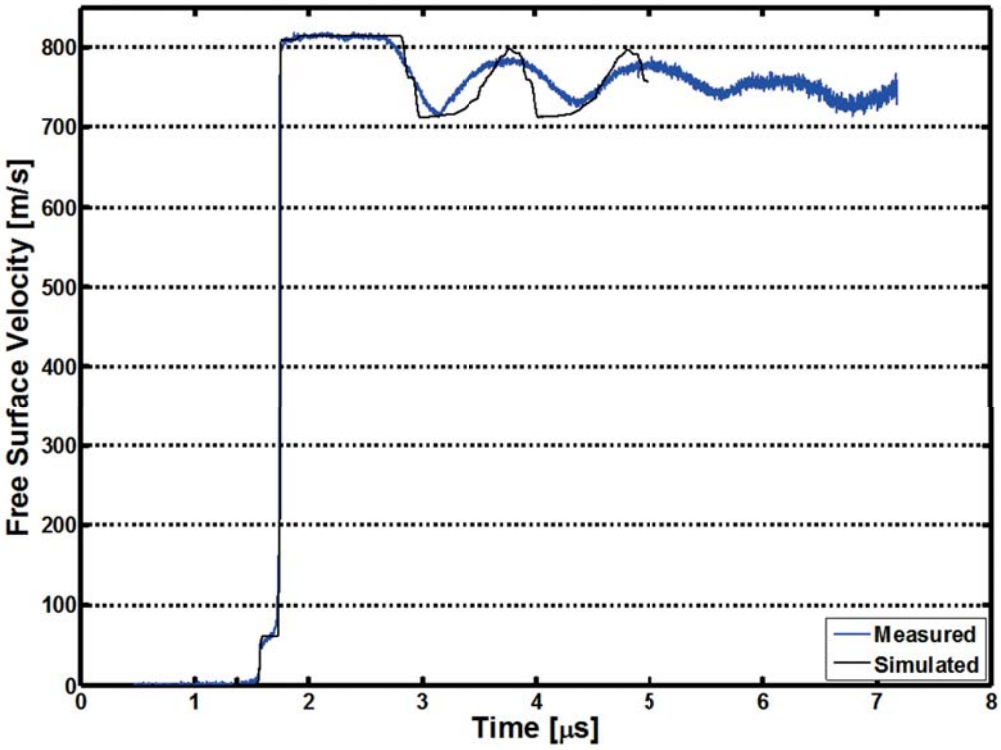

Figure 75: Rear free surface velocity vs. time for both experimental and simulated impact of Al 5083-H116 near 830 m/s. The simulated data was fit to the HEL and peak state for this simulation. The pullback velocity is similar, as the spall strength from experimental measurements was used in the 1-D simulation. The location of the pullback signal is different from experiment due to the quasi-elastic release behavior in the experimental data that cannot be captured using 1-D simulations.

9.2.2 Modeling of Spall Response

The spall behavior for each of the three Al 5083 microstructures (rolled Al 5083-H116, Al 5083 processed using ECAP, and stretched and annealed Al 5083 with an equiaxed grain structure) was simulated for impact near 430 m/s. The peak state (mean stress) was modeled using the EOS data presented in the previous section.

The viscoplastic response was estimated using tensile test data available in the literature [120, 121]. Tensile test data for the H116 and O (fully annealed) tempers as well as that for Al 5083 processed using ECAP are shown in Table 12. The O temper was used to estimate the viscoplastic behavior for the equiaxed grain structure, as it was stretched and then annealed for 24 h prior to testing. The tensile data presented in Table 12 was used to calculate the yield strength (σys) and strain hardening parameter (H') used in Equation 35. These two parameters were then modified to give the best fit to the HEL and shock arrival time for each of the Al 5083 samples.

Table 12: Tensile test data for Al 5083 for different processing conditions. The three materials are strain hardened (H116), processed using ECAP, and fully annealed (O). [120, 121]

	σ_{ys} [MPa]	σ_{uts} [MPa]	Elongation [%]
H116	228	317	16
ECAP	290	366	18
O	145	290	22

The spall response after the pullback was modeled by varying the spall strength (σ_{spall}) and damage parameter (D_0) from the Cochran and Banner spall model [107]. The spall strengths were increased from the measured values so that the simulated data after the pullback velocity could intersect the measured free surface velocity data. The best fits of the viscoplastic input variables (σys and H'), the measured and simulated spall strength values ($\sigma_{spall,meas}$ and $\sigma_{spall,sim}$), and the simulated damage parameter are listed in Table 13. In all cases, the simulated spall strength is artificially higher than the measured value and is not intended to be a true representation of the spall strength. Instead, the parameter

of interest for these simulations is the damage parameter, which varies from 14 μm for the equiaxed grain structure to 24 μm for the rolled plate microstructure.

Table 13: Variables used to calculate the deviatoric stress and spall behavior in one-dimensional simulations. The shear stress (G_0) from measured ultrasonic data was used for each microstructure.

	σ_{y0} [MPa]	H' [GPa]	$\sigma_{spall,meas}$ [GPa]	$\sigma_{spall,sim}$ [GPa]	D_0 [μm]
H116	210	1.3	0.82	0.969	24
ECAP	290	1.2	0.90	0.960	20
Equiaxed	210	1.6	0.86	0.960	14

The best fits of the simulated free surface velocity data to the experimental data for the rolled plate, the material processed using ECAP, and the material with an equiaxed grain structure are presented in Figures 76–78 respectively. Only a single HEL value can be obtained for simulations with the 1-D model used, as opposed to yielding over a variety of free surface velocities evidenced in the experimental data. Therefore, an average HEL value was fit to the experimental data by varying σys and H'. As shown in Table 13, the fitted yield strength values show good agreement with the data available in the literature (shown in Table 12). The yield strength for the equiaxed grain structure was larger than the literature value, as this sample showed upper and lower yielding behavior. The upper yield point resultant from the stress required to nucleate dislocations [112] yields a higher average HEL value than predicted using the tensile test data for a fully annealed specimen. As mentioned previously, the simulated pullback velocity (resultant form the simulated spall strength value) was intentionally larger than that from experiments so that the data after the pullback could be superimposed. Specifically, the slope during re-compression was an important feature to be fit as this will depend on the value chosen for the damage parameter (D_0). D_0 describes the void size distribution prior to coalescence [107]. In each case, the simulation shows a good fit to the experimental data after the velocity pullback, indicating that D_0 is a good estimation of the void sizes for each of the microstructural states studied. The next section will quantify the grain and inclusion sizes for each of these microstructures and relate them to the simulated D_0 value.

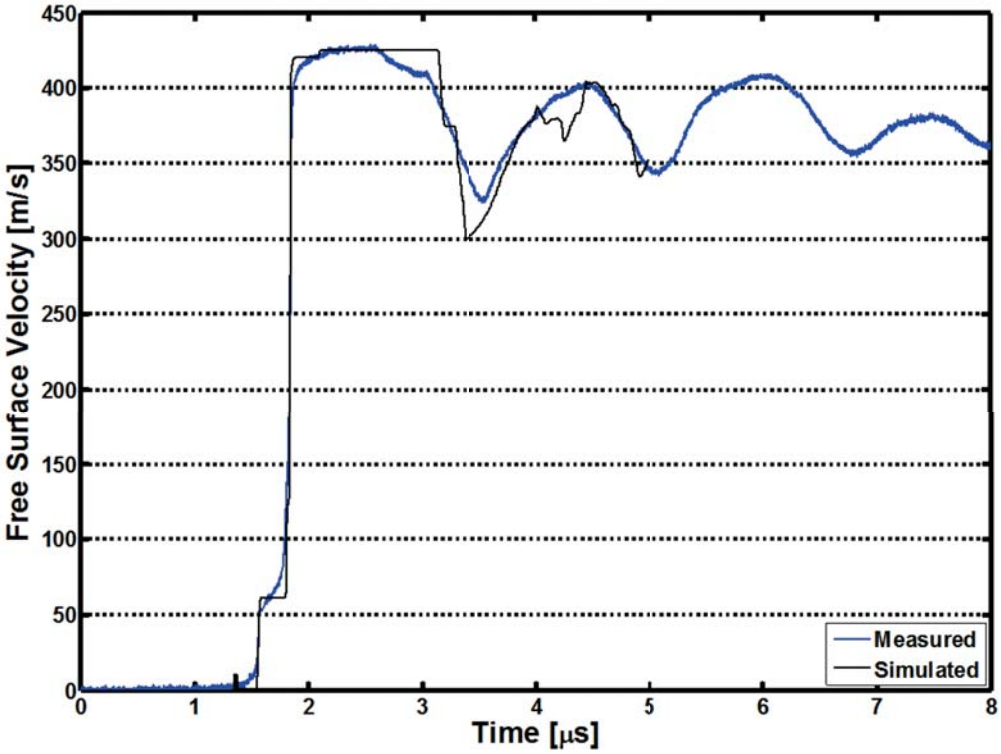

Figure 76: Rear free surface velocity vs. time for both experimental and simulated impact of Al 5083-H116 near 430 m/s using a spall damage model. The simulated data was fit to the first peak after the pullback velocity using the spall damage parameter from the Cochran and Banner [107] model. The spall strength was arbitrarily increased so that the free surface velocity during release and recompression would intersect. The release data does not match the experimental data due to quasi-elastic release behavior that cannot be captured using 1-D simulations.

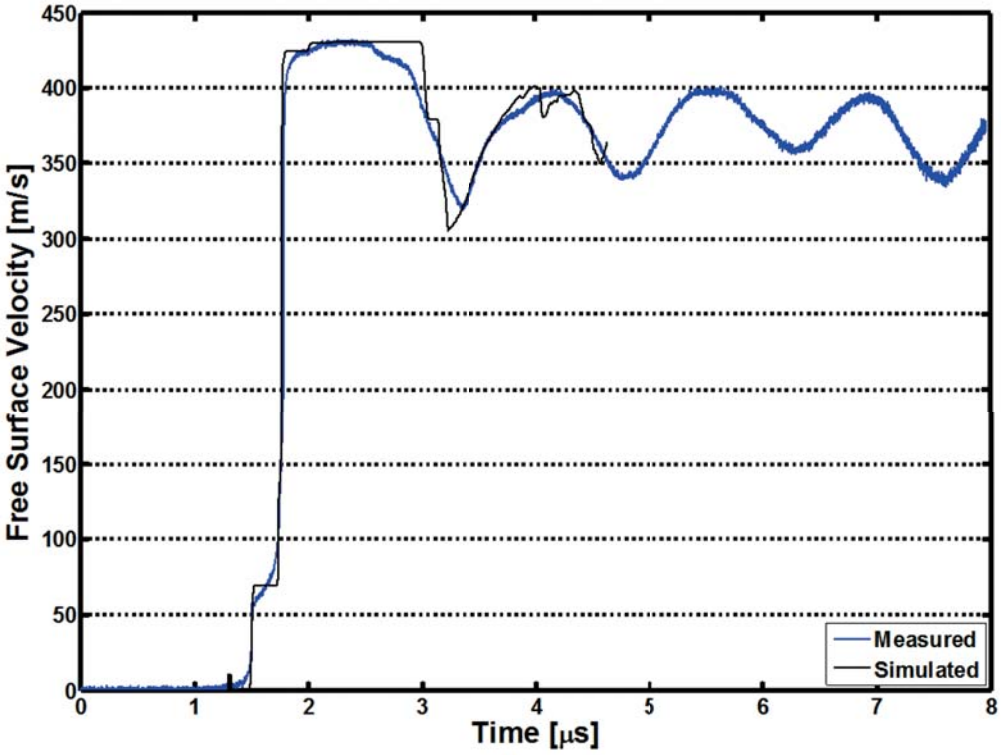

Figure 77: Rear free surface velocity vs. time for both experimental and simulated impact of Al 5083 processed using ECAP. The simulated data was fit to the first peak after the pullback velocity using the spall damage parameter from the Cochran and Banner [107] model. The spall strength was arbitrarily increased so that the free surface velocity during release and recompression would intersect. The release data does not match the experimental data due to quasi-elastic release behavior that cannot be captured using 1-D simulations.

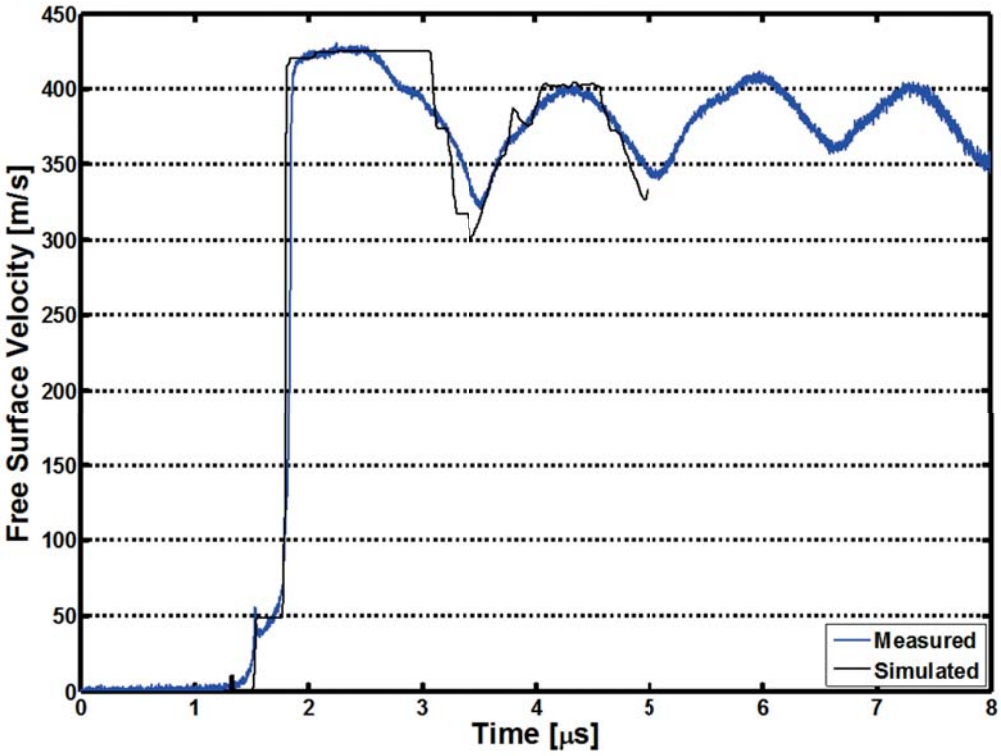

Figure 78: Rear free surface velocity vs. time for both experimental and simulated impact of Al 5083 with an equiaxed grain structure. The simulated data was fit to the first peak after the pullback velocity using the spall damage parameter from the Cochran and Banner [107] model. The spall strength was arbitrarily increased so that the free surface velocity during release and recompression would intersect. The release data does not match the experimental data due to quasi-elastic release behavior that cannot be captured using 1-D simulations.

9.3 Comparison of Microstructure to Simulation

The previous section discussed the use of 1-D simulations to obtain a damage parameter, D_0, which describes void size just prior to complete coalescence. Specifically, D_0 is the void volume per unit void cross-sectional area within the spall plane and has units of length (see Equation 25). Equation 25 can be simplified to that given by Equation 40, where the variables r_2 and N_A are the characteristic void radius and areal number density of voids prior to coalescence.

$$D_0 = 8\pi r_2^3 N_A \tag{40}$$

Equation 40 shows that D_0 depends on the void size to the third power, making r_2 the dominant parameter affecting D_0. Thus, if a microstructural feature is responsible for the spall behavior of the Al 5083 specimens tested, then it is expected that the size of this feature should be similar to r_2. As shown in Appendix B, the characteristic void size ranges from 5.74 μm to 7.20 μm for recovered Al 5083-H116 specimens. These void sizes are similar to both the through thickness grain size (9 μm) and the size of brittle particles such as inclusions and dispersoids for Al 5083-H116. The next sections will quantify the grain and inclusion size for each of the three Al 5083 microstructures to show which microstructural feature is controlling the spall response.

9.3.1 Grain Size

The grain structures for each of the three Al 5083 microstructures are shown in Figures 34, 44, and 54 with the grain size varying by several orders of magnitude. The grain size for each of these three sample types was 9 μm for Al 5083-H116 in the through-thickness direction, 0.4 μm for the ECAP specimen, and 34 μm for the sample with equiaxed grains. If the grain size is the dominant microstructural feature affecting the spall response, then D_0 should vary widely for each of the three microstructures; however, as shown in Table 13, this is not the case. D_0 is of the same order of magnitude for each of the three microstructural states and varies from 14 μm for the equiaxed sample to 24 μm for the rolled plate sample. A plot of D_0 versus the grain size for each microstructure is shown in Figure 79.

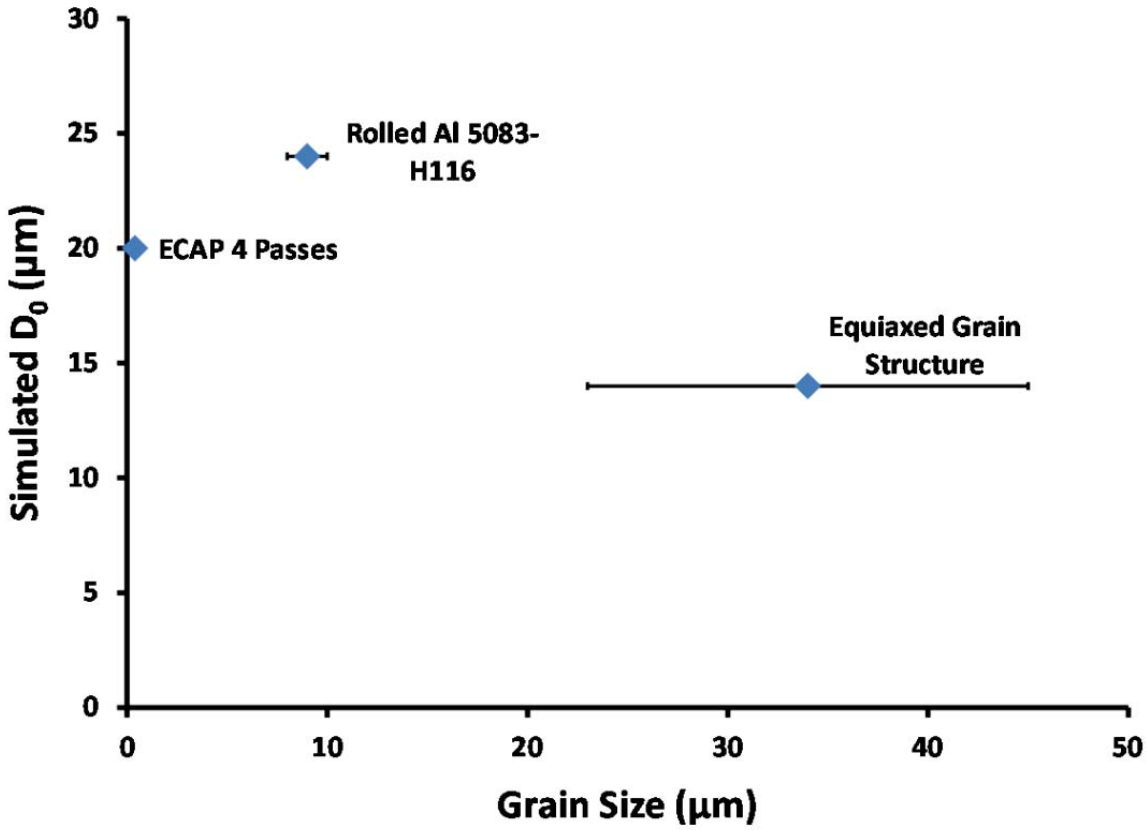

Figure 79: Simulated damage parameter vs. grain size of Al 5083 samples with different microstructures. The materials studied were a rolled Al 5083-H116 plate, Al 5083 processed using ECAP, and Al 5083 with an equiaxed grain structure. The simulated damage size parameter does not match the trends in grain size.

If there is any trend for D_0 as a function of the grain size, it is an inverse trend; however, this trend is not one-to-one, as the sample processed using ECAP (having the smallest grain size) has a D_0 value slightly smaller than the rolled specimen, which has a much larger grain size. The simulated D_0 values suggest that grain size is not the microstructural feature affecting the spall response. Instead, the microstructural feature should be similar in size for each of the three microstructures studied. The next section will discuss the trends in the size of the inclusion and dispersoid phases (which are similar for each of the three microstructures) compared to D_0.

9.3.2 Inclusion and Dispersoid Size

Al 5083 contains iron and silicon rich inclusions present from the casting process as well as manganese rich dispersoid phases formed from solid solution during pre-heat treatments. These phases are brittle and are known to crack during dynamic tension, often resulting in decreased spall strength [44]. For every microstructure studied in this research, these brittle particles have been present in the fracture surface and next to large voids at the spall plane (see for example Figures 41, 42, and 53). The size of these brittle particles for each of the three Al 5083 microstructures can be seen in Figure 80. Figures 80(a) and 80(c) show several instances of cracked inclusions with small broken particles nearby for Al 5083-H116 and Al 5083 with an equiaxed grain structure. The equiaxed grain structure shows an especially large number of such small cracked particles. This microstructure was produced by first stretching the rolled Al 5083-H116 plate followed by annealing, so it is likely that stretching resulted in even greater instances of particle cracking than for the original rolled plate. The material processed using ECAP, shown in Figure 80(b), shows mainly large intact particles.

The areal number density (N_A) of dispersoids and inclusions was calculated using micrographs such as those shown in Figure 80. The areal particle size distribution for each of the three Al 5083 microstructures are shown in Figures 81–83. The distributions show that the equiaxed microstructure displays a large number of very small particles (between 2.3 μm and 4.6 μm), but the ECAP microstructure displays a smaller number density of

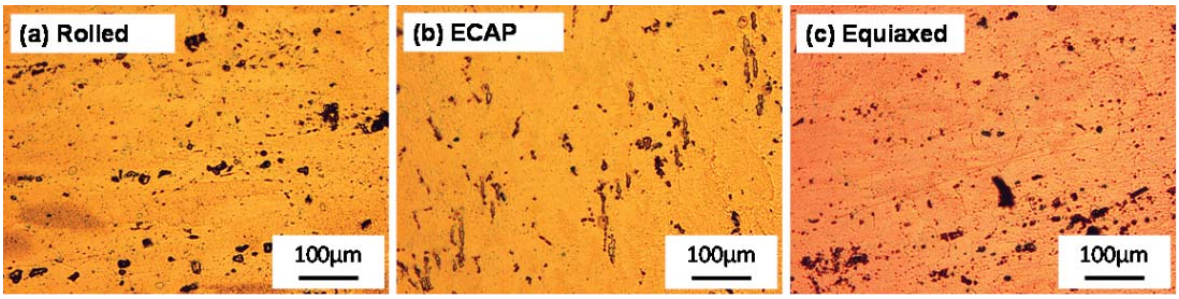

Figure 80: Optical microscope images showing inclusions and dispersoid phases in Al 5083 for a variety of processing conditions. The different specimens correspond to (a) rolled Al 5083-H116, (b) Al 5083 processed using ECAP, and (c)Al 5083 stretched and annealed to produce an equiaxed grain structure. Al 5083 processed using ECAP shows mainly large intact particles. Al 5083 processed using rolling or with equiaxed grains show regions with many small particles due to cracking of larger particles.

particles that are much larger (greater than 11.6 μm). The rolled plate shows particle sizes and number densities lying between these two extremes.

The total areal number density of particles for each microstructure was calculated by plotting the number density of particles greater than a given size ($N_{A,G}$), shown in Figure 84. The data were fit with an exponential equation employing non-linear least-squares regression for each dataset. The extrapolated value of the exponential fit as size goes to zero then gives the total areal number density of particles (N_A). Figure 84 shows that the equiaxed microstructure has the largest value of N_A, followed by the rolled plate and the plate processed using ECAP respectively. This data matches with the qualitative observations from Figure 80, whereby the ECAP microstructure displayed a small number of intact particles, but the rolled plate and equiaxed microstructures displayed several small cracked particles.

The values of N_A from the exponential fits in Figure 84 along with the average particle size ($< D >$) for each Al 5083 microstructure are listed in Table 14. If these two parameters are inserted into Equation 40, it yields a measured damage parameter variable $D_{0,meas}$ for the brittle particles present in the Al 5083 microstructure. $D_{0,meas}$ is also listed in Table 14 for each microstructure. If these particles are the dominant microstructural feature affecting the spall behavior of Al 5083, then the simulated damage parameter value from the Cochran and Banner [107] model should be similar to the measured value for each microstructure.

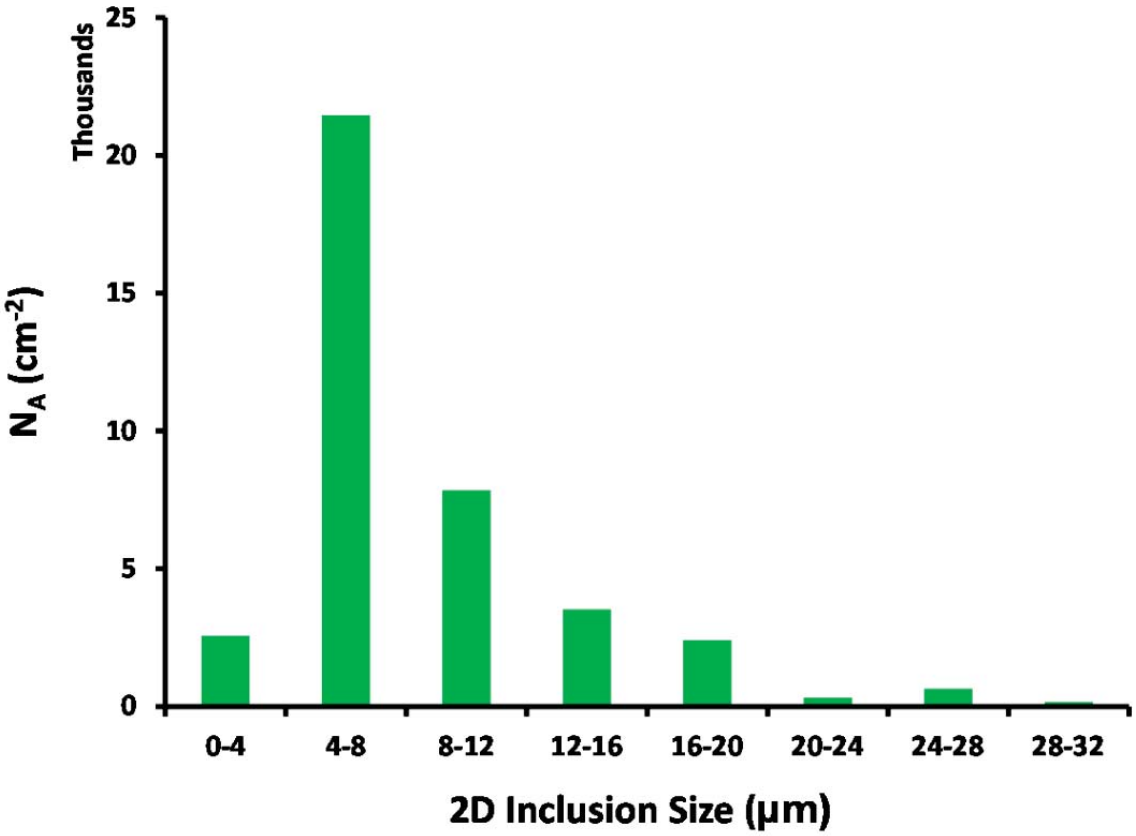

Figure 81: Areal size distribution of brittle particles in rolled Al 5083-H116

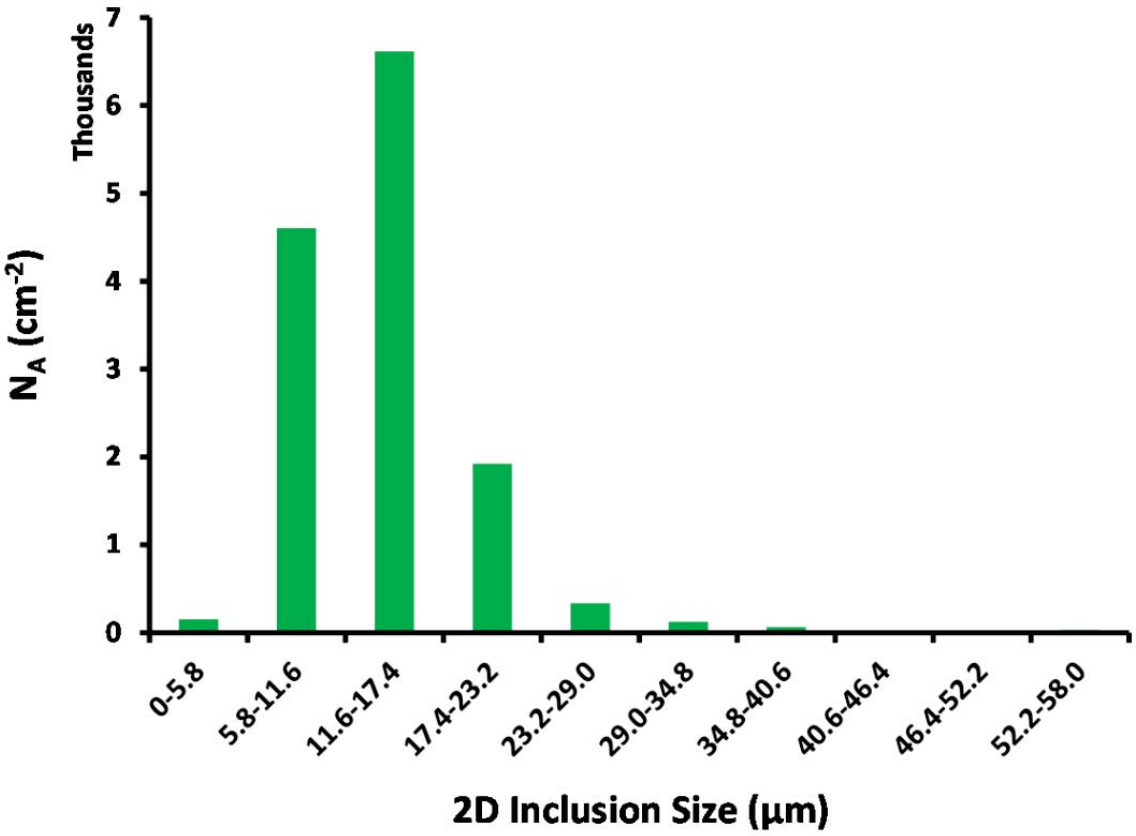

Figure 82: Areal size distribution of brittle particles in Al 5083 processed using ECAP

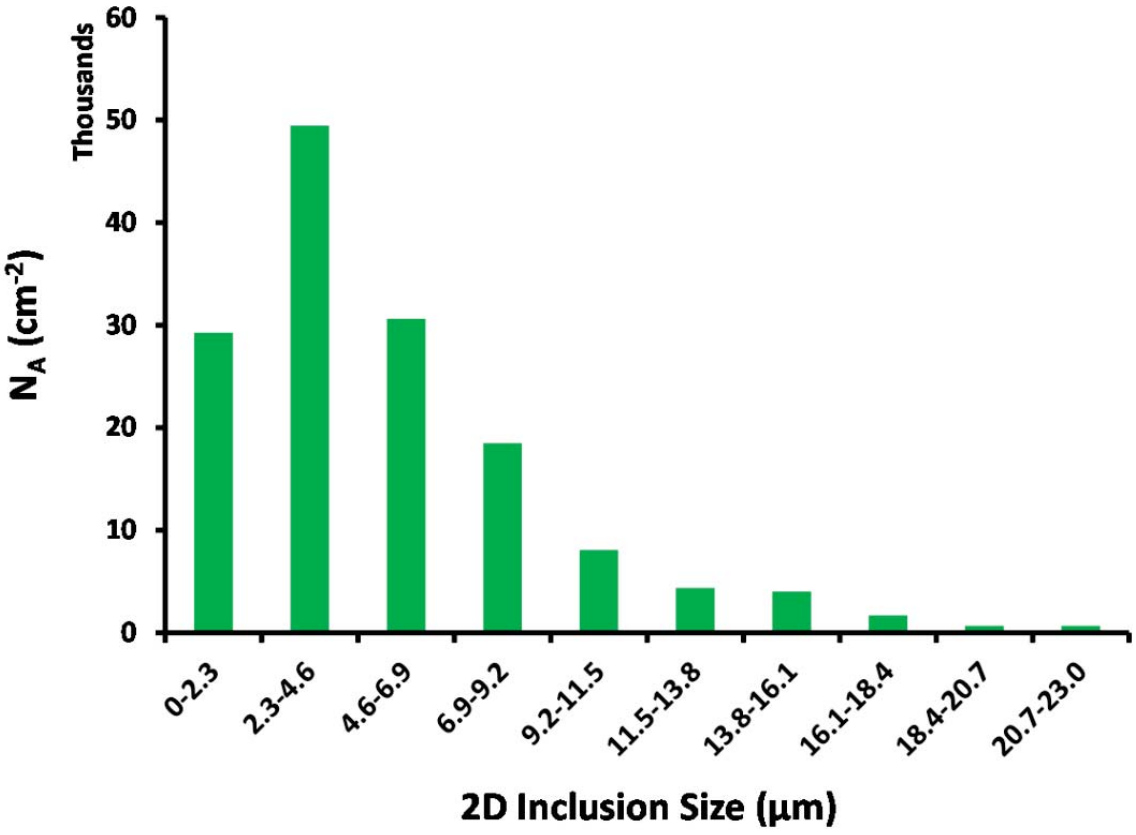

Figure 83: Areal size distribution of brittle particles in Al 5083 with an equiaxed grain structure

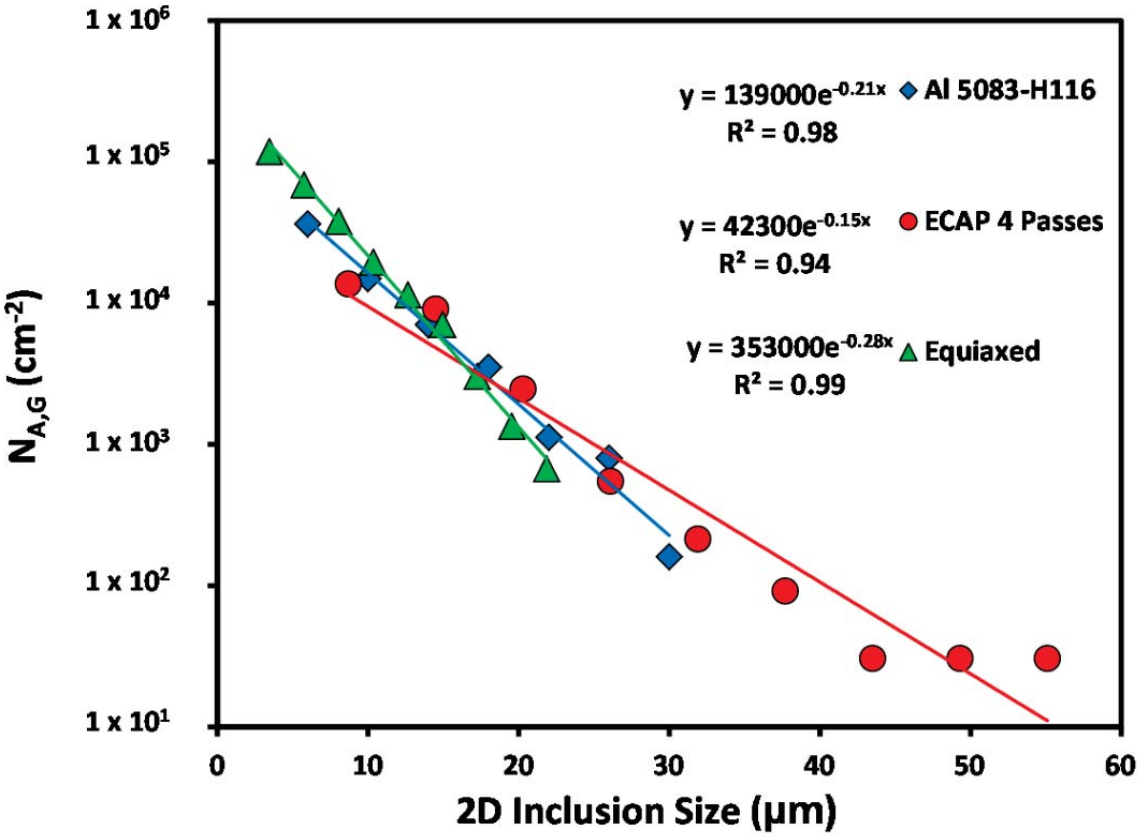

Figure 84: Areal density of brittle particles larger than a given size for Al 5083 processed under different conditions. The materials studied were a rolled Al 5083-H116 plate, Al 5083 processed using ECAP, and Al 5083 with an equiaxed grain structure. The equiaxed microstructure displays a larger number density of small particles compared to the rolled plate. The ECAP microstructure displays a smaller number density of large particles.

The simulated versus the measured values of the damage parameter are plotted in Figure 85.

Table 14: Parameters quantifying the microstructure of brittle particles in Al 5083 for different processing conditions. The parameters are the areal density of particles (N_A), the average particle size ($< D >$), and the measured damage size parameter ($D_{0,meas}$)

	N_A [$\mathbf{cm^{-2}}$]	$< D >$ [μm]	$D_{0,meas}$ [μm]
H116	1.39 x 10^5	8.6	23
ECAP	4.23 x 10^4	13.8	22
Equiaxed	3.53 x 10^5	5.4	14

Figure 85 shows a clear increasing trend in the measured damage parameter relative to the simulated damage parameter. The data are fit with a line that intersects the origin. Since the linear fit has a slope near unity (0.99), this proves that the relationship between the two damage parameters is one-to-one. The data suggests that changes to the inclusion size and distribution (quantified by $< D >$ and N_A respectively) are responsible for the changes in the simulated damage parameter for each microstructure. The simulated parameter models the distribution of voids prior to coalescence due to spall; therefore, the simulated data and the microstructures quantified in this chapter provide quantitative evidence that inclusions—and not grain boundaries—are the dominant microstructural feature affecting the spall behavior of Al 5083.

9.4 Conclusions

The measured free surface velocity data for plate impact testing of Al 5083 was simulated using the Shock-1D program and the Cochran and Banner spall model. Simulations were performed for rolled Al 5083-H116 plate, Al 5083 processed using ECAP, and Al 5083 stretched and annealed to produce an equiaxed grain structure. The simulations provided a value of the damage parameter, which is related to the size and distribution of voids prior to coalescence, for each of the microstructures studied. The damage parameter ranged from 14 μm for the equiaxed microstructure to 24 μm for the rolled plate microstructure. The damage parameter value was widely different from the measured grain sizes, which varied

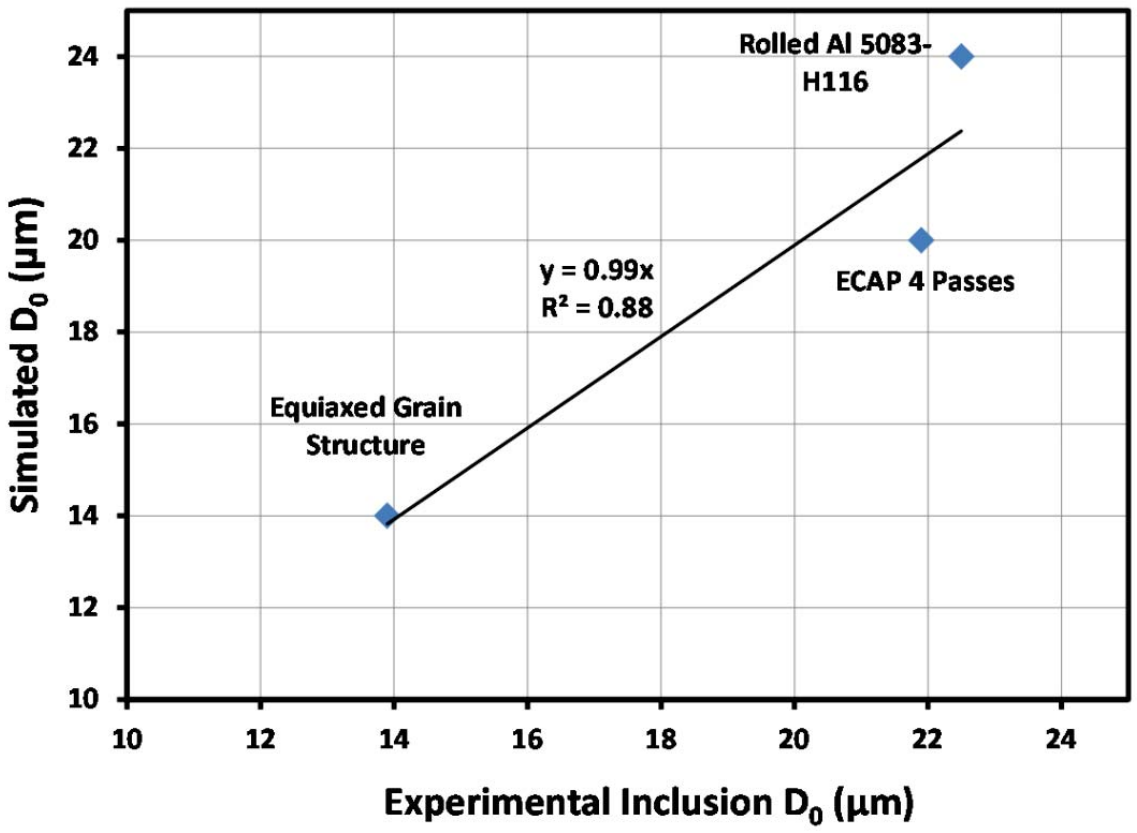

Figure 85: Simulated damage parameter vs. measured damage parameter using the size and distribution of brittle particles. The simulated damage parameter was fit to experimental plate impact data using the Cochran and Banner spall model [107]. The measured damage parameter was calculated using the average size and areal density of brittle particles for each microstructure.

by orders of magnitude between each sample type. Instead, the size and areal distribution of brittle particles, such as inclusions and dispersoids, matched well with the trends in the damage parameter. A measured damage parameter value calculated using the size distributions of brittle particles shows a one-to-one correlation with the damage parameter obtained from simulations. The results indicate that the brittle particles are overwhelmingly responsible for the spall response of Al 5083, which has been suggested in previous chapters due to the presence of such particles near damaged regions observed in recovered specimens.

CHAPTER 10

INFLUENCE OF MICROSTRUCTURE ON SPALL STRENGTH AND HUGONIOT ELASTIC LIMIT IN AL-MG ALLOYS

This chapter discusses the trends in the spall strength and the Hugoniot elastic limit (HEL) as a function of the four microstructures investigated in this work. The microstructures corresponded to that of a rolled Al 5083-H116 plate, sub-micron grained Al 5083 formed using equi-channel angular pressing (ECAP), equiaxed grain microstructure produced by stretching and annealing the rolled Al 5083-H116 plate, and precipitation hardened microstructure of an Al-9wt.% Mg alloy. The corresponding details of the microstructure for each material are summarized in Table 15.

10.1 Peak Stress Dependence of the HEL and Spall Strength

10.1.1 Hugoniot Elastic Limit (HEL)

The HEL values for all microstructures studied for plate impact using 10 mm thick specimens are shown in Figure 86 as a function of the peak stress. It can be seen that for any given microstructure, the HEL varies little with the peak stress. The effects of microstructure on the HEL can be ascertained by comparing the data points near a peak stress of 3 GPa in the figure. Using the rolled Al 5083 plate as a baseline, it is obvious that the equiaxed microstructure shows less resistance to dynamic yielding, having an HEL value (0.32 GPa) significantly less than that of the rolled plate (0.45 GPa). The equiaxed microstructure was produced by annealing a pre-strained rod, which would also remove a significant amount of dislocation density. It is expected that this softer material would display a decreased HEL value. Increasing resistance to dynamic yielding is observed for both the microstructure produced by ECAP (0.48 GPa) and that produced by precipitation hardening (0.52 GPa). These two materials attain their strengthening in different ways—one by severe plastic deformation, and the other by aging heat treatment. The average HEL value is highest for the precipitation hardened sample; however, the value for the sample processed using ECAP is

Table 15: Microstructural characteristics of Al-Mg alloys investigated

Rolled Al 5083-H116 plate (As-received from McMaster Carr)	**Al 5083 processed using ECAP**	**Stretched and annealed Al 5083-H116**	**Precipitation hardened Al-9wt.% Mg (As-extruded from Universal Alloys, Inc.)**
Composition excluding Al (in wt.%)			
4.0–4.9 Mg, 0.4–1.0 Mn	4.0–4.9 Mg, 0.4–1.0 Mn	4.0–4.9 Mg, 0.4–1.0 Mn	9 Mg, Trace Ag
Processing			
Cold rolling	ECAP 4 passes followed by warm and/or cold rolling	Stretched to 3% strain followed by annealing for 24 h	Dual solution heat treated and aged at 150°C for 200 h
Texture			
Grains and brittle particles align in rolling direction.	Uniform microstructure after ECAP. Post-ECAP rolling aligns brittle particles in the rolling direction.	Uniform microstructure	Grains and brittle particles align in extrusion direction.
Grain Structure			
Grain size varies from 9 μm to 66 μm with orientation	Uniform grain structure with grain size of 0.4 μm	Uniform grain structure with grain size of 34 μm	Textured grain structure that evolves with heat treatment
Secondary Phases: Brittle particles (Mn dispersoids and Fe and Si rich inclusions) and Precipitate phases			
Brittle particles align in rolling direction at grain boundaries with some instances of cracking	Large brittle particles are uniformly dispersed after ECAP. Rolling cracks brittle particles and aligns them in the rolling direction.	Uniform distribution of small particles	Brittle particles align in extrusion direction at grain boundaries with some instances of cracking
β (non-strengthening fcc) precipitate phase present	β (non-strengthening fcc) precipitate phase present	β (non-strengthening fcc) precipitate phase present	β (non-strengthening fcc) precipitate phase present along with the T (strengthening bcc) precipitate phase

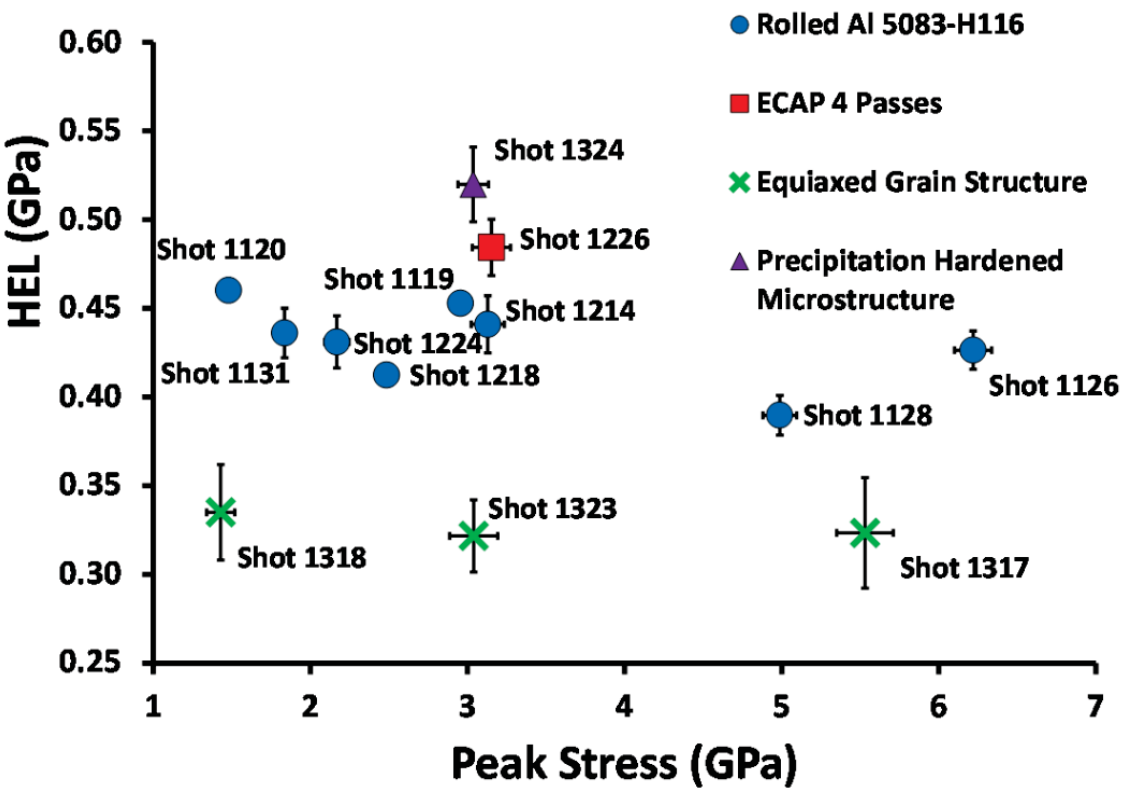

Figure 86: Hugoniot elastic limit (HEL) values as a function of the peak stress for all microstructures investigated. The four samples were a rolled Al 5083-H116 plate, an Al 5083 plate pressed four times using ECAP, Al 5083 with an equiaxed grain structure produced by stretching and annealing, and a precipitation hardened Al-9wt.% Mg plate. Impact was performed through the plate thickness in each case.

just within the error bars and is also significantly larger than the baseline, rolled plate, HEL value. A high HEL value is indicative of increased penetration resistance; therefore, the precipitation hardened Al-9wt.% Mg material and Al 5083 processed using ECAP should both display good resistance to penetration during ballistic impact.

10.1.2 Spall Strength

The spall strength values for all microstructures studied for plate impact experiments using 10 mm thick target specimens are presented in Figure 87 as a function of the peak stress. For each microstructure, the spall strength also shows little peak stress dependence, except for the case of the equiaxed grain structure, which shows a possible increasing trend with peak stress, but within the range of the large error bars. Ductile materials do not often display peak stress dependence unless the stress is large enough to melt the material or

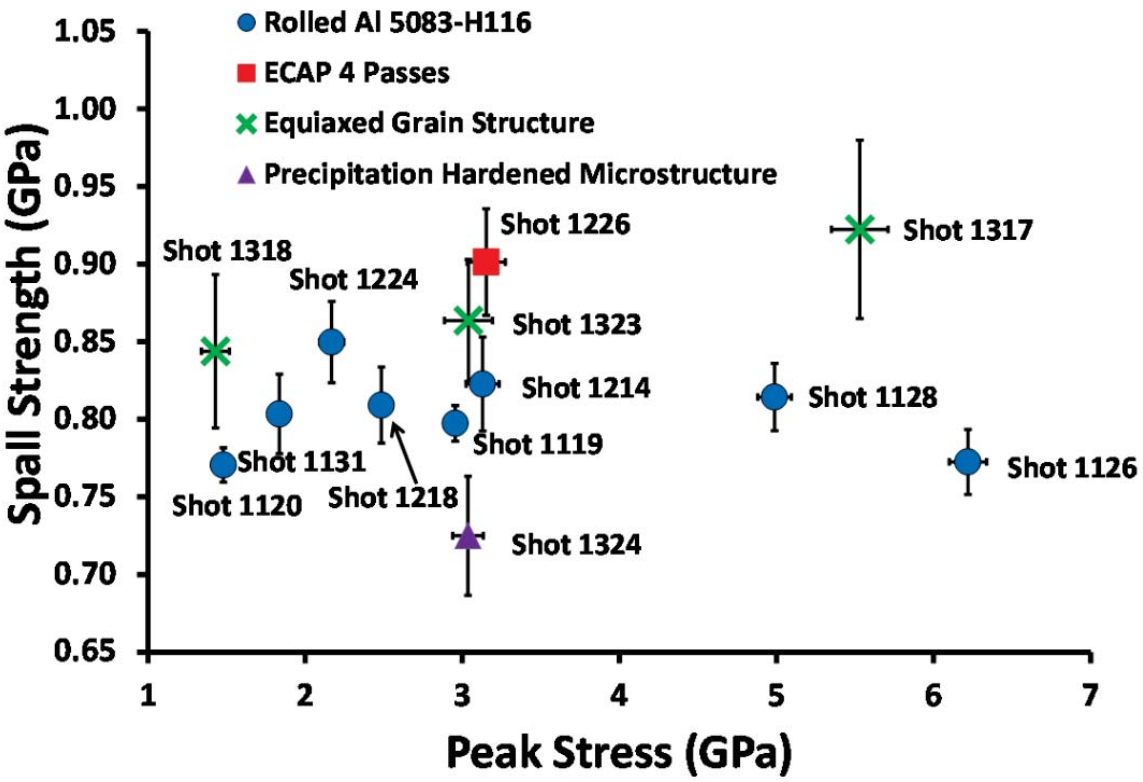

Figure 87: Spall strength values as a function of the peak stress for all microstructures investigated. The four samples were a rolled Al 5083-H116 plate, an Al 5083 plate pressed four times using ECAP, Al 5083 with an equiaxed grain structure produced by stretching and annealing, and a precipitation hardened Al-9wt.% Mg plate. Impact was performed through the plate thickness in each case.

induce a high pressure phase change [44]. With the rolled Al 5083 plate again acting as the baseline, the trends in the spall strength near a peak stress of 3 GPa can be used to compare all of the microstructures studied. In contrast to the HEL trends, where the precipitation hardened microstructure displayed the highest value, this same microstructure displays the lowest spall strength value (0.72 GPa). Increases in the spall strength are observed for both of the more uniform microstructures—the equiaxed microstructure (0.86 GPa) and the microstructure produced by ECAP (0.90 GPa). It is interesting that both of these microstructures result in higher spall strength compared to the rolled plate (0.80 GPa), despite a large difference in the grain size (34 μm for the equiaxed microstructure versus 0.4 μm for the ECAP microstructure respectively). The next section will discuss the grain size dependence of the HEL and spall strength for impact near 3 GPa.

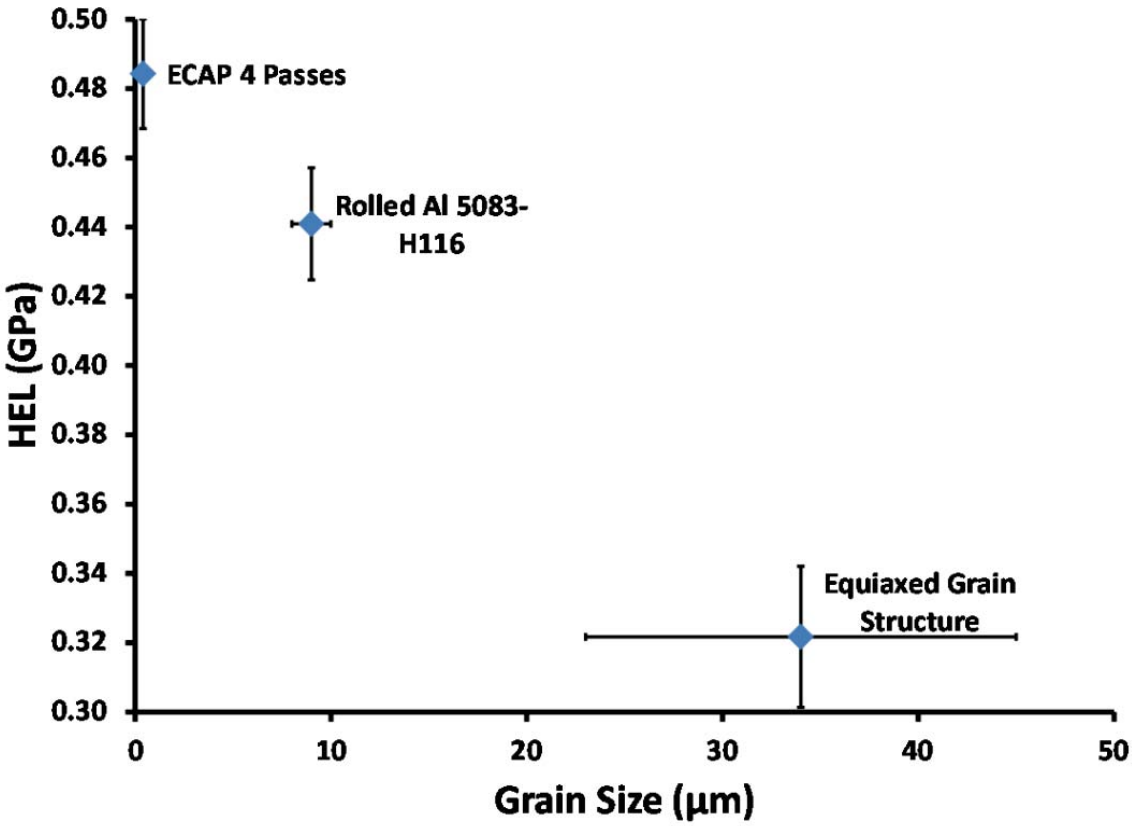

Figure 88: Hugoniot elastic limit (HEL) values as a function of the grain size for all Al 5083 microstructures investigated. The three samples were a rolled Al 5083-H116 plate, an Al 5083 plate pressed four times using ECAP, and Al 5083 with an equiaxed grain structure produced by stretching and annealing. Impact was performed through the plate thickness near 3 GPa in each case.

10.2 Grain Size Dependence of the HEL and Spall Strength

10.2.1 Hugoniot Elastic Limit (HEL)

Figure 88 displays the HEL as a function of the grain size for all Al 5083 microstructures impacted near 3 GPa using 10 mm thick specimens. Since the precipitation hardened material was a different composition than that of Al 5083, it was excluded from the comparison in Figure 88. There is an obvious decrease in the HEL with increasing grain size, as would be expected consistent with the Hall-Petch relationship. The ECAP microstructure, having approximately 0.4 μm grain size, displays the highest HEL value for any of the Al 5083 microstructures studied. Refining the grain size thus results in increased resistance to dynamic yielding and thus increased penetration resistance for armor plates.

10.2.2 Spall Strength

Figure 89 displays the spall strength as a function of the grain size for all Al 5083 microstructures impacted near 3 GPa using 10 mm thick specimens. In contrast to the HEL, the spall strength shows no obvious trend with grain size. Both increasing the grain size by stretching and annealing the rolled plate and decreasing the grain size through ECAP results in increased spall strength. This is similar to results of experiments shown in Chapter 5 along each direction of the rolled plate. In that case, impact in both the short transverse and long transverse directions resulted in identical values of the spall strength despite a large difference in the grain size for each direction (9 μm vs. 39 μm respectively). Furthermore, as shown in Chapter 9, brittle particles such as inclusions and dispersoids are most responsible for nucleating voids during spalling, regardless of the grain size. Hence it appears that grain size is not a direct metric for predicting changes to the spall strength or blast resistance of Al-Mg alloy armor plates when impacted using similar conditions. The next section will explain why the trends in spall strength with grain size are more complex.

10.3 Decompression Rate Dependence of the Spall Strength

Chapter 4 discussed the decompression rate dependence of the spall strength for Al 5083-H116. The decompression rate can be experimentally varied by changing the impact velocity, flyer plate material, or target sample thickness. This section will discuss the effects of microstructure on the decompression rate, and the rate dependence, on the spall strength.

Figure 90 displays the spall strength as a function of the decompression rate, given by Equation 26, for all plate impact spall experiments performed in this work. It can be seen that the spall strength for every microstructure studied obeys a power law function with the decompression rate. The change in decompression rate in Figure 90 is due to changes in the impact velocity, sample thickness, microstructure, and impact direction. The next two sections will discuss the effects of microstructure and impact direction on the spall strength trends with decompression rate, so that the material effects can be differentiated from the experimental impact conditions.

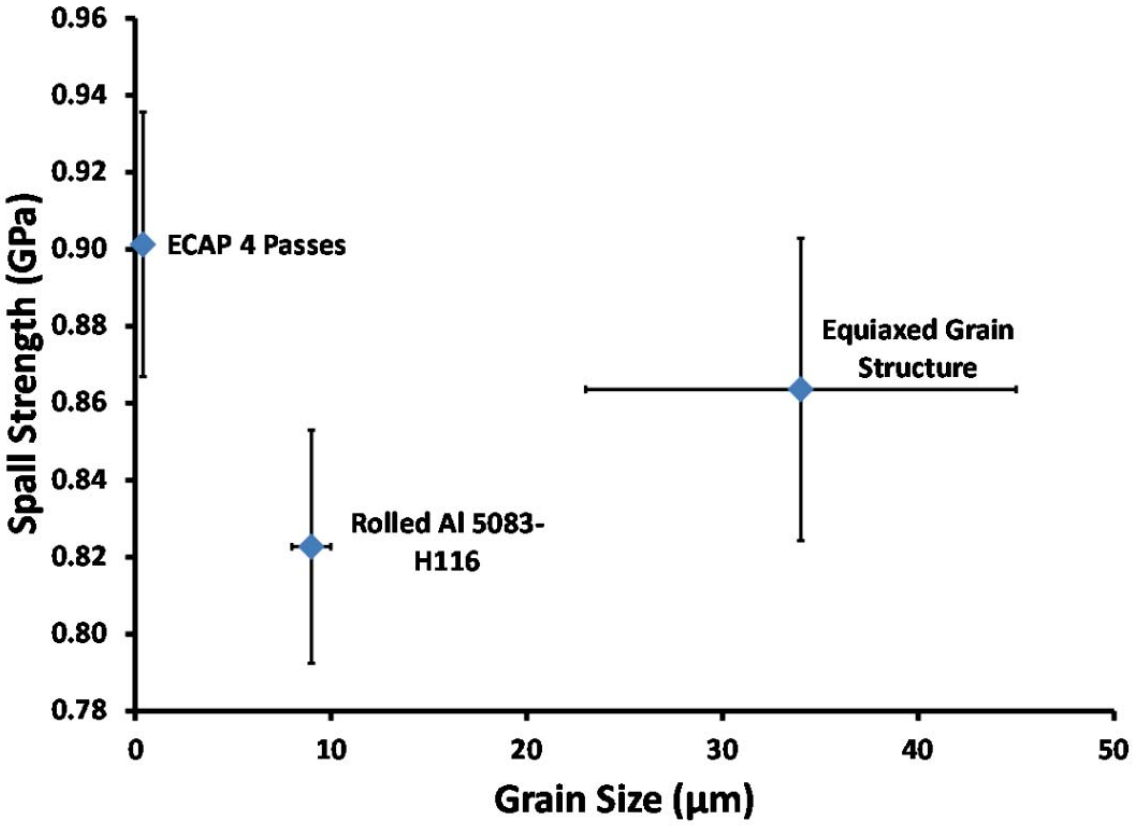

Figure 89: Spall strength values as a function of the grain size for all Al 5083 microstructures investigated. The three samples were a rolled Al 5083-H116 plate, an Al 5083 plate pressed four times using ECAP, and Al 5083 with an equiaxed grain structure produced by stretching and annealing. Impact was performed through the plate thickness near 3 GPa in each case.

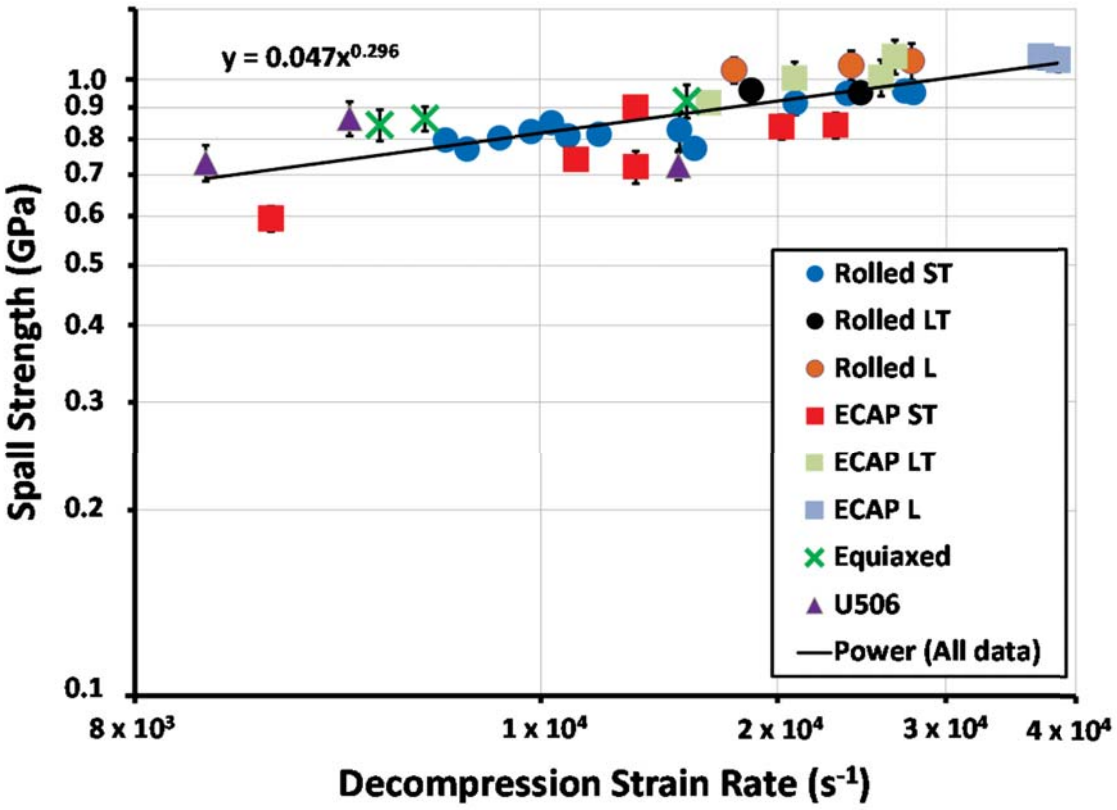

Figure 90: Spall strength values as a function of the decompression rate for every plate impact experiment performed. The data are fit with a power law function.

10.3.1 Effects of Al 5083 Microstructure

Figure 91 displays the spall strength as a function of the decompression rate for every through-thickness plate impact spall experiment performed on Al 5083 samples. Each Al 5083 microstructure (having widely different grain sizes) displays a unique power law fit with the decompression rate. The equiaxed grain structure, having the largest grain size, displays the smallest power law exponent, and the exponent progressively increases as the grain size decreases (equiaxed $\rightarrow$ rolled plate $\rightarrow$ ECAP). Figure 91 also shows that changes to the microstructure for a given grain size (due to strain hardening or cracking of inclusions) occur by moving along that microstructure's decompression curve. For example, the curve for the ECAP specimens includes data for samples that were given post-ECAP rolling. This did not affect the grain size significantly, but it did increase dislocation density and align and crack inclusions. It can be seen that post-ECAP rolling resulted in a lower decompression rate compared to similar impact conditions with the sample only processed with ECAP. This in turn resulted in a lower spall strength.

It is interesting that grain size plays such a significant role in the decompression rate dependence of the spall strength, as there is otherwise no obvious trend for the spall strength as a function of the grain size for similar impact conditions (see Figure 89). Figure 91 gives some explanation for this behavior, as seen by the three data points corresponding to impact with a peak stress near 3 GPa using 10 mm thick samples. While the impact conditions were essentially identical for these three experiments, the decompression rates are widely different for each microstructure. In addition, decompression rate dependence of spall strength, quantified by the fitted power law exponents, is also different for each microstructure. Consequently, the spall strength versus decompression rate curve for the equiaxed grain structure in Figure 91 (having the lowest power law exponent and lowest decompression rate for impact near 3 GPa), is above the curve for the rolled plate microstructure in this region. The spall strength curve for the material processed using ECAP (having the highest power law exponent and highest decompression rate for impact near 3 GPa), is near the intersection point with the rolled plate's curve, which also results in a higher spall strength. Thus, for a given set of impact conditions, the spall strength for a particular

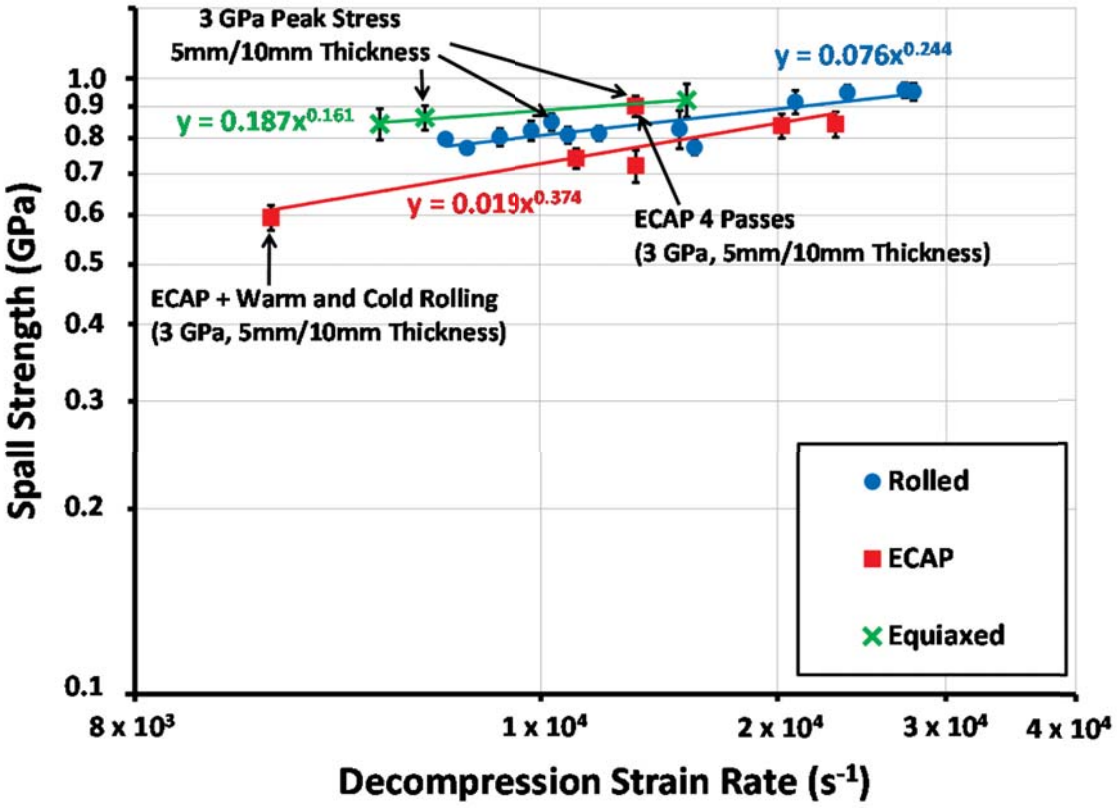

Figure 91: Spall strength values as a function of the decompression rate for impact through the thickness of Al 5083 having different microstructures. The data for each microstructure type (rolled Al 5083-H116 plate, Al 5083 processed with ECAP, and Al 5083 with equiaxed grain structure) are fit with a power law function, with each microstructure displaying a unique power law exponent. Identical peak stress values and plate thicknesses resulted in widely different decompression rates for each microstructure, which explains the differences in the spall strength values as a function of the microstructure.

grain size depends on decompression rate and decompression rate power law exponent for the corresponding microstructure. The trends in the rate dependence of the spall strength with grain size will be quantified in Section 10.3.3.

10.3.2 Effects of Impact Orientation

Plotting the spall strength versus the decompression rate also explains the effects of impact orientation on the spall strength. As described in Chapter 5, the spall strength for rolled Al 5083-H116 plate was lower for impact through the plate thickness (in the short transverse direction) and highest for impact in the rolling (longitudinal direction). The spall strength as a function of the decompression rate for rolled Al 5083-H116 is shown in Figure 92 for impact in both the short transverse and longitudinal directions. These two impact directions have widely different grain sizes (9 μm vs. 66 μm respectively), and display different power law fits to the data. Similar to the fits shown in Figure 91, the power law exponent increases as the grain size decreases (longitudinal direction $\rightarrow$ short transverse direction).

The spall strength versus decompression rate is shown in Figure 93 for impact along different orientations of the plates processed using ECAP. The specimens processed with ECAP had a uniform grain structure with an approximate grain size of 0.4 μm along any direction of the plate. As Figure 93 shows, the power law fits are similar for impact in the short transverse or long transverse directions. This provides further evidence that the grain size controls the power law fitting constants for spall strength with decompression rate.

10.3.3 Trends in Power Law Fits

The power law fits displayed in Figures 90–93 have fitting constants A and m (see Equation 38). The fitting constants are plotted against grain size in Figures 94 and 95 respectively for the three different Al 5083 microstructures. The fitting constants for impact along the longitudinal direction of the rolled plate are included to yield data for grain sizes ranging from 0.4 μm to 66 μm. Figures 94 and 95 show that the constant, A, increases linearly with increasing grain size, while the exponent, m, decreases logarithmically with increasing grain size. Thus, decreasing the grain size can drastically increase the decompression rate dependence of the spall strength for Al 5083.

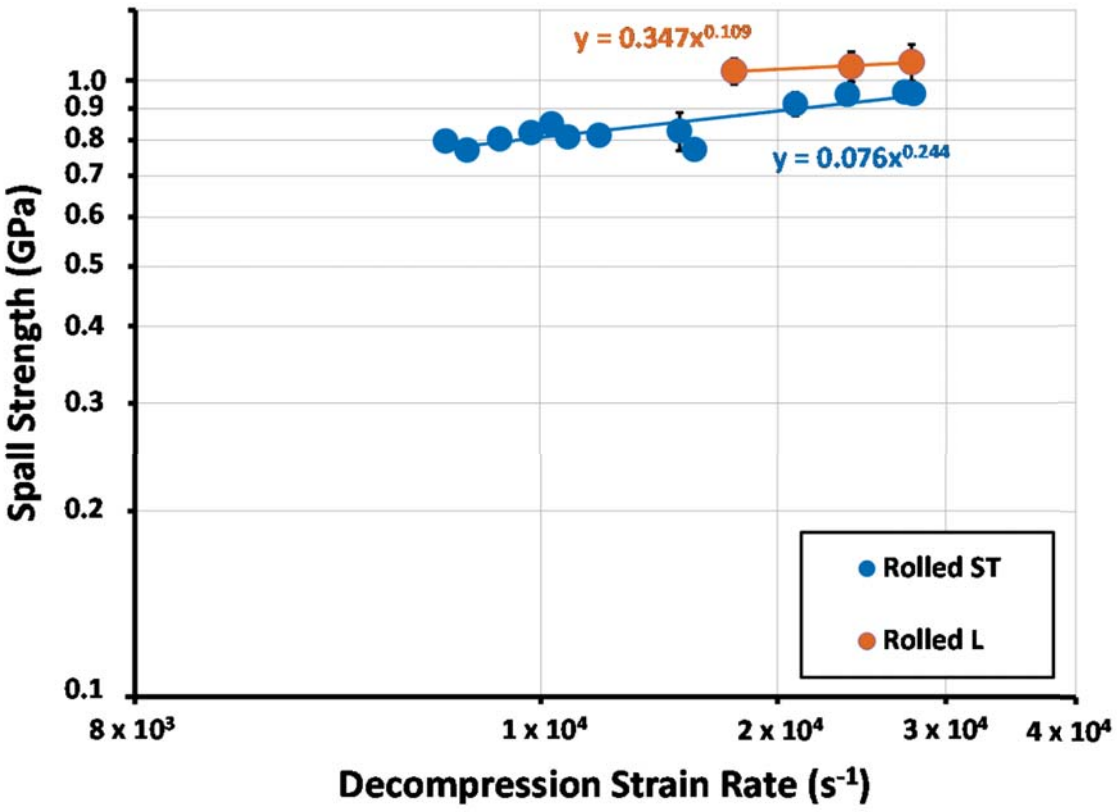

Figure 92: Spall strength values as a function of the decompression rate for impact along different orientations of an Al 5083-H116 plate. The data for each impact direction are fit with a power law function, with the longitudinal direction showing a lower power law exponent than for the through-thickness (short transverse) direction.

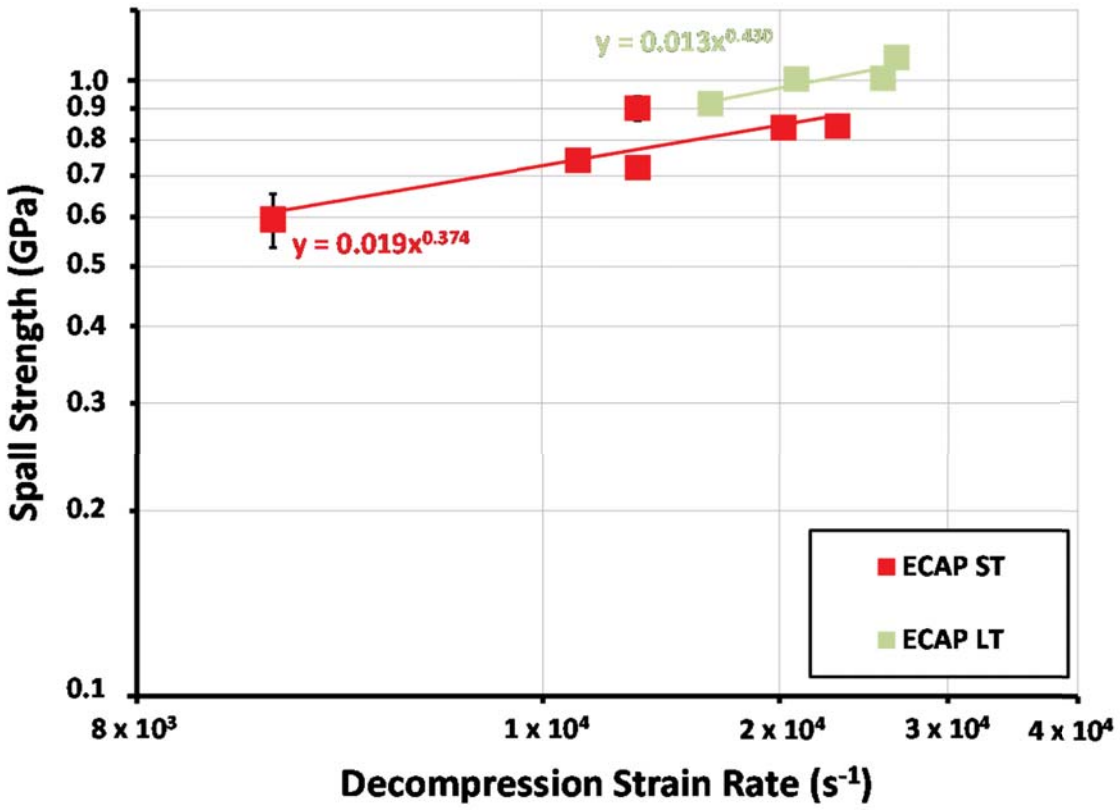

Figure 93: Spall strength values as a function of the decompression rate for impact along different orientations of Al 5083 processed using ECAP. The data for each impact direction are fit with a power law function, with both directions having similar power law exponents.

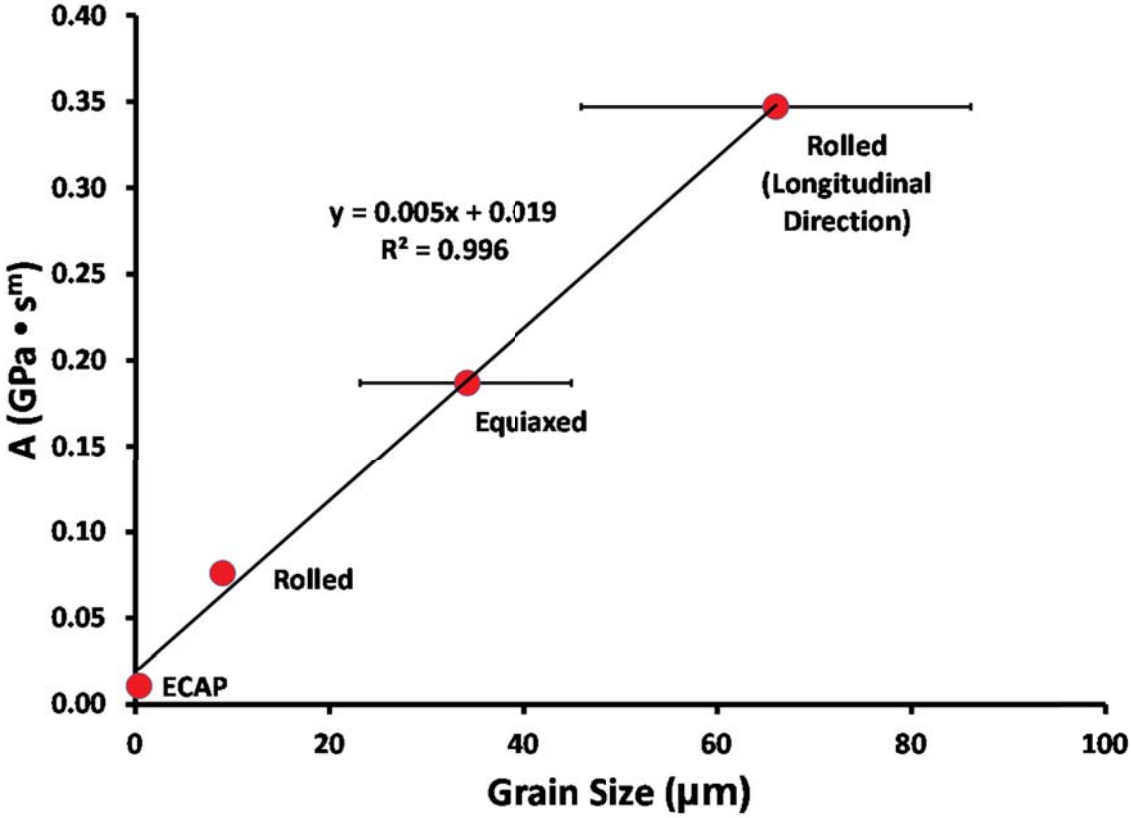

Figure 94: Fitted power law multiplier describing spall strength vs. decompression rate for Al 5083, plotted as a function of the grain size. The power law multiplier increases linearly with grain size.

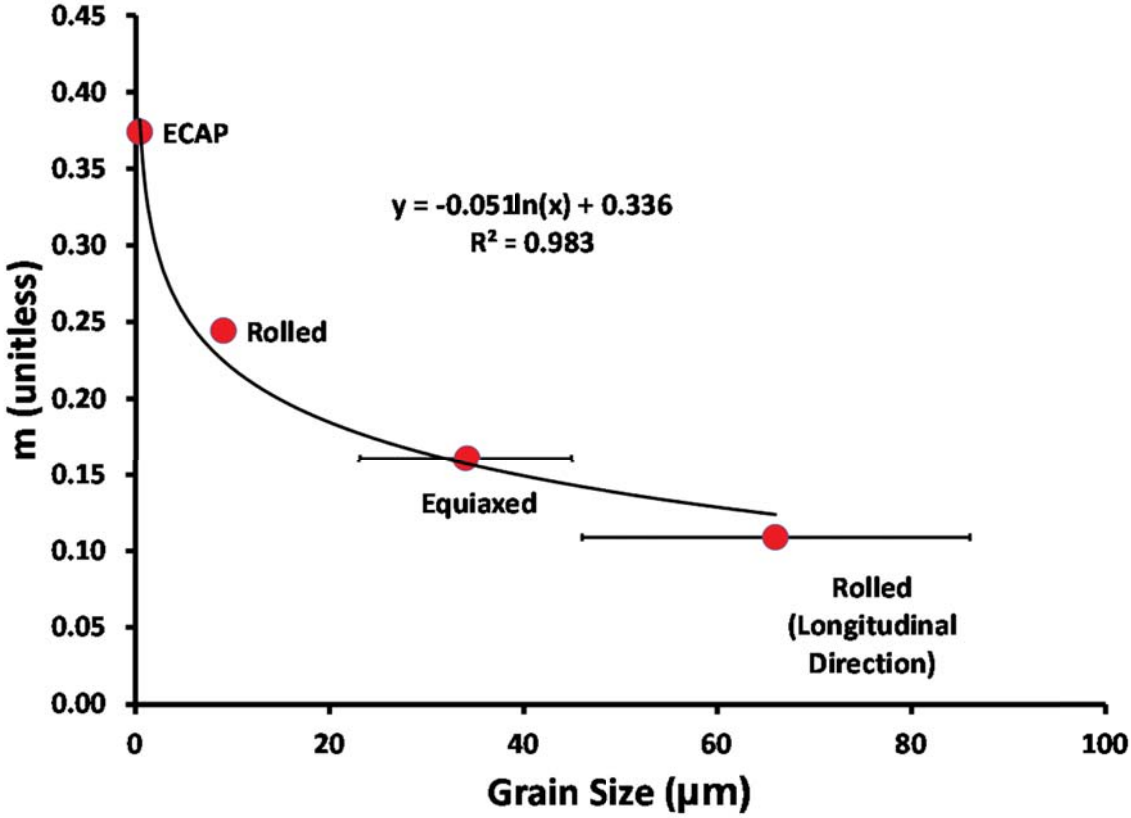

Figure 95: Fitted power law exponent describing spall strength vs. decompression rate for Al 5083, plotted as a function of the grain size. The power law exponent shows a logarithmic decrease with increasing grain size.

10.4 Conclusion

Four different microstructures were produced in various Al-Mg alloys by varying the processing conditions. These four microstructures are a rolled Al 5083-H116 plate, Al 5083 with sub-micron grains formed using equi-channel angular pressing (ECAP), Al 5083 with an equiaxed grain structure produced by stretching and annealing the rolled Al 5083-H116 plate, and a precipitation hardened microstructure for an Al-9wt.% Mg alloy. The spall strength and HEL show little peak stress dependence for any of the four microstructures produced. The HEL for Al 5083 shows a clear increase with decreasing grain size, as would be expected for a Hall-Petch type relationship, but the spall strength shows no trends with grain size for similar impact conditions. However, the grain size does control the decompression rate dependence for each microstructure, with smaller grain size resulting in a higher power law exponential fitting term describing spall strength as a function of decompression rate.

When impacted similarly near a peak stress of 3 GPa, the equiaxed grain structure results in decreased HEL and increased spall strength when compared to the rolled Al 5083 plate. The precipitation hardened microstructure results in increased HEL and decreased spall strength. Finally, the microstructure produced by ECAP results in both increased HEL and increased spall strength, making this processing technique the ideal candidate for producing armor plate with high resistance to both blast and projectile impacts.

CHAPTER 11

SUMMARY AND CONCLUSIONS

This research investigated the effects of microstructure on the dynamic tensile fracture (spall) and dynamic yielding behavior of Al 5083 and similar Al-Mg alloys. The overall objective of this research was to determine the influence of processing methods and resultant microstructure on the spall and Hugoniot elastic response of Al-Mg alloys for superior armor plate performance. The spall response was experimentally measured using symmetric (same material) plate impact testing in a single-stage light-gas gun. Experiments were performed at peak stresses ranging between 1.4 and 6.2 GPa and as a function of plate orientation with respect to the direction of impact.

11.1 Summary of Results

For the experimental conditions used in this work, it was found that the change in stress pulse duration (resultant from changing the flyer plate thickness from 3 mm to 5 mm) had little effect on the spall strength, as the duration from either experiment was long enough to influence similar nucleation and growth of voids. Instead, changing the sample plate thickness had a profound effect on the spall strength values of Al 5083-H116, with the spall strength decreasing from 1.09 GPa for a 6 mm thick sample to 0.83 GPa for a 10 mm thick sample impacted using 3 mm thick flyer plates. The higher spall strength for thinner samples is due to the increase in the decompression rate from the peak stress state. The HEL showed no dependence on the flyer plate or target sample thickness for these experiments.

Baseline experiments were focused on widely available Al 5083-H116 plate, which has a highly textured grain structure and some degree of brittle inclusions and dispersoids located near grain boundaries. The average HEL and spall strength for the H116 samples are 0.43 GPa and 0.81 GPa respectively. Experiments that used thinner target samples resulted in a higher spall strength value of 0.95 GPa due to a faster decompression rate, but the

HEL was unaffected by changes to the flyer plate or sample thickness. For impact along multiple plate directions, the long transverse direction displayed the largest HEL at 0.465 GPa, followed by the short transverse direction and longitudinal directions at 0.44 GPa and 0.40 GPa respectively. The longitudinal direction displayed the highest spall strength of 1.06 GPa as compared to 0.95 GPa along either transverse direction—despite a large difference in grain size for these two orientations (9 μm versus 39 μm).

Post impact microscopy revealed that the damage for impact along the longitudinal direction took a more tortuous path through the microstructure than for the other two directions. Spall damage often propagated along the grain boundaries in the direction of impact rather than growing laterally across the sample. The large grain size in this direction prevented this type of spall damage from coalescing, which could account for the higher spall strength along the direction of impact. SEM images of the fracture surfaces revealed a ductile dimpled fracture surface for both the longitudinal and long transverse directions, but a mixed mode of intergranular and dimple fracture for impact through the thickness of the plate. This mixed fracture mode corresponds to a shoulder in the free surface velocity data observed just after the velocity pullback. The effects of brittle inclusions as spall nucleation sites are seen in all recovered samples, with cracked and debonded inclusions occurring near large voids in all cases.

In contrast to the textured grain structure investigated for the rolled plate, a uniform microstructure was investigated in the form of Al 5083 plates processed using equi-channel angular pressing (ECAP). Processing using ECAP alone resulted in a uniform (0.4 μm grain size) grain structure consisting largely of sub-grains and low angle grain boundaries. Large inclusions and dispersoid particles were present in the microstructure after ECAP, but the particles were uniformly dispersed. Post-ECAP rolling cracked the brittle particles and aligned them along the rolling direction. The alignment and cracking of these brittle phases during processing ultimately controlled the spall behavior of the Al 5083 plates.

The plate processed using ECAP alone showed both increased spall strength and HEL when compared to a standard rolled plate. The spall strength and HEL have values of 0.90 GPa and 0.48 GPa respectively for impact through the plate thickness. In addition,

the plates processed using ECAP show little orientation dependence for either property. Subsequent rolling of the ECAP plates resulted in significant increases to the HEL, but at the expense of the spall strength. The HEL values were 0.72 GPa and 0.63 GPa for two differently rolled plates—one processed using warm and cold rolling, and the other processed only using cold rolling after ECAP. The spall strength, on the other hand, decreased dramatically through the plate thickness for both samples rolled after ECAP. The through-thickness spall strength was 0.60 GPa for the sample processed using warm and cold rolling and 0.74 GPa for the sample processed using cold rolling. Post-ECAP rolling also resulted in orientation dependent spall properties. For experiments performed along all three plate orientations, the spall strength fell from a maximum value of 1.09 GPa for both samples processed using post-ECAP rolling. The spall strength fell to 0.72 GPa for the sample processed using warm and cold rolling and to 0.84 GPa for the sample processed using cold rolling alone. The minimum in spall strength was for impact through the plate thickness in both cases. Post-impact microscopy showed that spall damage grows from large and damaged inclusions for these sample types. Since rolling aligns brittle particles along planes perpendicular to the through-thickness direction, the number of spall nucleation sites is maximized for impact in this direction.

Stretching and annealing a rolled Al 5083-H116 plate resulted in an equiaxed grain structure with a 34 μm grain size. Plate impact testing of this material between 1.4 and 5.5 GPa revealed an upper and lower yielding behavior at the HEL. The lower HEL value remained relatively constant at 0.33 GPa, but the upper HEL value increased from 0.38 GPa to 0.48 GPa as peak stress increased. It is believed that the upper yield point is related to the stress necessary to nucleate dislocations. The lower yield behavior is due to ease of deformation after dislocations have already been nucleated and corresponds well to the DeBroglie limiting HEL value of 0.24 GPa. The spall strength of the equiaxed grain structure was 0.87 GPa, which is higher than that of the rolled Al 5083 plate measured over a similar peak stress range.

An Al-9wt.% Mg alloy with trace additions of silver was found to be precipitation hardenable when heat treated properly. The high magnesium content required that the

material be solution treated using a two-step heat treatment method. Age hardening after this two-step heat treatment resulted in more instances of bulk precipitation, rather than precipitation at the grain boundaries. Three specimens were tested using plate impact experiments near 3 GPa—the as-extruded plate, a dual solution heat treated sample, and a precipitation hardened sample. Precipitation hardening resulted in the largest value of the HEL at 0.52 GPa, but the lowest value of the spall strength at 0.72 GPa. The solution treated specimen displayed an identically low spall strength value of 0.73 GPa, while the as-received plate displayed the largest spall strength value of 0.87 GPa. The results indicate that precipitates have no effect on the spall strength for Al-Mg alloys, with strain hardening being the better strengthening mechanism for these alloy types.

Figures 96 and 97 summarize the high strain-rate behavior of Al-Mg alloys as a function of the processing conditions used in this project. The VISAR free surface velocity data for all four of the microstructures investigated is shown in Figure 96 for a similar impact velocity near 430 m/s. This velocity corresponds to the middle of the investigated peak stress range, having a value near 3 GPa. The spall strength and HEL values for impact through the plate thickness for the four microstructures investigated is shown in Figure 97.

Using the rolled plate as the baseline, the HEL can be increased using either ECAP or precipitation hardening; however, precipitation hardening is not an effective means of increasing the spall strength, as the precipitation hardened sample displays the lowest spall strength of any microstructure. The equiaxed microstructure displays a lower HEL value due to the lower dislocation density produced by annealing. Both the equiaxed grain structure and the grain structure produced by ECAP result in increases to the spall strength, despite large differences in the grain size (34 μm versus 0.4 μm respectively). In fact one-dimensional modeling using the Cochran and Banner spall model has shown that the grain size is not related to the distribution of voids formed during spalling. Instead, the size and number density of brittle particles (such as inclusions and dispersoids) controls void formation for spalling of Al 5083. However, the grain size does control the decompression rate dependence of the spall strength, with smaller grain size resulting in more dependence on the decompression rate.

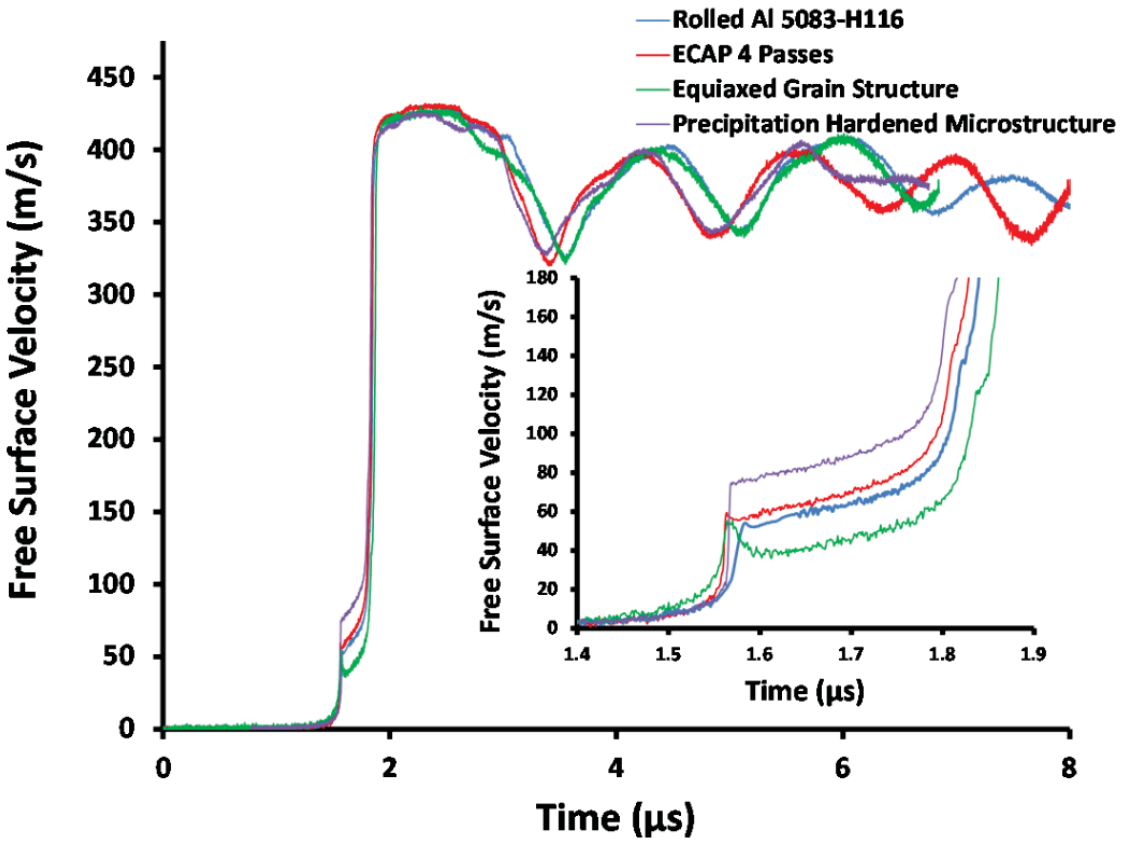

Figure 96: Free surface velocity traces for all microstructures investigated. The four samples were a rolled Al 5083-H116 plate, an Al 5083 plate pressed four times using ECAP, Al 5083 with an equiaxed grain structure produced by stretching and annealing, and a precipitation hardened Al-9wt.% Mg plate. Impact was performed through the plate thickness near 3 GPa in each case.

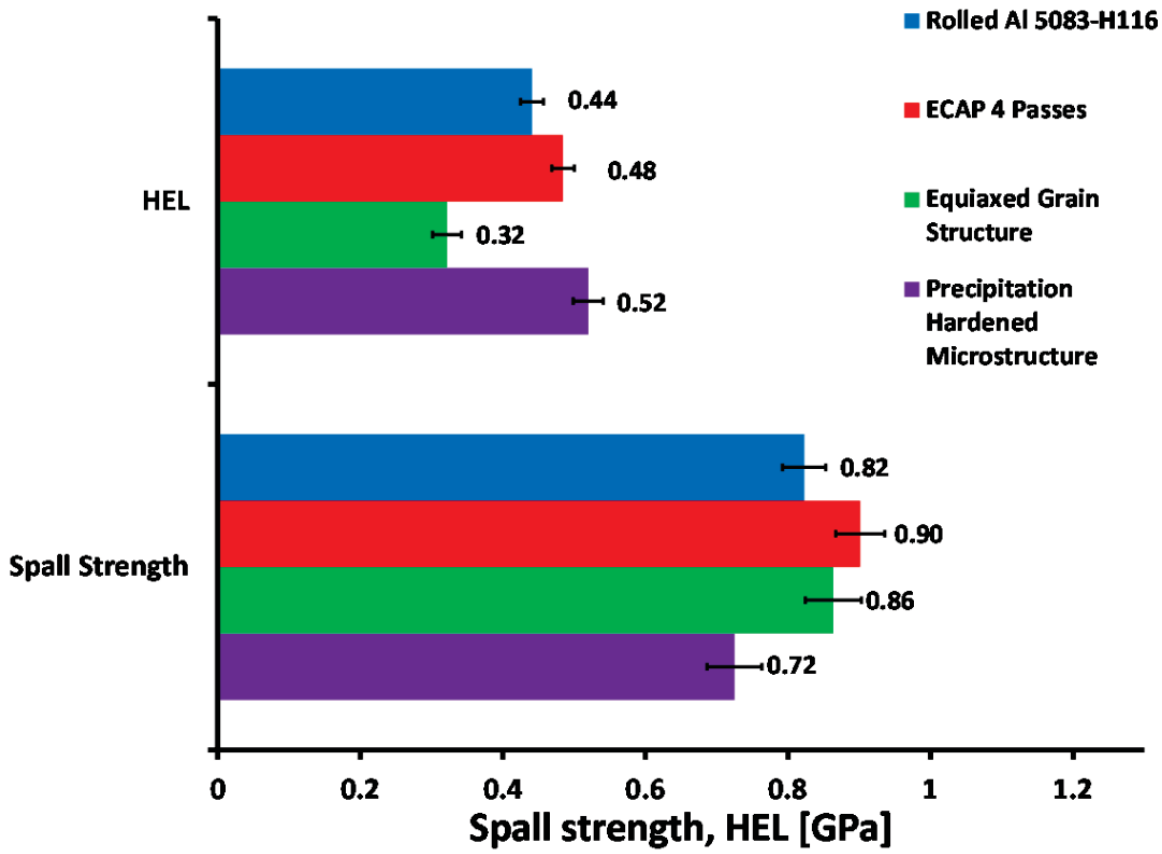

Figure 97: Spall strength and HEL values for all microstructures investigated. The four samples were a rolled Al 5083-H116 plate, an Al 5083 plate pressed four times using ECAP, Al 5083 with an equiaxed grain structure produced by stretching and annealing, and a precipitation hardened Al-9wt.% Mg plate. Impact was performed through the plate thickness near 3 GPa in each case.

Processing via ECAP alone shows promise for increasing the impact resistance of aluminum alloy plates, as this resulted in the best combination of both HEL and spall strength when compared to similar impact conditions with other microstructures. The grain structure produced by ECAP is uniform throughout the plate, which removes the orientation specific spall properties evidenced in a rolled plate. Furthermore, the inclusions (which control void formation) are also uniformly dispersed, which results in a smaller number density of spall failure sites for the plane normal to the through-thickness direction. Therefore, processing using ECAP is expected to yield better penetration resistance and blast resistance for Al 5083 armor plates.

11.2 Conclusions

The processing history of Al-Mg alloy armor plates affects the underlying microstructure, which ultimately determines the dynamic yield and fracture properties (quantified by the HEL and spall strength respectively). Al-Mg armor plates are normally processed through rolling, with a large degree of cold rolling to promote significant strain hardening. Strain hardening increases the HEL, resulting in better ballistic properties. Rolling of Al 5083 also results in a textured grain structure with grains aligning along the rolling direction and thinning in the through-thickness direction. The textured microstructure results in varying HEL and spall strength values with impact orientation. For these experiments, the longitudinal direction displayed the highest spall strength value.

The large difference in grain size along each orientation of rolled Al 5083 plate results in different decompression rate dependence of the spall strength, with impact through the plate thickness (having the smallest grain size) resulting in the highest power law exponent for spall strength versus decompression rate, and impact in the longitudinal direction (having the largest grain size) resulting in the lowest power law exponent. The effects of grain size on the power law fit were also observed for equiaxed Al 5083 microstructures produced via ECAP and annealing, with the power law exponent again increasing with decreasing grain size. Thus, Al 5083 shows increasing decompression rate dependence with decreasing grain size regardless of the processing route used to produce the grain structure.

For identical impact conditions, the amount and orientation of brittle particles, such as inclusions and dispersoids, is the most dominant microstructural feature affecting the spall strength of Al 5083. Iron and silicon rich inclusions are formed during the casting process, whereas manganese rich dispersoids are formed from solid solution during the pre-heat treatment. The particles act as nucleation sites for spall damage and ultimately determine the void size distributions formed during spallation. Rolling or stretching an armor plate aligns and cracks the brittle particles in the longitudinal direction, which results in a larger number density of brittle particles within the short transverse plane, making void nucleation (and spalling) easier for impact perpendicular to this direction. Rolling of plates containing large brittle particles (as in the ECAP microstructure) results in especially poor spall strength through the plate thickness.

Al-Mg alloys with high magnesium content (along with trace silver additions) are precipitation hardenable; however, precipitate phases do not affect the spall strength in these materials. Heat treatment at high temperature ($> 400°C$), such as solution treatment or annealing, removes significant dislocation density, which results in upper and lower yielding at the HEL. Precipitation hardening removes this upper and lower yielding, and results in increased HEL values, but it is at the expense of decreased spall strength.

Based on the results of this research, the best processing route for Al-Mg alloy armor plate would use strain hardening, rather than heat treatment, to increase the HEL. In order to increase the spall strength, the grain structure should be uniform and have a uniform distribution of brittle particles, with the smallest number density of particles achievable. Of the four microstructures studied, Al 5083 processed using ECAP is the best fit to these requirements and shows promise for yielding superior armor plate material.

11.3 Suggestions for Future Work

More research should be performed on the use of ECAP as a processing technique for Al-Mg alloy armor plates. Specifically, an alloy other than Al 5083, with lower iron and silicon contents, should be investigated. This would result in a lower density of brittle inclusions within the alloy, possibly leading to higher spall strength.

In addition, the decompression rate dependence of Al 5083 should be investigated over a larger range of decompression rates. The experiments presented within this thesis were performed using a single-stage light-gas gun, which limits the available strain-rate range. Higher strain rates could be investigated using multiple-stage gas guns, powder guns, explosive-driven flyer plates, or laser-driven flyer plates. These experiments should also investigate the power law fits to the decompression rate over a larger range of grain sizes than those reported here.

APPENDIX A

EQUATION OF STATE

This appendix presents the equation of state (EOS) data for Al 5083-H116 in terms of the shock velocity (U_S) versus the particle velocity (u_p). As shown in Equation 4, the EOS is often a linear empirical equation, having an intercept of C_0 and a slope of S. The EOS data is listed in Table 4, and is plotted in Figure 98.

The data in Figure 98 were fit using linear least squares regression to yield a C_0 value of 5.2 and an S value of 1.0. This value of C_0 is identical to the value of the bulk sound speed (C_B), listed in Table 3 for this material, which is an indicator that the measurements are accurate.

The EOS data for Al 5083-H32 and Al 5083-H131 measured by Boteler and Dandekar [94] are also included in Figure 98. The EOS for the H32 temper fits the measured H131 data extremely well. Since the H32 and H116 tempers have nearly identical mechanical properties [115], it is expected that the EOS data would be similar. The EOS for the H131 temper has a higher C_0 and S value than the H116 data presented in Figure 98. The H131 temper has a higher bulk modulus than either the H32 or H116 temper, which would account for the difference in the EOS data.

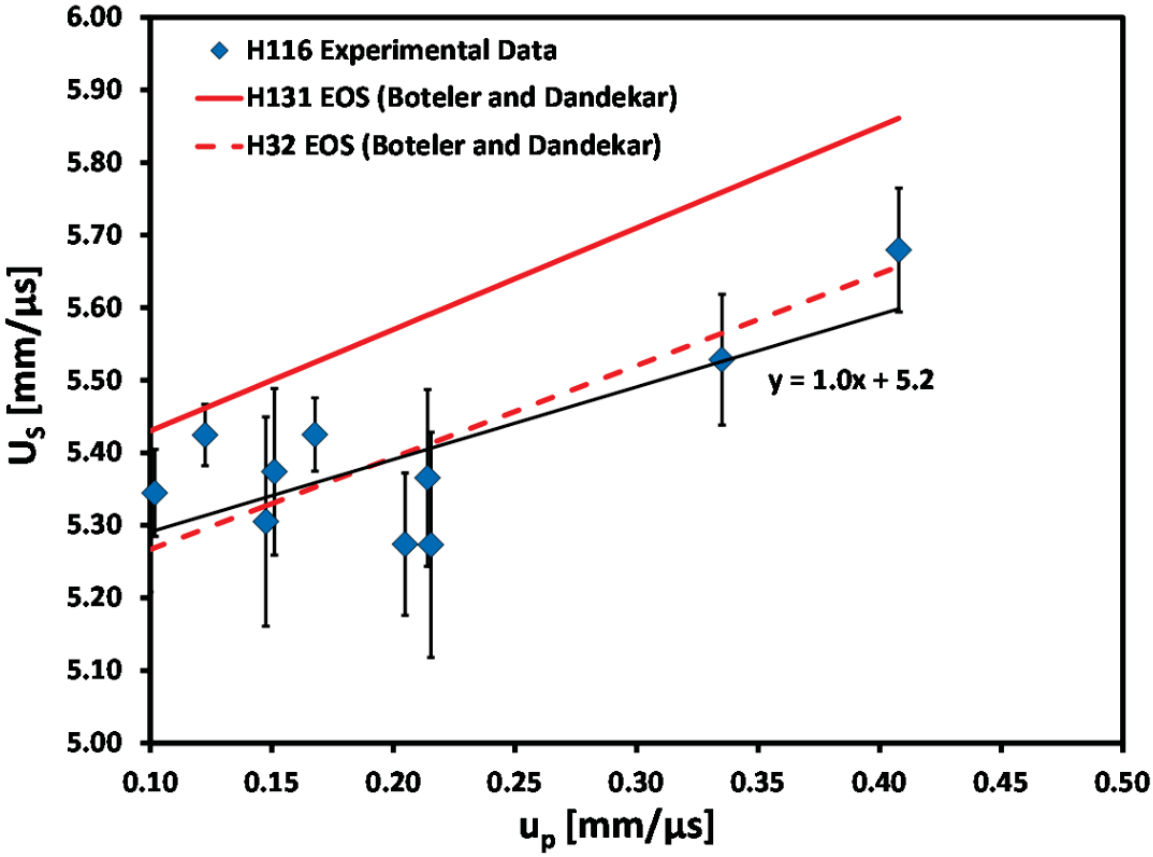

Figure 98: Equation of state (EOS) plot for Al 5083-H116 impacted through the plate thickness compared to other Al 5083 tempers. The EOS is a linear fit to the shock speed versus particle velocity. The EOS data for the H32 and H131 tempers were published by Boteler and Dandekar [94].

APPENDIX B

VOID SIZE DISTRIBUTIONS

This appendix quantifies and discusses the void size distributions measured for the Al 5083-H116 sample impacted through the plate thickness near 200 m/s. This is the only sample that did not completely spall during plate impact testing, making it the only recovered sample suitable for void size quantification prior to the completely spalled state. Post-impact void counting was performed on the soft-recovered sample to quantify the void volume fraction (f_V) and size distribution (N_g) as a function of location within the sample. These data are shown in Figures 99 and 100 respectively. Figure 99 displays the volume fraction of voids calculated from a standard point counting technique as a function of distance from the spall plane. The volume fraction is roughly symmetric with respect to the spall plane, and the highest degree of damage is at the spall plane itself. These data are consistent with other plate impact spall tests available in the literature [44, 100].

The size distribution of the voids was quantified by measuring the areal density of voids as a function of location within the sample, followed by using Saltykov's [122] technique for converting areal density to volume density. The data in Figure 100 are presented as the cumulative void density (N_g), indicating the number density of voids greater than a given size. The data is presented for five distance (d) intervals from the rear free surface.

The data in Figure 100 were fit with an exponential function given by Equation 41, where N_0 and R_1 are the total number density of voids and a characteristic size fitting parameter respectively. The best fit values of N_0 and R_1 from non-linear least squares regression are given in Table 16. The values in Table 16 can be compared to the damage parameter from one-dimensional modeling of the spall response of Al 5083 presented in Chapter 9.

$$N_g = N_0 exp\left(\frac{-R}{R_1}\right) \tag{41}$$

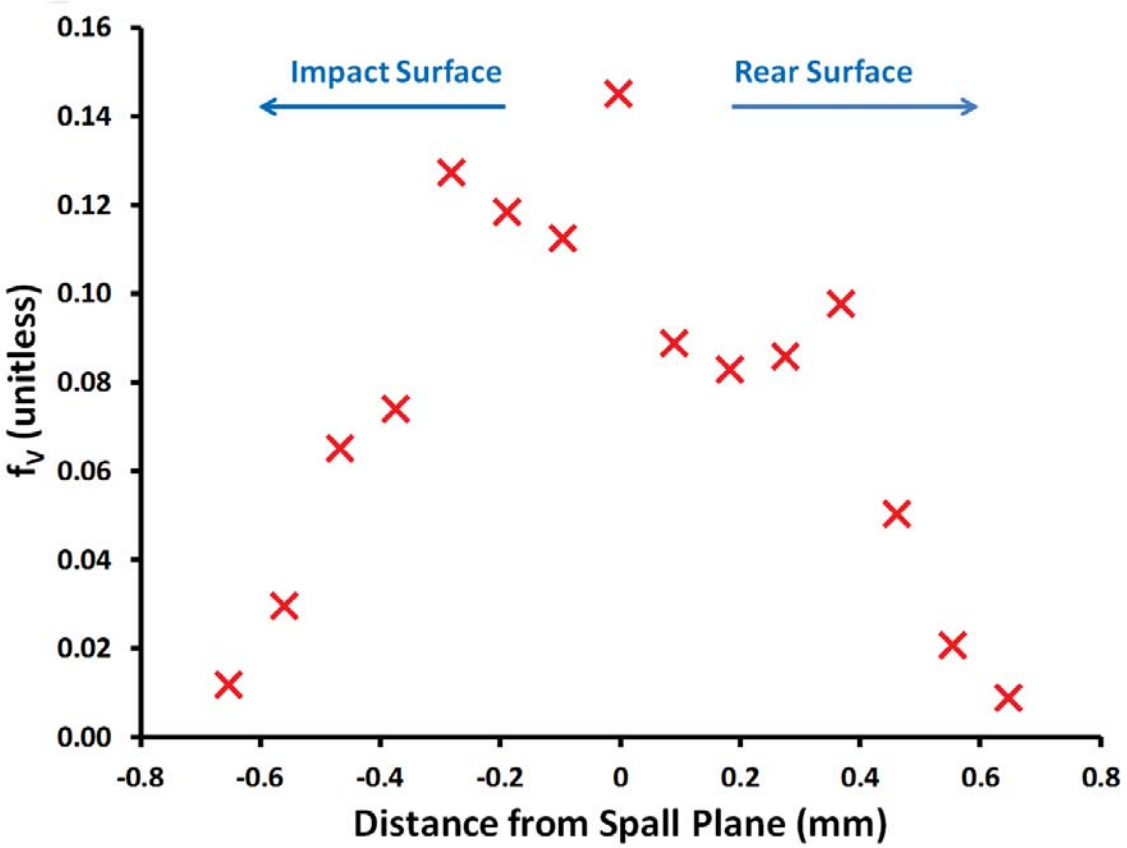

Figure 99: Volume fraction of voids as a function of distance from the spall plane for an Al 5083-H116 sample impacted near 200 m/s. Positive distances correspond to locations approaching the rear surface, and negative distances correspond to locations approaching the impact surface of the sample.

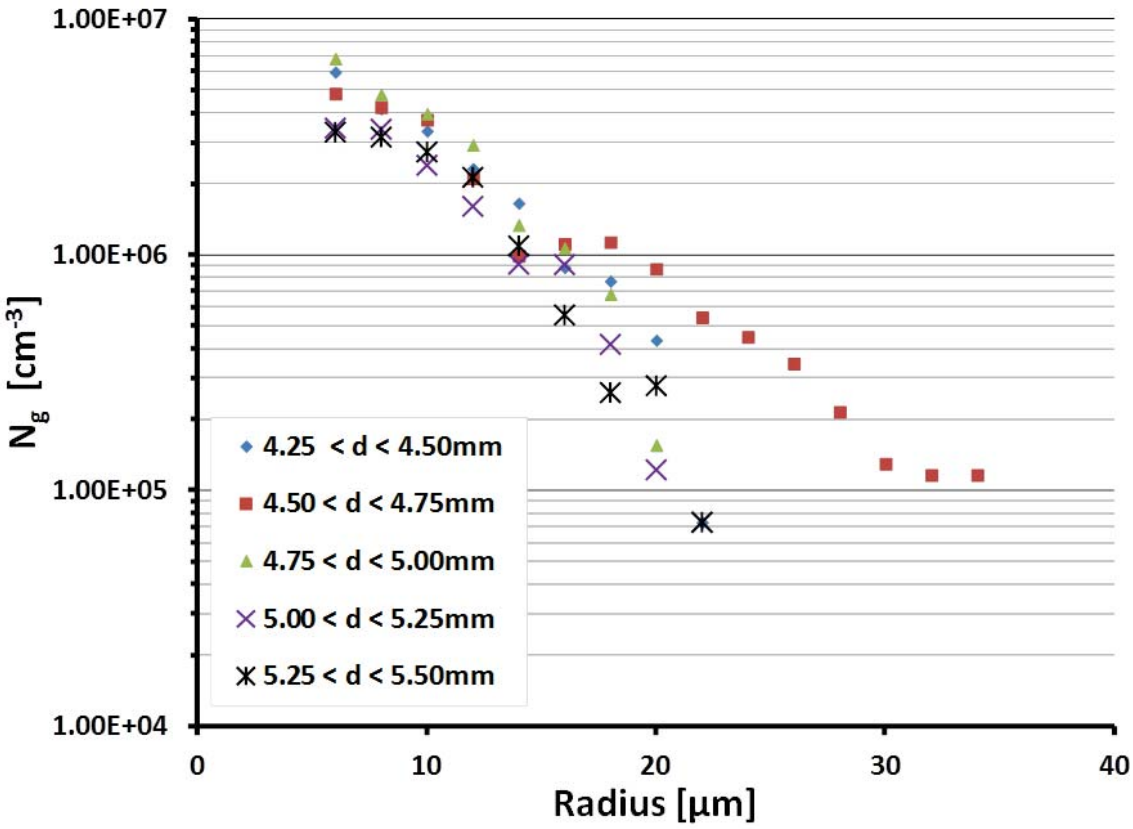

Figure 100: Cumulative number density of voids as a function of distance from the rear surface for an Al 5083-H116 sample impacted near 200 m/s

Table 16: Exponential fitting parameters as a function of distance from the rear free surface for the void size distributions measured from Al 5083-H116 impacted at 200 m/s

	4.25–4.50 mm	**4.50–4.75 mm**	**4.75–5.00 mm**	**5.00–5.25 mm**	**5.25–5.50 mm**
$\boldsymbol{N_0}$ $[\mathbf{cm^{-3}}]$	1.67 X 10^7	1.20 X 10^7	1.98 X 10^7	9.84 X 10^6	9.00 X 10^6
$\boldsymbol{R_1}$ $[\boldsymbol{\mu}\mathbf{m}]$	5.90	7.20	5.74	6.48	6.99

Bibliography

[1] Davis, J. R., *Aluminum and Aluminum Alloys*. ASM Specialty Handbook, Materials Park, OH: ASM International, 1993.

[2] Kubota, M., Nie, J. F., and Muddle, B. C., "Characterisation of Precipitation Hardening Response and As-Quenched Microstructures in Al-Mg(-Ag) Alloys," *Materials Transactions*, vol. 45, no. 12, pp. 3256–3263, 2004.

[3] Mondolfo, L. F., *Aluminium Alloys : Structure and Properties*. London: Butterworths, 1976.

[4] Martin, J. W., Doherty, R. D., and Cantor, B., *Stability of Microstructure in Metallic Systems*. Cambridge University Press: Cambridge, 2nd ed., 1997.

[5] McQueen, H. and Blum, W., "Dynamic Recovery: Sufficient Mechanism in the Hot Deformation of Al (< 99.99%)," *Materials Science and Engineering A*, vol. 290, no. 1, pp. 95–107, 2000.

[6] Gourdet, S. and Montheillet, F., "A Model of Continuous Dynamic Recrystallization," *Acta Materialia*, vol. 51, no. 9, pp. 2685–2699, 2003.

[7] Porter, D. A. and Easterling, K. E., *Phase Transformations in Metals and Alloys*. New York: Van Nostrand Reinhold, 1981.

[8] Montheillet, F. and Le Coze, J., "Influence of Purity on the Dynamic Recrystallization of Metals and Alloys," *Physica Status Solidi A*, vol. 189, no. 1, pp. 51–58, 2002.

[9] Yamagata, H., "Multipeak Stress Oscillations of Five-Nine-Purity Aluminum during a Hot Compression Test," *Scripta Metallurgica et Materialia*, vol. 27, no. 2, pp. 201–203, 1992.

[10] Yamagata, H., "Dynamic Recrystallization and Dynamic Recovery in Pure Aluminum at 583 K," *Acta Metallurgica et Materialia*, vol. 43, no. 2, pp. 723–729, 1995.

[11] Ponge, D., Bredehoft, M., and Gottstein, G., "Dynamic Recrystallization in High Purity Aluminum," *Scripta Materialia*, vol. 37, no. 11, pp. 1769–1775, 1997.

[12] Sheppard, T., Parson, N., and Zaidi, M., "Dynamic Recrystallization in Al-7Mg Alloy," *Metal Science*, vol. 17, no. 10, pp. 481–490, 1983.

[13] Gourdet, S. and Montheillet, F., "Experimental Study of the Recrystallization Mechanism during Hot Deformation of Aluminium," *Materials Science and Engineering A*, vol. 283, no. 1, pp. 274–288, 2000.

[14] McQueen, H. and Celliers, O., "Application of Hot Workability Studies to Extrusion Processing: Part II. Microstructural Development and Extrusion of Al, Al-Mg, and Al-Mg-Mn Alloys," *Canadian Metallurgical Quarterly*, vol. 35, no. 4, pp. 305–319, 1996.

[15] Cerri, E., Evangelista, E., and McQueen, H., "Overview of the High Temperature Substructure Development in Al-Mg Alloys," *High Temperature Materials and Processes*, vol. 18, no. 4, pp. 227–240, 1999.

[16] Tensi, H. M., Dropmann, P., and Borchers, H., "Plastic Deformation of Aluminum-Magnesium Single Crystals," *Zeitschrift fuer Metallkunde*, vol. 61, no. 7, pp. 518–524, 1970.

[17] Gardner, K. and Grimes, R., "Recrystallization during Hot Deformation of Aluminium Alloys," *Metal Science*, vol. 13, no. 3–4, pp. 216–222, 1978.

[18] McQueen, H., "Development of Dynamic Recrystallization Theory," *Materials Science and Engineering A*, vol. 387-389, no. 1–2, pp. 203–208, 2004.

[19] Solberg, J., McQueen, H., Ryum, N., and Nes, E., "Influence of Ultra-High Strains at Elevated Temperatures on the Microstructure of Aluminium I," *Philosophical Magazine A*, vol. 60, no. 4, pp. 447–471, 1989.

[20] McQueen, H., Solberg, J., Ryum, N., and Nes, E., "Evolution of Flow Stress in Aluminium during Ultra-High Straining at Elevated Temperatures II," *Philosophical Magazine A*, vol. 60, no. 4, pp. 473–85, 1989.

[21] Kassner, M. and McMahon, M., "Dislocation Microstructure of Aluminium Deformed to very Large Steady-State Creep Strains," *Metallurgical Transactions A*, vol. 18A, no. 5, pp. 835–846, 1987.

[22] Kassner, M., Myshlyaev, M., and McQueen, H., "Large-Strain Torsional Deformation in Aluminum at Elevated Temperatures," *Materials Science and Engineering A*, vol. 108A, pp. 45–61, 1989.

[23] Henshall, G., Kassner, M., and McQueen, H., "Dynamic Restoration Mechanisms in Al-5.8 at. pct. Mg Deformed to Large Strains in the Solute Drag Regime," *Metallurgical Transactions A*, vol. 23A, no. 3, pp. 881–889, 1992.

[24] Blum, W., Zhu, Q., Merkel, R., and McQueen, H., "Geometric Dynamic Recrystallization in Hot Torsion of Al-5Mg-0.6Mn (AA5083)," *Materials Science and Engineering A*, vol. A205, no. 1–2, pp. 23–30, 1996.

[25] Blum, W., Zhu, Q., Merkel, R., and McQueen, H., "Dynamic Restoration Mechanisms in Hot Torsion of Al-5Mg and Al," *Zeitschrift fur Metallkunde*, vol. 87, no. 1, pp. 14–23, 1996.

[26] McQueen, H., Evangelista, E., and Kassner, M., "The Classification and Determination of Restoration Mechanisms in the Hot Working of Al Alloys," *Zeitschrift fur Metallkunde*, vol. 82, no. 5, pp. 336–345, 1991.

[27] McQueen, H., Evangelista, E., Bowles, J., and Crawford, G., "Hot Deformation and Dynamic Recrystallization of Al-5Mg-0.8Mn Alloy," *Metal Science*, vol. 18, no. 8, pp. 395–402, 1984.

[28] Sheppard, T. and Tutcher, M., "Effect of Process Parameters on Structure and Properties of Al-5Mg-0.8Mn Alloy (AA 5456)," *Metals Technology*, vol. 8, no. 8, pp. 319–327, 1981.

[29] Castro-Fernandez, F. and Sellars, C., "Static Recrystallisation and Recrystallisation during Hot Deformation of Al-1Mg-1Mn Alloy," *Materials Science and Technology*, vol. 4, no. 7, pp. 621–627, 1988.

[30] Humphreys, F. and Kalu, P., "Dislocation-Particle Interactions during High Temperature Deformation of Two-Phase Aluminium Alloys," *Acta Metallurgica*, vol. 35, no. 12, pp. 2815–2829, 1987.

[31] Thanaboonsombut, B. and Sanders Jr., T., "Effect of Cooling Rate from the Melt on the Recrystallization Behavior of Aluminum Alloy 6013," *Metallurgical and Materials Transactions A*, vol. 28A, no. 10, pp. 2137–2142, 1997.

[32] Gray, G. T., Bourne, N. K., Millett, J. C. F., Lopez, M. F., and Vecchio, K. S., *Influence of Microstructural Anisotropy on the Spallation of 1080 Eutectoid Steel*, vol. 620 of *AIP Conference Proceedings*, pp. 479–482. 2002.

[33] Clements, B. E., Mas, E. M., and Gray, G. T., *Investigation of the Observed Anisotropic Fracture in Steels*, vol. 620 of *AIP Conference Proceedings*, pp. 535–538. 2002.

[34] Edwards, M. R., Bourne, N. K., and Millett, J. C. F., *The Effect of Orientation on the Spall Strength of the Aluminium Alloy 7010-T6*, vol. 620 of *AIP Conference Proceedings*, pp. 523–526. 2002.

[35] Appleby-Thomas, G. J. and Hazell, P. J., "A Study on the Strength of an Armour-Grade Aluminum under High Strain-Rate Loading," *Journal of Applied Physics*, vol. 107, no. 12, pp. 123508–1—123508–12, 2010.

[36] Christy, S., Pak, H.-R., and Meyers, M. A., "Effect of Metallurgical Parameters on Dynamic Fracture by Spalling of Copper," in *Metallurgical Applications of Shock-Wave and High-Strain-Rate Phenomena* (Murr, L. E., Staudhammer, K. P., and Meyers, M. A., eds.), (New York), pp. 835–863, Marcel Dekker Inc, 1986.

[37] Schwartz, A. J., Cazamias, J. U., Fiske, P. S., and Minich, R. W., *Grain Size and Pressure Effects on Spall Strength in Copper*, vol. 620 of *AIP Conference Proceedings*, pp. 491–494. 2002.

[38] Chen, X., Asay, J. R., Dwivedi, S. K., and Field, D. P., "Spall Behavior of Aluminum with Varying Microstructures," *Journal of Applied Physics*, vol. 99, no. 2, pp. 023528–1—023528–13, 2006.

[39] Pedrazas, N. A., Worthington, D. L., Dalton, D. A., Sherek, P. A., Steuck, S. P., Quevedo, H. J., Bernstein, A. C., Taleff, E. M., and Ditmire, T., "Effects of Microstructure and Composition on Spall Fracture in Aluminum," *Materials Science and Engineering A*, vol. 536, pp. 117–123, 2012.

[40] Dalton, D. A., Worthington, D. L., Sherek, P. A., Pedrazas, N. A., Quevedo, H. J., Bernstein, A. C., Rambo, P., Schwarz, J., Edens, A., Geissel, M., Smith, I. C., Taleff, E. M., and Ditmire, T., "Microstructure Dependence of Dynamic Fracture and Yielding in Aluminum and an Aluminum Alloy at Strain Rates of $2x10^6$ s^{-1} and Faster," *Journal of Applied Physics*, vol. 110, pp. 103509–1—103509–10, 2011.

[41] Riddle, Y. and Sanders Jr., T., "A Study of Coarsening, Recrystallization, and Morphology of Microstructure in Al-Sc-(Zr)-(Mg) Alloys," *Metallurgical and Materials Transactions A*, vol. 35A, no. 1, pp. 341–350, 2004.

[42] Zener, C., "Grains, Phases, and Interfaces: An Interpretation of Microstructure," *Transactions of TMS-AIME*, vol. 175, pp. 15–51, 1949. (Private Communication to C.S. Smith).

[43] Sanders Jr., T., "Observation of Nonuniform Precipitation of Mn in an Al-Mg Ingot," *Metallography*, vol. 14, no. 3, pp. 177–189, 1981.

[44] Antoun, T., Seaman, L., Curran, D. R., Kanel, G. I., Razorenov, S. V., and Utkin, A. V., *Spall Fracture*. High-Pressure Shock Compression of Condensed Matter, New York: Springer, 2003.

[45] Valiev, R. Z. and Langdon, T. G., "Principles of Equal-Channel Angular Pressing as a Processing Tool for Grain Refinement," *Progress in Materials Science*, vol. 51, no. 7, pp. 881–981, 2006.

[46] Luri, R., Luis Perez, C. J., Salcedo, D., Puertas, I., Leon, J., Perez, I., and Fuertes, J. P., "Evolution of Damage in AA-5083 Processed by Equal Channel Angular Extrusion using Different Die Geometries," *Journal of Materials Processing Technology*, vol. 211, no. 1, pp. 48–56, 2011.

[47] Nakashima, K., Horita, Z., Nemoto, M., and Langdon, T. G., "Development of a Multi-Pass Facility for Equal-Channel Angular Pressing to High Total Strains," *Materials Science and Engineering A*, vol. 281, no. 1, pp. 82–87, 2000.

[48] Soliman, M. S., El-Danaf, E. A., and Almajid, A. A., "Effect of Equal-Channel Angular Pressing Process on Properties of 1050 Al Alloy," *Materials and Manufacturing Processes*, vol. 27, no. 7, pp. 746–750, 2012.

[49] Nagarajan, D., Chakkingal, U., and Venugopal, P., "Influence of Cold Extrusion on the Microstructure and Mechanical Properties of an Aluminium Alloy Previously Subjected to Equal Channel Angular Pressing," *Journal of Materials Processing Technology*, vol. 182, no. 1–3, pp. 363–368, 2007.

[50] Llorca-Isern, N., Luis-Perez, C., Gonzalez, P. A., Laborde, L., and Patino, D., "Analysis of Structure and Mechanical Properties of AA 5083 Aluminium Alloy Processed by ECAE," *Reviews on Advanced Materials Science*, vol. 10, no. 5, pp. 473–478, 2005.

[51] Rebhi, A., Makhlouf, T., Njah, N., Champion, Y., and Couzinie, J. P., "Characterization of Aluminum Processed by Equal Channel Angular Extrusion: Effect of Processing Route," *Materials Characterization*, vol. 60, no. 12, pp. 1489–1495, 2009.

[52] Mishin, O. V., Segal, V. M., and Ferrasse, S., "Quantitative Microstructural Characterization of Thick Aluminum Plates Heavily Deformed using Equal Channel Angular Extrusion," *Metallurgical and Materials Transactions A*, vol. 43, no. 12, pp. 4767–4776, 2012.

[53] Jin, H., Gallerneault, M., Segal, V. M., Young, P. J., and Lloyd, D. J., "Grain Structure and Texture in Aluminium Alloy AA5083 after Equal Angular Channel Extrusion, Warm Rolling and Subsequent Annealing," *Materials Science and Technology*, vol. 27, no. 4, pp. 789–792, 2011.

[54] Apps, P. J., Berta, M., and Prangnell, P. B., "The Effect of Dispersoids on the Grain Refinement Mechanisms during Deformation of Aluminium Alloys to Ultra-High Strains," *Acta Materialia*, vol. 53, no. 2, pp. 499–511, 2005.

[55] Hockauf, M., Meyer, L. W., Zillmann, B., Hietschold, M., Schulze, S., and Kruger, L., "Simultaneous Improvement of Strength and Ductility of Al-Mg-Si Alloys by Combining Equal-Channel Angular Extrusion with Subsequent High-Temperature Short-Time Aging," *Materials Science and Engineering A*, vol. 503, no. 1–2, pp. 167–171, 2009.

[56] Garcia-Infanta, J. M., Zhilyaev, A. P., Carreno, F., Ruano, O. A., Su, J. Q., Menon, S. K., and McNelley, T. R., "Strain Path and Microstructure Evolution during Severe Deformation Processing of an As-Cast Hypoeutectic Al-Si Alloy," *Journal of Materials Science*, vol. 45, no. 17, pp. 4613–4620, 2010.

[57] Kim, K. J., Yang, D. Y., and Yoon, J. W., "Microstructural Evolution and its Effect on Mechanical Properties of Commercially Pure Aluminum Deformed by ECAE (Equal Channel Angular Extrusion) via Routes A and C," *Materials Science and Engineering A*, vol. 527, no. 29–30, pp. 7927–7930, 2010.

[58] Mishin, O. V., Bowen, J. R., and Lathabai, S., "Quantification of Microstructure Refinement in Aluminium Deformed by Equal Channel Angular Extrusion: Route A vs. Route B_c in a 90° die," *Scripta Materialia*, vol. 63, no. 1, pp. 20–23, 2010.

[59] Nikulin, S. A., Dobatkin, S. V., Khanzhin, V. G., Rogachev, S. O., and Chakushin, S. A., "Effect of Submicrocrystalline Structure and Inclusions on the Deformation and Failure of Aluminum Alloys and Titanium," *Metal Science and Heat Treatment*, vol. 51, no. 5–6, pp. 208–217, 2009.

[60] Bate, P. S., Hyde, K. B., Court, S. A., and Humphreys, F. J., "Dynamic Grain Growth in Superplastic and Non-Superplastic Aluminium Alloys," *Materials Science Forum*, vol. 447–448, pp. 61–66, 2004.

[61] Chen, H. H., Wang, J. Y., Lee, J., and Lee, S., "Superplasticity of AA5083 Alloy as Processed by Equal Channel Angular Extrusion," *Journal of Alloys and Compounds*, vol. 460, no. 1–2, pp. 305–308, 2008.

[62] Chen, Y. C., Huang, Y. Y., Chang, C. P., and Kao, P. W., "The Effect of Extrusion Temperature on the Development of Deformation Microstructures in 5052 Aluminium Alloy Processed by Equal Channel Angular Extrusion," *Acta Materialia*, vol. 51, no. 7, pp. 2005–2015, 2003.

[63] Kawazoe, M., Shibata, T., Mukai, T., and Higashi, K., "Elevated Temperature Mechanical Properties of a 5056 Al-Mg Alloy Processed by Equal-Channel-Angular-Extrusion," *Scripta Materialia*, vol. 36, no. 6, pp. 699–705, 1997.

[64] Kawazoe, M., Shibata, T., and Higashi, K., "Grain Refinement and Mechanical Properties at Elevated Temperature of Al-Mg Alloy by Hard-Strain-Process," *Materials Science Forum*, vol. 233–234, pp. 207–214, 1997.

[65] Mabuchi, M., Iwasaki, H., and Higashi, K., "Microstructure and Mechanical Properties of 5056 Al Alloy Processed by Equal Channel Angular Extrusion," *Nanostructured Materials*, vol. 8, no. 8, pp. 1105–1111, 1997.

[66] Mukai, T., Kawazoe, M., and Higashi, K., "Strain-Rate Dependence of Mechanical Properties in AA5056 Al-Mg Alloy Processed by Equal-Channel-Angular-Extrusion," *Materials Science and Engineering A*, vol. A247, no. 1–2, pp. 270–274, 1998.

[67] Musin, F., Kaibyshev, R., Motohashi, Y., and Itoh, G., "High Strain Rate Superplasticity in a Commercial Al-Mg-Sc Alloy," *Scripta Materialia*, vol. 50, no. 4, pp. 511–516, 2004.

[68] Ning, J. L. and Jiang, D. M., "Development of Microstructure and Mechanical Properties of As Cast Al-Mg-Mn Alloy during High Temperature ECAP," *Materials Science and Technology*, vol. 24, no. 1, pp. 90–96, 2008.

[69] Jiang, L. N., Jiang, D. M., Fan, X. G., Lai, Z. H., Meng, Q. C., and Wang, D. L., "Mechanical Properties and Microstructure of Al-Mg-Mn-Zr Alloy Processed by Equal Channel Angular Pressing at Elevated Temperature," *Materials Characterization*, vol. 59, no. 3, pp. 306–311, 2008.

[70] Berta, M., Apps, P. J., and Prangnell, P. B., "Effect of Processing Route and Second Phase Particles on Grain Refinement during Equal-Channel Angular Extrusion," *Materials Science and Engineering A*, vol. 410–411, pp. 381–385, 2005.

[71] Kubota, M., "Characterisation of Precipitate Microstructures of Natural and Artificial Ageing in Al-Mg(-Ag) Alloys," *Materials Transactions*, vol. 46, no. 2, pp. 241–250, 2005.

[72] Kubota, M., Nie, J. F., and Muddle, B. C., "Identification of Metastable Rod-Like Particles in an Isothermally Aged Al-10Mg-0.5Ag (mass%) Alloy," *Materials Transactions*, vol. 46, no. 6, pp. 1288–1294, 2005.

[73] Kubota, M., "Identification of β Phase Particles in an Isothermally Aged Al-10 mass%Mg-0.5 mass% Ag Alloy," *Materials Transactions*, vol. 46, no. 11, pp. 2437–2442, 2005.

[74] Kubota, M. and Muddle, B., "Effect of Trace Additions of Ag on Precipitation in Al-Mg Alloys," *Materials Transactions*, vol. 46, no. 12, pp. 2968–2974, 2005.

[75] Auld, J. and Cousland, S., "The Metastable T' Phase in Al-Zn-Mg and Al-Ag-Mg Alloys," *Metal Science*, vol. 10, no. 12, pp. 445–448, 1976.

[76] Auld, J., "X-ray Investigation of Ageing in an Aluminium-5% Magnesium Alloy with Small Silver Additions," *Acta Metallurgica*, vol. 16, no. 1, pp. 97–101, 1968.

[77] Cousland, S. M. and Tate, G., "Structural Changes Associated with Solid-State Reactions in Al-Ag-Mg Alloys," *Journal of Applied Crystallography*, vol. 19, pp. 174–180, 1986.

[78] Lim, S., Tibballs, J., and Rossiter, P., "An Assessment of Thermodynamic Equilibria in the Ag-Al-Cu-Mg Quaternary System in Relation to Precipitation Reactions," *Zeitschrift fur Metallkunde*, vol. 88, no. 3, pp. 236–245, 1997.

[79] Meyers, M. A. and Aimone, C. T., "Dynamic Fracture (Spalling) of Metals," *Progress in Materials Science*, vol. 28, no. 1, pp. 1–96, 1983.

[80] Jones, W. B., "Effects of Solid State Precipitation on Dynamic Fracture," Master's thesis, University of Washington, 1973.

[81] Meyers, M. A., *Dynamic Behavior of Materials*. New York: Wiley, 1994.

[82] Rankine, W. J. M., "On the Thermodynamic Theory of Waves of Finite Longitudinal Disturbance," *Philosophical Transactions of the Royal Society of London*, vol. 160, pp. 277–288, 1870.

[83] Hugoniot, H. J., "Memoir on the Propagation of Movements in Bodies, Especially Perfect Gases (First Part)," *Journal de l'Ecole Polytechnique*, vol. 57, pp. 3–97, 1887.

[84] Kanel, G. I., Razorenov, S. V., and Fortov, V. E., "Kinetics of Spallation Rupture in the Aluminum Alloy AMg6M," *Journal of Applied Mechanics and Technical Physics*, vol. 25, no. 5, pp. 707–711, 1984.

[85] Barker, L. M. and Hollenbach, R. E., "LASER Interferometer for Measuring High Velocities of any Reflecting Surface," *Journal of Applied Physics*, vol. 43, no. 11, pp. 4669–4675, 1972.

[86] DeCarli, P. S., Erlich, D. C., Hall, L. B., Bly, R. G., Whitson, A. L., Keough, D. D., and Curran, D., "Stress-Gage System for the Megabar (100 GPa) Range," Defense Nuclear Agency DNA 4066F, Stanford Research Institute, 1976.

[87] Chhabildas, L. C. and Graham, R. A., "Developments in Measurement Techniques for Shock-Loaded Solids," in *Techniques and Theory of Stress Measurements for Shock-Wave Applications*, vol. 83, pp. 1–18, American Society of Mechanical Engineers, Applied Mechanics Division, 1987.

[88] Benedick, W. B. and Neilson, R. W., "Measurement of Wave Profiles in Shock-Loaded Solids," *High Temp High Pressures*, vol. 10, no. 4, p. 379, 1978. as reported by Graham, R. A. and Asay, J. R.

[89] Bauer, F., *Behavior of Ferroelectric Ceramics and PVF_2 Polymers Under Shock Loading*, pp. 251–267. No. 78 in AIP Conference Proceedings, 1981.

[90] Graham, R., Neilson, F., and Benedick, W., "Piezoelectric Current from Shock-Loaded Quartz—A Submicrosecond Stress Gauge," *Journal of Applied Physics*, vol. 36, no. 5, pp. 1775–1783, 1965.

[91] Graham, R., *Shock Compression of Solids as a Physical-Chemical-Mechanical Process*, pp. 11–18. Proceedings of the American Physical Society, 1988.

[92] Boteler, J. M. and Dandekar, D. P., *Dynamic Response of 5083-H131 Aluminum Alloy*, vol. 955 of *AIP Conference Proceedings*, pp. 481–484. 2007.

[93] Dwivedi, S. K., Asay, J. R., and Gupta, Y. M., "Two-Dimensional Mesoscale Simulations of Quasielastic Reloading and Unloading in Shock Compressed Aluminum," *Journal of Applied Physics*, vol. 100, no. 8, pp. 083509–1—083509–15, 2006.

[94] Boteler, J. M. and Dandekar, D. P., "Dynamic Response of Two Strain-Hardened Aluminum Alloys," *Journal of Applied Physics*, vol. 100, no. 5, pp. 054902–1—054902–8, 2006.

[95] Borvik, T., Clausen, A. H., Hopperstad, O. S., and Langseth, M., "Perforation of AA5083-H116 Aluminium Plates with Conical-Nose Steel Projectiles—Experimental Study," *International Journal of Impact Engineering*, vol. 30, no. 4, pp. 367–384, 2004.

[96] Clausen, A. H., Borvik, T., Hopperstad, O. S., and Benallal, A., "Flow and Fracture Characteristics of Aluminium Alloy AA5083-H116 as Function of Strain Rate, Temperature and Triaxiality," *Materials Science and Engineering A*, vol. 364, no. 1–2, pp. 260–272, 2004.

[97] Fagerholt, E., Grytten, F., Gihleengen, B. E., Langseth, M., and Borvik, T., "Continuous Out-of-Plane Deformation Measurements of AA5083-H116 Plates Subjected to Low-Velocity Impact Loading," *International Journal of Mechanical Sciences*, vol. 52, no. 5, pp. 689–705, 2010.

[98] Grytten, F., Brvik, T., Hopperstad, O. S., and Langseth, M., "Low Velocity Perforation of AA5083-H116 Aluminium Plates," *International Journal of Impact Engineering*, vol. 36, no. 4, pp. 597–610, 2009.

[99] Laber, M. W., Brar, N. S., and Rosenberg, Z., *Shock Response of 5083-O Aluminum*, vol. 429 of *AIP Conference Proceedings*, pp. 451–454. 1998.

[100] Seaman, L., Curran, D. R., and Shockey, D. A., "Computational Models for Ductile and Brittle Fracture," *Journal of Applied Physics*, vol. 47, no. 11, pp. 4814–4826, 1976.

[101] Thissell, W. R., Zurek, A. K., Macdougall, D. A. S., Miller, D., Everett, R., Geltmacher, A., Brooks, R., and Tonks, D., *The Effect of Material Cleanliness on Dynamic Damage Evolution in 10100 Cu*, vol. 620 of *AIP Conference Proceedings*, pp. 475–478. 2002.

[102] Davison, L. and Stevens, A. L., "Continuum Measures of Spall Damage," *Journal of Applied Physics*, vol. 43, no. 3, pp. 988–994, 1972.

[103] Tuler, F. R. and Butcher, B. M., "Criterion for Time Dependence of Dynamic Fracture," *International Journal of Fracture Mechanics*, vol. 4, no. 4, pp. 431–437, 1968.

[104] Barbee, T., Seaman, L., Crewdson, R., and Curran, D., "Dynamic Fracture Criteria for Ductile and Brittle Metals," *Journal of Materials*, vol. 7, no. 3, pp. 393–401, 1972.

[105] Seaman, L., Curran, D. R., and Crewdson, R. C., "Transformation of Observed Crack Traces on a Section to True Crack Density for Fracture Calculations," vol. 49, no. 10, pp. 5221–5229, 1978.

[106] Curran, D. R., Shockey, D. A., and Seaman, L., "Dynamic Fracture Criteria for a Polycarbonate," *Journal of Applied Physics*, vol. 44, no. 9, pp. 4025–4038, 1973.

[107] Cochran, S. and Banner, D., "Spall Studies in Uranium," *Journal of Applied Physics*, vol. 48, no. 7, pp. 2729–2737, 1977.

[108] Turneaure, S. J., Dwivedi, S. K., and Gupta, Y. M., "Shock-Wave Induced Tension and Spall in a Zirconium-Based Bulk Amorphous Alloy," *Journal of Applied Physics*, vol. 101, no. 4, pp. 043514–1—043514–5, 2007.

[109] Gray III, G. T., Bourne, N. K., and Henrie, B. L., "On the Influence of Loading Profile upon the Tensile Failure of Stainless Steel," *Journal of Applied Physics*, vol. 101, no. 9, pp. 093507–1—093507–9, 2007.

[110] Escobedo, J. P., Brown, E. N., Trujillo, C. P., Cerreta, E. K., and Gray III, G. T., "The Effect of Shock-Wave Profile on Dynamic Brittle Failure," *Journal of Applied Physics*, vol. 113, no. 10, 2013.

[111] Billingsley, J. P., "The Decay Limit of the Hugoniot Elastic Limit," *International Journal of Impact Engineering*, vol. 21, no. 4, pp. 267–281, 1998.

[112] Arvidsson, T. E., Gupta, Y. M., and Duvall, G. E., "Precursor Decay in 1060 Aluminum," *Journal of Applied Physics*, vol. 46, no. 10, pp. 4474–4478, 1975.

[113] Barker, L. M., Butcher, B. M., and Karnes, C. H., "Yield-Point Phenomenon in Impact-Loaded 1060 Aluminum," *Journal of Applied Physics*, vol. 37, no. 5, pp. 1989–1991, 1966.

[114] Nicholas, T., Rajendran, A. M., and Grove, D. J., "Analytical Modelling of Precursor Decay in Strain-Rate Dependent Materials," *International Journal of Solids and Structures*, vol. 23, no. 12, pp. 1601–1614, 1987.

[115] U.S. Department of Defense, *Detail Specification MIL-DTL-46027K(MR): Armor Plate, Aluminum Alloy, Weldable 5083, 5456, & 5059*, 2007.

[116] Dwivedi, S. K., "Shock-1D: A Generic One-Dimensional (1D) Code for Shock Response of Materials," January 2013. Unpublished Report.

[117] U.S. Department of Defense, *Military Handbook - MIL-HDBK-5H: Metallic Materials and Elements for Aerospace Vehicle Structures (Knovel Interactive Edition)*, 2003. http://www.knovel.com/web/portal/browse/display?_EXT_KNOVEL_DISPLAY_bookid=754&VerticalID=750.

[118] Huang, H. and Asay, J. R., "Compressive Strength Measurements in Aluminum for Shock Compression over the Stress Range of 4-22 GPa," *Journal of Applied Physics*, vol. 98, no. 3, pp. 033524–1—033524–16, 2005.

[119] Johnson, J. N., Hixson, R. S., Tonks, D. L., and Zurek, A. K., "Rate-Dependent Spallation Properties of Tantalum," in *Shock Compression of Condensed Matter* (Schmidt, S. C. and Tao, W. C., eds.), no. 370, Part 1&2 in AIP Conference Proceedings, pp. 523–526, 1996.

[120] U.S. Army Research Laboratory, *Fabrication of High-Strength Lightweight Metals for Armor and Structural Applications*, 2013. SBIR Contract W911QX-11-C-0023, Topic No. A10-060.

[121] Chandler, H., *Heat Treater's Guide: Practices and Procedures for Nonferrous Alloys*. Materials Park, OH: ASM International, 1996.

[122] Saltykov, S. A., *The Determination of the Size Distribution of Particles in an Opaque Material from a Measurement of the Size Distribution of their Sections*, ch. Stereology, pp. 163–173. New York: Springer-Verlag, 1967.

VITA

Publications

1. R.L. Whelchel, G.B. Kennedy, S.K Dwivedi, T.H. Sanders, and N.N. Thadhani, "Spall Behavior of Rolled Aluminum 5083-H116 Plate," *Journal of Applied Physics*, vol. 113, pp. 233506-1-233506-10, 2013.

2. R.L. Whelchel, N.N. Thadhani, T.H. Sanders, L.J. Kecskes, and C.L. Williams, "Spall Properties of Al 5083 Plate Fabricated using Equi-Channel Angular Pressing (ECAP) and Rolling," in *Shock Compression of Condensed Matter - 2014, Seattle, Washington, USA, 2013*

Presentations

1. "Spall Properties of Al 5083 Plate Fabricated using Equi-Channel Angular Extrusion and Rolling," *APSSCCM/AIRAPT Joint Conference*, Seattle, WA, July 2013.

2. "Effects of Microstructure on Dynamic Mechanical Behavior of Al 5083," *PRICM-8*, Waikola, Hawaii, August 2013.

Awards and Activities

1. **President's Fellow**: 2010-2012

2. **Graduate Chair**, Graduate Student Advisory Group (School of MSE): 2011-2013

3. **Graduate Representative**, Library Graduate Student Advisory Board: 2011-2012

4. **Secretary**, Materials Research Society (Student Chapter): 2011-2012

5. **Secretary**, Georgia Tech Materials Society (Student Chapter): 2011-2012

6. **Graduate Chair**, Georgia Tech Materials Society: 2010-2011